Performance Evaluation of Satellite Communication Systems Operating in the Q/V/W Bands

Dr. Lorenzo Luini and Prof. Carlo Capsoni

Politecnico di Milano
Dipartimento di Elettronica, Informazione e Biongegneria
Piazza Leonardo Da Vinci 32
Milano, 20133 ITALY

Report Date: June 2013

Final Report from 1 July 2012 to 30 June 2013

REPORT DOCUMENTATION PAGE

1. REPORT DATE *(DD-MM-YYYY)* 30 June 2013	2. REPORT TYPE Final Report	3. DATES COVERED *(From – To)* 1 July 2012 – 30 June 2013

4. TITLE AND SUBTITLE **Performance Evaluation of Satellite Communication Systems Operating in the Q/V/W Bands**	5a. CONTRACT NUMBER **FA8655-12-1-2062**
	5b. GRANT NUMBER **Grant 12-2062**
	5c. PROGRAM ELEMENT NUMBER **61102F**
6. AUTHOR(S) Dr. Lorenzo Luini and Prof. Carlo Capsoni	5d. PROJECT NUMBER
	5d. TASK NUMBER
	5e. WORK UNIT NUMBER

7. PERFORMING ORGANIZATION NAME(S) AND ADDRESS(ES) Politecnico di Milano Dipartimento di Elettronica, Informazione e Biongegneria Piazza Leonardo Da Vinci 32 Milano, 20133 ITALY	8. PERFORMING ORGANIZATION REPORT NUMBER N/A

9. SPONSORING/MONITORING AGENCY NAME(S) AND ADDRESS(ES) EOARD Unit 4515 APO AE 09421-4515	10. SPONSOR/MONITOR'S ACRONYM(S) AFRL/AFOSR/IOE (EOARD)
	11. SPONSOR/MONITOR'S REPORT NUMBER(S) **AFRL-AFOSR-UK-TR-2013-0029**

12. DISTRIBUTION/AVAILABILITY STATEMENT

Distribution A: Approved for public release; distribution is unlimited.

13. SUPPLEMENTARY NOTES

14. ABSTRACT

In the near future, Satellite Communication (SatCom) systems are expected to deliver advanced services both in the broadcasting domain (e.g. multiple parallel information streams using different code rates) and in the interactive domain (e.g. worldwide high data rate connectivity to the Internet). The need of very large bandwidths, necessary to support these kinds of services, is pushing towards the employment of high operational frequencies (Ka band and possibly above for the user terminals, Q/V and W bands for gateways). Whilst other advantages originate from the use of frequencies higher than 20 GHz (e.g. smaller and lighter terminals, reduced channel congestion, limited interference issues), the main drawback certainly comes from the increasingly detrimental effects induced by atmospheric constituents on radio waves. Thus, as the frequency increases, the design of reliable SatCom systems becomes critical, especially in the Q/V and W bands in which atmospheric fades are so strong that the traditional planning approach based on fixed power margins is no longer effective either because of technological constraints and/or extremely high costs. In this scenario, smart solutions known as Fade Mitigation Techniques (FMTs) are mandatory to optimize the system resources (e.g. dynamic reconfiguration of the available onboard power) or to guarantee high-availability of the system even under extreme atmospheric conditions (e.g. site diversity). This, in turn, triggers the need of more complex models not only aiming at accurately and reliably predicting the attenuation caused by all atmospheric constituents (gases, clouds and hydrometeors), but also able to simulate complex systems implementing FMTs and to estimate their performance in enhancing the delivered Quality of Service (QoS). This research activity focused on the performance evaluation of SatCom systems operating in the Q/V and W bands. Given the lack of direct beacon measurements and the limited availability of radiometric measurements at frequencies higher than 50 GHz, in order to achieve this goal, it is of paramount importance to employ the most reliable and accurate propagation prediction models available nowadays in the literature.

15. SUBJECT TERMS

EOARD, Satellite Communications, Atmospheric Interferance Modeling

16. SECURITY CLASSIFICATION OF:			17. LIMITATION OF ABSTRACT	18, NUMBER OF PAGES	19a. NAME OF RESPONSIBLE PERSON James H. Lawton, PhD
a. REPORT UNCLAS	b. ABSTRACT UNCLAS	c. THIS PAGE UNCLAS	SAR	164	19b. TELEPHONE NUMBER *(Include area code)* +44 (0)1895 616187

Dipartimento di Elettronica, Informazione e Biongegneria

Politecnico di Milano

20133 Milano (Italy)
Piazza Leonardo Da Vinci 32
Tel. (+39) 02-23993400
Telefax (+39) 02-23993587

Reference: Final Report of EOARD Award FA8655-12-1-2062
Issue: v01

PERFORMANCE EVALUATION OF SATELLITE COMMUNICATION SYSTEMS OPERATING IN THE Q/V/W BAND

EOARD AWARD FA8655-12-1-2062

EOARD Program Manager: Dr. James Lawton

PERFORMANCE EVALUATION OF SATELLITE COMMUNICATION SYSTEMS OPERATING IN THE Q/V/W BAND

Final Report

Table of contents

List of Figures

List of Tables

1.　INTRODUCTION

In the near future, Satellite Communication (SatCom) systems are expected to deliver advanced services both in the broadcasting domain (e.g. multiple parallel information streams using different code rates) and in the interactive domain (e.g. worldwide high data rate connectivity to the Internet). The need of very large bandwidths, necessary to support these kinds of services, is pushing towards the employment of high operational frequencies (Ka band and possibly above for the user terminals, Q/V and W bands for gateways). Whilst other advantages originate from the use of frequencies higher than 20 GHz (e.g. smaller and lighter terminals, reduced channel congestion, limited interference issues), the main drawback certainly comes from the increasingly detrimental effects induced by atmospheric constituents on radio waves. Thus, as the frequency increases, the design of reliable SatCom systems becomes critical, especially in the Q/V and W bands in which atmospheric fades are so strong that the traditional planning approach based on fixed power margins is no longer effective either because of technological constraints and/or extremely high costs. In this scenario, smart solutions known as Fade Mitigation Techniques (FMTs) are mandatory to optimize the system resources (e.g. dynamic reconfiguration of the available onboard power) or to guarantee high-availability of the system even under extreme atmospheric conditions (e.g. site diversity). This, in turn, triggers the need of more complex models not only aiming at accurately and reliably predicting the attenuation caused by all atmospheric constituents (gases, clouds and hydrometeors), but also able to simulate complex systems implementing FMTs and to estimate their performance in enhancing the delivered Quality of Service (QoS).

This research activity is focused on the performance evaluation of SatCom systems operating in the Q/V and W bands whose Earth station(s) is (are) located in the area of Rome, NY (USA). Given the lack of direct beacon measurements and the limited availability of radiometric measurements at frequencies higher than 50 GHz, in order to achieve this goal, it is of paramount importance to employ the most reliable and accurate propagation prediction models available nowadays in the literature.

Chapter 2 includes a brief description of the fundamental physical concepts at the basis of the impairments induced by atmospheric constituents on radio waves. Afterwards, this chapter deals with the review of the main propagation prediction models available in the literature, specifically of models for the estimation of attenuation statistics associated to gases (water vapor and oxygen), clouds and hydrometeors (both effects of rain and of the melting layer), as well as of methodologies for the prediction of rain rate statistics (the main input to any rain attenuation model) and of the advantage, in terms of system availability, achieved using site diversity schemes under rainy conditions.

Chapter 3 focuses on MultiEXCELL (Multi EXponential CELL) and SMOC (Stochastic MOdel Of Clouds), two models recently developed at Politecnico di Milano for the simulation of the interaction of SatCom systems with rain fields and cloud fields, separately. The rationale and the development of the two models are described in detail to highlight their usefulness and potentialities in the comprehensive evaluation of the performance of SatCom systems, including those implementing site diversity schemes.

Chapter 4 deals with the assessment of the prediction accuracy of some propagation models, including MultiEXCELL and SMOC, which have been selected on the basis of their soundness and reliability. Such models are first described in detail and afterwards extensive

tests are carried out to evaluate their performance in predicting rain attenuation, cloud attenuation and the advantage offered by the implementation of site diversity. The reference database employed in this testing activity consists of measurements gathered by Study Group 3 of the International Telecommunication Union – Radio communication sector (ITU-R) for rain attenuation and site diversity, and collected from data previously published in the literature for cloud attenuation.

Based on the models' performance results, Chapter 5 presents the thorough assessment of the atmospheric attenuation impairing a high frequency (Q/V and W bands) SatCom system with transceiver(s) located in the area of Rome, NY, and transponders in the 100° W orbital position. The attenuation statistics separately due to gases, clouds and rain are predicted by making only use of the methodologies recommended by ITU-R on one side (P.676-9, P.840-5 and P.618-10), as well as by exploiting the potentialities of MultiEXCELL and SMOC, on the other side. Predictions using the different models are compared and duly commented to provide a quantitative evaluation of the total atmospheric attenuation expected to impair the system at 50, 70, 80 and 90 GHz. In addition, rain fields and cloud fields generated by MultiEXCELL and SMOC are used to investigate the performance of site diversity schemes employing two or three Earth stations to exploit the inhomogeneity of atmospheric constituents and, thus, mitigate the associated high fades.

Finally, based on the results obtained in Chapter 5, Chapter 6 draws conclusions on the feasibility and performance of the considered SatCom system.

2.   REVIEW OF STATISTICAL ATTENUATION PREDICTION MODELS

This Chapter offers a state-of-the-art review of the models conceived for the prediction of the attenuation suffered from Earth-space links due to the constituents having a direct impact on the propagation of electromagnetic waves at frequencies higher than 10 GHz, namely gases, clouds (non-precipitating atmosphere) and hydrometeors (precipitating atmosphere).

2.1.   Non-precipitating atmosphere

The atmosphere is a thermodynamic system containing water in vapor and liquid state, gases and aerosol, surrounding the Earth up to 100 km. For radio wave propagation only the lower layer up to approximately 30 km in height is of concern. The atmosphere is commonly described through temperature, pressure and density of its main components (gases and water). These parameters are highly variable both in space and in time, but to a first approximation, it is possible to make reference to the "standard atmosphere" based on the USA Standard Atmosphere generalized model, which describes the average conditions at mid latitude of the vertical structure of the atmosphere through profiles of temperature, pressure and water vapor density [STD ATM].

Nitrogen is the gas with the highest volume content but its effects are of some relevance only in the infrared region. Oxygen is around 21% of the total mass in volume with a concentration that decreases with altitude and pressure. The space-time distribution of oxygen can be considered as constant to a first approximation. Other gases (argon, neon, pollutants such as carbon dioxide, CO_2, and sulphur dioxide, SO_2) do not affect the propagation at in the 1-100 GHz range.

Water vapor is always present in the atmosphere and is characterized by a moderate time and space variability. Its amount depends mostly on temperature and humidity, and, therefore, on the climatic zone and on the season. The range of variability of water vapor concentration is between 0.01 g/m^3 in very cold, dry climates and 30 g/m^3 in hot humid climates.

Liquid water is present in the atmosphere in forms of large precipitating drops (rain), as well suspended (small) droplets in clouds and fog. Cloud occurrence (clouds cover about 50% of the Earth surface and 50% of the yearly time) mainly depends on humidity and temperature.

Oxygen, water vapor and clouds have a definite impact on radio waves above approximately 20 GHz, and cause extra path attenuation whose amount is strictly dependent on frequency as detailed below.

2.1.1.   Gaseous attenuation modeling

Oxygen and water vapor are the gaseous components of the atmosphere which influence the electromagnetic wave propagation in the frequency range from 20 up to 300 GHz. Other gases have to be taken into account only at higher frequencies. The weather situation with no clouds (and therefore no rain) and no fog is usually addressed as "clear sky" condition.

The oxygen absorption is mainly due to the resonance of oxygen molecules especially in the band from 50 GHz to 70 GHz, at 118.7 GHz and above 300 GHz. For this reason, oxygen

attenuation is negligible up to 40 GHz, becomes important around 50 GHz and is dominant around 60 GHz.

The oxygen concentration depends on air pressure and temperature. The former is characterized by a decreasing exponential profile with the height, while the latter is highly influenced by daily, seasonal and geographical variations. Oxygen absorption increases with the decrease in the temperature.

The water vapor absorption, due to the molecular interaction with electromagnetic waves, can be calculated as the sum of two terms, which are linear and quadratic functions of the water vapor density, respectively. Examples of absorption lines are 22.253 GHz, 183.3 GHz and 324.4 GHz. Water vapor absorption is related to meteorological parameters like pressure, temperature and water vapor density.

The basic procedure to calculate the gaseous attenuation consists in two steps:

1) calculation of the specific attenuation at each point along the propagation path;

2) calculation of the total path attenuation by integration of all the contributions.

In practice this approach is routinely unfeasible because it would require the knowledge at any time of the complete spatial distribution along the path of meteorological parameters like air pressure, temperature and gases concentration. Therefore, mainly two alternative approaches are typically considered:

1) Physically-based models (Liebe) [Liebe et al., 1993]: the most precise (but also computationally demanding) method consists in dividing the propagation path into horizontally homogeneous layers and in computing the specific attenuation, for each of them, from the related meteorological parameters. Finally the total attenuation is built up by all the layers' contributions. This method requires vertical profiles of meteorological data as input.

2) Semi-empirical models (ITU-R) [ITU-R P.676-9, 2012]: these approaches approximate the calculation of the specific attenuation for a reference level (typically the ground level) and use the equivalent height concept to account for the vertical gaseous distribution. These methods only require reference values at ground level.

The main drawback of physically-based methods, which allow the precise calculation of the gases contribution to the total path attenuation, is the difficulty in obtaining in any site the vertical profiles of air pressure, temperature and relative humidity. In fact, radio sounding profiles are collected only in a limited number of locations and launches are performed typically only two or four times per day. Moreover, the reliability of radio sonde data is not always assured. On the other hand, statistics of many meteorological parameters at ground level are easily retrievable all over the world and it is therefore straightforward to use semi-empirical models, which, however, give less accurate results.

Thanks to the computational accuracy of the Liebe's model, its outputs are usually considered as the reference, against which all the other models are tested.

2.1.1.1.   Liebe's Model (MPM93) for the calculation of gaseous attenuation

The "Microwave Propagation Model", in its 1993 version MPM93 [Liebe et al., 1993], developed by H. J. Liebe at the end of a long-term research on spectroscopic effects, is generally recognized as one of the most accurate and complete model for electromagnetic

wave propagation in the atmosphere at millimeters wavelengths. Other well-accredited models have been proposed by Rosenkranz [Rosenkranz, 1998] and Liljegren et al [Liljegren et al., 2005].

Using vertical profiles of the atmospheric parameters of pressure, temperature and relative humidity, duly validated after proper processing and consistency tests, the MPM93 model computes the atmospheric radio refractivity, at any frequency, for each layer along the propagation path. Input data are routinely collected for weather forecasting purposes by national and international meteorological organizations, such as ECMWF in Europe or NOAA in America. Hereinafter the MPM93 model is presented in its latest version.

The radio refractive index n of a medium is defined as the ratio of the light speed in the vacuum to the speed in the medium itself. Being n very close to unity, the radio refractivity N, i.e. deviation of n from unity in parts per million, is commonly used:

$$N = 10^6 (n - 1) \quad \text{(ppm)} \qquad (2\text{-}1)$$

where $n = n' - jn'' = \sqrt{\varepsilon}$ is the refractive index and $\varepsilon = \varepsilon' - j\varepsilon''$ is the complex permittivity of the medium (the imaginary part of the refractive index accounts for the medium losses).

The radio refractivity N is a complex variable, locally function of meteorological parameters and can be expressed as:

$$N = N_0 + N(f) \quad \text{(ppm)} \qquad (2\text{-}2)$$

where:

f = frequency in GHz

N_0 = non-dispersive term of radio refractivity

$N = N'(f) + jN''(f)$ = dispersive term of radio refractivity

$N'(f)$ = dispersive phase shifting term

$N''(f)$ = frequency dependent absorption term

The frequency independent term of the radio refractivity can be expressed as the sum of three terms:

$$N_0 = N_1 + N_2 + N_3 \quad \text{(ppm)} \qquad (2\text{-}3)$$

where:

$N_1 = 0.2588 \, p_d \, \theta$ = non-dispersive contribution of oxygen

$N_2 = (4.163\theta + 0.239) \, e \, \theta$ = non-dispersive contribution of water vapor

$N_3 = N0_w$ = non-dispersive term due to liquid water or ice particles

p_d = pressure of dry air (hPa)

$\theta = 300/(T+273.15)$ reciprocal temperature (K^{-1})

$\theta_1 = 373.16/(T+273.15)$ (K^{-1})

$\theta_2 = 273.16/(T+273.15)$ (K^{-1})

T = temperature (°C)

$e = \dfrac{RH}{100} 10^F$ = water vapor pressure (hPa)

For $T > -40\,^\circ$ C:

$$F = -7.90298\,(\theta_1 - 1) + 5.02808\,\log_{10}(\theta_1) +$$
$$-1.3816\cdot 10^{-7}\,(10^\alpha - 1) + 8.1328\,10^{-3}\,(10^\beta - 1) + \log_{10}(1013.246)$$

(2-4)

with $\alpha = 11.344\,(1 - 1/\theta_1)$ and $\beta = -3.49149\,(\theta_1 - 1)$.

For $T <= -40\,^\circ$ C:

$$F = -9.09718\,(\theta_2 - 1) - 3.56654\,\log_{10}(\theta_2) + 0.876793\,(1 - 1/\theta_2) + \log_{10}(6.1071) \quad (2\text{-}5)$$

$p = p_d + e$ = total air pressure (hPa)

RH = relative humidity (%)

$\rho_v = \dfrac{216.51}{T + 273.15}\,e$ = water vapor density (g/m^3)

The frequency dependent terms of radio refractivity, $N(f)$, consists of the contributions of line spectra of oxygen and water vapor, non resonant oxygen terms, water vapor continuum:

$$N(f) = N_0(f) + N_N(f) + N_V(f) + N_C(f) \quad \text{(ppm)} \tag{2-6}$$

where:

$N_0(f) = \sum\limits_k S_k F_k(f)$ = line spectra component of oxygen, consisting in 44 lines (ppm)

$S_k = \dfrac{a_1}{v_k}\,p_d\,\theta^3\,\exp[a_2\,(1-\theta)]$ = strength of oxygen lines

$F_k(f) = f\left[\dfrac{1 - j\delta_k}{v_k - f - j\gamma_k} - \dfrac{1 + j\delta_k}{v_k + f + j\gamma_k}\right]$ = line shape of oxygen lines

v_k = resonant frequency of oxygen lines

$\gamma_k = a_3\,10^{-3}\,\left(p_d\,\theta^{(0.8 - a_1)} + 1.1\,e\,\theta\right)$ = line width of oxygen lines

$\delta_k = \left(a_5\,p_d\theta^{(0.8 - a_4)} + a_6\theta\right)\cdot p\theta^{0.8}$ = overlap parameter of oxygen lines

$N_N(f) = S_0 F_0(f) + j\,S_n F''_n(f)$ = non-resonant term due to oxygen and N_2 (ppm)

$S_0 = 6.14\,10^{-5}\,p_d\theta^2$ = line strength of Debye spectrum of oxygen

$F_0(f) = -f/(f + j\gamma_0)$ = Debye line shape of oxygen

$\gamma_0 = 0.56\,10^{-3}\,p_d\,\theta^{0.8}$ = oxygen relaxation frequency

$S_n = 1.4\,10^{-12}\,p_d^2\,\theta^{3.5}$ = strength of N_2 absorption line

$F_n''(f) = f/(1 + 19\,10^{-5}\,f^{1.5})$ = shape of N_2 absorption line

$N_V(f) = \sum\limits_i S_l F_l(f)$ = line spectra component of water vapor (34 lines) (ppm)

$$S_l = \frac{b_1}{v_l} \, e \, \theta^{3.5} \, \exp\left[b_2 \, (1-\theta)\right] = \text{strength of water vapor lines}$$

$$F_l(f) = f\left[\frac{1}{v_l - f - j \, \gamma_l} - \frac{1}{v_l + f + j \, \gamma_l}\right] = \text{line shape of water vapor lines}$$

l = resonant frequency of water vapor lines

$$\gamma_l = b_3 \, 10^{-3} \left(b_4 \, e \, \theta^{b_6} + p_d \, \theta^{b_5}\right) = \text{line width of water vapor lines}$$

$N_C(f)$ = water vapor continuum term (ppm), *pseudo-line* located at 1780 GHz

The specific attenuation, $\gamma_a(z,f)$ at height z and frequency f, can be derived from the frequency dependent absorption term $N''(f)$:

$$\gamma_a(z, f) = 0.1820 \, f \, N''(f) \quad \text{(dB/km)} \tag{2-7}$$

The specific path delay, $d(z,f)$ at height z and frequency f, can be derived from the sum of the non-dispersive term, N_0, with the dispersive phase shifting term, $N'(f)$:

$$d(z, f) = 3.3356 \left[N_0 + N'(f)\right] \quad \text{(ps/km)} \tag{2-8}$$

The total path attenuation due to gases, at frequency f and along a slant path at elevation θ, can be derived assuming that the atmosphere is longitudinally homogeneous as:

$$A_g = \int_h^\infty \frac{\gamma_a(z)}{\sin[\Phi(z)]} \, dz \quad \text{(dB)} \tag{2-9}$$

where:

$\gamma_a(z, f) = 0.1820 \, f \, N''(f)$ = specific attenuation of gases at height z and frequency f, see equation (7) (dB/km)

$$\Phi(z) = \arccos\left[\frac{(r+h) \, n(h) \, \cos(\vartheta)}{(r+z) \, n(z)}\right]$$

r = Earth's radius = 6 370 km

$n(z)$ = air refractive index

h = station altitude

φ = elevation angle (degree). $\varphi \geq 10°$. For elevation angles lower than 10° the ray bending has to be considered.

The Liebe's model allows to calculate the gaseous attenuation up to 1000 GHz. Figure 2-1 shows the frequency spectrum of the zenith gaseous attenuation in Milano, calculated using mean monthly vertical profiles of meteorological parameters [Barbaliscia et al., 1995].

The total attenuation due to atmospheric gases, $A_g(f)$, can be expressed as the sum of total attenuation due to oxygen and water vapor, $A_o(f)$, $A_V(f)$:

$$A_g(f) = A_o(f) + A_V(f) \quad \text{(dB)} \tag{2-10}$$

where:

$$A_o(f) = \frac{1}{\sin(\theta)} \int_0^\infty \gamma_0(z,f)\,dz \; ; \quad A_V(f) = \frac{1}{\sin(\theta)} \int_0^\infty \gamma_V(z,f)\,dz$$

$\gamma_0(z,f) = 0.1820\, f\, [N_0''(f) + N_N''(f)]$ = specific attenuation due to oxygen at frequency f and height z (dB/km)

$N_o''(f)$ = imaginary part of refractivity due to line spectra component of oxygen (ppm)

$N_N''(f)$ = imaginary part of refractivity due to non resonant term due to oxygen and N_2 (ppm)

$\gamma_V(z,f) = 0.1820\, f\, [N_V''(f) + N_C''(f)]$ = specific attenuation due to vapor at frequency f and height z (dB/km)

$N_V''(f)$ = imaginary part of refractivity due to line spectra component of vapor (ppm)

$N_C''(f)$ = imaginary part of refractivity due to vapor continuum term (ppm)

Milano, Mean Monthly Profiles
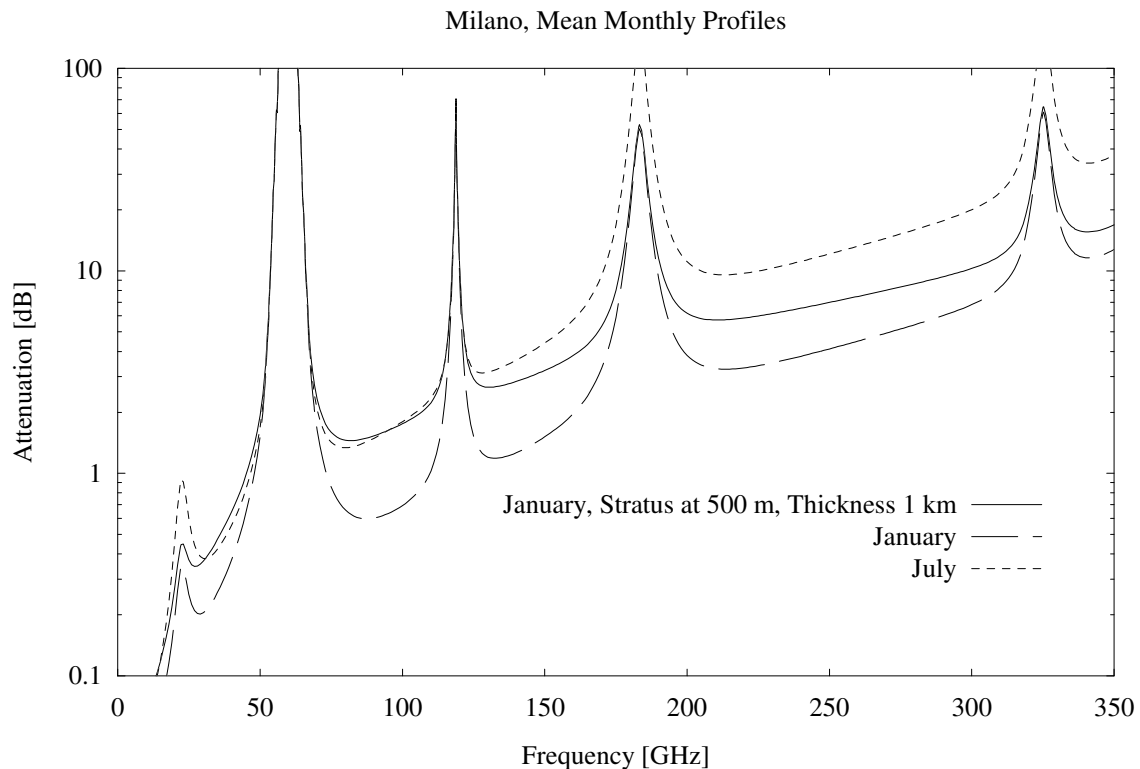
Figure 2-1. Frequency spectrum of the zenith gaseous attenuation in Milano calculated using the mean monthly profiles (January/July). The zenith attenuation due to gases and stratus cloud is also plotted

2.1.1.2.   ITU-R model for gaseous attenuation prediction

As for water vapor, ITU-R Recommendation P.676-9 [ITU-R P.676-9, 2012] first calculates the zenith attenuation in reference conditions at 20.6 GHz as a function of the water vapor total content (*WVC*) in mm (global maps of this parameters are available in [ITU-R P.836-4, 2009]) and then applies a frequency scaling factor. The zenith attenuation can then

be scaled in elevation by the cosecant law [ITU-R P.676-9, 2012], under the assumption of local homogeneity of the atmosphere (absolutely plausible for water vapor).

WVC at an arbitrary site is calculated by bilinear interpolation over the four nearby grid points provided by the global maps [ITU-R P.836-4, 2009], after a preliminary correction to take into account the different height above sea level of the grid points. The formula is:

$$WVC = \sum_{i=1}^{4} w_i \, WVC_i \, e^{(h-h_i)/h_{sh}} \tag{2-11}$$

Where w_i is the weight of the *i*-th contributing grid point, h is the altitude above mean sea level and h_{sh} is the scale height.

The path attenuation (dB) at frequency *f* is obtained from the *WVC* through the following relationship:

$$A_{wv}(f) = \frac{0.0173 \, WVC \, A_{wv,s}(f,T,V,p)}{A_{wv,s}(f_{ref},T_{ref},V_{ref},p_{ref})\sin(\theta)} = \frac{0.0173 \, WVC \, A_{wv,s}(f,T_{ref},V_{ref},p_{ref})}{A_{wv,s}(f_{ref},T_{ref},V_{ref},p_{ref})\sin(\theta)} \tag{2-12}$$

where $A_{wv,s}$ is the specific water vapor attenuation (dB/km) as a function of frequency (*f*), temperature (*T*), water vapor density (*V*) and pressure (*p*), whilst θ is the elevation angle. As $A_{wv,s}$ is rather insensitive to *T*, *V* and *p*, it is possible to use the same values for the above three parameters both at the numerator and at the denominator of the formula (as shown on the right side of (2-12)). The reference values used in the calculations are:

- $f_{ref} = 20.6$ GHz

- $p_{ref} = 780$ hPa

- $V_{ref} = WVC / HV$ ($HV = 4$ km) g/m^3

- $T_{ref} = 14 \ln(0.22 \, WVC/4) + 3$ °C

The complete expression of $A_{wv,s}(f,T,V,p)$ can be found in equation (23a) of recommendation ITU-R P.676-9 [ITU-R P.676-9, 2012].

As for oxygen, recommendation ITU-R P.676-9 proposes a simplified method to calculate the path attenuation $A_o(f)$:

$$A_o(f) = \frac{\gamma_o \, h_o}{\sin(\theta)} \tag{2-13}$$

The term γ_o in equation (2-13) is the approximate specific attenuation due to oxygen (valid up to an altitude of 10 km from the sea level), which results from curve-fitting to the line-by-line calculation reported in the previous section and agrees with the more accurate calculations to within an average of about ±10% at frequencies removed from the centers of major absorption lines. The absolute difference between the results from these algorithms and the line-by-line calculation is generally less than 0.1 dB/km and reaches a maximum of 0.7 dB/km near 60 GHz. The expression of γ_o, reported in detail in equations (22a)-(22u) of [ITU-R P.676-9, 2012], is a function frequency *f* and of the mean annual values of surface pressure p_s and surface temperature T_s, which, in turn can be extracted from global meteorological maps (e.g. recommendation ITU-R P.1510 [ITU-R P.1510, 2001]). The second term in (2-13),

h_0, is the equivalent height for oxygen which is dependent on pressure as follows ($r_p = p_s/1013$):

$$h_o = \frac{6.1}{1 + 0.17 \, r_p^{-1.1}} (1 + t_1 + t_2 + t_3) \qquad (2\text{-}14)$$

where:

$$t_1 = \frac{4.64}{1 + 0.066 \, r_p^{-2.3}} \exp\left[-\left(\frac{f - 59.7}{2.87 + 12.4 \exp(-7.9 \, r_p)}\right)^2\right]$$

$$t_2 = \frac{0.14 \exp(2.12 \, r_p)}{(f - 118.75)^2 + 0.031 \exp(2.2 \, r_p)}$$

$$t_3 = \frac{0.0114}{1 + 0.14 \, r_p^{-2.6}} f \frac{-0.0247 + 0.0001f + 1.61 \times 10^{-6} f^2}{1 - 0.0169f + 4.1 \times 10^{-5} f^2 + 3.2 \times 10^{-7} f^3}$$

2.1.2.   Clouds

A first broad classification of clouds can be made according to their height and their shape or appearance. There are three main categories which are based on the physical structure and process of formation. *Stratiform* clouds appear as extensive thin to moderately thick layers, with some vertical development. In general they are the result of large scale lift of stable air. *Cumuliform* clouds mostly are born in very small areas of limited convection in slightly unstable air or in large areas when the air mass is very unstable. *Cirriform* clouds are high and thin, and appear most of the time at the leading edges of organized weather disturbances. Stratus and stratocumulus clouds from limited convection are usually at low altitudes (2 kilometers or even less).

2.1.2.1.   *Cloud classification*

In Table 2-1, the second column, labeled as *H/V*, represents the ratio between the typical horizontal and the vertical extensions of the cloud type, V_{min} (third column) is the minimum height at which the cloud is usually found, ΔV and H are the physical vertical and horizontal extensions, respectively. ΔV_{eq}, H_{eq} are the equivalent vertical and horizontal extensions of the cloud types assumed as a slab with homogeneous characteristics. As one may appreciate from the table, some cloud types are strictly related to high precipitation probability (rain, snow or hail). As for hail events, they have a very low probability of occurrence and a very limited extent.

Table 2-1. Basic classification of clouds and associated main features

Cloud type	H/V	V_{min} (km)	ΔV (km)	H (km)	ΔV_{eq}	H_{eq}	Constituent	Precipitation type
Cumulus	1	< 2	3-15	ΔV	3	4	Water	Heavy rain hailstones
Stratus	>> 1	Low	00.1-0.1	Several			Water	Rain
Strato-cumulus	>> 1	Low	0.5 -1	Several	0.6	10	Water	Low intensity rain
Alto-stratus	>> 1	Medium		>100			Water	Average intensity rain, snow
Nimbo-stratus	>> 1	Low	2-8		0.8	10	Water	Rain, snow
Cirrus		> 7	Small				Ice crystals	None
Thin cirrus		> 7	Small				Ice crystals	None

2.1.2.2. Water clouds

Water clouds and fog consist of suspended water droplets (whose diameter *D* lies between 1 μm and 100 μm, i.e. 10 to 1000 times smaller than rain drops) of a size much smaller than the wavelengths of interest in this study. As a consequence, the Rayleigh approximation of the Mie scattering theory can be used, according to which cloud attenuation is independent of the drop size distribution (DSD) in cloud for frequencies below about 300 GHz. Thus, cloud attenuation turns out to depend only on the liquid water content (hereinafter referred to as *L*) and on the temperature through its effect on the dielectric properties of water [Liebe et al., 1993]. Unfortunately, *L* is not a standard observable quantity and the main problem in modeling is to estimate *L* from available meteorological data or remote sensing measurements.

Usually, cloud particles are in liquid form above 0 °C and in ice form below about -20 °C to -40 °C depending on the cloud type. In between, cloud droplets exist in a mixture of supercooled water and ice. The attenuation due to ice clouds can be neglected in the microwave region, although ice is responsible for strong signal depolarization.

Typical values of liquid water content are 0.05-0.25 g/m^3, 0.3-1.3 g/m^3 and 2.5 g/m^3 for stratiform, stratocumulus and cumulonimbus, respectively.

Figure 2-2 provides a sketch of the expected DSD for different cloud types [Shettle, 1989].
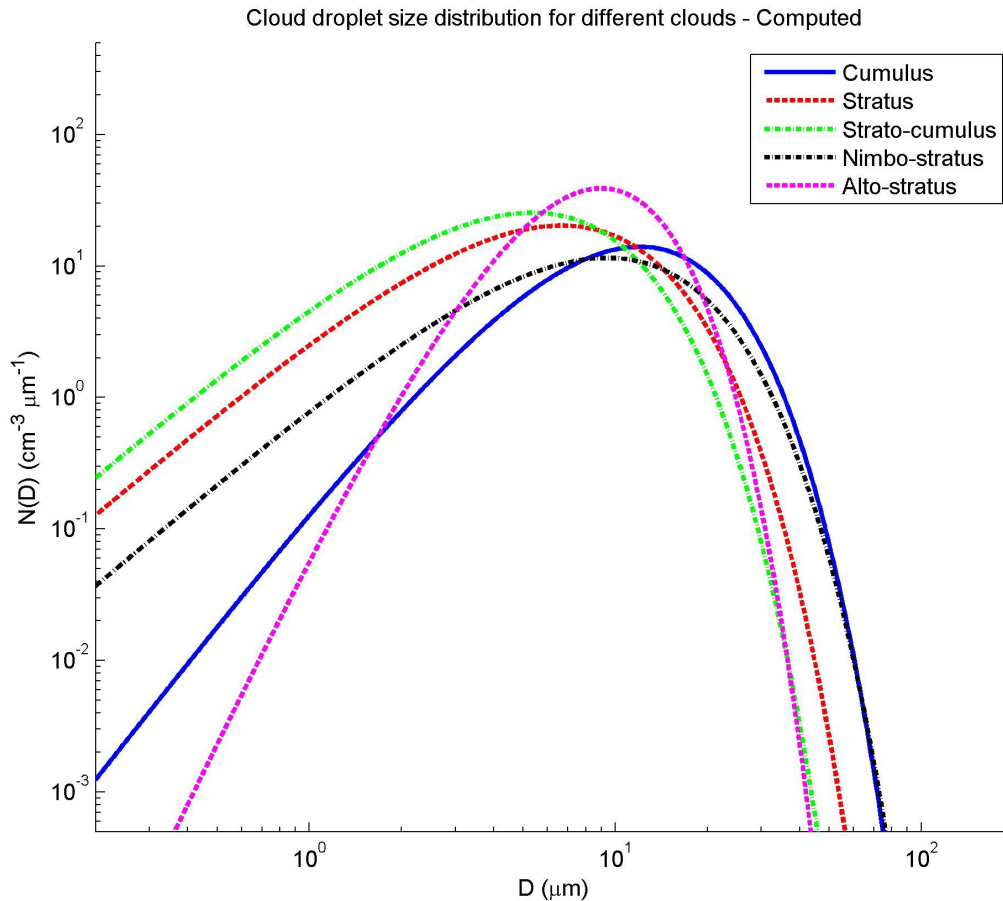
Figure 2-2. Sketch of the expected DSD for different cloud types [Shettle, 1989]

2.1.2.3.   *Ice clouds*

As indicated in Table 2-1, ice clouds form at high altitude. Suspended ice crystals are present for temperatures in the range for $0°$ C $< T <$ -70° and the most frequent habits are plates and needles. At temperatures below -25 °C ice crystals are mainly needles, at temperatures from -25 °C to -9 °C they are mainly plates with a hexagonal basis.

Sizes vary from 20 μm to 4 mm. Characteristic relationships exist between the thickness *h* of plates and their diameter *D*. Similar relationships exist between the diameter *d* and the length *l* of needles [Pruppacher and Klett, 1980].

Common geometrical models used to describe these habits are oblate or prolate spheroids as they are much simpler to manage by electromagnetic solvers. In particular:

- ice needles are modeled as long and narrow prolate spheroids;

- ice plates are modeled as flat oblate spheroids.

The PSD (Particle Size Distribution) is assumed to be of the Gamma type, the parameters being related to air temperature *T* and total ice content.

As in the case of water droplets, aerodynamic effects tend to align the major axes of ice crystals with the horizontal plane. However, differently from what happens with the water droplets, electromagnetic fields of high intensity and rapid variation, as the ones generated

during thunderstorms, can orient ice crystals in a preferred direction. This is one of the reasons for sudden changes that occur in depolarization measurements.

2.1.3.   Cloud attenuation modeling

Also for the calculation of the attenuation due to clouds, two alternative approaches are typically considered:

1) <u>Physically-based models (Liebe)</u> [Liebe et al., 1993]: the most precise (but also more demanding) method consists in dividing the propagation path into horizontally homogeneous layers and in calculating the specific attenuation, for each of them, from the associated meteorological parameters. A middle step of this procedure consists in estimating the liquid water density of clouds as a function of the height by means of cloud detection models [Salonen and Uppala, 1991]. Finally the total attenuation is obtained by summing up all the layers' contributions. This method requires vertical profiles of meteorological data as input.

2) <u>Semi-empirical models (ITU)</u>: these approaches employ effective quantities (e.g. to take into account the vertical profile of the liquid water content as in the ITU-R model [ITU-R P.840-5, 2012]) or integral/cumulative information on clouds (cloud coverage statistics) to approximate the calculation of the attenuation due to clouds.

As already mentioned, the main drawback of physically-based methods, which allow the precise calculation of the clouds contribution to the total path attenuation, is the difficulty in obtaining vertical profiles of air pressure, temperature and relative humidity in any site of interest. In fact, radio sonde profiles are collected only in a limited number of locations and launches are performed typically only two or four times per day. Moreover, the reliability of radio sonde data is not always assured. On the other hand, semi-empirical methods require less complex information as input but also provide less accurate predictions.

2.1.3.1.   *Liebe's Model (MPM93) for the calculation of cloud attenuation*

Accoding to the method proposed by Liebe [Liebe et al., 1993], the specific attenuation γ_c (dB/km) due to clouds is expressed as:

$$\gamma_c = 0.1820\, f\, N_w''(f) \quad \text{(dB/km)} \tag{2-15}$$

where f is the frequency (GHz). The imaginary part of the complex refractivity $N_w''(f)$, dependent on the liquid water content, the temperature and the frequency, can be written in the form:

$$N_w'' = \frac{9}{2} \frac{w}{\varepsilon''(1+\eta^2)} \quad \text{(ppm)} \tag{2-16}$$

where:

w = liquid water density (g/m^3)

$\eta^2 = (2+\varepsilon')\big/\varepsilon''$

ε' = real part of the permittivity of water

ε'' = complex part of the permittivity of water.

The real and imaginary part of the permittivity of water are determined using the double-Debye model of [Liebe et al., 1993]:

$$\varepsilon'(f) = \varepsilon_2 + \frac{(\varepsilon_0 - \varepsilon_1)}{1 + (f/f_D)^2} + \frac{(\varepsilon_1 - \varepsilon_2)}{1 + (f/f_S)^2} \tag{2-17}$$

$$\varepsilon''(f) = \frac{f(\varepsilon_0 - \varepsilon_1)}{f_D [1 + (f/f_D)^2]} + \frac{f(\varepsilon_1 - \varepsilon_2)}{f_S [1 + (f/f_S)^2]} \tag{2-18}$$

where:

$\varepsilon_0 = 77.67 + 103.3(\Theta - 1)$

$\varepsilon_1 = 5.48$ and $\varepsilon_2 = 3.51$

$f_D = 20.09 - 142(\Theta - 1) + 294(\Theta - 1)^2$ and $f_S = 590 - 1500(\Theta - 1)$ (GHz)

$\Theta = 300/T$ (with T in Kelvin).

Equations above are valid for frequencies up to 300 GHz over a temperature range from -40 °C to 30 °C.

The liquid water density, the knowledge of which is necessary to apply the model in [Liebe et al., 1993], can be estimated using the cloud detection model developed by Salonen and Uppala in [Salonen and Uppala, 1991] (here the slight modification proposed in [Martellucci et al., 2002] is presented). The model calculates the liquid water content of clouds starting from humidity and temperature relative to different height/pressure levels. Moreover, it allows the computation of the total attenuation due to clouds.

Thus, the overall procedure for the calculation of cloud attenuation from radio sonde data consists in the following four steps:

- cloud detection
- calculation of liquid water density in the cloud
- calculation of the specific attenuation
- numerical integration along the height to calculate total zenith attenuation.

In this section only the first two phases are presented.

Cloud detection

The modified critical humidity function U_C, used for cloud detection, is expressed as:

$$U_C = 1 - \alpha \cdot \sigma(1 - \sigma)[1 + \beta(\sigma - 0.5)] \tag{2-19}$$

where $\alpha = 1.0$, $\beta = \sqrt{3}$ and σ is ratio of the pressure at the considered level and at the surface level. If the measured humidity is higher than the critical one at the same pressure level, i.e. U_C, the level is assumed to be in the cloud. A linear interpolation has been used for the calculation of the base and top of the cloud.

Calculation of liquid water content

Once a level is evaluated to be in the cloud, the next phase is to predict the liquid water content w at that level, which, according to the latest version of [Salonen and Uppala, 1991], is expressed as:

$$w = \begin{cases} w_0\,(1+ct)\left(\dfrac{h_c}{h_r}\right)^{1.4} p_w(t) & t \geq 0\,^\circ C \\[4mm] w_0\,e^{ct}\left(\dfrac{h_c}{h_r}\right)^{1.4} p_w(t) & t < 0\,^\circ C \end{cases} \qquad (\text{g/m}^3) \qquad (2\text{-}20)$$

where:

t = temperature (°C)

h_c = height from the cloud base (m)

$w_0 = 0.17$ (g/m^3)

$c = 0.04$ (°C^{-1})

$h_r = 1500$ (m).

The liquid water fraction $p_w(t)$ is given by:

$$p_w(t) = \begin{cases} 1 & 0\,^\circ C < t \\[2mm] 1 + \dfrac{t}{20} & -20\,^\circ C < t \leq 0\,^\circ C \\[2mm] 0 & t \leq -20\,^\circ C \end{cases} \qquad (2\text{-}21)$$

Figure 2-3 provides an idea of the amount of cloud attenuation (zenithal path) that is expected to affect wireless links operating between 10 GHz and 100 GHz. Different types of clouds are considered with constant liquid water density along the whole cloud profile (see the figure's legend for more details), which points out the strong effects caused by cumulonimbus clouds both because of their large thickness and of their high opacity.

As an example of the whole physically-based procedure outlined above (radio sonde data + Salonen's model for the detection of clouds + Liebe's model for the attenuation calculation), Figure 2-4 depicts the complementary cumulative distribution function (CCDF) of the attenuation due to clouds obtained by exploiting 10 years of radio sonde data collected at Milano-Linate airport twice a day (frequency shifting from 20 to 100 GHz): as expected, significant attenuation levels are expected to strongly affect links in the W band (e.g. approximately 5 dB are exceeded for 1 hour/year).
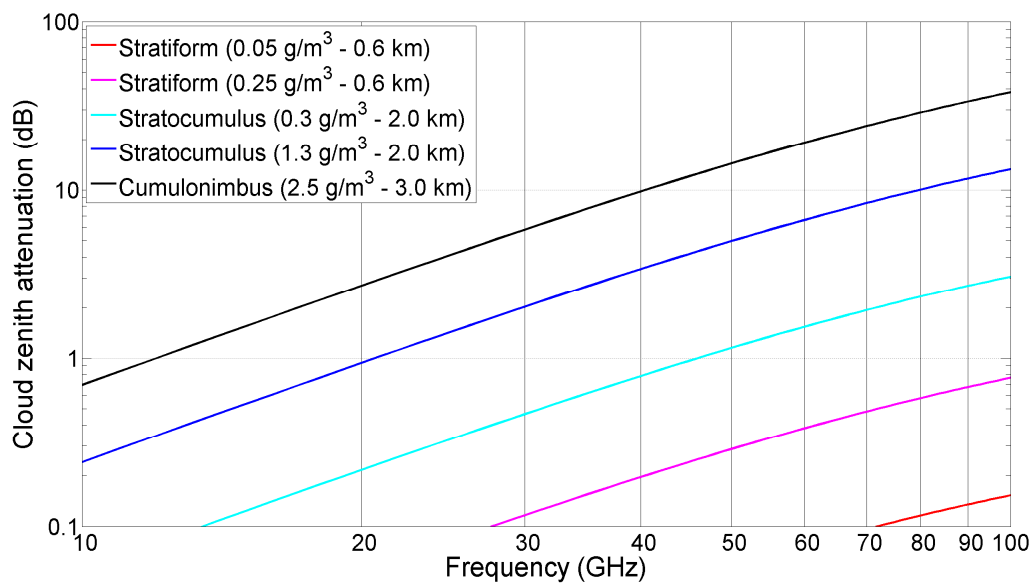
Figure 2-3. Zenith attenuation for different type of clouds as a function of frequency between 10 and 100 GHz (refer to the figure's legend for more details on the values employed in the calculation)
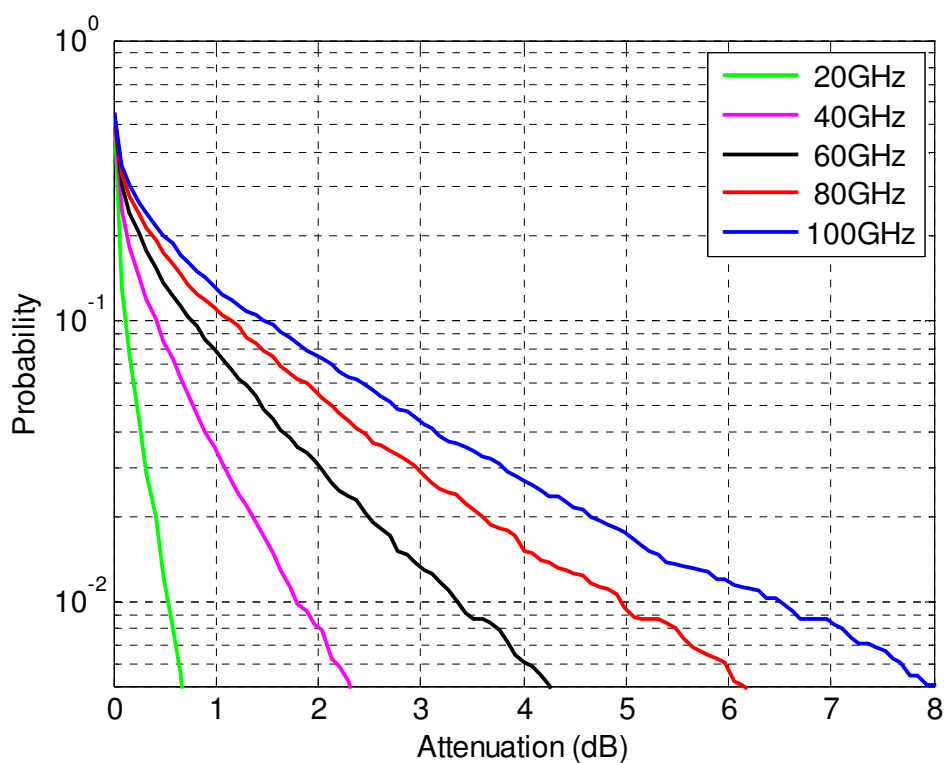
Figure 2-4. CCDF of total due to clouds calculated in Milano/Linate (1980-1989) for a slant path at 37.7° elevation angle; local radio soundings + Salonen's model + Liebe's model

2.1.3.2.   Other models for the prediction of cloud attenuation statistics

In the ITU-R model [ITU-R P.840-5, 2012], the dependence of clouds specific attenuation on droplets temperature is taken into account by defining the liquid water content reduced to the temperature of 0 °C (W_{red}) which, in addition, is frequency dependent. The integration of W_{red} as a function of the height results in the reduced total liquid water content (L_{red}) measured in kg/m^2 = mm. Global statistics of this parameter have been calculated, for the frequency range 20-50 GHz, by using global data from ECMWF numerical analysis (ERA40 database) and are made available through global maps [ITU-R P.840-5, 2012]. Cloud attenuation is finally obtained as a function of L_{red}, the frequency, the elevation angle and the dielectric constant of the water. The comparisons against cloud attenuation distributions measured via a dual-channel radiometer have shown quite a good agreement in different climates [Salonen et al., 1994].

Other simple models have been proposed in the past for the prediction of cloud attenuation statistics, such as those by [Altshuler and Marr, 1989] and [Dintelmann and Ortgies, 1989], but comparisons with respect to experimental data (radiometric data) showed that they have scarce climatic validity [Salonen et al., 1991].

Recently, other models have been proposed by [Salonen and Uppala, 1991], [Konefal et al., 2000], [Dissanayake et al., 1997] and [Wrench et al., 1999]. The Salonen model [ITU-R P.840-5, 2012] requires the introduction of radio-meteorological parameters available worldwide, such as temperature, humidity or L_{red}. The Konefal model is a variation of the Salonen model in order to calculate monthly clouds attenuation. The DAH (Dissanayake-Allnut-Haidara) model calculates the cloud attenuation distribution due to four types of clouds using their average properties (vertical and horizontal extent, and water content) and their coverage percentage, which can be obtained, for example, from the database described in [Hahn et al., 1996]. Finally, the Wrench model relies on the definition of 4 classes of clouds (stratocumulus, cumulus, nimbostratus and cumulonimbus), defined by their physical extent, liquid water content and percentage of occurrence.

Table 2-2 summarizes the main characteristics of the clouds attenuation statistical prediction models discussed above, in terms of input and output parameters.

As an example of the application of the ITU-R model, Figure 2-5 shows the predicted complementary cumulative distribution function (CCDF) of the attenuation due to clouds obtained for the Milano-Linate airport (frequency shifting from 20 to 100 GHz).

All the models listed above rely on the well-known concept of stratified atmosphere which allows to calculate the slant path attenuation by simply dividing the zenith attenuation by the sine of the elevation angle. However, for low elevation angles (say 15-20 degrees) the spatial structure of the clouds (especially heavy clouds) could play an important role, still to be duly assessed, in the calculation of the cloud attenuation.

Table 2-2. Clouds attenuation statistical prediction models

Model	Input data			Output parameters
	Geometrical	Radiowave	Climatic	
ITU-R P.840-5	Elevation	Frequency	L_{red}	K_{cl}, A_{cl}
Altshuler and Marr	Elevation	Frequency	Temperature WV density	A_{cl}
Dintelmann and Ortgies	Elevation	Frequency	Temperature Relative humidity	A_{cl}
Dissanayake-Allnutt-Haidara	Elevation	Frequency	Vertical extent Horizontal extent WV density	A_{cl}
Konefal	Elevation	Frequency	L_{red} Mean humidity –20°C isotherm h	K_{cl}, A_{cl}
Wrench	Elevation	Frequency	Physical extent Temperature L_{red}	A_{cl}
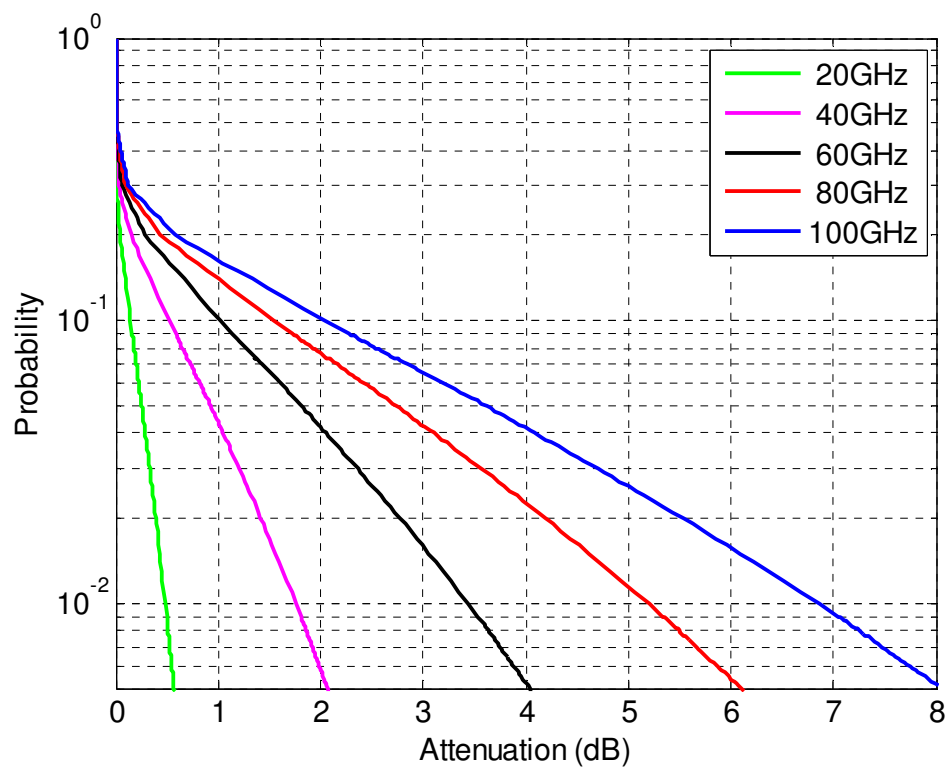
Figure 2-5. CCDF of attenuation due to clouds calculated in Milano/Linate for a slant path at 37.7° elevation angle; predictions using the ITU-R model

2.1.4.   Measurements in non-precipitating atmosphere

2.1.4.1.   Radio sonde observations (RAOBS)

A radio sonde is a balloon-borne device that measures vertical profiles of meteorological variables, typically, air temperature, humidity and pressure. Profiles are usually obtained twice a day up to approximately 30 km.

The radio sonde contains instruments capable of making direct in-situ measurements of the physical parameters, as well as to transmit data immediately to the ground station by a radio transmitter located within the instrument package. The ascent of a radio sonde provides also an indirect measurement of the wind speed and direction at various levels throughout the troposphere by means of ground based antennas tracking its motion during its ascent: the recorded elevation and azimuth information are converted into wind speed and direction at various levels by triangulation techniques. A plot of the vertical variations of observed weather variables as function of air pressure is called sounding, an example of which is reported in Figure 2-6.
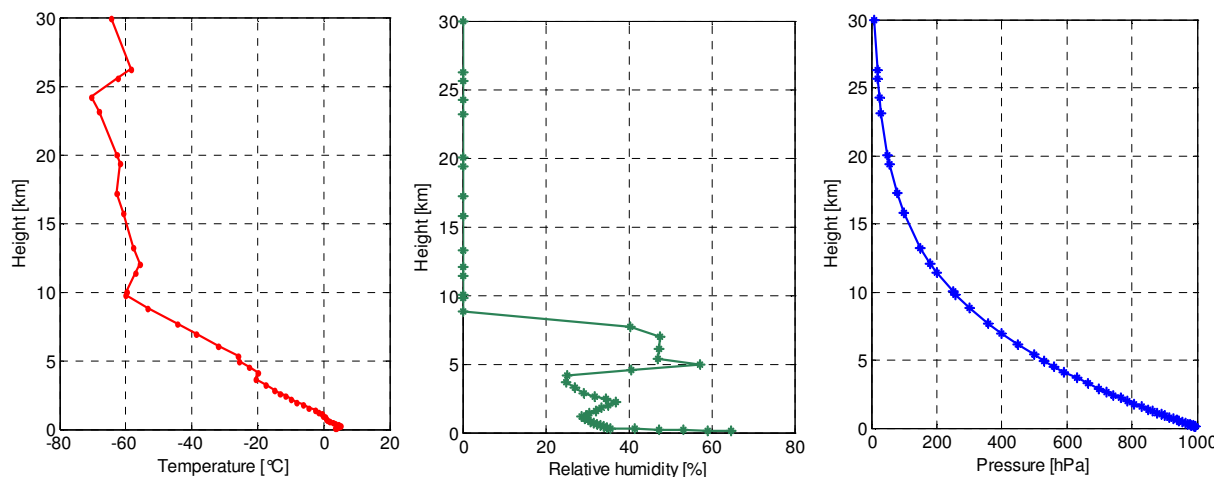
Figure 2-6. Example of the profiles obtained from a radio sonde ascent: temperature (°C), relative humidity (%) and pressure (hPa) as a function of height

Different organizations and countries use various radio sonde types. The most common radio sondes are "PTU-only" systems, i.e., the primary output measurements are pressure, temperature, and relative humidity. Altitude and dew point temperature are quantities derived from the measured data. Recently, GPS receivers have been integrated into the radio sonde electronics, so that altitude and coordinates are directly provided by GPS and pressure is a derived quantity, computed by using the hydrostatic equation.

Many comparisons between radio sonde types and from different manufacturers, as well as between various types of remote sensors, have been performed [Miloshevich et al., 2006], [Vömel et al. 2003], [Mattioli et al. 2007]. Vaisala RS80 radio sondes are known to have a dry bias [Turner et al. 2003], [Westwater et al. 2003], and Sippican VIZ and Mark radio sondes are known to have large relative humidity biases at high altitude due to the slow response time of the carbon hygristor sensor at lower temperatures [Blackmore and

Taubvurtzel 1999], [Mattioli et al. 2007]. With the development of the technology, the sensors quality and accuracy have been increased, whilst calibration and correction tables for the major sensor errors have been introduced. Although questions arise on how inconsistencies and systematic biases affect long term measurements obtained from radio sondes, so far, radio soundings provide the most accurate information on the vertical structure of the troposphere and lower stratosphere.

2.1.4.2.   *Radiometers*

Radiometry is a passive remote sensing technique based on the measurement of the natural absorption and emission of electromagnetic energy by matter (e.g. atmospheric constituents). Energy radiation results from the emission and extinction processes in each layer of the medium. Radiometers are, in their essence, wideband receivers with very high sensitivity and measure the brightness temperature T_B seen by the antenna.

As already mentioned, scattering effects can be substantially ignored for clear air atmosphere (presence of only gases). When clouds and rain are present, scattering by water droplets and precipitant ice may be negligible or not, depending upon the density and size of water particles relatively to the wavelength.

Typical ground based microwave radiometer for observing a non-precipitating atmosphere operate at 23.8 GHz, near the weak vapor resonant line, and at 31.4 GHz, within the almost transparent (with respect to gases) window region. At zenith, in the case of non-scattering atmosphere in local thermodynamic equilibrium, T_B (K) is related to the absorptive and emissive processes of the medium by the linearized form of the RTE (Radiative Transfer Equation):

$$T_B(f) = T_C\, e^{-\tau_f(0,\infty)} + \int_0^\infty T(z)\alpha(f,z)e^{-\tau_f(0,z)}dz \qquad (2\text{-}22)$$

where T_c is the cosmic background emission, commonly assumed as 2.73 K in the microwave range, $T(z)$ is the absolute physical air temperature (K), z is the spatial position of the emitting air volume (km), $\alpha(f,z)$ is the atmospheric volume absorption coefficient (Np/km) at frequency f, and $\tau_f(0,z)$ (Np) is the optical depth of the atmospheric layer between $(0,z)$, called atmospheric opacity when z goes to infinity:

$$\tau_f(0,\infty) = \tau(f) = \int_0^\infty \alpha(f,z)dz \qquad (2\text{-}23)$$

The atmospheric opacity $\tau(f)$ can be expressed in terms of brightness temperature T_B after introducing the atmospheric mean radiating temperature:

$$T_{mr}(f) = \frac{\int_0^\infty T(z)\alpha(f,z)e^{-\tau_f(0,z)}dz}{\int_0^\infty \alpha(f,z)e^{-\tau_f(o,z)}dz} \qquad (2\text{-}24)$$

which leads to the well-known expression for the atmospheric opacity:

$$\tau(f) = \ln\left[\frac{T_{mr}(f)-T_c}{T_{mr}(f)-T_B}\right] \qquad (2\text{-}25)$$

and, in terms of attenuation:

$$A(f) = 10 \log_{10} \left[\frac{T_{mr}(f) - T_c}{T_{mr}(f) - T_B} \right] \qquad (2\text{-}26)$$

Equation (2-25) shows that radiometers can measure the atmospheric attenuation at frequency f from the knowledge of T_{mr} which can be estimated from standard surface meteorological measurements. Equation (2-26) is the key equation to retrieve the amount of non-scattering atmospheric constituents by means of radiometers, namely, integrated water vapor (V) and integrated cloud liquid water (L). Considering a dual-channel instruments with one frequency mainly sensitive to water vapor (subscript 1) and the other to the liquid water (subscript 2), V and L can be estimated starting from the following equations which express the atmospheric attenuation as the sum of the three separate contributions due to oxygen (A_{ox}), water vapor ($a_V V$) and liquid water ($a_V L$) [Mattioli et al., 2005]:

$$A(f_1) = a_V(f_1)V + a_L(f_1)L + A_{ox}(f_1)$$
$$A(f_2) = a_V(f_2)V + a_L(f_2)L + A_{ox}(f_2) \qquad (2\text{-}27)$$

where a_L and a_V are the frequency and site dependent mass absorption coefficients for L and V, respectively. The inversion of (2-27) leads to the estimation of V and L:

$$V = a_0 + a_1 A(f_1) + a_2 A(f_2)$$
$$L = b_0 + b_1 A(f_1) + b_2 A(f_2) \qquad (2\text{-}28)$$

As an example, Figure 2-7 shows the brightness temperature time series at three different frequencies (13, 23.8, 31.6 GHz) collected at Spino d'Adda on 10th August 1994, whilst Figure 2-8 and Figure 2-9 depict the corresponding time series of L and V, respectively, retrieved from such measurements.
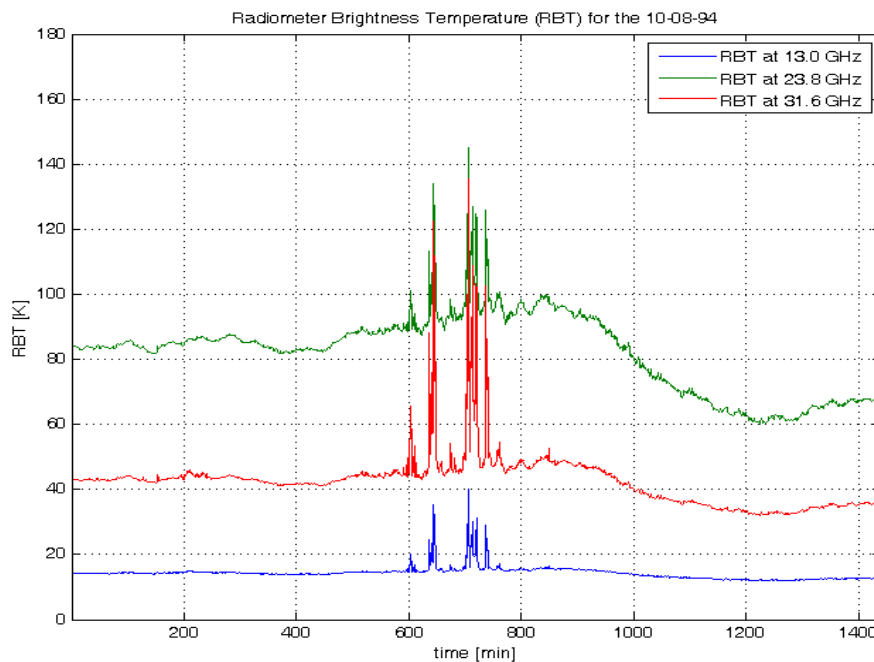
Figure 2-7. Example of brightness temperature time series at three different frequencies (13, 23.8, 31.6 GHz) collected at Spino d'Adda on 10th August 1994
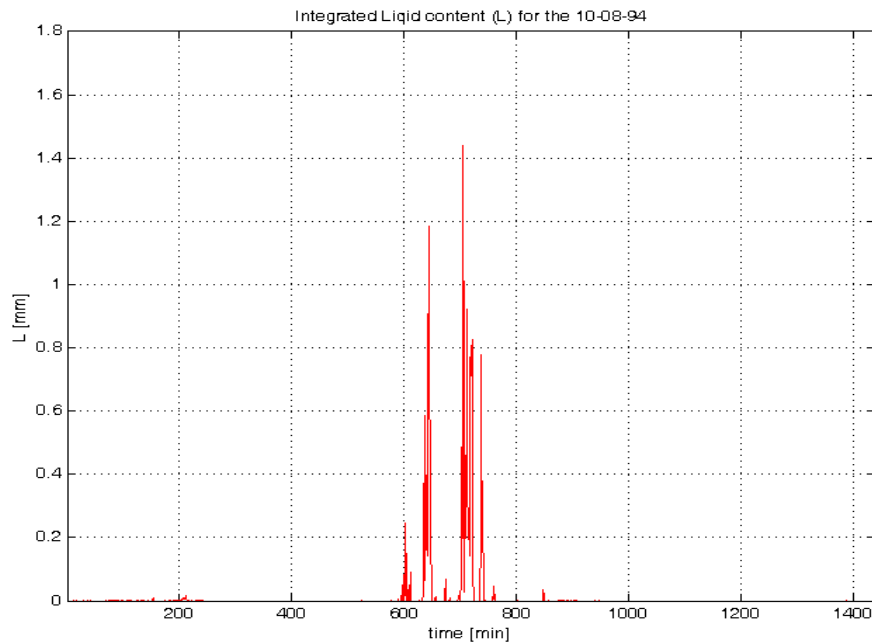
Figure 2-8. L as retrieved from the radiometric measurements shown in Figure 2-7
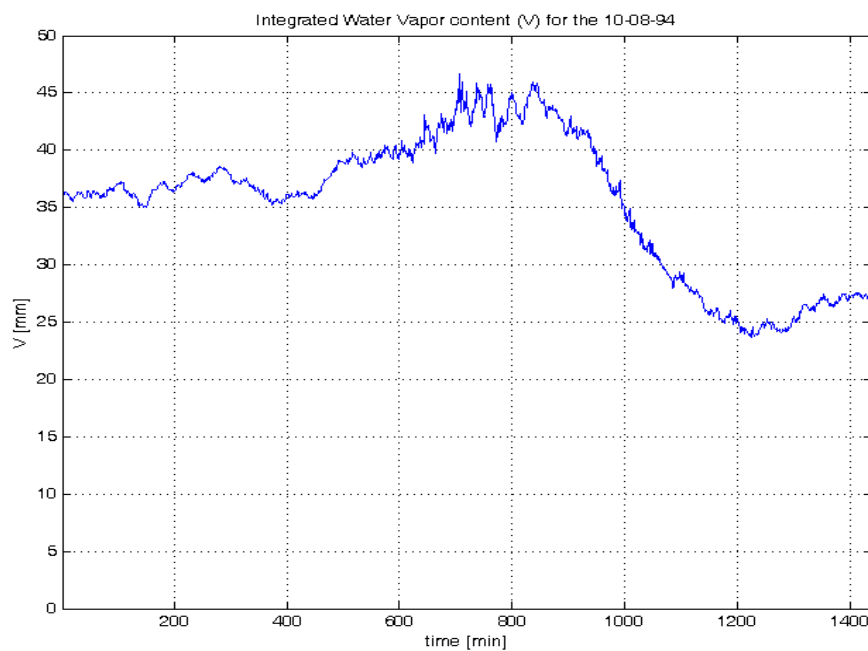
Figure 2-9. V as retrieved from the radiometric measurements shown in Figure 2-7

2.2.   Precipitating atmosphere

Rain is the prevailing phenomenon related to precipitating particles in the atmosphere and, depending on the site, it occurs for a period of time approximately comprised between 1% to 10% in a year (the year is considered as the basic repetition period of weather phenomena). Values as large as 3%-7% are quite common in temperate climates. Rain affects

the lower part of the atmosphere; specifically, making reference to temperate climates, rain develops up to few kilometers during winter because of the low height of the 0 °C isotherm layer (typically assumed as the vertical limit for the presence of water particles during stratiform events) and up to 10-15 km during thunderstorms (typical of summer periods) because of the strong updrafts/downdrafts which carry water/ice particles also to the highest layers of the atmosphere. Above rain, in stratiform precipitation, there exists a well-structured melting layer consisting of a mixture of ice crystals and snow particles gradually melting into water, while in convective precipitation, frozen particles are present only at higher altitudes. Rain consists of drops of spheroidal shape with equivolumetric diameters varying between few tenths of millimeters to a maximum of 6 millimeters. Larger drops do not occur because the cohesive force is not as strong as the aerodynamical force.

For what concerns the impact of hydrometeors on electromagnetic waves, rain represents the main drawback to their propagation at frequencies above 10 GHz because the hydrometeor dimensions are comparable with the wavelength of the incident wave. Other types of precipitation such as hail and snow are not considered here because their effects on the propagation of the electromagnetic waves are marginal and their occurrence probability is well below the one of rain.

As it is well known and exhaustively described in many textbooks [Van de Hulst, 1957], [Deirmendjian, 1969], the effect of a water drop on the incident electromagnetic wave is twofold: absorption and scattering. Both effects subtract energy to the wave. They are described through equivalent areas, called respectively σ_{abs} (absorption) and σ_{scat} (scattering) cross sections, which, summed up, give the extinction cross section σ_{ext}, i.e. the area that, multiplied by the incident electromagnetic flux, indicates the total power subtracted to the incident wave. Generally, the above areas are functions of the orientation of the particle and the polarization of the incident wave. In fact, hydrometeor shapes are far from being spherical if the dimension is not small, because of the balance between the internal and external forces acting on the surface of the drop in its falling path. Measurements have shown that drops larger than about 1 mm in radius are of oblate spheroidal shape with flattened base [Oguchi, 1983].

Although not exhaustive for the description of the rainfall process, the most important parameter to identify the meteorological characteristics of a given site is the rain rate CCDF, typically also referred to as $P(R)$.

2.2.1.   Rain rate prediction models

When experimental propagation data are not available, the statistics of the rain induced electromagnetic attenuation, required for system design purpose, can be obtained by resorting to attenuation prediction models. The main input of such models is the $P(R)$, whose values, tightly linked to the local climatology, have a direct impact on the predicted attenuation statistics.

The International Telecommunication Union (ITU) recommends the use of rainfall rate CCDFs with 1-minute integration time in order to properly estimate also extreme fade values. In fact, such integration interval guarantees a good level of accuracy in reproducing the time variability of attenuation, as it is confirmed by various authors [Segal, 1986], [Chebil and Rahman, 1999]. Unfortunately, however, 1-minute integration time is not the standard time

interval used in meteorological applications for which there is no interest in rapid changes of rain intensity, but rather in reliable average quantities (half-hourly, hourly, daily, monthly or yearly cumulated rain). Therefore, rain gauge data routinely collected for meteorological purposes and covering long observation periods are easily available worldwide, whilst specialized measurements for propagation applications are carried out on spot basis at specific sites (usually associated to other experimental activities on wave propagation).

This fact has driven research efforts towards the development of procedures aimed at deriving $P(R)$s with 1-minute integration time from the knowledge of rain rate CCDFs with much longer integration time or, alternatively, from the knowledge of standard meteorological products. In general, existing prediction methods can be grouped into three different categories:

- *Meteorology based methods* which use as input general meteorological information, like the annual or monthly average rain rate, the number of rainy days per year, the peak annual rain rate and so on. The most acknowledged ones are the Rice-Holmberg [Rice and Holmberg, 1973], Dutton-Dougherty [Dutton and Dougherty, 1974] and Crane [Crane, 1980] methods.

- *Analytical methods* based on the assumption that the analytical form of the $P(R)$ is maintained whilst changing the integration time; in other words, the 1-minute and 1-hour rain rate statistics are different because the parameters of the $P(R)$ analytical equation are different. These methods predict how the parameters of the distribution change according to the integration time. In this group of models, the ones proposed by Moupfouma [Moupfouma and Martin, 1995] and Karasawa [Karasawa and Matsudo, 1991] deserve citation.

- *Empirical methods* like the ones proposed by Segal, Burgueño and Watson et al., which provide conversion factors between the known CCDF (with integration time longer than 1 minute) and the one to be estimated. In particular, Segal in [Segal, 1986] analyzed long-term data of various locations in Canada and thus derived a fitting power-law (on probability) for the 1-hour to 1-minute conversion factors. This relationship has been modified and adapted to Malaysian data by Chebil and Rahman in [Chebil and Rahman, 1999]. In [Burgueño et al., 1988], Burgueño observed long-term data in Barcelona, Spain, and proposed another fitting power-law (on rain rate). Additional conversion coefficients based on this power-law have been derived by several authors: although all the aforementioned methods provide only regional coefficients since they were developed as initiating from local data, recently the ITU-R has proposed a global conversion method based on the average value of such coefficients [ITU-R P.837-6, 2012].

The rainfall rate prediction model currently adopted by the ITU-R in Annex 1 of recommendation P.837-6 [ITU-R P.837-6, 2012] belongs to the first class of models described above and relies on global long-term meteorological maps. Specifically, the method estimates the 1-minute integrated $P(R)$ worldwide from the simple knowledge of the site's geographical coordinates and receives as input the mean yearly local amounts of the convective and stratiform rain (M_c and M_s, respectively), together with the 6-hour rainy probability (P_{r6}). All this information is extracted from the ERA40 database [Uppala et al., 2005], provided by the ECMWF (European Centre for Medium-Range Weather Forecast).

Table 2-3 summarizes the main characteristics of some rain rate CCDF prediction models, in terms of input and output parameters.

Recently some research activity has been carried out to develop new techniques (and to improve the existing ones) to convert rainfall intensity CCDFs collected with long integration time to CCDFs with 1-minute integration time. Specifically, in [Capsoni and Luini, 2009], a semi-physical approach to the problem, based on the EXCELL model, has been proposed. More specifically, EXCELL Rainfall Statistics Conversion (RSC), now adopted in recommendation ITU-R P.837-6 (Annex 3), relies on the simulated translation of synthetic rain cells on a virtual rain gauge with tunable integration time. Moreover, in [Emiliani et al., 2009], the rain rate CCDF conversion based on the Burgueño's power-law (listed among the empirical methods above) has been recently enhanced by introducing more reliable global coefficients which have been derived from an extensive worldwide database of measured rain rate CCDFs collected with different integration times, from 1 to 60 minutes.

Table 2-3. Rain rate CCDF prediction models

Model	Input data		Output parameters
	Geometrical	Climatic	
Crane	Latitude Longitude	/	$R(P)$
Dutton-Dougherty	Latitude Longitude	M, β	$R(P)$
Rice-Holmberg	Latitude Longitude	M, β	$R(P)$
Tattelmann and Scharr	Latitude Longitude	Temperature Rain amount Number of rainy days	$R(P)$
Segal	/	1-hour integrated CCDF	$R(P)$
ITU-R P.837-6	Latitude Longitude	M_c M_s P_{r6}	$R(P)$

Legend:
M_c: annual cumulated convective rain amount (mm)
M_s: annual cumulated stratiform rain amount (mm)
P_{r6}: rainy time percentage with integration time of 6 hours (%)
M: cumulative rain amount
β: thunderstorm ratio
$R(p)$: rainfall intensity exceeded for the p probability in an average year (mm/h)

2.2.2. Vertical profile and horizontal distribution of rain

As far as the spatial variability of rain is concerned, the issue covers two different, but related, aspects: the vertical profile and the horizontal distribution. The first one is peculiar of slant-path links and is in close relationship with the estimation of the rain height, with the melting-layer effects and, to a minor extent, with the polarization mismatching induced by the ice-clouds, particularly important at low elevation angles. The attempts to solve the problem of the vertical rain profile have often led to the definition of "effective" rain heights. Significant studies on this subject tried also to relate the rain height to various conditions,

unfortunately not always clearly applicable in the predictions. In 2001, the ITU-R produced and distributed a global map of the mean yearly rain height [ITU-R P.839-3, 2001]. A significant refinement of the rain height modeling for the estimation of the rain induced attenuation has been afterwards introduced in [Capsoni et al., 2009], in which the authors have proposed a method to derive two different heights peculiar of stratiform and convective rain by properly taking into account the monthly mean values of the 0 °C isotherm heights (conditioned to the presence of rain) and the associated monthly mean values of the convective-over-total rain amount ratio (both extracted from the global ERA15 database). In fact, stratiform events are typically associated with a lower vertical extent with respect to convective ones, in which rain drops are pushed well beyond the 0 °C isotherm height by strong updrafts and downdrafts. In addition, stratiform precipitations are usually coupled with a well marked melting layer (the layer just below the 0 °C isotherm height where the falling snowflakes and ice particles melt into water drops), whose effect, in terms of signal attenuation, can be taken in due account through the introduction of an "equivalent rain height" to be added to the stratiform rain height.

Table 2-4 compares the rain height (km) for Spino d'Adda and Rome as extracted from recommendation ITU-R P.839-3 [ITU-R P.839-3, 2001] and as calculated using the ERA15 database according to the formulations included in the SC EXCELL model [Capsoni et al., 2009].

Table 2-4. Rain height for Spino d'Adda and Rome as extracted from recommendation ITU-R P.839-3 [ITU-R P.839-3, 2001] and as calculated using the ERA15 database according to the formulations included in the SC EXCELL model [Capsoni et al., 2009] (km)

	ITU-R P.839-3	ERA15 stratiform	ERA15 convective	ERA15 annual
Spino d'Adda	2.8421	1.9064	3.2158	2.5611
Rome	2.8055	2.0595	3.4348	2.7471

Also the investigation of the horizontal distribution of the rain intensity has originated several different modeling proposals during the past decades: a class of attempts tries, similarly to the previous case, to concentrate in a single parameter, the path reduction coefficient, the relevant information contained in the horizontal profile [Dissanayake et al., 1997], [ITU-R P.618-10, 2009]. Alternative approaches are more statistically- and/or physically-oriented. In some cases, radar derived rain fields allowed to formulate a direct link between attenuation and rainfall statistics. In some other cases, the observation of radar derived rainfall data led to the development of models of the rain spatial distribution based on the concept of rain cells, which is defined by the spatially contiguous values of rain intensity exceeding a given threshold (typically, from 0.5 to 10 mm/h). Several analytical profiles have been proposed in order to adequately model the rainfall spatial distribution within a single cell, among which the cylindrical [Misme and Waldteufel, 1980], the Gaussian [Lane and Stutzman, 1980], the exponential [Capsoni et al., 1987] (EXCELL model) and the hybrid Gaussian-exponential [Feral et al., 2003] (HYCELL) ones are worth being cited. Among the various proposals, the EXCELL and the HYCELL models also include methodologies that allow to derive the correct rain cells' probability of occurrence from the knowledge of the

local $P(R)$ and, as a result, they permit the global statistical estimation of the attenuation induced on a radio link by means of synthetic rain cells.

2.2.3.   Rain rate specific attenuation

The calculation of σ_{ext}, the parameter summarizing the overall effect of each drop with diameter D on the propagating electromagnetic wave, can be achieved starting from the knowledge of the complex quantity called amplitude function $S_D(\theta,\phi)$, being (θ,ϕ) the angular coordinates in a spherical reference system (in particular, the forward amplitude function $S_D(0)$ is used to derive σ_{ext}, the cross section we are interested in).

According to the ratio of the size of the drop to the wavelength inside the particle and to the form of the drop, different electromagnetic techniques can be used to compute the amplitude functions. If drops are small with respect to the wavelength, the Rayleigh scattering approach (approximation to the Mie theory) can be used; if they are large, but spherical, the exact Mie solution can be applied; in the general case, approximate numerical methods have to be used. A list of the more popular computational methods are reported below:

- Rayleigh (1871)
- Mie (1908)
- Point Matching (1960)
- Extended Boundary Condition Method (EBCM) or T- matrix (1975)
- Fredholm-Integral-Method (FIM) (1978)
- Unimoment method (1978)
- Spheroidal expansion (1980)
- Boundary element method (1993)

In order to compute the amplitude function of a drop with equivolumetric diameter D at a given frequency f, with specified polarization, it is necessary to choose the water temperature T and the shape of the drop usually expressed in terms of aspect ratio, i.e. the ratio of the minor to the major axis of the drop b/a. Some of the most used in the propagation community are listed below:

- Pruppacher and Beard (1970)
- Pruppacher and Pitter (1971)
- Oghuci (1973)
- Beard and Chuang (1987)
- Chuang and Beard (1990)
- RAL/Beard-Chuang (1995)

From f and T, the complex refractive index of water is deduced; from f and λ the so called size parameter of the drop, i.e. its electrical dimension, is derived; from the assumed drop shape and the equivolumetric diameter D, the aspect ratio is found. These parameters are the input data of any electromagnetic technique for the calculation of $S_D(0)$.

In order to evaluate the effect of rain on the propagation of the electromagnetic wave, additional information is necessary: the drop size distribution (DSD), which provides a

quantification of the average drop density, N, as a function the drop diameter D. Such information is usually given in terms of analytical functions which can be grouped as:

- Negative exponential distributions
- Gamma function distributions
- Lognormal distributions
- Weibull distributions

Out of the several DSDs proposed by different authors and present in the open literature, the most known ones are listed below:

- Marshall and Palmer (1948)
- Joss et al.- drizzle (1968)
- Joss et al.- widespread (1968)
- Joss et al.- thunderstorm (1968)
- Moupfouma and Tiffon (1982)
- Ulbrich (gamma distribution) (1983)
- Ulbrich (Laws & Parson) (1983)
- Ajayi and Olsen (1985)
- Brussard and Watson (1995)

Note that the DSD is rain intensity dependent, i.e. $N(D,R)$.

Some DSDs have been proposed as typical for specific kind of precipitation (Joss drizzle, Joss thunderstorm), others for specific climates (Moupfouma), others again as general DSDs (M&P, Laws-Parson). DSDs based on the gamma distribution include in their analytical formulation a shape parameter which allows to fit them to specifics rain event.

By integrating numerically (2-29) below, the specific rain attenuation is obtained:

$$\gamma_{R,H,V} = 8.68610^{-3}\frac{2\pi}{\lambda}\mathrm{Im}\int_{D_{\min}}^{D_{\max}}S_{D,H,V}(0)\,N(D,R)\,dD \quad \text{(dB/km)} \qquad (2\text{-}29)$$

where subscripts H,V indicate horizontal and vertical polarization, respectively.

Analogously, the rain intensity R is obtainable by integrating the following equation:

$$R = \frac{\pi}{6}\int_{D_{\min}}^{D_{\max}}N(D,R)\,D^3 v(D)\,dD \quad \text{(mm/h)} \qquad (2\text{-}30)$$

which requires as input the drop terminal velocity $v(D)$, of which, again, there are some different proposals (e.g. [Gunn and Kinzer, 1949] and [Brussaard and Watson, 1994]).

The results from (2-29) and (2-30) for different rain intensity values can be fitted with high accuracy using the following power law equation:

$$\gamma_{R,H,V} = K_{H,V}\,R^{\alpha_{H,V}} \quad \text{(dB/km)} \qquad (2\text{-}31)$$

The results shown in the following tables have been obtained according to the assumptions listed below:

- *Calculation method*: Fredholm-Integral-Method (FIM)

- Water temperature: $T = 10\ ºC$

- *Water/ice refractive index*: as proposed by Ray [Ray, 1972]

- *Drop shape*: Pruppacher and Beard

- Drop diameter range: 0.1 – 8 mm

- *Number of diameter steps*: 17 (0.1, 0.2, 0.3, 0.5, 1.0, 1.5, 2.0, 2.5, 3.0, 3.5, 4.0, 4.5, 5.0, 5.5, 6.0, 6.5, 8.0). This choice has been made in order to properly sample the non negative exponential DSDs

- *Raindrop terminal velocity:* $v(D) = 9.65\text{-}10.30\ \exp(\text{-}0.6\ D)$ [Gunn and Kinzer, 1949]

- Rain rate interval: 1 – 100 mm/h

- *Determination K_H, α_H, K_V and α_V coefficients*: linear best-fit procedure on log-log axes in the $R\text{-}\gamma$ plane

- *Rain rate step*: variable according to the DSD

A sample of the results obtained are reported in the tables below (from Table 2-5 to Table 2-10) for different DSDs and fixed frequencies. In particular, as the DSDs considered are relative to different conditions of rain intensity (e.g. drizzle and thunderstorm for two of the Joss DSDs), the best-fit procedure was applied over the following sets of rain rates:

- JD: $R = 0.5, 1, 2, 3, 4, 5$, mm/h

- JT: $R = 10, 20, 25, 30, 40, 50, 100$ mm/h

- JW, LP, G-2, G2: $R=0.5, 1, 2, 5, 10, 25, 50, 100$ mm/h

Table 2-5. Coefficients of (2-31) for vertical and horizontal polarizations. DSD: Joss drizzle (JD)

Frequency (GHz)	K_H	α_H	K_V	α_V
12.5	0.0172	1.0760	0.0163	1.0524
18.7	0.0485	1.0614	0.0466	1.0359
19.8	0.0553	1.0628	0.0531	1.0374
20.2	0.0579	1.0632	0.0556	1.0378
27.5	0.1164	1.0672	0.1114	1.0400
29.7	0.1384	1.0679	0.1322	1.0402
39.6	0.2639	1.0645	0.2513	1.0382
49.5	0.4326	1.0539	0.4070	1.0371

Table 2-6. Coefficients of (2-31) for vertical and horizontal polarizations. DSD: Joss thunderstorm (JT)

Frequency (GHz)	K_H	α_H	K_V	α_V
12.5	0.0314	1.1385	0.0291	1.0830
18.7	0.0793	1.0752	0.0714	1.0174
19.8	0.0910	1.0612	0.0808	1.0082
20.2	0.0955	1.0561	0.0845	1.0048
27.5	0.1969	0.9697	0.1679	0.9421
29.7	0.2329	0.9469	0.1986	0.9239
39.6	0.4017	0.8669	0.3511	0.8547
49.5	0.5331	0.8309	0.4785	0.8239

Table 2-7. Coefficients of (2-31) for vertical and horizontal polarizations. DSD: Joss widespread (JW)

Frequency (GHz)	K_H	α_H	K_V	α_V
12.5	0.0200	1.1954	0.0183	1.1634
18.7	0.0549	1.1362	0.0509	1.0943
19.8	0.0628	1.1287	0.0581	1.0867
20.2	0.0658	1.1261	0.0608	1.0842
27.5	0.1331	1.0786	0.1218	1.0440
29.7	0.1584	1.0636	0.1447	1.0322
39.6	0.2993	0.9941	0.2731	0.9752
49.5	0.4750	0.9292	0.4354	0.9192

Table 2-8. Coefficients of (2-31) for vertical and horizontal polarizations. DSD: Laws-Parsons (LP)

Frequency (GHz)	K_H	α_H	K_V	α_V
12.5	0.0213	1.1890	0.0193	1.1573
18.7	0.0576	1.1297	0.0528	1.0879
19.8	0.0657	1.1220	0.0601	1.0804
20.2	0.0688	1.1193	0.0629	1.0778
27.5	0.1383	1.0699	0.1250	1.0369
29.7	0.1642	1.0544	0.1482	1.0247
39.6	0.3058	0.9842	0.2766	0.9670
49.5	0.4758	0.9213	0.4340	0.9123

Table 2-9. Coefficients of (2-31) for vertical and horizontal polarizations. DSD: Gamma with shape parameter $\mu = -2$ (G-2)

Frequency (GHz)	K_H	α_H	K_V	α_V
12.5	0.0227	1.2319	0.0205	1.1699
18.7	0.0608	1.1391	0.0559	1.0689
19.8	0.0691	1.1249	0.0634	1.0580
20.2	0.0722	1.1199	0.0662	1.0542
27.5	0.1416	1.0369	0.1290	0.9907
29.7	0.1668	1.0142	0.1520	0.9730
39.6	0.3011	0.9243	0.2767	0.8992
49.5	0.4500	0.8724	0.4133	0.8600

Table 2-10. Coefficients of (2-31) for vertical and horizontal polarizations. DSD: Gamma with shape parameter $\mu = 2$ (G2)

Frequency (GHz)	K_H	α_H	K_V	α_V
12.5	0.0191	1.1626	0.0175	1.1427
18.7	0.0538	1.1171	0.0496	1.0915
19.8	0.0616	1.1117	0.0568	1.0851
20.2	0.0646	1.1099	0.0595	1.0830
27.5	0.1317	1.0806	0.1205	1.0536
29.7	0.1572	1.0709	0.1434	1.0456
39.6	0.3019	1.0180	0.2742	1.0023
49.5	0.4860	0.9593	0.4440	0.9510

Figure 2-10 shows the difference in the γ-R relationship obtained using the FIM method and the one adopted in recommendation ITU-R P.838-3 at 49.5 GHz [ITU-R P.838-3, 2005] (horizontal polarization). As it can be noticed, the differences between the two curves are very limited over the whole range of R.

The impact of the DSD on the γ-R relation is shown in Figure 2-11, Figure 2-12 and Figure 2-13, at 12.5, 27.5 and 49.5 GHz, respectively. The discrepancy among the curves is quite marked and frequency dependent, being the difference in specific attenuation for a given value of rain rate at 12.5 and 49.5 GHz as large as a factor of 1.5 when moving between the two extreme DSDs, but almost negligible at 27.5 GHz. Note that at 12.5 GHz the largest attenuation is given by the gamma G–2 DSD, while at 49.5 GHz this is true for gamma G+2 DSD.
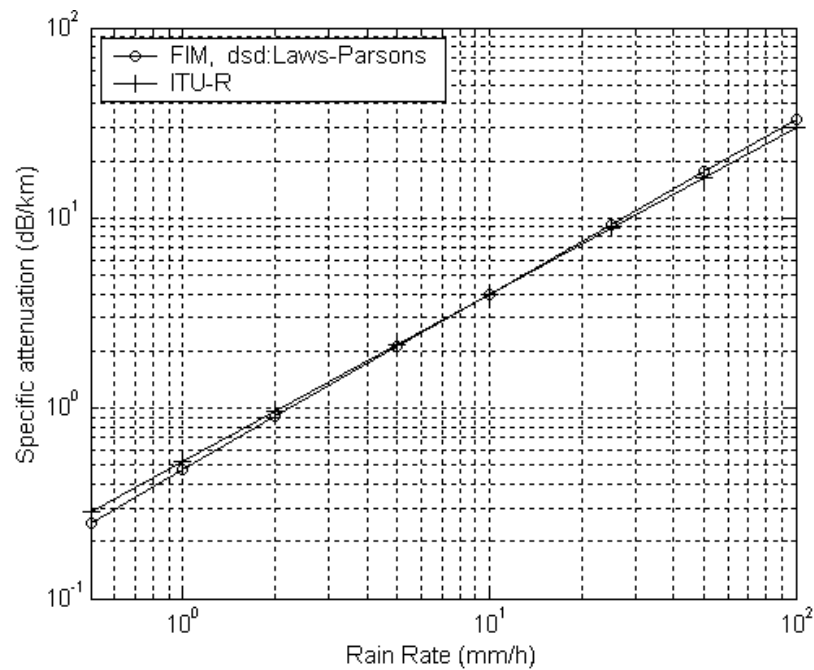
Figure 2-10. Comparison between two expressions for the 49.5 GHz specific attenuation with horizontal polarization
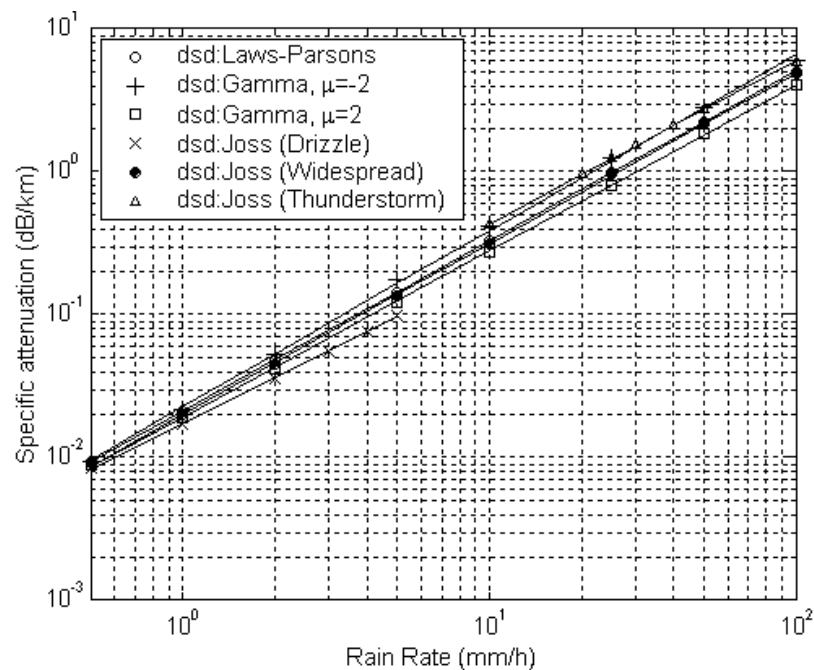
Figure 2-11. Specific attenuation (12.5 GHz) with horizontal polarization: comparison between 6 DSDs
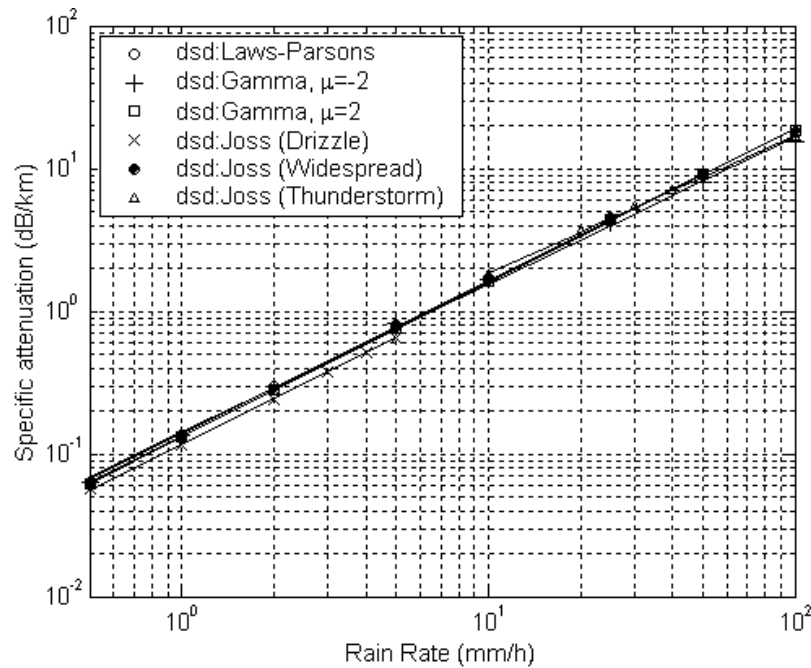
Figure 2-12. Specific attenuation (27.5 GHz) with horizontal polarization: comparison between 6 DSDs
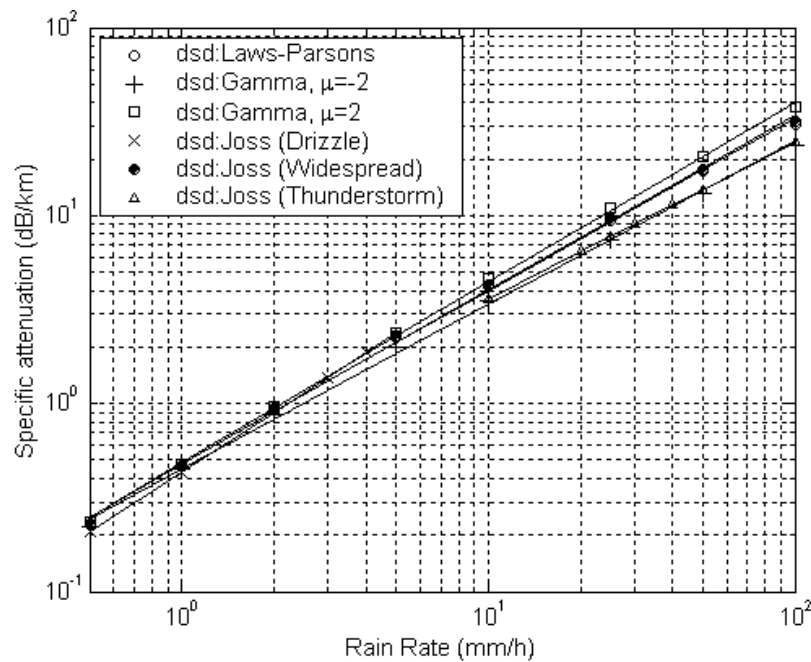
Figure 2-13. Specific attenuation (49.5 GHz) with horizontal polarization: comparison between 6 DSDs

2.2.4. Rain attenuation prediction models

The prediction of the rain attenuation CCDF starting from the rain intensity CCDF has been the subject of huge efforts from many researchers in the last three decades. Several methods have been developed and their performance evaluated using as reference statistical

data from propagation experiments at frequencies up to 50 GHz. The difference in the performance of the best methods is often negligible and their errors are of the same order of the year-to-year variability of precipitation (around 20%-30%). Australian [Flavin, 1996], Bryant [Bryant et al., 2001], EXCELL [Capsoni et al., 1987b], SC EXCELL [Capsoni et al., 2009], ITU-R P.618-10 [ITU-R 618-10, 2009], Matricciani [Matricciani, 1991], SST [Matricciani, 2008] and Misme-Waldteufel [Misme and Waldteufel, 1980] are methods showing the best performance according to recent testing activities [Riva, 2002], [Riva et al., 2006]. Gibbins and Walden [Gibbins and Walden, 2003] proposed a new prediction model of rain attenuation relying on the full rainfall rate distribution and on the new specific attenuation coefficients provided in recommendation ITU-R P.838-3 [ITU-R P.838-3, 2005]. The interest in this approach is because it relies on path adjustment factors that are independent of the frequency and specific attenuation. Furthermore, the horizontal adjustment factor is the same for terrestrial and Earth-space applications, whereas the vertical adjustment factor is used for Earth-space geometry only. The main drawback of this model is that it is fitted on the whole available experimental database without strong physical significance.

Table 2-11 summarizes the key features of the most accredited rain attenuation statistical prediction models, in terms of input and output parameters. Apart from when specifically mentioned, the validity of the models is for yearly time percentages lower than 1%. The frequency range extends from 1 to 50 GHz.

Table 2-11. Rain attenuation statistical prediction models

Model	Input data			Output parameters	Validity range
	Geometrical	Radiowave	Climatic		
ITU-R P.618-10	Altitude, Latitude, Elevation	Frequency k, α	$R_{0.01}$ 0 °C isotherm height	γ_{rain}, A_{rain}	$P \le 5\ \%$
Improved Assis-Einloft	Altitude, Latitude, Elevation	k, α	$R(P)$ Rain height	γ_{rain}, A_{rain}	/
Bryant	Latitude, Elevation	k, α	$R(P)$	γ_{rain}, A_{rain}	/
CETUC	Latitude, Elevation	k, α	$R(P)$	γ_{rain}, A_{rain}	/
Crane global	Altitude, Elevation	Frequency	$R(P)$ $H_{0\,°C}(P)$	γ_{rain}, A_{rain}	/
Crane-2C	Altitude, Latitude, Elevation	k, α	$R(P)$	γ_{rain}, A_{rain}	/
SC-EXCELL	Altitude, Latitude, Elevation	k, α	$R(P)$ Stratiform rain height Convective rain height	γ_{rain}, A_{rain}	/
Flavin	Altitude, Latitude, Elevation	Frequency k, α	$R(P)$	γ_{rain}, A_{rain}	$5° \le E_{sat} \le 90°$
Garcia-Lopez	Altitude, Latitude, Elevation	k, α	$R(P)$	γ_{rain}, A_{rain}	/
Karasawa	Altitude, Latitude, Elevation	k, α	$R_{0.1}$ $R_{0.01}$ 0 °C isotherm height	γ_{rain}, A_{rain}	/
Leitao-Watson	Altitude, Elevation	Frequency Polarisation	$R(P)$ Rain height	γ_{rain}, A_{rain}	$E_{sat} \ge 10°$
SST	Altitude, Elevation	Frequency Polarisation	$R(P)$ Rain height	γ_{rain}, A_{rain}	/
Misme-Waldteufel	Altitude, Elevation	k, α	$P_0, R(P)$ 0 °C isotherm height -15 °C isotherm height	γ_{rain}, A_{rain}	/
SAM	Altitude, Latitude, Elevation	k, α	$R(P)$	γ_{rain}, A_{rain}	/
Svjatogor	Altitude, Elevation	k, α	$R(P)$	γ_{rain}, A_{rain}	/
China	Altitude, Latitude, Elevation	Frequency k, α	$R_{0.01}$	γ_{rain}, A_{rain}	To be tested
Gibbins and Walden	Altitude, Latitude, Elevation	k, α	$R(P)$ 0°C isotherm height	γ_{rain}, A_{rain}	To be tested

Legend:

k, α: parameters for calculation of rain specific attenuation [ITU-R P.838-3, 2005]

$R_{0.1}$: rainfall intensity exceeded for 0.1% of the time in an average year (mm/h)

$R_{0.01}$: rainfall intensity exceeded for 0.01% of the time in an average year (mm/h)

$R(P)$: rainfall intensity exceeded for P% of the time in an average year (mm/h)

$H_{0\,°C}(P)$: 0 °C isotherm altitude exceeded for P% of the time in an average year (km)

γ_R: specific rain attenuation (dB/km)

A_{rain}: rain attenuation (dB)

f: frequency (GHz)

P: time percentage in a year (%)

E_{sat}: path elevation angle (°)

P_0: probability to have rain in a year (%)

2.2.5.   Site diversity (rain attenuation)

Diversity is a radio communication technique aimed at improving the system performance during periods of adverse propagation conditions by providing more than one transmission path or channel [Goldhirsh et al., 1997]. Knowledge of the propagation medium sufficient to design effective diversity reception systems is demanded. For example, in Earth-space site diversity, the minimum site separation for the diversity terminals is dictated mainly by the characteristics of the rain environment, although performance elements of the Earth terminals (e.g. antenna gain, link fade margin) are also important. For diversity to be effective, impairments on the separate channels are preferably independent (decorrelated), or sufficiently decorrelated, such that simultaneous severe signal impairments are rare. Even with only partial decorrelation, well-designed diversity reception systems can yield impressive benefits in the system performance [Bolea-Alamanãc, 2004].

Two standard figures are typically used to quantify the advantages provided by diversity reception on slant paths. The *diversity gain* indicates the reduction in single-path impairment level (signal fading in dB) achieved with diversity schemes for a given operating time percentage (of the year or worst-month). On the other hand, the *diversity improvement* (or *diversity improvement factor* or *diversity advantage*), is defined in the orthogonal sense as the ratio of the non-diversity and diversity probabilities of exceeding a specified impairment level.

While usually considered for protection against high rain attenuation, diversity can also offer performance benefits against other path impairments, including low-angle fading [Bryant and Allnutt, 1990], depolarization [Marshall and Bostian, 1982], and tropospheric scintillation [Haïdara et al., 1992].

2.2.5.1.   *Site diversity prediction models (rain attenuation)*

For site diversity to be effective, the propagation medium must exhibit sufficient spatial inhomogeneity to decorrelate, at least partially, the propagation impairments on the separate paths. As already mentioned above, rain is characterized by a marked variability both in time (1-minute integration time is required to properly sample the fast dynamics of the process) and in space (stormy rain cells may be limited to just some few kilometers), which makes site diversity a very interesting technique to mitigate the strong fades due to very intense rain rates.

Like for rain attenuation prediction, site diversity models can be classified into two broad categories:

1) <u>Physically-based models</u>: prediction models of this class rely on key physical features of the rainfall process and on the simulation of the interaction of the rainfall environment with the site diversity scheme of interest. Typical examples are those models based on the cellular representation of the rain field, such as EXCELL [Capsoni et al., 1987] and MultiEXCELL [Luini and Capsoni, 2011], or those assuming that rain attenuation follows a lognormal process both in time and space, such as Matricciani's [Matricciani, 1994] and Paraboni and Barbaliscia's [Barbaliscia and Paraboni, 2002] methods (the latter currently adopted in recommendation ITU-R P.618-10, Section 2.2.4.1 [ITU-R P.618-10, 2009]). Although of non trivial application, these models offer potential for incorporating physical inputs into site

diversity predictions and are more reliable on a wide frequency range because their parameters are not tuned against existing measurements but originate from physical considerations.

2) <u>Semi-empirical models</u>: these models offer simple analytical expressions for the diversity gain and/or diversity improvement as a function of the basic (electrical and geometrical) characteristics of the diversity scheme (baseline length and orientation, operational frequency, path elevation angle). Simplicity is obviously the main advantage of semi-empirical models, which, on the other side, offer a limited prediction accuracy, flexibility and reliability because they have been typically derived from a specific set of measurements. Among the numerous models belonging to this class, the method proposed by Hodge [Hodge, 1982] is worth being cited because of its good accuracy [Riva, 2002] and because it is currently included in recommendation ITU-R P.618-10 (Section 2.2.4.2) as a simplified model to calculate diversity gain and/or diversity improvement.

Table 2-12 presents an overview of the site diversity prediction models available in the open literature.

Table 2-12. Summary of site diversity prediction models

Model	Year	Input parameters	Validity range	Comments
Rec. ITU-R P.618-10 (Section 2.2.4.1)		distance azimuth angle frequency elevation angle attenuation	11-30 GHz	Balanced diversity Improvement factor
Rec. ITU-R P.618-10 (Section 2.2.4.2)		distance azimuth angle frequency elevation angle attenuation	11-30 GHz	Balanced diversity gain
Allnutt & Rogers	1982	altitude, latitude frequency elevation angle attenuation, time percentage	11-30 GHz	Balanced diversity gain
Crane	1996	distance time percentage	11-30 GHz	Unbalanced diversity Improvement factor
Dissanayake	2000	attenuation, balanced diversity gain	20-30 GHz	Unbalanced diversity gain
EXCELL	1998	station coordinates distance k, α, attenuation rain rate rain height	11-30 GHz $d \leq 15$ km	Unbalanced diversity gain Unbalanced diversity Improvement factor
Goldhirsh	1982	distance attenuation	11-30 GHz	Balanced diversity gain
Hodge	1982	distance azimuth angle frequency elevation angle attenuation	11-30 GHz	Balanced diversity gain
Mass	1987	distance azimuth angle frequency, Esat rain zone time percentage	11-30 GHz	Balanced diversity gain
Matricciani	1994	station coordinates distance, azimuth frequency, polar. Elevation angle Rain rate	11-30 GHz	Balanced diversity gain
Barbaliscia-Paraboni	2004	distance time percentage attenuations at both locations μ, σ (log-normal law)		Unbalanced diversity Improvement factor

2.2.6. Melting layer

As already mentioned, two distinct rain types are usually identified in radio propagation, although not really considered as such by meteorologists: stratiform (or widespread/large-scale) rain and convective (or shower-type) rain. The former type of rain events are associated to the presence of a melting layer (or bright band in radar terminology), located below the 0 °C isotherm [Raynaud et al., 2000]. It consists in a slab about 600 to 1000 m thick where the ice particles aloft melt in their fall to the ground. Above and below the melting layer there are dry snowfall and liquid rainfall, respectively. The altitude of the melting layer is very variable from event to event being associated to the 0 °C isotherm height: roughly, the melting layer height ranges from less than 1 km in the temperate regions to 4-5 km in the tropics. On the other hand, convective rain is usually characterized by nearly vertical columnar cells. As a consequence, from the physical point of view, attenuation models for stratiform rain (plus the associated melting layer) and for convective rain should be developed separately, though it is not trivial to identify input parameters for the two types of rain. Figure 2-14 shows a sketch of the vertical profile for stratiform events and Figure 2-15 shows a typical vertical profile of the specific attenuation, estimated using the physically-based isotropic simulator of the effects of the melting layer on electromagnetic waves (ESA/POLIMI model, [D'Amico et al., 1998]).

Several methods to calculate the attenuation and the scattering properties of the melting layer are available in the literature [Poiares Baptista, 1994], [Raynaud et al., 2000]. Investigations have clearly shown that the dependence on frequency of the melting layer extinction properties definitely differ from the one of stratiform rain. The average specific attenuation within the melting layer is much higher at 10 GHz, only slightly higher at 35 GHz, and lower at 90 GHz than the specific attenuation of stratiform rain for the same rain intensity [Zhang et al., 1996], [Capsoni et al., 2009]. This behavior is clearly reflected in Figure 2-16 which shows the total attenuation due to the melting layer in the 50-90 GHz range, compared to the one associated to a rain layer of 1 km (calculations according to [D'Amico et al., 1998]); notwithstanding the relative decrease in the impact of bright band with respect to the underlying rain layer, Figure 2-16 definitely points out that the contribution due to the melting layer is not at all negligible in the Q/V and W bands.
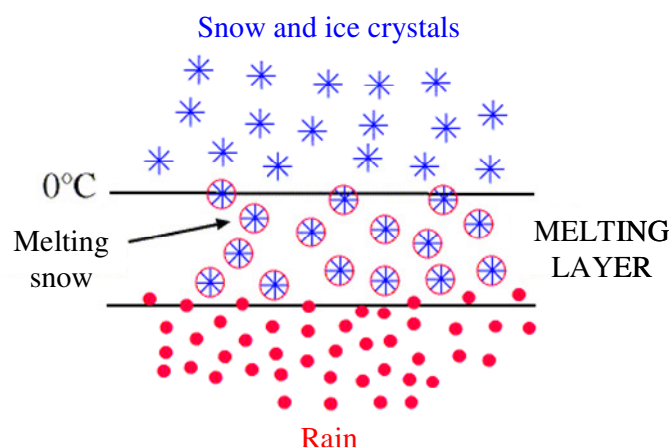
Figure 2-14. Schematic view of the vertical profile for stratiform rain with the melting layer in evidence
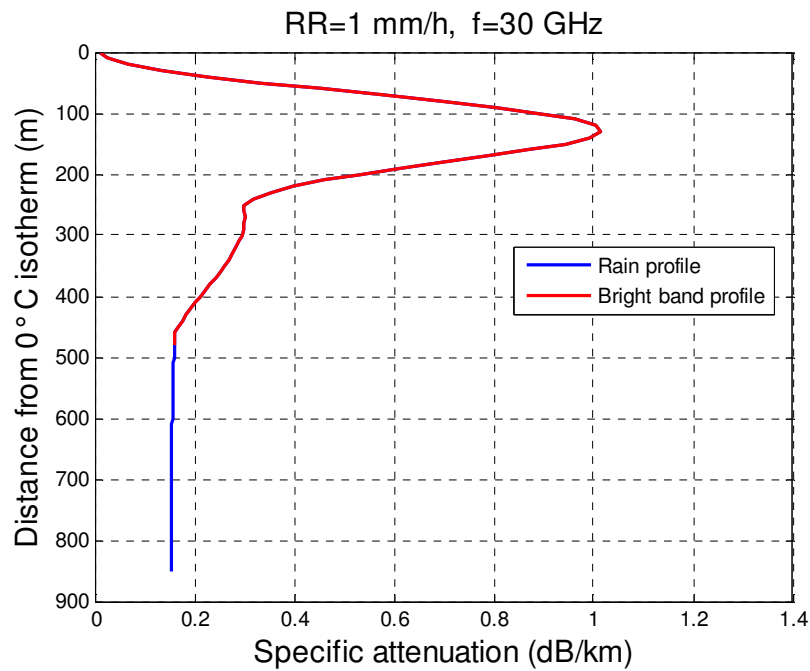
Figure 2-15. Typical average vertical profile of specific attenuation, estimated using the physically-based isotropic simulator of the effects of the melting layer on electromagnetic waves (ESA/POLIMI model, [D'Amico et al., 1998])
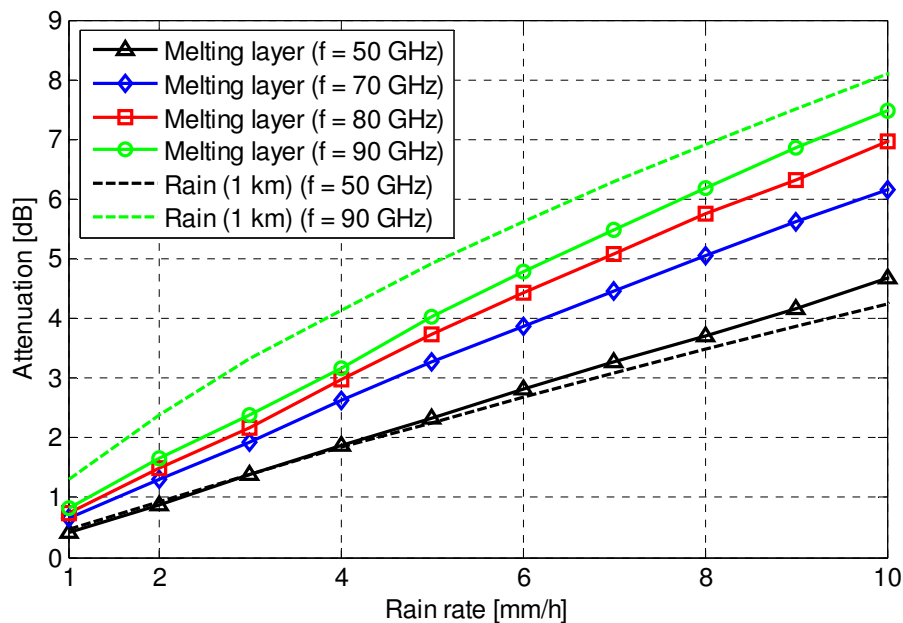
Figure 2-16. Total attenuation due to the melting layer in the 50-90 GHz range, compared to the one associated to a rain layer of 1 km (calculations according to [D'Amico et al., 1998])

A key problem in the modeling of the melting layer is how its effects can be taken into account to calculate the total attenuation along, for example, an Earth-space link. Physical models are difficult to use because it is almost impossible to feed them with the full required description of the meteorological scenario; therefore, simple prediction models have to be used. An empirical prediction model of the melting layer has been proposed in [Dissanayake et al., 1997], whilst in [Pavageau et al., 2001] the authors proposed, as a first level of approximation, to use an effective rain height in the calculation of the rain attenuation in order to take into account also the melting layer effects, namely the -2 °C isotherm (instead of the 0 °C) height.

Other prediction models that explicitly include the effects of the melting layer are:

- Leitao-Watson model [Leitao and Watson, 1986], in which, starting from radar observations of the melting layer reflectivity, the authors included in the model effective parameters accounting for the bright band contribution to attenuation.
- The SST model [Matricciani, 2008] based on a dual-layer representation of rain. In this model, the relationship between the rain rate in the first layer above the ground (A) and the apparent precipitation rate in the second layer (B) (modeling the melting layer) is theoretically derived, assuming a log-normal distribution of rain rate values in both layers, with the same standard deviation, but higher median value in layer B, (3.134 times larger than in layer A).
- The SC EXCELL model [Capsoni et al., 2009], in which the effect of the melting layer, in terms of induced attenuation, is taken into account through an additional frequency dependent "equivalent rain layer".

Table 2-13 summarizes the main characteristics of the physically-based models of the attenuation due to the melting layer, in terms of input and output parameters, as well as in terms of validity range.

Table 2-13. Physically-based models of the attenuation due to the melting layer

Model	Input data			Output parameters	Tested range
	Geometrical	**Radiowave**	**Climatic**		
CFPS (Onera)	Elevation	Frequency	ρ_0, Rain rate	$Z_h, Z_{dr}, \sigma_{ML}, \gamma_{ML}, A_{ML}$	3 GHz $\leq f \leq$ 35 GHz
Delft	Elevation	Frequency	ρ_0, Rain rate	$Z_h, Z_{dr}, \sigma_{ML}, \gamma_{ML}, A_{ML}$	3 GHz $\leq f \leq$ 20 GHz
POLIMI/ESA	/	Frequency	ρ_0, Rain rate	$Z_h, Z_{dr}, \sigma_{ML}, \gamma_{ML}, A_{ML}$	3 GHz $\leq f \leq$ 50 GHz
HUT	Elevation	Frequency	Rain rate	$Z_h, Z_{dr}, \sigma_{ML}, \gamma_{ML}, A_{ML}$	3 GHz $\leq f \leq$ 20 GHz

Legend:

ρ_0: dry snow density (g/m^3)

Z_h: radar reflectivity (dBZ)

Z_{dr}: differential radar reflectivity (dBZ)

σ_{ML}: melting layer cross section (cm^2/m^3)

γ_{ML}: melting layer specific attenuation (dB/km)

A_{ML}: melting layer attenuation (dB)

f: frequency (GHz)

3.　　SYNTHESIS OF RAIN AND CLOUD FIELDS

This Chapter presents a complete description of MultiEXCELL (Multi EXponential CELL) and SMOC (Stochastic MOdel of Clouds), developed at Politecnico di Milano for the reliable and accurate prediction of the attenuation due to rain and clouds impairing wireless systems operating at frequencies higher than 10 GHz. The main advantage offered by these models is the possibility to synthesize realistic maps of rain rate and integrated liquid water content, which, on turn, allow the simulation and performance evaluation of advanced systems implementing Fade Mitigation Techniques (FMTs) such as site diversity.

3.1.　　MultiEXCELL (Multi EXponential CELL)

MultiEXCELL is a rain field model with the aim of predicting the interaction between rain fields and advance wireless systems operating at high frequency, specifically in the Ka band and above, in which the use of FMTs is necessary to counteract the extremely strong atmospheric fades [Luini and Capsoni, 2011]. By generating synthetic rain fields realistically reproducing both the local rainfall statistics and the spatial distribution of the rain intensity, MultiEXCELL is a useful tool to evaluate the performance of FMTs such as site diversity schemes, in which simultaneously receiving (and in some cases also transmitting) stations are employed to mitigate the effects of rain on SatCom systems. The next sections describe in details the rationale of MultiEXCELL and how it has been developed starting from the observation of radar-derived rain fields.

3.1.1.　　Rain cell modeling

Inspired to EXCELL [Capsoni et al., 1987], MultiEXCELL relies on the "rain cell" concept, the fundamental "brick" composing rain fields. In the literature, the most commonly accepted definition of rain cell is "the continuous area inside which the rain rate R is higher than a given threshold R_{th}" [Drufuca, 1977].

3.1.1.1.　　*Radar derived rainfall databases*

The experimental station of Spino d'Adda, located a few kilometers East of Milan (latitude 45.4° N, longitude 9.5° E, altitude 84 m a.m.s.l), Italy, is equipped with an S-band Doppler weather radar (refer to Table 3-1 for its detailed technical specification), that allowed the collection of an extensive database of rain fields, whose main characteristics are provided below.

NPC database

The NPC (Nastri Pioggia Cartesianizzata) database is the result of a long-term measurement campaign undertaken from 1988 to 1992, which led to collect several rain events, each of them including radar snapshots of the rain field in the Padana Valley. As shown in Figure 3-1, each radar image is a pseudo CAPPI (Constant Altitude Plane Position Indicator) at 1.5 km above the ground, resulting from the composition of three circular radar scans at elevation angles of 3°, 5° and 7°.

The maximum operational range considered in the NPC database is 40 km, in order to avoid the inclusion of clutter values originating from the mountains surrounding Spino d'Adda. The minimum rain rate value has been conservatively set to 0.5 mm/h, although the system could allow the detection of much lower rain rates at 40 km of distance.

Table 3-1. Technical specifications of the weather radar located at Spino d'Adda

Transmitter	
Type	Magnetron
Power	Peak = 475 kW; Mean = 125 W
Pulse duration	0.5 or 1.5 μsec
Pulse Repetition Frequency	500 Hz or 1 kHz
Frequency	2.8 GHz (S-band)
Receiver	
TR recovery time	≤ 3 μsec
Noise figure	2 dB
Minimum detectable signal	-104 dBm
Antenna	
Type	parabolic reflector
Dimension	3.6 m diameter
Rotation velocity	30°/sec
Gain	38.4 dB
Beam width (-3 dB)	2°
Polarization	Vertical

The radar reflectivity Z (mm^6/m^3) has been converted into rain rate R (mm/h) using the well established relationship:

$$Z = 200\, R^{1.6} \tag{3-1}$$

whose coefficients 200 and 1.6 have been proposed by Marshall-Palmer and have proven to suitably represent also the type of precipitation occurring in the Padana Valley [Pawlina and Binaghi, 1995]. Finally, CAPPI data have been remapped from their original polar format to a 0.5 km×0.5 km Cartesian grid. Consecutive images, an example of which is shown in Figure 3-2, have been collected approximately each 77 seconds, the time necessary to complete three PPI scans.

In order to isolate only reliable rainfall data to be used for rain modeling, radar snapshots have been carefully checked and problematic images have been removed, i.e. those affected by anomalous propagation effects, presence of the bright band, possible interference coming from other radio sources. The resulting NPC radar database consists of more than 2000 radar pictures, which are fully representative of the yearly rainfall statistics in the Padana Valley.
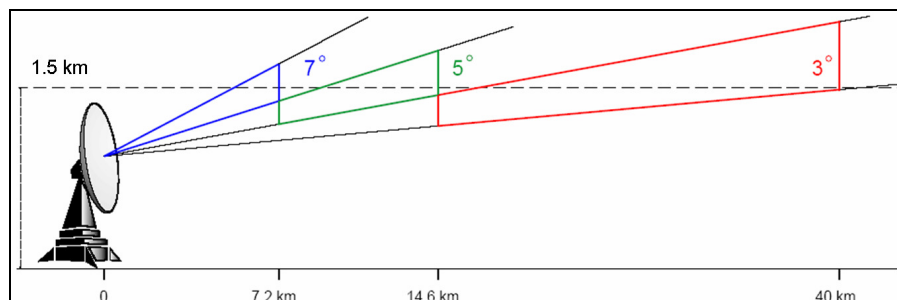
Figure 3-1. Combination of three PPIs (Plane Position Indicator) collected by the weather radar of Spino d'Adda to obtain CAPPI (Constant Altitude Plane Position Indicator) images
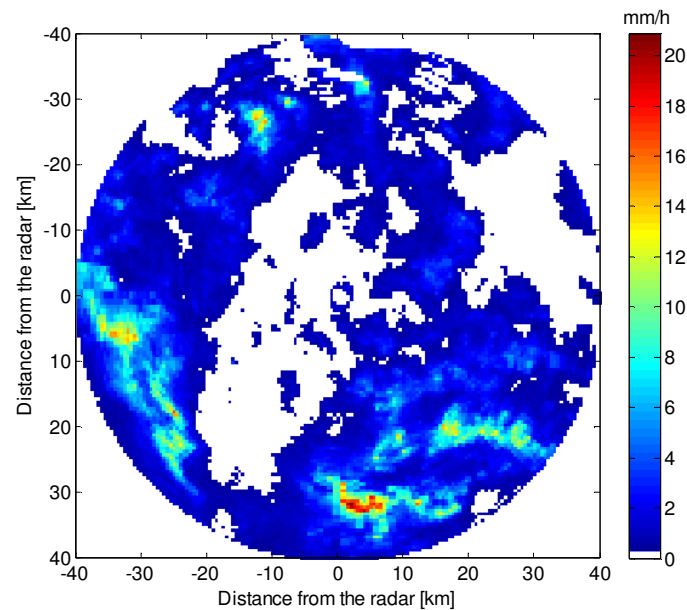
Figure 3-2. Example of the CAPPI images obtained from the weather radar in Spino d'Adda

LR database

In order to extend the limited coverage area of the NPC database, and, therefore, to investigate also the large-scale spatial distribution of the rain field, the Spino d'Adda weather radar has been operated also at lower elevation angles (1.5°, 2.5° and 4.5°), which allowed to obtain pseudo CAPPI images with 150-km radius (hereinafter these rainfall maps will be named "Long-Range" (LR) maps). However, this goal can be achieved at the expense of a reduced quality of the snapshots: the clutter mainly originating from the surrounding mountains reduces the useful observation area and sometimes corrupts the rain patterns, whilst the longer the range, the lower the spatial resolution because of the inherent widening of the radar beam. Sophisticated processing procedures (not reported here from brevity's sake) have been employed to maximize data quality and prevent the inclusion of inaccurate estimates of the rain rate at ground level.

The resulting LR database consists of more than 3000 maps of ground rain collected during several rain events occurred in the years 1998, 1999, 2000 and 2006. As for the NPC database, the pixel dimension of the Cartesian grid is 0.5 km×0.5 km, whereas the temporal resolution is approximately 15 minutes.

3.1.1.2. Optimum rain cell profile

The rain cell modeling implies the choice of an analytical profile that describes in a simple way the spatial distribution of the rain intensity inside the single cell. On one side, the most adequate profile should preserve at best the main characteristics of the real rain cell (such as its average rain rate and its area), rather than mimic exactly its shape; on the other side, it should be mathematically manageable so as to make it applicable in practice. To this aim, the following simple rain cell profile, already employed in the EXCELL model [Capsoni et al., 1987], is adopted in MultiEXCELL:

$$R(\rho) = R_M \exp\left[-(\rho/\rho_0)^{\frac{2}{k}}\right] \tag{3-2}$$

In (3-2), R (mm/h) is the rain rate, ρ (km) is the distance from the cell center, where the peak rain rate R_M (mm/h) is located, whereas ρ_0 (km) is the equivalent radius for which $R = R_M/e$. Actually, equation (3-2) identifies multiple profiles, depending on k, the shape factor: $k = 1$, $k = 2$ and $k = 3$ respectively define Gaussian, exponential and hyper-exponential cell profiles.

The NPC radar images have been processed to isolate rain cells at different rain thresholds R_{th} from 1 to 10 mm/h. Afterwards, cells have been classified as corrupted (C) or uncorrupted (UC), depending on whether they are affected by (even one pixel of) clutter and/or their perimeter touches the limits of the observation area. Moreover, the minimum rain cell area was set to $A_{min} = 2$ km×2 km = 4 km^2 in accordance with the resolution limitations introduced by the radar beam width (-3 dB beam width $\theta_{-3dB} = 2°$). The analysis has shown that $R_{th} = 5$ mm/h is a good compromise between the need to work with single-peaked cells (for which analytical models as the ones proposed in (3-2) appear adequate) and with a significant number of cells. The number of UC cells is 20379.

According to (3-2), a synthetic rain cell is completely identified by R_M, ρ_0 and k. For any given cell, after selecting $k = 1, 2$ or 3, R_M and ρ_0 are determined by imposing two conditions. A good choice is to involve integral quantities, as they are definitely more reliable and meaningful than point values if derived by radar images; specifically, the area $A(R_{th})$ and the mean rain rate $\overline{R}(R_{th})$ were selected, as in [Capsoni et al., 1987]:

$$A(R_{th}) = \pi \rho_0^2 \ln^k(R_M/R_{th}) \tag{3-3}$$

$$\overline{R}(R_{th}) = \frac{1}{A(R_{th})} \int_{A(R_{th})} R(x,y)\,dx\,dy = R_M \frac{k\gamma(k,\ln(R_M/R_{th}))}{\ln^k(R_M/R_{th})} \tag{3-4}$$

In (3-4), $\gamma(a,x)$ indicates the incomplete gamma function.

The left side of (3-3) and (3-4) is calculated numerically from radar data, whereas the expressions on the right side are valid for synthetic cells whose profile is defined by (3-2). The most suitable profile was chosen by comparing additional descriptors of measured and synthetic rain cells, namely, the peak rain value as measured by the radar ($\overline{R}_{max}$), the root mean square of the rain intensity (R_{rms}) and the cell dynamic (R_{din}), respectively defined as:

$$\overline{R}_{max} = \frac{1}{A_p} \int_0^{\overline{\rho}} R_M \exp\left[-(\rho/\rho_0)^{\frac{2}{k}}\right] 2\pi\rho\,d\rho \tag{3-5}$$

where $\overline{\rho} = \sqrt{A_p/\pi}$ indicates the maximum distance from the cell center and $A_p = 0.25$ km^2 (area of the radar pixel).

$$R_{rms}(R_{th}) = \sqrt{\frac{1}{A(R_{th})} \int_{A(R_{th})} R^2(x,y)\,dx\,dy} = \sqrt{\frac{kR_M^2}{2^k \ln^k(R_M/R_{th})} \gamma(k,2\ln(R_M/R_{th}))} \tag{3-6}$$

$$R_{din} = \frac{\overline{R}(R_{th})}{R_{\max}} = \frac{k\,\gamma(k, \ln(R_M/R_{th}))}{\ln^k(R_M/R_{th})} \qquad (3\text{-}7)$$

Results, not reported here but completely detailed in [Luini and Capsoni, 2011], clearly indicate that the exponential profile reproduces at best the three descriptors mentioned above. As a further motivation for the choice of a purely exponential profile, the work in [von Hardenberg et al., 2003] deserves to be cited. The authors analyzed precipitation fields from the TOGA-COARE and GATE experiments and found that, on the average, the exponential profile is the most adequate to model rain cells in tropical climates as well.

3.1.1.3. Rain cells' probability of occurrence

The MultiEXCELL model assumes that the exponential profile in (3-2) has a global validity, as also suggested by [Capsoni et al., 1987] and [von Hardenberg et al., 2003]: what changes from site to site is the rain cells' probability of occurrence, such that, for instance, in tropical areas, convective cells prevail over stratiform ones, whereas in temperate sites, their relative occurrence is more balanced.

For the practical application of MultiEXCELL to different sites, it is therefore of paramount importance to derive a closed-form analytical expression that allows to adapt the synthetic rain cells' probability of occurrence, $N(R_M, \rho_0)$, to the local input rainfall statistics. As a preliminary step towards this aim, R_M and ρ_0 values extracted from the NPC database are used to compute the distribution of ρ_0 conditioned to R_M, $p(\rho_0|R_M)$.

The probability density function (PDF) of ρ_0 is illustrated in Figure 3-3, based on which the lognormal law appears to be a suitable fitting distribution.
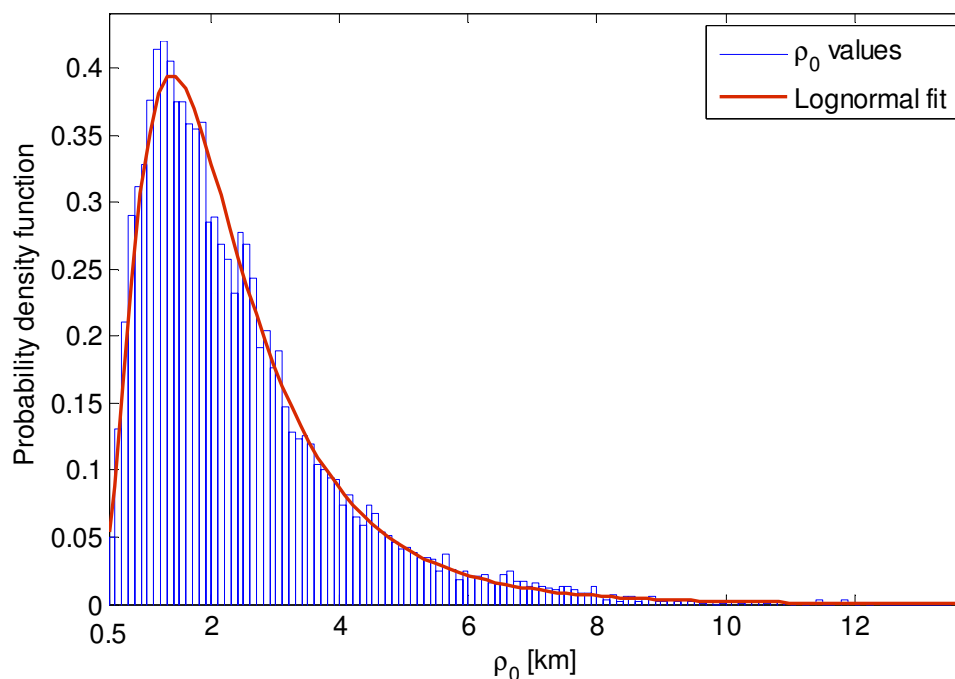
Figure 3-3. Distribution of ρ_0 and MLE (Maximum Likelihood Estimation) lognormal PDF

The general expression of the lognormal probability density function (PDF) is:

$$p(\rho_0) = \frac{1}{\rho_0 \sigma \sqrt{2\pi}} \exp\left[-\left(\frac{\ln(\rho_0) - \mu}{\sqrt{2}\sigma}\right)^2\right] \tag{3-8}$$

where μ and σ are the mean and standard deviation of the variable's logarithm, that is normally distributed. The Maximum Likelihood Estimation (MLE) of the distribution parameters provides the PDF plotted in Figure 3-3 (solid line), for which $\mu = 0.692$ and $\sigma = 0.609$.

Further investigation on the data revealed that also the distribution of ρ_0 conditioned to R_M, $p(\rho_0|R_M)$, follows the lognormal law (e.g. refer to Figure 3-4, where the complementary cumulative distribution functions of ρ_0 conditioned to R_M are shown as derived from the data and from the fitted lognormal distribution). ρ_0 values have been grouped into eight classes of R_M (ranging from 5 to 250 mm/h) and the lognormal parameters $\mu(R_M)$ and $\sigma(R_M)$ have been determined as a function of the average R_M value of each class (refer to Figure 3-5).
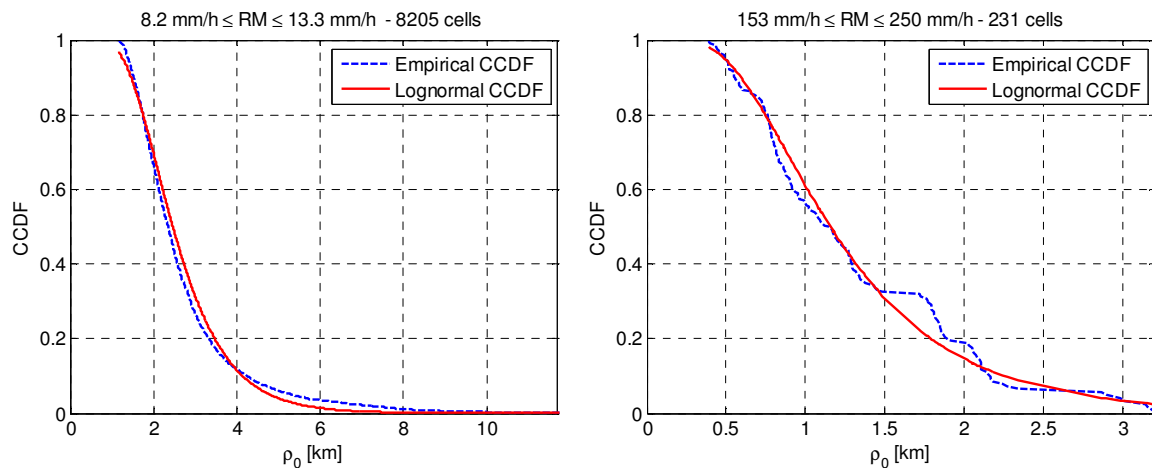
Figure 3-4. Comparison between $P_e(\rho_0|R_M)$ and $P_m(\rho_0|R_M)$, for the most (left side) and the least (right side) numerous classes among the eight chosen to classify ρ_0 as a function of R_M
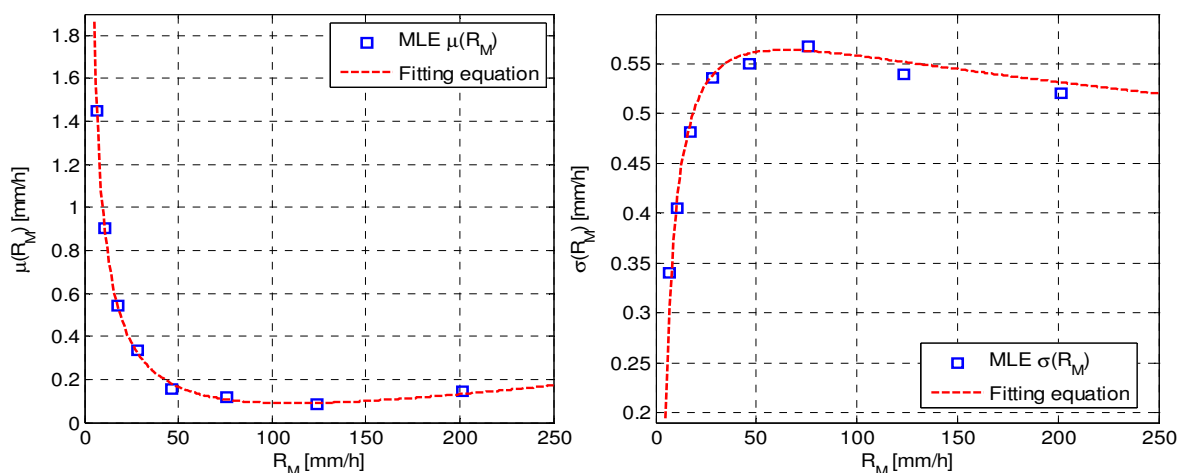
Figure 3-5. Trend of $\mu(R_M)$ and $\sigma(R_M)$ as a function of the average R_M value of each class

As is clear from Figure 3-5, both trends can be accurately fitted by the following expressions (dashed lines):

$$\mu(R_M) = 7.86\,R_M^{-0.84} - 6.03\,R_M^{-17.27} + 0.001 R_M - 0.19 \tag{3-9}$$

$$\sigma(R_M) = 33.32\,R_M^{-0.32} - 34.22\,R_M^{-0.35} \tag{3-10}$$

which, together with (3-8), give the complete description of the statistical distribution of ρ_0 conditioned to R_M.

In order to allow the adaptation of the rainfall cellular model described above to the local meteorological environment, it is useful to consider the relationship in (3-11) which expresses the superposition of the cells' contributions to generate the $P(R)$ and, thus, links the rain cells' probability of occurrence, $N(R_M,\rho_0)$, to the local rainfall statistic (for clarity's sake, although $N(R_M,\rho_0)$ is identified as a probability, its dimensions are [1/(km²·km·mm/h)]):

$$P(R) = \int\limits_{R}^{\infty}\int\limits_{a}^{b} A(R_M,\rho_0,R)\,N(R_M,\rho_0)\,d\rho_0\,dR_M \quad R_M \geq 5 \text{ mm/h} \tag{3-11}$$

where $A(R_M,\rho_0,R) = \pi[\rho_0 \ln(R_M/R)]^2$ is the area of the cell with parameters R_M and ρ_0, for which the rain intensity R is exceeded, $a = 0.5$ km and $b = 14$ km are respectively the minimum and the maximum value of ρ_0 deduced from the radar observations. The imposition of bounds a and b in (3-11) is not necessary from an analytical point of view, but, as a matter of fact, this constraint is what allows to practically apply MultiEXCELL: if no bounds were imposed, also rain cells with extremely small or extremely large equivalent radius (necessarily discarded in synthesizing realistic rain maps) would be required to exactly match the input $P(R)$.

As a result of the inversion of (3-11) (whose details are fully included in [Luini and Capsoni, 2011]), $N(R_M,\rho_0)$ assumes the final expression:

$$N(R_M,\rho_0) = -\frac{1}{\pi(\psi_m - \psi_M)\exp\left(2\sigma^2(R_M) + 2\mu(R_M)\right)}\frac{d^3P(R)}{d\ln(R)^3}\bigg|_{R=R_M}$$
$$\cdot\frac{1}{\rho_0\sigma(R_M)\sqrt{2\pi}}\exp\left[-\left(\frac{\ln(\rho_0) - \mu(R_M)}{\sqrt{2}\sigma(R_M)}\right)^2\right] \tag{3-12}$$

where:

$$\psi_m = \psi\left[\frac{\mu(R_M) + 2\sigma^2(R_M) - \ln(a)}{\sqrt{2}\sigma(R_M)}\right] \quad \text{and} \quad \psi_M = \psi\left[\frac{\mu(R_M) + 2\sigma^2(R_M) - \ln(b)}{\sqrt{2}\sigma(R_M)}\right] \tag{3-13}$$

and $\psi(x)$ is the error function:

$$\psi(x) = \frac{2}{\sqrt{\pi}}\int\limits_{0}^{x}\exp\left(-t^2\right)dt \tag{3-14}$$

whereas $\mu(R_M)$, $\sigma(R_M)$ are given by (3-9) and (3-10).

For the practical application of (3-12), following the approach of several rainfall models such as [Jeannin et al., 2012], [Capsoni et al., 1987] and [Féral et al., 2006], the input $P(R)$ is fitted by the following analytical model [Capsoni et al., 2006]:

$$P(R) = P_0 \ln^n \left(\frac{R_a + R_{low}}{R + R_{low}} \right) \tag{3-15}$$

where P_0, n, R_{low} and R_a are regression coefficients that assure the best agreement between the input $P(R)$ and (3-15).

Figure 3-6 shows the rain cells' probability of occurrence calculated for Spino d'Adda (left) and for Miami (right) by means of (3-12), using as input the $P(R)$s predicted by recommendation ITU-R P.837-6 for the two sites (Spino d'Adda: lat = 45.4 °N and lon = 9.5 °E; Miami: lat = 25.65 °N and lon = -80.43 °E) [ITU-R P.837-6, 2012]. These results provide a hint of how the rain cells' probability of occurrence varies depending on the local input $P(R)$: whilst in Spino d'Adda different types of cell have a comparable probability of occurrence, in Miami, intense and spatially limited precipitation clearly prevails, as it is typically the case for tropical convective-like climates.
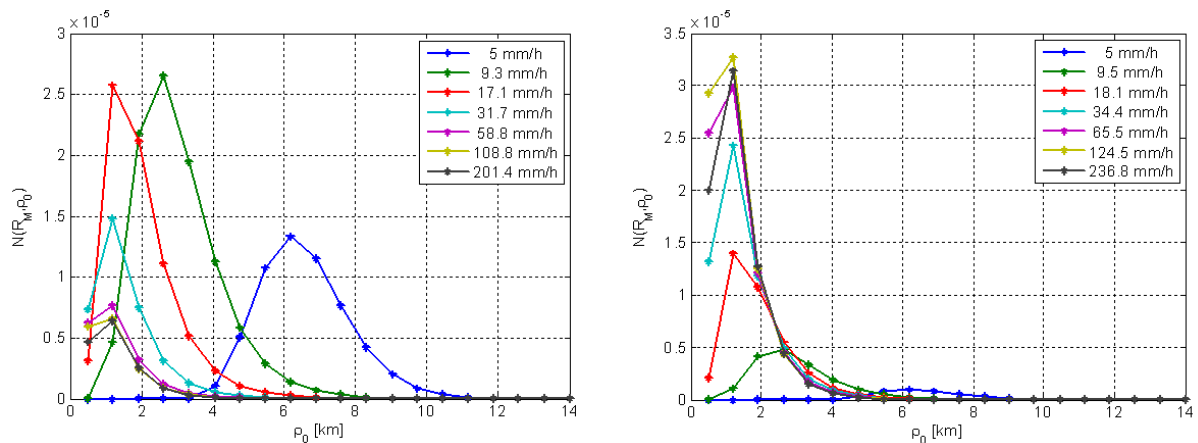
Figure 3-6. Rain cells' probability of occurrence, calculated through (3-12), relative to Spino d'Adda (45.4° N, 9.5° E) on the left side and to Miami (25.65° N, -80.43° E) on the right side

3.1.2. Rain field modeling

According to the features presented so far, MultiEXCELL is inherently a small-scale model that reproduces the rainfall process by means of a population of isolated rain cells. Thanks to its analytical formulation, the model is particularly suitable and efficient for investigating the interaction between a radio link and precipitations in various scenarios [Capsoni et al., 2009]. However, when mid/large-scale applications are concerned (from tens to some hundreds of kilometers), such as the simulation of site diversity systems and of terrestrial networks, the evaluation of non-geostationary satellite links performance (which involves also long paths at low elevation angles) and the estimation of the radio interference due to hydrometeor scattering, the probability that more than one cell is simultaneously interacting with the link (system) is high. As a result, the isolated-cell model's applicability to such scenarios becomes more and more critic with the increase of the system's dimension and it is necessary to further extend the model. Weather radar data are a unique source of information of the rainfall spatial characteristics as they provide consecutive snapshots of the rain field and a simple visual inspection of rain maps points out that rain cells are not randomly distributed in space, but rather, they tend to aggregate to form larger structures

[Féral et al., 2006], [Northrop, 1975]. This behavior is evident in Figure 3-7 that shows a typical rain field observed by the radar located at Spino d'Adda: the white ellipses identify single rain cells (two of them pertaining to the same aggregate) and the large red ellipses delimit aggregates.
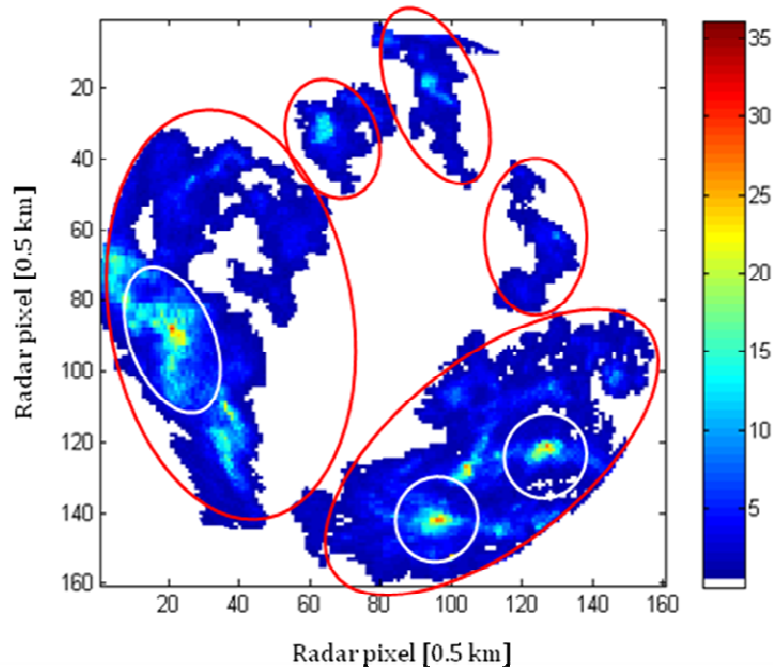
Figure 3-7. Typical aggregative process of rain cells

It appears from the figure that rain is organized on three spatial scales: the small-scale (up to approximately 20 km) which involves single rain cells; the mid-scale (roughly from 20 km to 50 km) that is related to how cells cluster together to form an aggregate, and finally, the large-scale (from 50 km to about 300 km) which is related to the mutual position of the aggregates on the map.

In the following subsections the spatial distribution of precipitation on the radar maps is investigated to extract useful information for rain field synthesis.

3.1.2.1.   Analysis of the spatial characteristics of rain fields: intercellular distance

An aggregate is considered as a rainy area with thresholded at 1 mm/h with more than one peak rain rate exceeding 5 mm/h inside. The statistical characterization of the intercellular distance (ICD) has been given here in terms of the nearest neighbor ICD (NNICD) and the NPC dataset was employed because of its increased accuracy. The ICD between two rain cells is defined as follows:

$$d_C = \sqrt{(x_1 - x_2)^2 + (y_1 - y_2)^2} - R_1 - R_2 \qquad (3\text{-}16)$$

where x_i, y_i represent the position of the center of mass of cell i and R_i is the radius of the equivalent circular cell with equal area and center of mass. The left side of Figure 3-8 shows the graphical definition of the ICD: the outer line indicates the aggregate at 1 mm/h, and the irregular shapes depicted in grey are two daughter cells, whose equivalent circular cells are

indicated by the two surrounding circles. The definition of the ICD according to (3-16) is adequate and consistent with the rain cell modeling mentioned above: the use of an effective distance instead of the more customary real distance between cells allows preserving the isolation between the circular synthetic rain cells, whatever their dimension, i.e., whatever R_1 and R_2.

The probability density function of the NNICD, based on 2474 values, is presented in Figure 3-8 (right side). The distribution shows that nearest neighbor cells tend to be quite close one to the other (the peak of the PDF is for $d_C = 2$ km) and also that the effective distance seldom exceeds 10 km (the maximum being approximately 37 km). It is worth noting from the figure that also negative values of d_C were found: they represent cells that are strongly anisotropic and tend to elongate orthogonally to the line connecting the centers of mass. In this case, in fact, the real distance between the cells is shorter than the sum of the two effective radii.
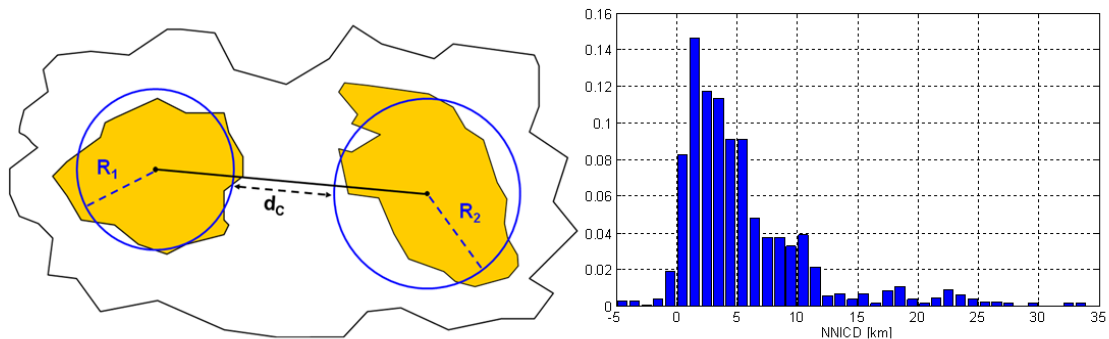
Figure 3-8. Definition of the ICD (left) and probability density function of the NNICD, derived from the NPC database (right)

3.1.2.2.   *Analysis of the spatial characteristics of rain fields: interaggregate distance*

Due to the large dimension of aggregates, only LR maps are suitable for the investigation of the IAD. As for the ICD, the quantity of interest is the nearest neighbor IAD (NNIAD), but, in this case, the real distance between the centers of mass is used:

$$d_A = \sqrt{(x_1 - x_2)^2 + (y_1 - y_2)^2}$$ (3-17)

where, again, x_i, y_i identify the position of the center of mass of cell i. In the calculation of d_A, all cells, also the ones that were assumed to be only marginally corrupted at a visual inspection, were taken into account, the rationale being: 1) aggregates at 1 mm/h are more likely affected by clutter than single cells, both because they result from the clustering of cells at 5 mm/h and because the area covered by rain at 1 mm/h is much more extended than the one covered at 5 mm/h; 2) LR maps are more affected by clutter with respect to NPC maps, and the exclusion of all corrupted aggregates would greatly reduce the available structures; 3) due to their large dimensions, when considering aggregates at 1 mm/h, the presence of some clutter pixels has a reduced effect on the average parameters describing the aggregate.

The probability density function of the NNIAD, based on 4366 values, is reported in Figure 3-9 (left side), which shows that most of the NNIAD values lie within 20 and 120 km,

being the most probable ones around 30 km. The minimum and the maximum measured d_A are 6 and 177 km, respectively.

3.1.2.3.   Analysis of the spatial characteristics of rain fields: number of aggregated cells

The last information necessary to complete the description of rain structures is the number of daughter cells (5 mm/h) per aggregate (1 mm/h). Again, LR maps were taken into account. The number of daughter cells N_{dc} was calculated in each aggregate used to derive the IAD. The PDF of the number of daughter cells is plotted in Figure 3-9 (right side) and shows an exponential behavior: most of the aggregates consist of two daughters and very few of them have more than 25.
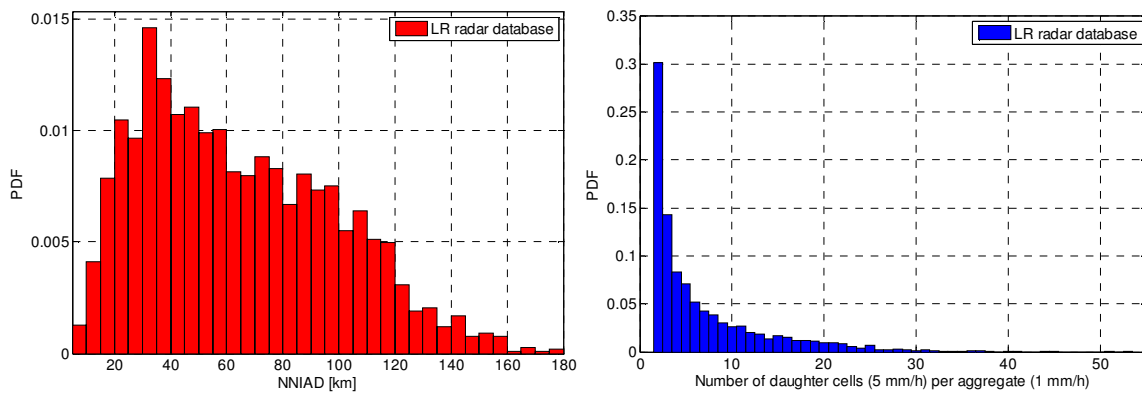
Figure 3-9. Probability density function of the NNIAD (left side) and probability density function of the number of daughter cells (5 mm/h) per aggregate (1 mm/h) (right side)

3.1.2.4.   Analysis of the spatial characteristics of rain fields: fractional rainy area

The generation of realistic rain fields requires the knowledge of the fraction of the area affected by rain. To this aim, the MultiEXCELL model relies on a method, originally presented in [Eltahir and Bras, 1993], that allows to derive the fractional rainy area, η, from Numerical Weather Prediction (NWP) data usually provided worldwide on a regular latitude/longitude grid:

$$\eta(R_{th}) = \frac{A_R(R_{th})}{A} = \frac{M_t}{\overline{R}\,\Delta t}\,P(R_{th}) \qquad (3\text{-}18)$$

where A and $A_R(R_{th})$ (km^2) are respectively the area of the map and the one affected by rain rates exceeding R_{th}, M_t (mm) is the amount of rain accumulated during the period Δt (hours), i.e. the temporal resolution of the available NWP data, $\overline{R}$ (mm/h) is the yearly mean value of the rain intensity, conditioned to $R > 0$ mm/h and, $P(R_{th})$ is the value of the local $P(R)$ calculated for $R = R_{th}$.

For the practical application of (3-18) to derive η worldwide, the ERA40 database provided by the ECMWF (European Center for Medium-range Weather Forecast) is a suitable choice: in fact, notwithstanding its limited spatial and temporal resolutions (regular 2.5°×2.5° lat/lon grid, $\Delta t = 6$ hours), ERA40 data represent a statistically stable database (approximately 40 years) available nowadays to retrieve η from NWP on a global basis. As for the calculation

of $\bar{R}$ in (3-18), recommendation ITU-R P.837-6 [ITU-R P.837-6, 2012] can be employed, which, although with a certain degree of approximation, allows to obtain $P(R_{th})$ worldwide (and hence $\bar{R}$).

As clearly stated in [Eltahir and Bras, 1993], equation (3-18) is valid under the assumption that the rain rate statistical distribution is substantially invariant within Δt. Consequently, the coarse temporal resolution of the ERA40 database is the limiting aspect in the application of equation (3-18) (based on the quasi-ergodicity property of rain fields, η is fairly independent of the observation area [Onof and Wheater, 1996]). In fact, if only a portion of the 6-hour period is actually affected by rain, since ERA40 M_t values are calculated as the average accumulated rain, the η value derived through (3-18) will underestimate the actual fractional area coverage. In order to obtain a more realistic distribution of η, the expression in (3-18) becomes:

$$\eta(R_{th}) = \frac{\bar{f}_{6h} M_t}{\bar{R} \Delta t} P(R_{th}) \qquad (3\text{-}19)$$

where $\bar{f}_{6h}$ is a correction factor that compensates for the average portion of Δt actually affected by rain. The optimum value of $\bar{f}_{6h} = 6$ has been found by observing the CDFs of η depicted in Figure 3-10: the solid blue line refers to the fractional rainy area obtained from the NPC database, the dotted black curve is relative to the application of (3-18) to 10 years of M_t ERA40 data for Spino D'Adda (years 1992-2001) and, finally, the dashed red line concerns the application of (3-19) to the same ERA40 data used for (3-18). The factor $\bar{f}_{6h} = 6$ allows to adjust ERA40 data so as to better take into account, on the average, the portion of Δt actually affected by rain.
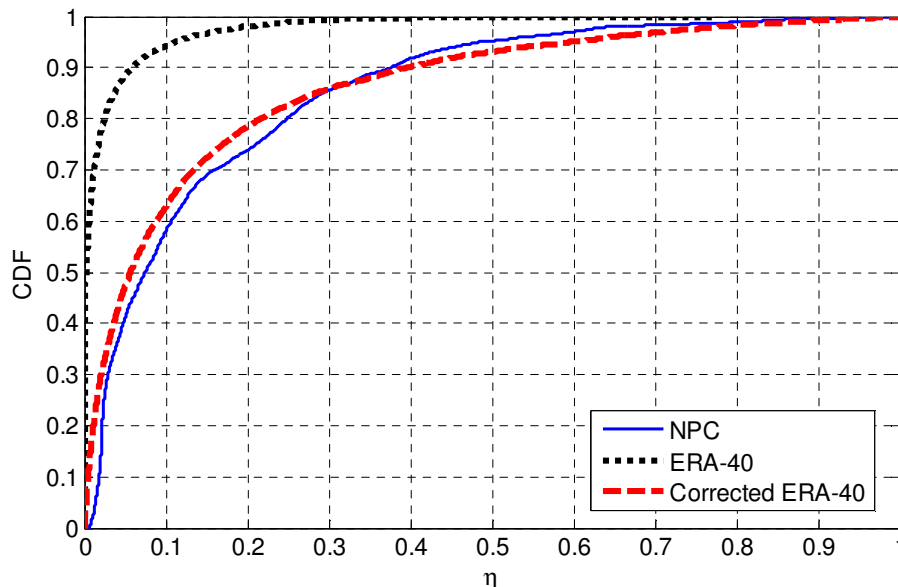
Figure 3-10. Distribution of η derived for Spino d'Adda from the ERA40 database, according both to (3-18) and (3-19), compared with the distribution obtained from the NPC database

3.1.3.   Generation of synthetic rain fields

The quasi-ergodicity of the rainfall process is a widely accepted and established concept [Eltahir and Bras, 1993], [Goldhirsh, 1990], [Drufuca, 1974], which, in fact, several rainfall models rely on, such as EXCELL [Capsoni et al., 1987], HYCELL [Féral et al., 2006], those proposed by Gremont-Filip [Gremont and Filip, 2004], by Jeannin [Jeannin et al., 2012] and by Callaghan-Vilar [Callaghan and Vilar, 2007]. This property implies that there is a negligible difference between the statistical results obtained from a set of radar derived rain maps or a single raingauge sampled over time: as a consequence, the $P(R)$ measured by a raingauge at a given site permits to determine the rain cells' probability of occurrence (first order statistic), as implicitly assumed in the derivation of (3-12). As for the spatial correlation of rain (second order statistics), such feature is tightly linked to the rain cells' aggregation and spatial distribution: the generation of the rain fields through MultiEXCELL, described in detail in the next section, preserves the correct NNICD among the cells belonging to the same aggregate, whose dimension is determined according to the distribution of the number of daughter cells per aggregate (mid-scale spatial correlation of the field). The large-scale spatial component of the field is instead regulated by the radar derived NNIAD distribution. Finally, the fractional rainy area, whose distribution can be obtained from the ERA40 database through (3-19) is preserved as well for the generation of realistic rain fields.

3.1.3.1.   Number of rain cells

The $N(R_M,\rho_0)$, calculated through (3-12), defines the appropriate proportion among the various types of synthetic rain cells that must be reproduced. In order to generate a finite number of synthetic rain maps, yet representative of the local $P(R)$, it is necessary to determine also a finite number of cells to be used. In principle, $N(R_M,\rho_0)$ could be normalized to its minimum value N_{min} so that the number of cells $N_C(R_M, \rho_0)$ to be employed for each class (R_M,ρ_0) turns out to be $N_C(R_M,\rho_0) = N(R_M,\rho_0)/N_{min}$.

It follows that the total number of rain cells is $N_t = \sum_{\rho_0=0.5}^{14} \sum_{R_M=5}^{Ra} N_C(R_M,\rho_0)$, depends on N_{min}, and, in turn, on the local $P(R)$ through (3-12). In order to avoid dealing with too many cells, it is possible to neglect the role of the less probable rain cells without any significant loss in the $P(R)$ modeling accuracy. In other words, it is possible to determine a proper threshold N_{th} to be imposed on $N(R_M,\rho_0)$, such that, on one side, the modeling accuracy is maintained and, on the other side, N_t is reduced to a manageable value. Thus N_t becomes:

$$N_t = \sum_{\rho_0=0.5}^{14} \sum_{R_M=5}^{Ra} \frac{N(R_M,\rho_0)}{N_{th}} \tag{3-20}$$

where all $N(R_M,*\rho_0*)$ values lower than N_{th} are set to zero and the associated rain cells $(R_M,*\rho_0*)$ discarded.

N_{th} has to be determined considering the following constraints: 1) obtain a manageable N_t value; 2) generate a sufficient number of rain maps to achieve statistical meaningfulness; 3) preserve the local rainfall statistics with a good degree of accuracy. As a rule of thumb, N_t between 15000 and 20000 (roughly corresponding to N_{th} around 10^{-8}) is a good choice as it allow to fulfill all the above mentioned constraints: 300 to 500 maps are generated and the associated $P(R)$ negligibly differs from the input rainfall statistics.

3.1.3.2.   Rain field synthesis

The procedure for rain field synthesis is based on a double aggregative process reflecting the physical characteristics of real rain fields observable in radar data: first, cells are clustered into aggregates and afterwards aggregates are combined to produce a complete synthetic rain map. Specifically, MultiEXCELL is founded on the following points:

1. Calculate the rain cells' probability of occurrence from the local rainfall statistics using (3-12).

2. Calculate the $N_C(R_M, \rho_0)$ values for each class of (R_M, ρ_0) using N_{th}. A total of 20 intervals both for ρ_0 (linear subdivision between 0.5 km and 14 km) and R_M (logarithmic subdivision between 5 mm/h and R_a mm/h) are selected, thus providing 400 different kinds of cell. The value of N_{th} is chosen so as to obtain $15000 < N_t < 20000$ cells.

3. Derive the distribution of the fractional rainy area (η) for the site of interest through (3-19). According to the rain threshold of the NPC maps used in this study, the minimum rain rate of the generated synthetic maps is set to 0.5 mm/h (therefore in (3-19), $R_{th} = 0.5$ mm/h). The lateral dimension L of the square synthetic map is chosen such that it maintains the area of the ERA40 pixel containing the site of interest: for Spino d'Adda, $L = 234$ km. Finally, the spatial resolution of the map is set to 1 km×1 km.

4. For each new rain map i, determine the associated rainy area by randomly extracting a value η_i from the distribution of the fractional rainy area obtained at step 3. The rain map is developed iteratively by adding sequentially (as specified in step 5) one new rain cell until the total fractional rainy area η_{map} reaches η_i. As a result, the number of cells on the map will depend also on η_i.

5. For each map, the first aggregate of cells is defined by randomly extracting the number of daughter cells, $N_{dc,q}$, from the radar derived correspondent distribution shown in Figure 3-9. The daughter cells are chosen uniformly from the set of available cells $N_C(R_M, \rho_0)$, whose dimension decreases by a unity each time a new cell is selected. The first cell is placed at a random point on the map, whereas each successive cell will be arranged such that its effective distance from the previous one equals a value $d_{C,j}$ randomly extracted from the NNICD distribution shown in Figure 3-8. The orientation of the line connecting the current and next cells' centers of mass is extracted from a uniform distribution between 0 and 2π (isotropic spatial distribution). The construction of the aggregate is stopped either if its number of daughter cells equals $N_{dc,q}$ or if η_{map} reaches η_i. After its completion, the aggregate is randomly placed on the rain map.

6. If $\eta_{map} < \eta_i$, a new aggregate is built according to the procedure outlined in step 5: its position on the map is determined such that the distance between the centers of mass of the new and the previous aggregates (at 1 mm/h) equals a value d_A randomly extracted from the NNIAD distribution shown in Figure 3-9.

The arrangement of the cells belonging to the same aggregate (step 5) deserves some additional comments. According to how the NNICD distribution was derived, rain cells at 5 mm/h should not overlap. In some cases, however, during the generation of the synthetic rain

field, cells at 5 mm/h overlap each to the other due to either negative values extracted from the NNICD distribution or when η_i assumes high values (both situations, however, are quite rare, as clearly indicated by the NNICD and η_i distributions).

In this case, however, it is not possible to sum up the rain intensity values associated to the same area because, in this way, the local $P(R)$ would not be properly reproduced anymore ($N_C(R_M,\rho_0)$ is calculated under the assumption of isolated rain cells). The solution adopted for this problem consists in redistributing around the structure of the aggregated cells all the overlapping rain rate values smaller than R_o, as shown in Figure 3-11, such that the overall trend of the rain profile still decreases exponentially as moving away from the center of the structure, but more slowly than the original rain cells' profile. This solution allows to preserve the original total rainy area of the aggregate (in other words, the local $P(R)$) as well as its average rain rate.
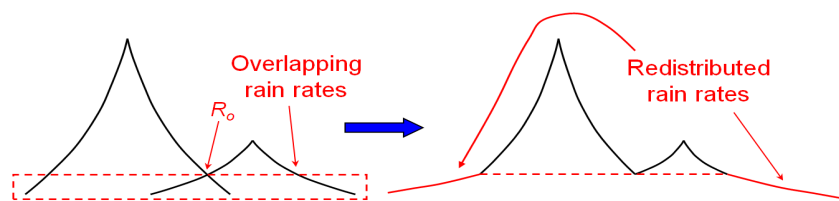
Figure 3-11. Redistribution of the overlapping rain rates around the structure

Moreover, as a byproduct, this solution provides the shape of the synthetic rain structures with a more irregular and realistic trend (if compared to the purely exponential one): in fact, the core of a real rain cell tends to be more uniform than the surrounding debris. This is clearly visible in Figure 3-12, which shows a typical synthetic rain map generated by the MultiEXCELL model: several clusters of rain cells can be identified.
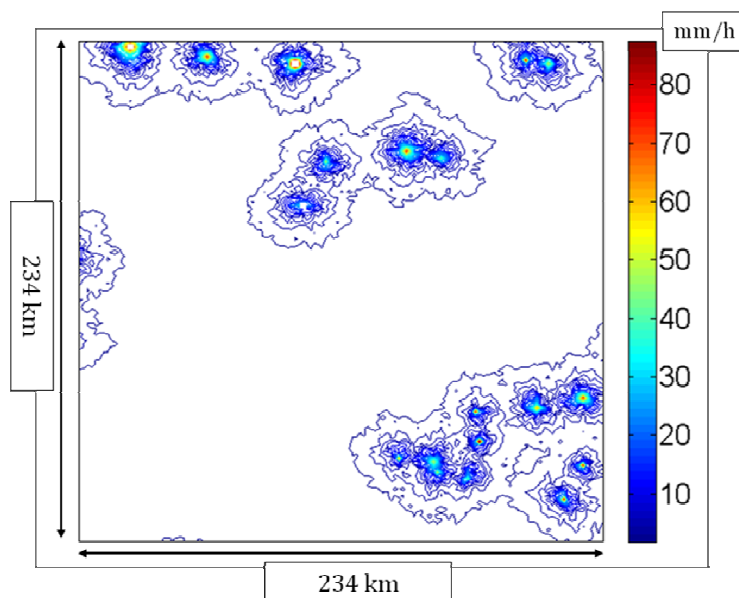
Figure 3-12. Example of a synthetic rain map generated by the MultiEXCELL model for Spino d'Adda (234 km×234 km)

In order to provide an overview of the MultiEXCELL features and further clarify the procedure for the generation of synthetic rain maps, the workflow of the model is reported in Figure 3-13.
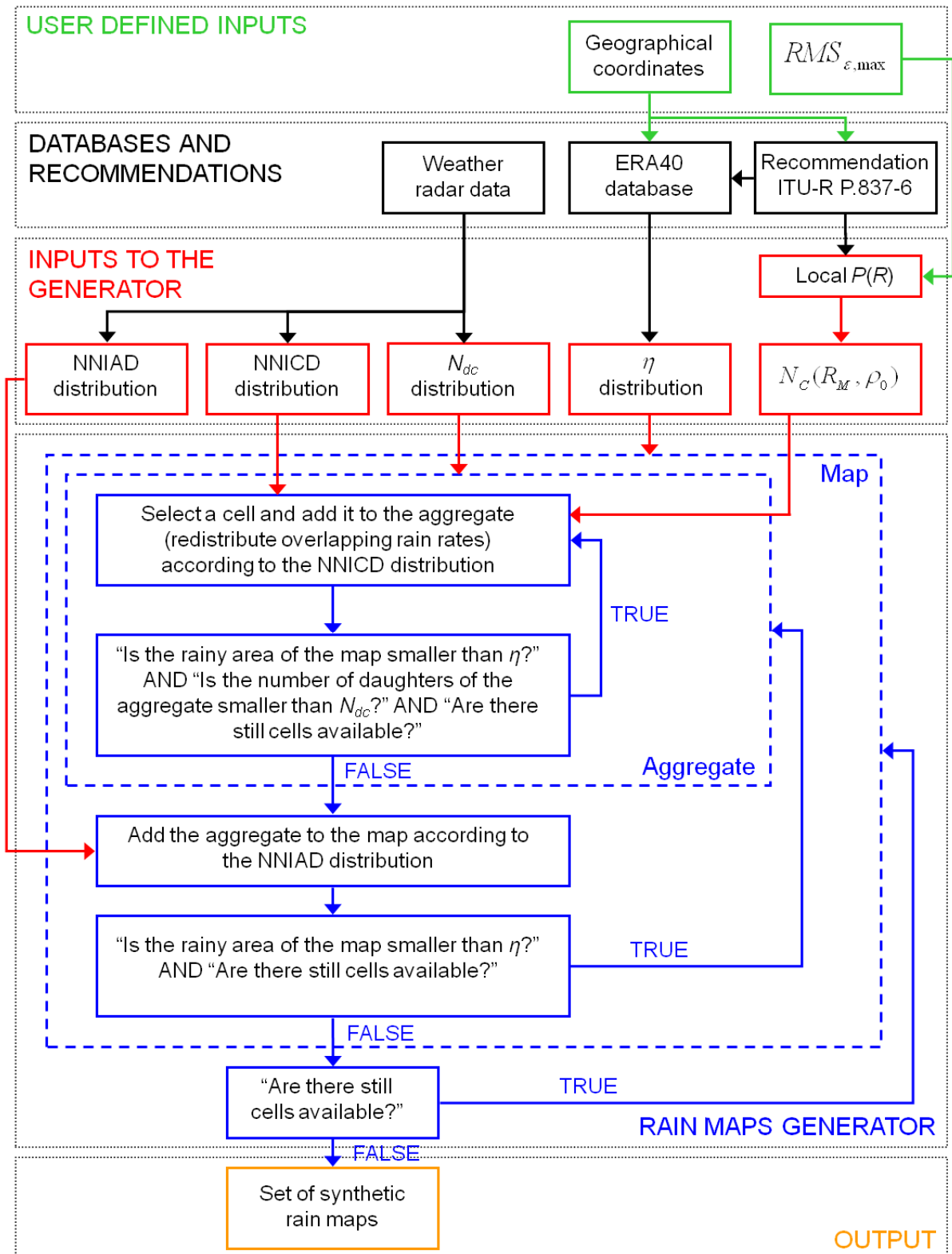
Figure 3-13. Workflow of the MultiEXCELL model

3.1.4. Preliminary validation of MultiEXCELL

This section deals with the preliminary validation of MultiEXCELL against the Spino d'Adda NPC and LR radar databases. The synthetic rain maps generated by the model are analyzed in order to assess their ability in reproducing the local $P(R)$ and the rainfall spatial correlation that characterizes real rain fields.

Figure 3-14 shows the relative error ε, as a function of rain rate, between the $P(R)$ derived from NPC radar data (input to the model) and the one calculated from the MultiEXCELL synthetic maps, i.e. 420 rain images. The solid red line refers to the original area of the generated maps (234 km×234 km), whilst the dashed blue one was obtained by limiting the synthetic maps to a 40-km radius, i.e. the same dimension of the NPC maps. The figure indicates not only that, as expected, the synthetic maps correctly reproduce the input rainfall statistics, but also that they show the quasi-ergodicity property typical of real rain fields: the overall $P(R)$ derived from radar rain maps is fairly independent of the observation area, as long as areas approximately larger than 70 km×70 km and smaller than 300 km×300 km are considered [Onof and Wheater, 1996].
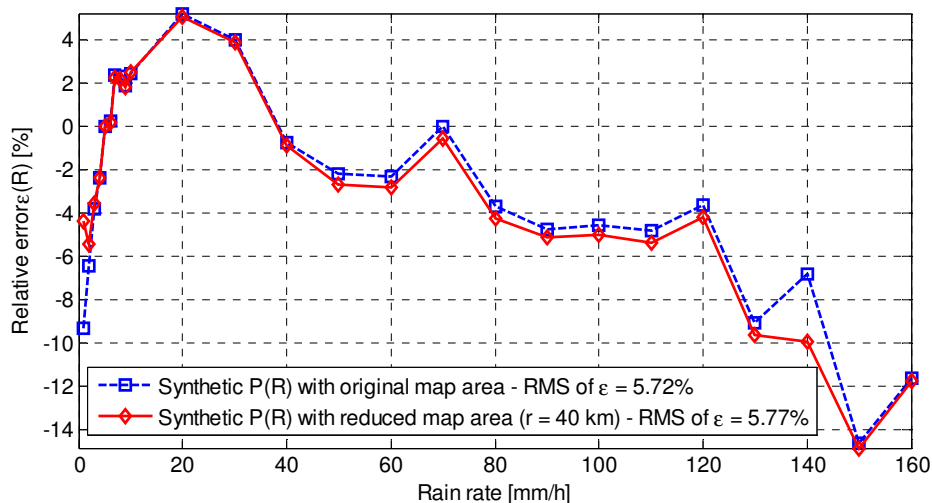
Figure 3-14. Relative error between the P(R) derived from for Spino d'Adda radar data and the one calculated from synthetic rain fields

The effectiveness of the procedure that arranges rain cells on the map can be evaluated by comparing the intercellular distance distributions derived from the radar maps and from the synthetic maps. Specifically, cells at 5 mm/h have been isolated and the distances between their centers of mass have been calculated (by applying (3-17)). The analysis produced the PDFs both of the nearest neighbor distance, NND (regardless of the fact that the cells belong to the same aggregate), and of the distance between each cell and all the others on the same map (named overall distance, OD). Obviously such distributions, especially the latter, depend on the observation area so that for the comparison with LR maps, the synthetic ones have been reduced to an area of 100-km radius (Figure 3-15) and, analogously, to an area of 40-km radius for the comparison with NPC maps (Figure 3-16). Overall, the results confirm the

effectiveness of the cell double aggregative process: the MultiEXCELL model clearly proves to arrange rain cells in a realistic way that resembles the rain cells' organization observable in real rain fields.
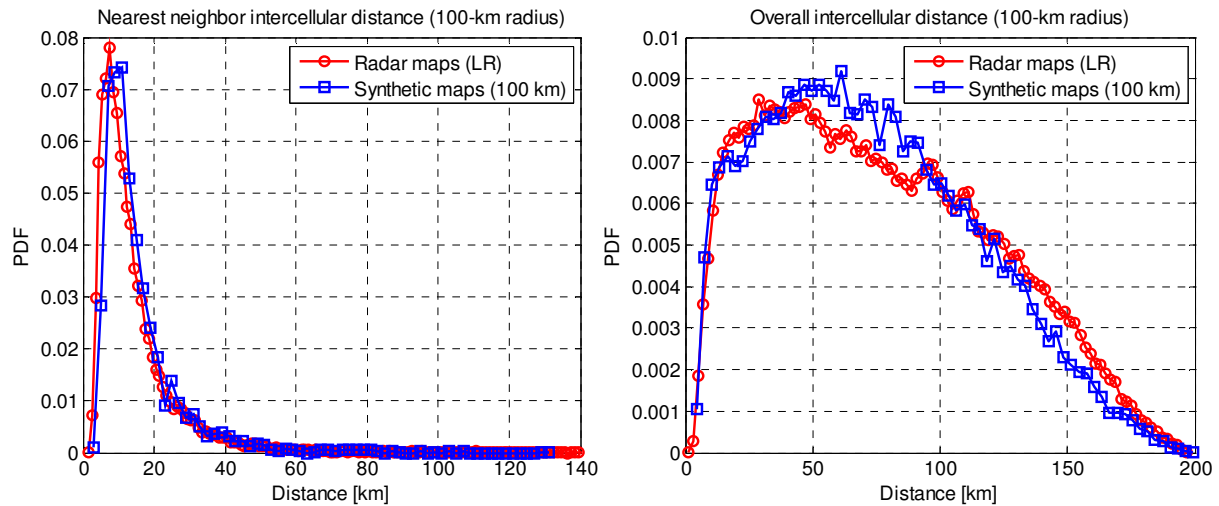
Figure 3-15. Comparison between LR maps and synthetic maps (100-km radius area): PDFs of the nearest neighbor intercellular distance and overall intercellular distance (5 mm/h)
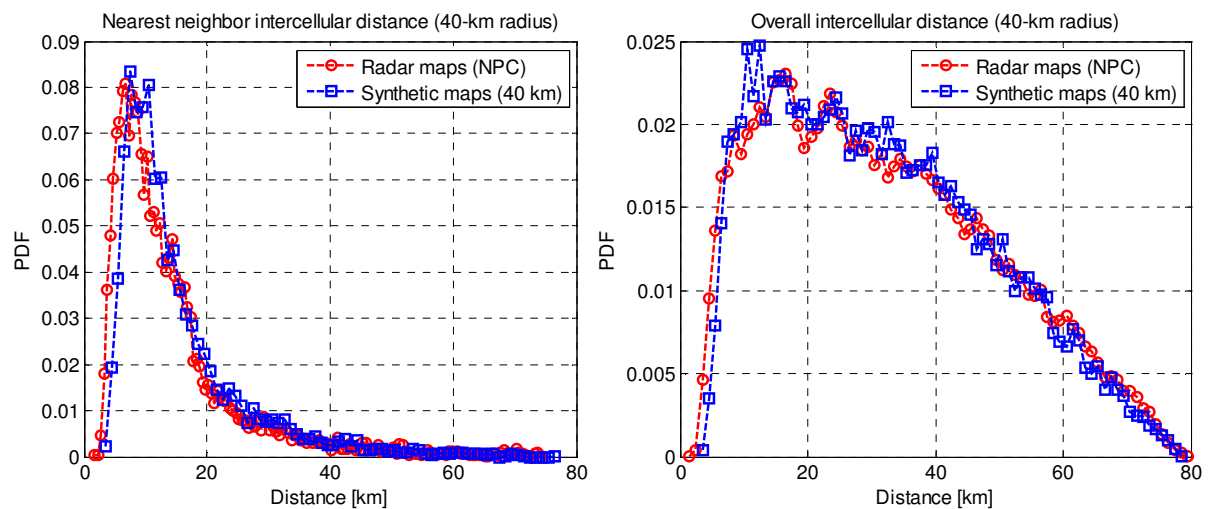
Figure 3-16. Comparison between NPC maps and synthetic maps (40-km radius area): PDFs of the nearest neighbor intercellular distance and overall intercellular distance (5 mm/h)

3.2.   SMOC (Stochastic MOdel of Clouds)

While rain certainly plays the prevailing role among the atmospheric impairments to radio waves propagating at frequencies above 10 GHz, at bands higher than 30 GHz (e.g. Q/V and W bands), the attenuation due to suspended liquid water is not marginal anymore, in particular when the use of VSAT (Very Small Aperture Terminals) is envisaged. It follows

that also cloud attenuation has to be taken in due account for the design of satellite communication systems. To this aim, suitable cloud field models are needed.

This section presents SMOC (Stochastic MOdel Of Clouds), a methodology developed at Politecnico di Milano to synthesize cloud fields on a global scale from Numerical Weather Prediction (NWP) products. Specifically, SMOC receives as input fractional cloud cover (f_{ERA}) data and average cloud liquid water content (L_{ERA}) data, both extracted from the ERA40 database [Uppala et al., 2005], to generate synthetic high-resolution (1 km×1 km) cloud fields which maintain some key features observed in real cloud fields. The development of SMOC, including the cloud field database exploited to this aim, is presented in the next sections.

3.2.1. Investigation of cloud field features

3.2.1.1. The Cloud Database

The database used for the development of SMOC consists in 3090 swaths collected over Europe during 2010 by the MODIS (MODerate resolution Imaging Spectroradiometer) sensor, which acquires data in 36 optical channels (0.4-14.4 µm band). The Aqua satellite embarking MODIS describes a 705-km high, sun-synchronous, near-polar orbit, thus achieving the full observation of the Globe every two days. Among the huge amount of data made available by the National Aeronautics and Space Administration (NASA), maps of cloud liquid water content (L) at 1 km×1 km spatial resolution for swaths as wide as 200 km × 2000 km have been extracted and processed (as an example see Figure 3-17) in order to investigate some fundamental features of cloud fields.

3.2.1.2. Data analysis

The main idea at the basis of SMOC is that spatially correlated cloud fields can be generated using the stochastic approach proposed by Bell in [Bell, 1987], originally devised for rain field synthesis. As shown in the following sections with more detail, according to such a method, a cloud field can be synthesized from the knowledge of: E_L, the mean value of the cloud liquid water content (including $L = 0$ mm) over the target area; S_L, the standard deviation of the cloud liquid water content (including $L = 0$ mm) over the target area; f, the fractional cloud cover. In addition, information on the spatial correlation of L is needed.
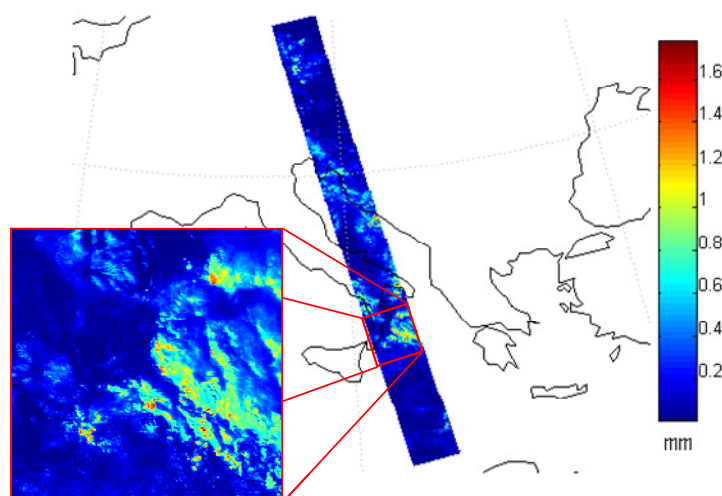
Figure 3-17. Example of the spatial distribution of cloud liquid water content as observed by MODIS on a swath over Italy

Such information on cloud fields has been extracted from MODIS observations. As a preliminary step, original swaths have been subdivided into 10 maps as wide as 200 km×200 km in order to deal with dimensions typical of NWP products (e.g. 2°×2° latitude/longitude grid).

Firstly, cloud maps have been processed to investigate the statistical distribution of L over the reference area (conditioned to $L > 0$ mm), which was found to be lognormal in accordance with other works reported in the literature [Al-Ansafi et al., 2003]. As an example, Figure 3-18 shows a cloud field observed by MODIS (left) and the statistical characterization of L (right): other than E_L, S_L, and f, the figure title includes μ_{LN} and σ_{LN}, the mean and standard deviation values, respectively, of the lognormal distribution fitting L data with satisfactory accuracy (Maximum Likelihood Estimation – MLE).
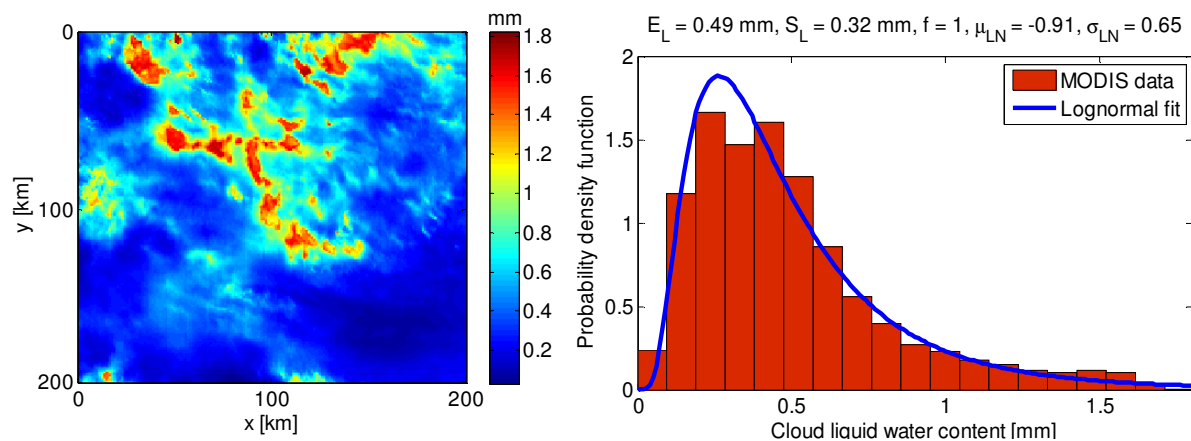
Figure 3-18. MODIS cloud field example (left) and statistical characterization of L (right)

The same processing has been applied to all the 30900 200 km×200 km clouds fields available from the MODIS database, with the aim providing a comprehensive description of all the above mentioned values characterizing the spatial distribution of L. The analysis of the results pointed out that the probability density function (PDF) of S_L conditioned to E_L, hereinafter referred to as $p(S_L|E_L)$, tends to be lognormal as well: Figure 3-19 depicts $p(S_L|E_L)$ for two classes of E_L (low values on the left and high values on the right), including μ_p and σ_p, the mean and standard deviation values, respectively, of the fitting MLE lognormal distribution.
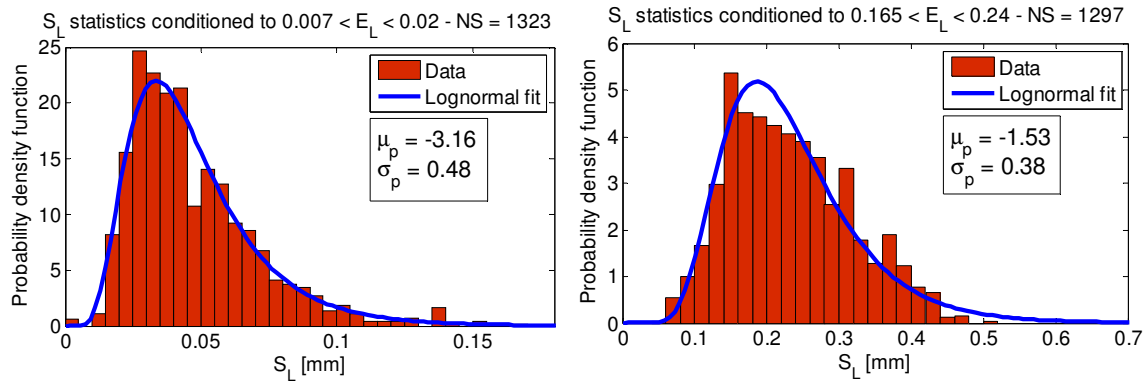
Figure 3-19. Statistical distribution of S_L conditioned to E_L (left: low values; right: high values)

In order to fully characterize $p(S_L|E_L)$, considering that E_L tends to be exponentially distributed, eleven classes of variable width for E_L have been defined with the aim of including in each of them approximately the same number of samples ($NS \approx 1300$). As a result, both μ_p and σ_p reveal quite a regular trend with E_L, as clearly shown in Figure 3-20, which can be fitted by the following analytical expressions:

$$\mu_p(E_L) = 5.6\,E_L^{-0.076} + 4.7$$
$$\sigma_p(E_L) = 1.5\,E_L^{-0.029} - 1.2$$

(3-21)
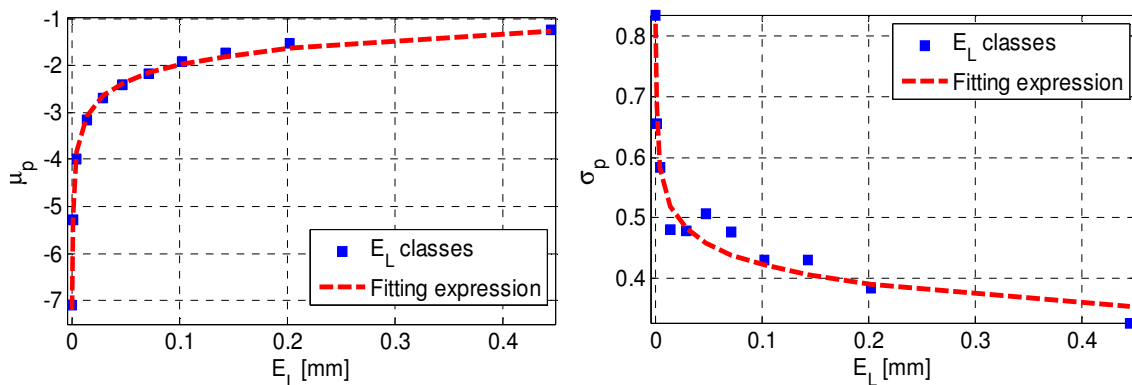
Figure 3-20. Trend of μ_p and σ_p with E_L

Second-order statistics of the cloud liquid water content have been investigated by means of the spatial correlation index defined as:

$$\rho(\mathbf{x}, \mathbf{y}) = \frac{E[L(\mathbf{x}) \cdot L(\mathbf{y})] - E[L(\mathbf{x})] E[L(\mathbf{y})]}{\sigma[L(\mathbf{x})]\,\sigma[L(\mathbf{y})]}$$

(3-22)

where E[•] and σ[•] are the mean and standard deviation operators, whilst $L(\mathbf{x})$ and $L(\mathbf{y})$ are the cloud liquid water content time series, respectively relative to pixels $\mathbf{x}$ and $\mathbf{y}$ in the 200 km×200 km cloud map. The main assumption in the calculation of ρ is that the cloud field is stationary in space (like for the rain field), which implies that the spatial correlation between two points depends only on their distance and not on their position on the map, i.e.

$\rho(\mathbf{x}, \mathbf{y}) = \rho(d = |\mathbf{x} - \mathbf{y}|)$. Figure 3-21 depicts the trend of the spatial correlation of L obtained by averaging ρ values relative to couple of pixels at the same distance. The blue line refers to the application of (3-22) to L values directly extracted from MODIS data, while the red one is associated to the spatial correlation of the underlying Gaussian process, ρ_g. As explained in detail in [Bell, 1987], ρ_g is a necessary information for the generation of synthetic lognormal fields starting from spatially correlated Gaussian fields. The calculation of ρ_g was achieved considering all the cloud maps available from MODIS after proper processing to convert the lognormally distributed values of L into Gaussian values with zero mean and unit variance.

For convenience, the average spatial correlation of rainfall as obtained from an extensive set of rain field collected by the NIMROD weather radar network [Luini and Capsoni, 2012] has been added to Figure 3-21: as expected from the high variability of precipitation, the decorrelation with distance of the rain rate is much steeper than the one of the cloud liquid water content.
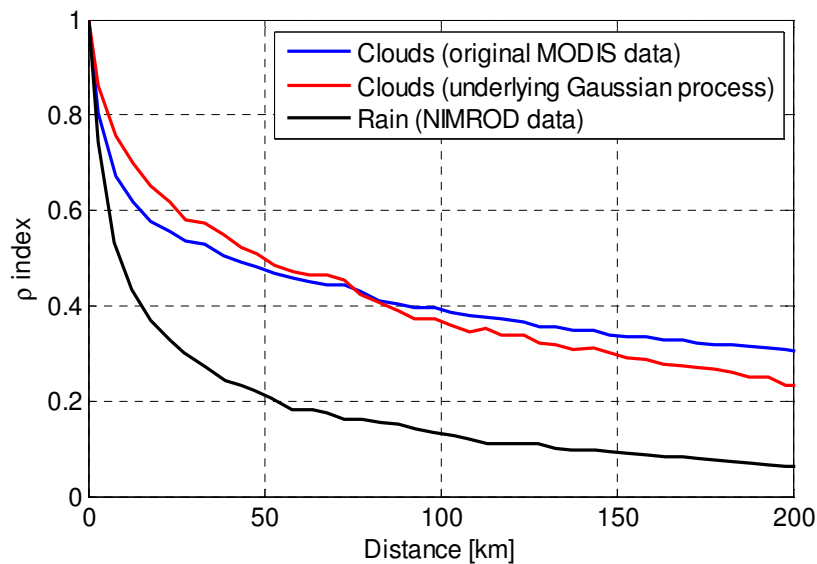
Figure 3-21. Decorrelation with distance of the cloud liquid water content (blue line = original MODIS data, red line = underlying Gaussian process) and of rainfall (NIMROD rain rate data)

3.2.2.   Synthesis of cloud fields

The proposed methodology for the synthesis of cloud fields relies on the stochastic approach outlined in detail in [Bell, 1987] and on the information acquired from MODIS in previous sections. Specifically, each cloud field is synthesized according to the following steps:

1. From an NWP database (in this work, we will make reference to the information extracted from the ERA40 database every 6 hours on a 2°×2° latitude/longitude grid), extract the fractional cloud cover (f_{ERA}) and the spatial average of the cloud liquid water content (L_{ERA}). For a given site with coordinates (*lat*, *lon*), f^*_{ERA} and L^*_{ERA} will result from a bilinear interpolation of the values relative to the four surrounding grid pixels, as suggested by the ECMWF. Thus $E_L = L^*_{ERA}$ and $f = f^*_{ERA}$.

2. From E_L, derive μ^*_p and σ^*_p, the mean and standard deviation values of the lognormal distribution $p(S_L|E_L)$ based on the expressions in (3-21).

3. Randomly extract S_L from $p(S_L|E_L)$ in (3-23), which is univocally defined by μ^*_p and σ^*_p:

$$p(S_L \mid E_L) = \frac{1}{\rho_0 \, \sigma^*_p(E_L)\sqrt{2\pi}} \exp\left[-\left(\frac{\ln(S_L) - \mu^*_p(E_L)}{\sqrt{2}\sigma^*_p(E_L)} \right)^2 \right] \tag{3-23}$$

4. Generate a spatially correlated random Gaussian field $g(x,y)$ according to the spectral approach outlined in [Bell, 1987], which requires as input the spatial correlation properties of such a field. Specifically, ρ_g, the trend of the correlation index with distance (red curve in Figure 3-21) is taken into account, which can be accurately represented by the following analytical expression:

$$\rho_g(d) = 0.49 \, e^{-\frac{d}{19.9}} + 0.51 \, e^{-\frac{d}{280.8}} \tag{3-24}$$

5. Calculate μ_{LN} and σ_{LN}, the mean and standard deviation values of the lognormal distribution characterizing the cloud map (obviously for $L > 0$ mm) to be generated, by imposing that the mean and standard deviation of such lognormal distribution are equal to E_L and S_L, respectively:

$$\begin{cases} E_L = f \exp(\mu_{LN} + \sigma^2_{LN}/2) \\ S_L = \sqrt{f \exp(2\mu_{LN} + 2\sigma^2_{LN}) - f^2 \exp(2\mu_{LN} + \sigma^2_{LN})} \end{cases} \tag{3-25}$$

The inversion of the system above yields:

$$\begin{cases} \mu_{LN} = \ln\left[\frac{1}{(f)^{1.5}} \frac{E_L^2}{\sqrt{E_L^2 + S_L^2}} \right] \\ \sigma_{LN} = \sqrt{\ln\left[f\left(\frac{S_L^2}{E_L^2} + 1 \right) \right]} \end{cases} \tag{3-26}$$

6. Transform the Gaussian field $g(x,y)$ into a lognormal (cloud) field $C(x,y)$ according to:

$$C(x,y) = 0 \quad g < g_{th}$$

$$C(x,y) = \exp\left\{ \mu_{LN} + \sqrt{2}\sigma_{LN} \, \mathrm{erfc}^{-1}\left[\frac{1}{f} \mathrm{erfc}\left(\frac{g(x,y)}{\sqrt{2}} \right) \right] \right\} \quad g \geq g_{th} \tag{3-27}$$

where $g_{th} = \sqrt{2} \, \mathrm{erfc}^{-1}(2f)$ and erfc is the complementary error function defined as:

$$\mathrm{erfc}(x) = \frac{2}{\sqrt{\pi}} \int_x^\infty \exp\left(-t^2\right) dt \qquad\qquad (3\text{-}28)$$

As a result, according to the procedure outlined above, it is possible to generate cloud fields (random lognormal fields) which maintain the basic integral information provided as input (f_{ERA} and L_{ERA}) and preserve the spatial correlation observed in real cloud fields. Figure 3-22 shows the whole synthesis procedure as well as an example of the synthetic cloud fields generated by SMOC ($L_{ERA} = 0.03$ mm and $f_{ERA} = 0.81$).
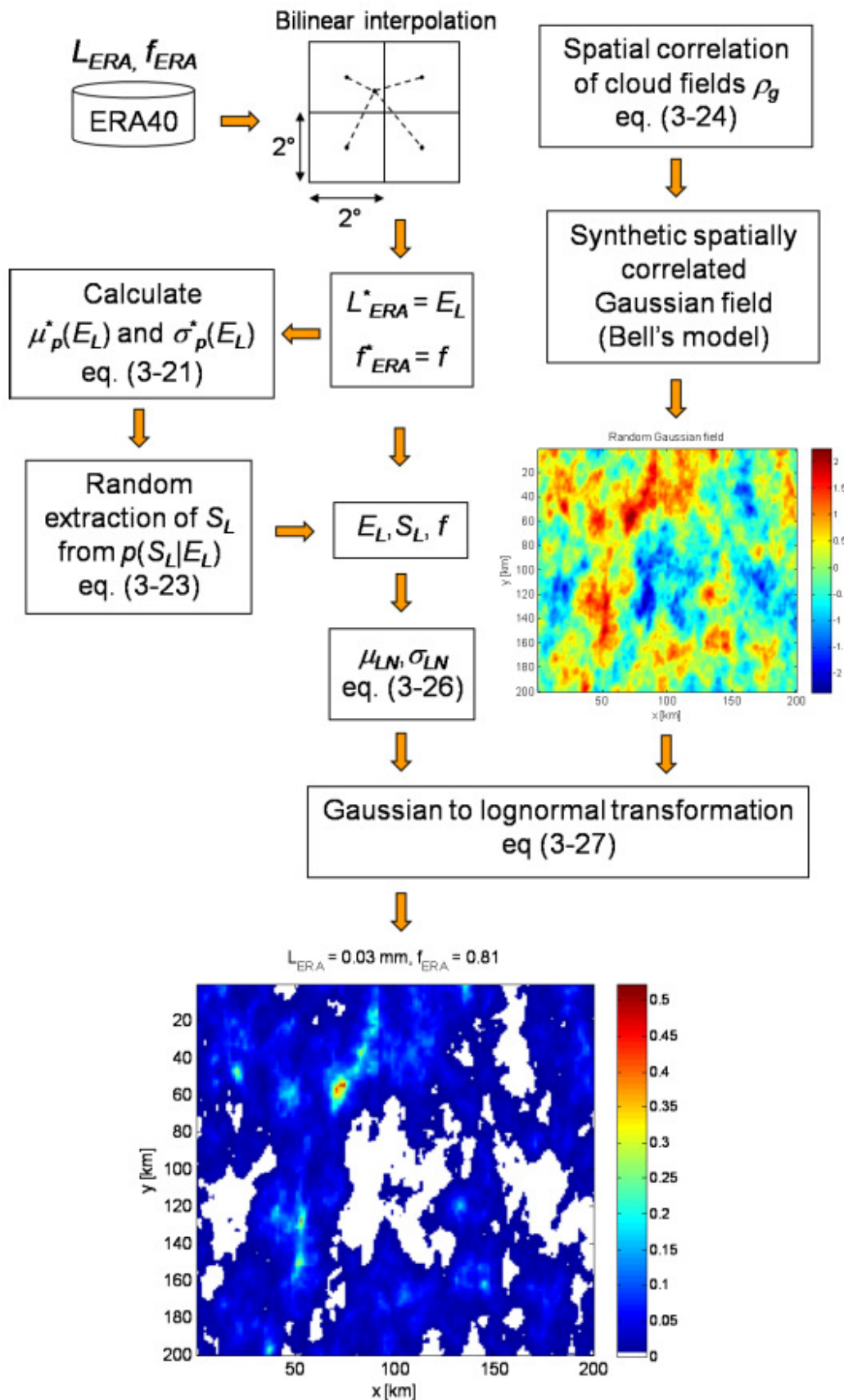
Figure 3-22. Whole procedure for the synthesis synthetic cloud fields using SMOC

3.2.3.   Preliminary validation of SMOC

Preliminary tests have been performed to validate SMOC. Time series of f_{ERA} and L_{ERA} in the period 1996-2000 have been extracted from the ERA40 database with spatial resolution of 2°×2° and temporal resolution of 6 hours. Approximately 7300 cloud fields have been generated and processed to calculate first- and second-order statistics of L. Concerning the former, considering the tight relationship between clouds and rainfall, cloud fields have been assumed to be ergodic, which implies that all L values of each map have been included in the Complementary Cumulative Distribution Function (CCDF) of L; concerning the latter, the expression in (3-22) has been used to assess the spatial correlation properties of the synthetic cloud fields generated by SMOC, again assuming stationarity in space (spatial correlation depending only on the separation distance between pixels and not on their position on the map).

Figure 3-23 and Figure 3-24 show the preliminary validation of SMOC for the sites of Milano/Linate (Italy) and Sodankyla (Finland). The reference data for first-order statistics are derived from 10 years of radio soundings (RAOBS) extracted from the FUB/ESA (FERAS) database [COST 255, 2002] (results already published in [Luini and Capsoni, 2012b]). Specifically, the cloud liquid water concentration in g/m^3 (hence the cloud liquid water content in $kg/m^2 = mm$) has been calculated from high-resolution vertical profiles of temperature, relative humidity and pressure (collected at 00 and 12 UTC in clear sky conditions) using the HUT cloud detection model [Salonen and Uppala, 1991].

The agreement between the CCDF derived from SMOC (solid blue line) and from the RAOBS (solid green line with circles) can be quantified by calculating the average (E) and root mean square (RMS) values of the following error figure:

$$\varepsilon(P) = 100 \frac{L_{SMOC}(P) - L_{RAOBS}(P)}{L_{RAOBS}(P)} \% \tag{3-29}$$

where $L_{SMOC}(P)$ and $L_{RAOBS}(P)$ represent the cloud liquid water content, both corresponding to the same probability level P, relative to the CCDF derived from the synthetic cloud fields and from FERAS RAOBS, respectively. The change in the concavity of the RAOBS curve, particularly visible in the data of Sodankyla around 1 mm is very likely due to the fact that the FERAS database only consists in data collected in non-rainy conditions, i.e. to the lack also of the L values associated to rainy clouds. Results indicate a good prediction accuracy of SMOC in both sites, which are characterized by very different climates.

Concerning second-order statistics, Figure 3-25 and Figure 3-26 show the comparison between the spatial correlation of L (refer to (3-22)) as calculated from MODIS data (solid blue line) and from SMOC synthetic cloud fields (red solid line with circles): the good agreement between the curves indicate that the synthetic cloud fields generated by SMOC reflect the spatial correlation of L observed in real cloud fields.
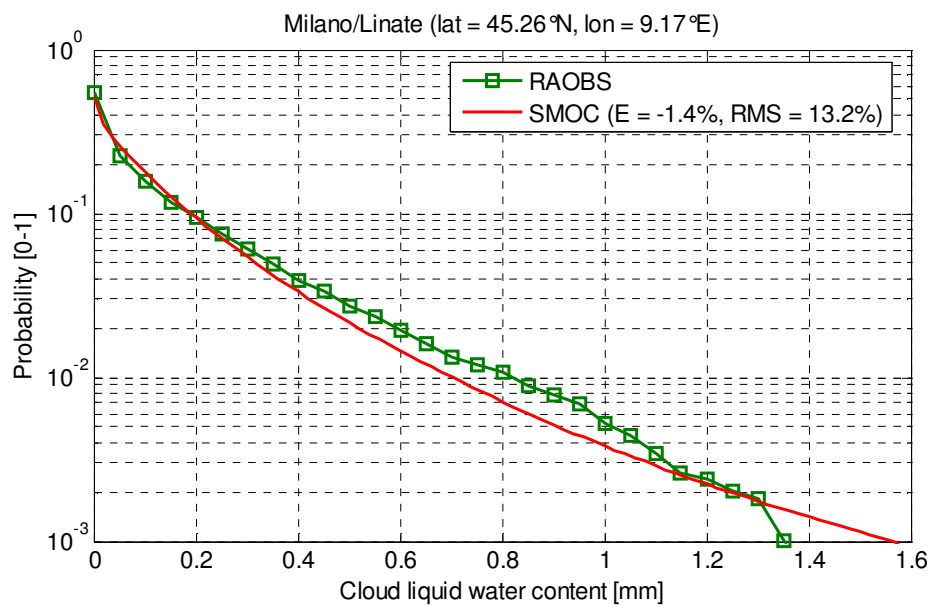
Figure 3-23. Validation of SMOC against FERAS data collected in Milano/Linate, Italy
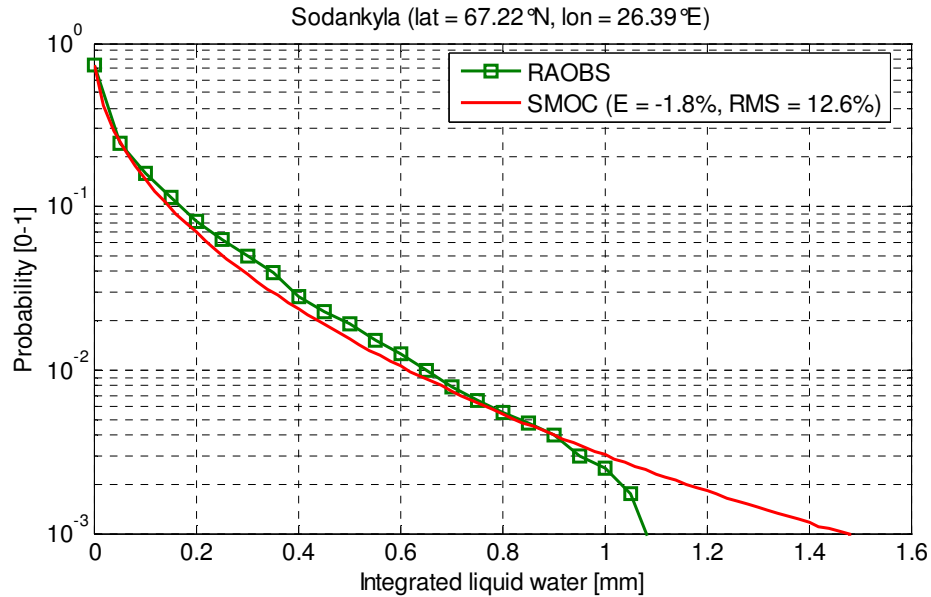
Figure 3-24. Validation of SMOC against FERAS data collected in Sodankyla, Finland
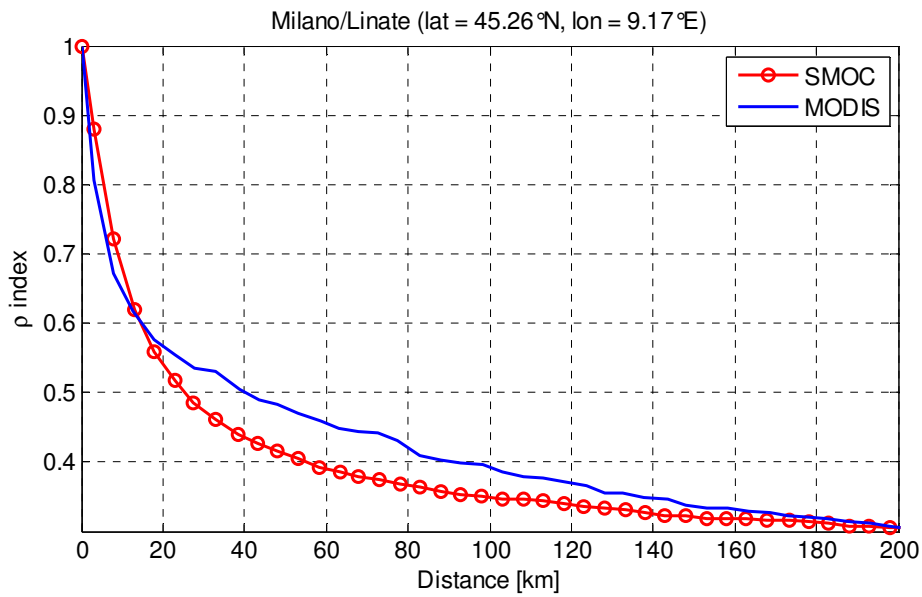
Figure 3-25. Validation of SMOC against MODIS data for Milano/Linate, Italy
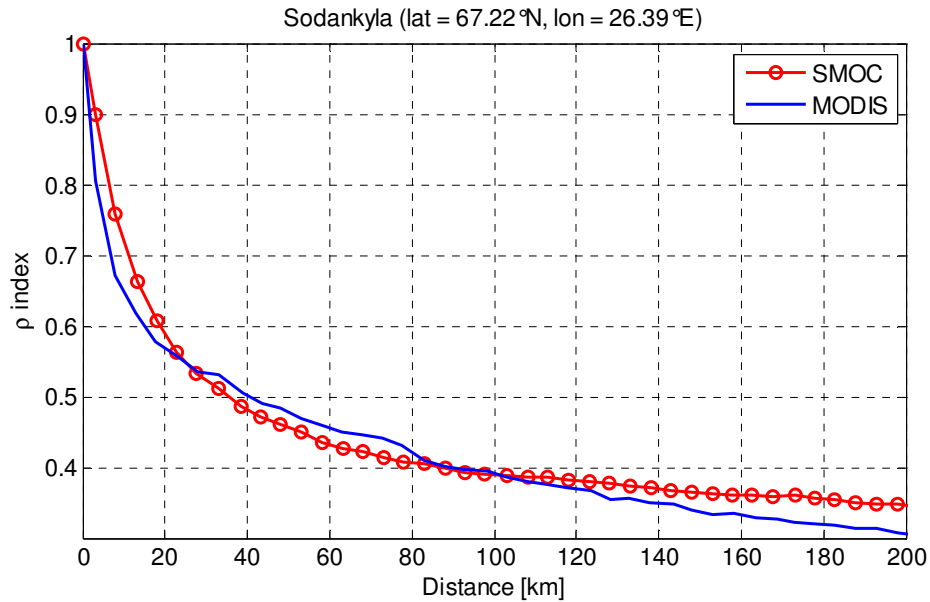
Figure 3-26. Validation of SMOC against MODIS data for Sodankyla, Finland

4. TEST OF STATISTICAL PREDICTION MODELS FOR ATMOSPHERIC ATTENUATION

This Chapter addresses the performance assessment of models aiming to predict rain attenuation, cloud attenuation and the advantage coming from site diversity schemes in SatCom systems. In this work, only models providing good prediction performances and relying on physical considerations (also simple ones like the concept of "effective rain cell") have been selected among those available in the literature. Models with physical basis, indeed in force of their nature (and in contrast to prevalently empirical models), are expected to provide similar prediction accuracy regardless of the frequency range considered; therefore they are of key interest for this activity focusing on high frequency bands (Q/V and W) for which no measurements are currently available for the proper assessment of the models' accuracy.

4.1. Models of rain attenuation statistics

In this section, selected models for the prediction of rain attenuation are reviewed and tested. Most of these models involve the same quantities/parameters typically specifying the geometrical/electrical features of the Earth-space link, which are therefore worth being defined here:

- k e α: as already mentioned in Chapter 1, they are the coefficients used to convert rain rate R into specific rain attenuation γ through the well-established power-law $\gamma = k R^{\alpha}$; unless specified differently, k e α are intended as extracted from recommendation ITU-R P.838-3 [ITU-R P.838-3, 2005]

- h_s: height of the station expressed in km

- h_R: rain height expressed in km; unless specified differently, h_R is intended as extracted from recommendation ITU-R P.839-3 [ITU-R P.839-3, 2001]

- θ: satellite link elevation expressed in degrees

4.1.1. Improved Assis-Einloft

The original Assis-Einloft model was developed for terrestrial links [Assis and Einloft, 1977] and was extended to satellite links by including information on the rain height and the satellite link elevation [Fiser, 1986]. The procedure for rain attenuation prediction relies on a simple model of the rain cell which, as shown in Figure 4-1, consists in the combination of two concentric cylindrical rain cells with different diameters and different rain intensity values. The improvement of the accuracy published in [Costa, 1983] is obtained by introducing (4-7).

The calculation of the rain attenuation statistics according to the Assis-Einloft model is achieved through the following steps:

1) For $\theta \geq 5°$ compute the slant-path length affected by rain, L_s, considering the height of the station:

$$L_s = \frac{(h_R - h_s)}{\sin(\theta)} \quad \text{(km)} \tag{4-1}$$

For $\theta < 5°$, the following expression applies for L_s:

$$L_s = \frac{2(h_R - h_s)}{\left[\sin^2(\theta) + \dfrac{2(h_R - h_s)}{R_e}\right]^{1/2} + \sin(\theta)} \quad \text{(km)} \qquad (4\text{-}2)$$

where $R_e = 8500$ km is the effective Earth radius. Afterwards, calculate the horizontal projection of the slant-path length, L:

$$L = L_s \cos(\theta) \quad \text{(km)} \qquad (4\text{-}3)$$

2) For a given rain intensity, R_P, exceeded with probability P in a year, calculate the rain cell parameters, i.e. internal cylindrical rain cell diameter (refer to Figure 4-1 for a graphical description of the reference model of the rain cell):

$$D_i = 2.2\left(\frac{100}{R_P}\right)^{0.4} \quad \text{(km)} \qquad (4\text{-}4)$$

and residual rain rate in the concentric external rain cell having diameter of 33 km:

$$R_0 = 10\left(1 - e^{0.0105 R_P}\right) \quad \text{(mm/h)} \qquad (4\text{-}5)$$

3) Calculate the rain attenuation associated to the rain cell with rain intensity R_0 and R_P:

$$A = \begin{cases} \dfrac{\left[k\, R_P^\alpha\, D_i + k\, R_0^\alpha\, (L - D_i)\right]}{\cos(\theta)} & L \le 33 \text{ km} \\[2mm] \dfrac{\left[k\, R_P^\alpha\, D_i + k\, R_0^\alpha\, (33 - D_i)\right]}{\cos(\theta)} & L > 33 \text{ km} \end{cases} \quad \text{(dB)} \qquad (4\text{-}6)$$

where k and α are the coefficient of the customary power law relationship used to convert the rain rate R_P into specific attenuation γ.

4) Calculate the exceedance probability associated to the attenuation A as:

$$P(A) = P(R_P) L / D_i \quad (\%) \qquad (4\text{-}7)$$
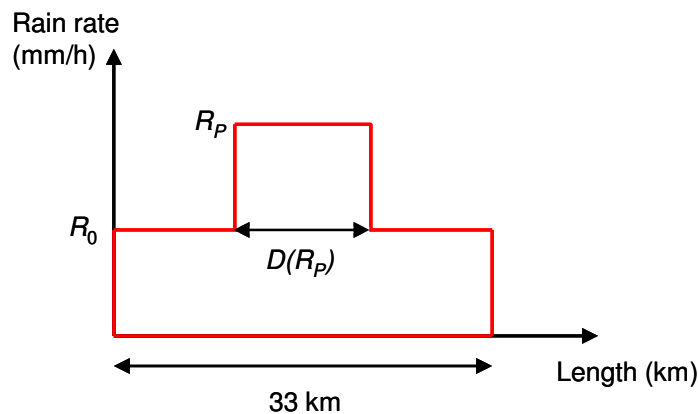
Figure 4-1. Reference model for the rain cell in the Assis-Einloft model

4.1.2. Brazilian Unified

L. da Silva Mello and M.S. Pontes have recently proposed in [Silva Mello and Pontes, 2011] a unified model for the prediction of rain attenuation statistics in satellite and terrestrial

links. The model is inspired to the methodology previously adopted in recommendation ITU-R P.530-10 [ITU-R P.530-10, 2001] for predictions on terrestrial links, which assumes that an equivalent cylindrical cell of uniform rain rate can model the non-uniform rainfall distribution along the propagation path. This is achieved by introducing an effective path length (which turns out to be shorter than the actual path length), which leads to the definition of a path reduction factor. With the aim of overcoming the main limitations associated to the ITU-R model mentioned above (use only of the measured rainfall rate exceeded for 0.01%, $R_{0.01\%}$, of the yearly time; limited accuracy in tropical and equatorial regions) and of defining a unified methodology for rain attenuation prediction both on terrestrial and Earth-space links, the authors have introduced also the concept of the effective rainfall rate R_{eff}. As a result, the rain attenuation value exceeded with probability P in a year turns out to be:

$$A(P) = \gamma_P \, L_{eff} = k \left[R_{eff}(R_P, L_s, \theta) \right]^\alpha \frac{L_s}{1 + \dfrac{L_s \cos(\theta)}{L_0}} \quad \text{(dB)} \qquad (4\text{-}8)$$

where, with reference to the geometry in Figure 4-2, L_s is the slant path calculated as in (4-1) and L_0 is the size of the rain cell. The effective rain rate R_{eff} is defined as:

$$R_{eff}(R_P, L_s, \theta) = 1.763(R_P)^{0.753 + 0.197/(L_s \cos(\theta))} \cos(\theta) + \\ a_1(R_P)^{a_2 + a_3/(L_s \cos(\theta))} L_s^{a_4} \sin(\theta) \quad \text{(mm/h)} \qquad (4\text{-}9)$$

a_1, a_2, a_3 and a_4 are fitting coefficients that have been determined from the existing experimental data, thus leading to the final expression for the prediction of the attenuation exceeded with probability P in a year:

$$A(P) = k \left[1.763(R_P)^{0.753 + 0.197/(L_s \cos(\theta))} \cos(\theta) + \frac{203.6}{L_s^{2.455}} (R_P)^{0.354 + 0.088/(L_s \cos(\theta))} \sin(\theta) \right]^\alpha \cdot \\ \cdot \frac{L_s}{1 + \dfrac{L_s \cos(\theta)}{119 \, R_P^{-0.244}}} \quad \text{(dB)} \qquad (4\text{-}10)$$
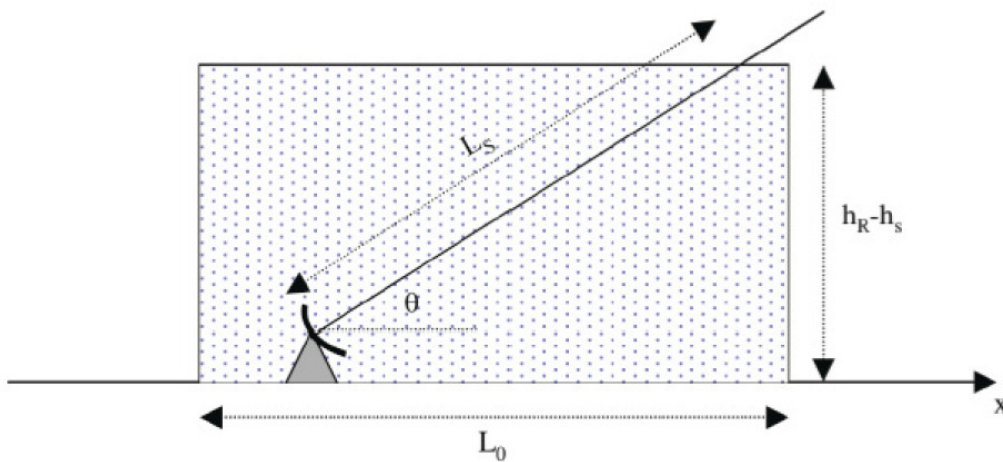
Figure 4-2. Equivalent rain cell for slant path (figure extracted from [Silva Mello and Pontes, 2012])

For the terrestrial case ($L_s \cos(\theta) = d$, being d the length of the link, and $\theta = 0°$), the model reduces to a simplified expression because the second term in the effective rain rate vanishes.

4.1.3.   Bryant

The Bryant model relies on the concepts of effective rain cell and variable rain height to calculate the rain attenuation distribution [Bryant et al., 2001]. The prediction procedure consists in the following steps:

1) Calculate the rain cell diameter as a function of the rain rate value exceeded with probability P in a year, R_P:

$$D_m = 540\, R_P^{-12} \quad \text{(km)} \tag{4-11}$$

2) Calculate the rain height h_R, which, differently from the many models, depends on R_P as well:

$$h_R = 4.5 + 0.0005\, R_P^{1.65} \quad \text{(km)} \tag{4-12}$$

3) Define the multiple cell factor as:

$$k_n = \exp(0.07 R_P) \tag{4-13}$$

4) The number of cells are calculated as:

$$\xi = \begin{cases} \dfrac{1}{\sqrt{2}} \exp(\sin(\theta)) & \theta \leq 55° \\ 1.1 \tan(\theta) & \theta > 55° \end{cases} \tag{4-14}$$

5) For $\theta \geq 5°$ compute the slant-path length affected by rain, L_s, considering the height of the station:

$$L_s = \frac{(h_R - h_s)}{\sin(\theta)} \quad \text{(km)} \tag{4-15}$$

For $\theta < 5°$, the following expression applies for L_s:

$$L_s = \frac{2(h_R - h_s)}{\left[\sin^2(\theta) + \dfrac{2(h_R - h_s)}{R_e} \right]^{1/2} + \sin(\theta)} \quad \text{(km)} \tag{4-16}$$

6) Finally, the rain attenuation exceeded with probability P in a year is given by:

$$A = 1.57\, D_m\, k_n\, \gamma_P\, \frac{L_s}{\xi L + D} \quad \text{(dB)} \tag{4-17}$$

$L = L_s \cos(\theta)$ is the horizontal projection of the rainy path length, $D = D_m\, \pi/2$ and $\gamma_P = k\, R_P^\alpha$ is the specific attenuation associated to rain rate R_P.

4.1.4.   Crane Two-Component

The Crane Two-Component model for the prediction of rain attenuation statistics separately addresses the contributions of rain showers, referred to as cells, and of the larger surrounding regions of light rain intensity, referred to as debris. All storms are assumed to contain both cells and debris, but the propagation path through rain does not always intersect

a single isolated cell: in fact, the Two-Component model assumes that a link may be impaired only by a single cell, only by the debris or by both of them. The Two-Component model handles the attenuation induced by the cells and the debris independently: after calculating the probability of occurrence associated with each component, the two contributions to attenuation are combined to provide the predicted total rain attenuation statistics.

Let's define A_s (dB) as the rain attenuation value suffered from a slant path (the path attenuation of interest) and $A = A_s \cos(\theta)$ as the reduced attenuation; for each value of A, the Crane Two-Component model consists in the following step by step procedure:

1) Determine the rain climate region for the propagation path using the maps provided in [Crane, 1980] and extract the region specific parameters P_c, R_c, P_d, R_d and S_d from [Crane, 1982].

2) Calculate the maximum projected path length for cells, L_c, and for the debris, L_d:

$$L_c = \begin{cases} \dfrac{(h_c - h_s)}{\tan(\theta)} & \theta > 10° \\[4mm] \dfrac{2(h_c - h_s)}{\tan(\theta) + \left[\tan^2(\theta) + 2(h_c - h_s)/8500\right]^{1/2}} & \theta \leq 10° \end{cases} \quad \text{(km)} \qquad (4\text{-}18)$$

where:

$$h_c = 3.1 - 1.7 \sin\left[2(\lambda - 45°)\right] \quad \text{(km)} \qquad (4\text{-}19)$$

and

$$L_d = \begin{cases} \dfrac{(h_d - h_s)}{\tan(\theta)} & \theta > 10° \\[4mm] \dfrac{2(h_d - h_s)}{\tan(\theta) + \left[\tan^2(\theta) + 2(h_d - h_s)/8500\right]^{1/2}} & \theta \leq 10° \end{cases} \quad \text{(km)} \qquad (4\text{-}20)$$

where:

$$h_d = 2.8 - 1.9 \sin\left[2(\lambda - 45°)\right] \quad \text{(km)} \qquad (4\text{-}21)$$

In the expressions of h_c and h_s, λ is the latitude of the site in degrees.

3) Calculate the initial cell rain rate estimate associated with attenuation A (dB):

$$R_i = \left(\frac{0.7A}{1.87k}\right)^{\frac{1}{\alpha - 0.04}} \quad \text{(mm/h)} \qquad (4\text{-}22)$$

4) Calculate the cell horizontal extent:

$$W_c = 1.87 R_i^{-0.04} \quad \text{(km)} \qquad (4\text{-}23)$$

If $W_c > L_c$, then set $W_c = L_c$.

5) Calculate the adjustment factor for the debris associated to the cell:

$$C = \frac{1 + 0.7(L_c - W_c)}{1 + (L_c - W_c)} \qquad (4\text{-}24)$$

6) Calculate W_T as:

$$W_T = \frac{3.2 R_i^{-0.24}}{\tan(\theta) + \left[\tan^2(\theta) + 3.2 R_i^{-0.24}/8500\right]^{1/2}} \quad \text{(km)} \tag{4-25}$$

If $W_c > W_T$, then set $W_c = W_T$.

7) Obtain the final cell rain rate estimate, R_f:

$$R_f = \left(\frac{C \cdot A}{k\, W_c}\right)^{1/\alpha} \quad \text{(mm/h)} \tag{4-26}$$

8) Calculate the probability of intersecting a cell on the propagation path as:

$$P_f = P_c\left(1 + L_c/W_c\right)\exp\left(-R_f/R_c\right) \tag{4-27}$$

9) Calculate the initial debris rain rate estimate for A:

$$R_a = \left(\frac{A}{k\,\Omega}\right)^{1/(\alpha-\delta)} \quad \text{(mm/h)} \tag{4-28}$$

where $\Omega = 29.7$ and $\delta = 0.34$ are the debris parameters.

10) Calculate the debris horizontal extent:

$$W_d = \Omega R_a^{-\delta} \quad \text{(km)} \tag{4-29}$$

If $W_d > L_d$, then set $W_d = L_d$.

11) Calculate W_L as for $R_a > 1$:

$$W_L = \frac{2T_D}{\tan(\theta) + \left[\tan^2(\theta) + 2T_D/8500\right]^{1/2}} \quad \text{(km)} \tag{4-30}$$

where:

$$T_d = (h_d - h_s)\left\{\frac{1 + 1.6(h_d - h_s)\ln R_a}{1 + \ln R_a}\right\} \quad \text{(km)} \tag{4-31}$$

If $W_d > W_L$, then set $W_d = W_L$.

12) Obtain the final debris rain rate estimate, R_z:

$$R_z = \left(\frac{A}{k\,W_d}\right)^{1/\alpha} \quad \text{(mm/h)} \tag{4-32}$$

13) Calculate the probability of intersecting the debris on the propagation path as:

$$P_g = P_d\left(1 + L_d/W_d\right)\frac{1}{2}\,\text{erfc}\left(\frac{\ln(R_a/R_d)}{\sqrt{2}S_d}\right) \tag{4-33}$$

where erfc(x) is the complementary error function defined as:

$$\text{erfc}(x) = \frac{2}{\sqrt{\pi}}\int_0^x \exp\left(-t^2\right)dt \tag{4-34}$$

14) Sum up the cell and debris probabilities to obtain the probability to exceed the attenuation A:

$$P(a > A) = P(A) = P_f + P_g \qquad (4\text{-}35)$$

As is clear from (4-35), the Two-Component model provides as output a probability value of the Complementary Cumulative Distribution Function (CCDF) for each path attenuation A_s.

4.1.5.   ITU-R P.618-10

The rain attenuation prediction model currently adopted by ITU-R in recommendation P.618-10 receives the rain rate value exceeded for 0.01% of the yearly time, $R_{0.01\%}$, as the sole input information on the local rainfall process [ITU-R P.618-10, 2009]. The model has been derived under the assumption that both the point rain intensity and path attenuation distributions generally conform to the log-normal distribution [Dissanayake et al., 1997]. The method takes into account both the uneven horizontal distribution of the rain rate as well as its vertical variation by introducing effective parameters. The model is applicable to frequencies up to 55 GHz and percentage probabilities ranging between 0.001% and 5%.

The step by step procedure for the prediction of the rain attenuation distribution is given below:

1) For $\theta \geq 5°$ calculate the slant-path length affected by rain, L_s, considering the height of the station h_s:

$$L_s = \frac{(h_R - h_s)}{\sin(\theta)} \quad \text{(km)} \qquad (4\text{-}36)$$

For $\theta < 5°$, the following expression applies:

$$L_s = \frac{2(h_R - h_s)}{\left[\sin^2(\theta) + \dfrac{2(h_R - h_s)}{R_e} \right]^{1/2} + \sin(\theta)} \quad \text{(km)} \qquad (4\text{-}37)$$

2) Calculate the horizontal projection of the slant-path length, L:

$$L = L_s \cos(\theta) \quad \text{(km)} \qquad (4\text{-}38)$$

3) Obtain the specific attenuation, γ_R, associated to $R_{0.01\%}$:

$$\gamma_R = k\left(R_{0.01\%}\right)^\alpha \quad \text{(dB/km)} \qquad (4\text{-}39)$$

4) Calculate the horizontal reduction factor associated to 0.01% of the time, $r_{0.01}$, which takes into account the horizontal inhomogeneity of the rain intensity:

$$r_{0.01} = \frac{1}{1 + 0.78\sqrt{\dfrac{\gamma_R L}{f}} - 0.38\left(1 - e^{-2L}\right)} \qquad (4\text{-}40)$$

5) Calculate the vertical adjustment factor associated to 0.01% of the time, $v_{0.01}$, which takes into account the variability of the rain intensity with height:

$$v_{0.01} = \frac{1}{1 + \sqrt{\sin(\theta)} \left[31 \left(1 - e^{-\frac{\theta}{(1+\chi)}} \right) \sqrt{\frac{\gamma_R L_R}{f}} - 0.45 \right]} \quad (4\text{-}41)$$

where, after defining:

$$\varsigma = \tan^{-1}\left(\frac{h_r - h_s}{r_{0.01}L} \right) \quad (\text{deg}) \quad (4\text{-}42)$$

the remaining parameters in (4-41) are:

$$L_R = \begin{cases} \dfrac{(r_{0.01}L)}{\cos(\theta)} & \varsigma > \theta \\[2mm] \dfrac{(h_r - h_s)}{\sin(\theta)} & \varsigma \le \theta \end{cases} \quad (\text{km}) \quad (4\text{-}43)$$

and (ϕ is the station latitude in degrees):

$$\chi = \begin{cases} 36 - |\phi| & |\phi| < 36° \\ 0 & |\phi| \ge 36° \end{cases} \quad (\text{deg}) \quad (4\text{-}44)$$

6) Define the effective path length as:

$$L_E = L_R v_{0.01} \quad (\text{km}) \quad (4\text{-}45)$$

7) The predicted attenuation exceeded for 0.01% of an average year is obtained as:

$$A_{0.01\%} = \gamma_R L_E \quad (\text{dB}) \quad (4\text{-}46)$$

8) The predicted attenuation exceeded for other percentages P of an average year, with $0.001\% \le P \le 5\%$, is a function of $A_{0.01\%}$ and of P:

$$A(P) = A_{0.01\%} \left(\frac{P}{0.01} \right)^{-[0.655 + 0.033\ln(P) - 0.045\ln(A_{0.01}) - \beta(1-P)\sin(\theta)]} \quad (\text{dB}) \quad (4\text{-}47)$$

where:

$$\beta = \begin{cases} 0 & |\phi| \ge 36° \ or \ P \ge 1\% \\ -0.005(|\phi| - 36) & |\phi| < 36° \ and \ P < 1\% \ and \ \theta > 25° \\ -0.005(|\phi| - 36) + 1.8 - 4.25\sin(\theta) & \text{Otherwise} \end{cases} \quad (4\text{-}48)$$

4.1.6. MultiEXCELL (Multi EXponential CELL)

The prediction of rain attenuation statistics using MultiEXCELL relies on the physically-based integration of the rain specific attenuation along the propagation path, starting from the generated synthetic rain maps and from the geometric/electrical characteristics of the link. Specifically, the prediction procedure consists in the following steps:

1) For each synthetic rain map, define the radio link geometry for a given position on the map (see Figure 4-3) by calculating the slant path length as:

$$L_s = \frac{(h_R - h_s)}{\sin(\theta)} \quad (\text{km}) \quad (4\text{-}49)$$

and by projecting it to the ground:

$$L_H = L_s \cos(\theta) \quad \text{(km)} \tag{4-50}$$
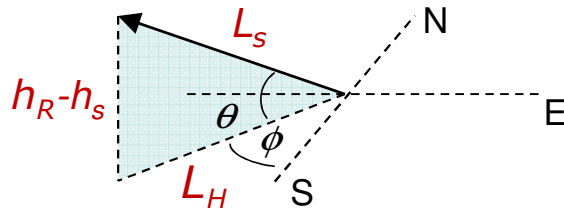
Figure 4-3. Reference geometry for the calculation of rain attenuation statistics

2) Convert each rain rate value of the map into specific attenuation using the customary power-law relationship:

$$\gamma_R = kR^\alpha \quad \text{(dB/km)} \tag{4-51}$$

3) Making reference to Figure 4-4, which shows the geometry for the calculations relative to two sample positions of the link on the rain map, calculate the total rain attenuation affecting the radio link as:

$$A = \int_{L_s} \gamma_R(l)\,dl = \sum_{i=1}^{N} k(R_i)^\alpha \frac{\Delta l_i}{\cos(\theta)} \quad \text{(dB/km)} \tag{4-52}$$
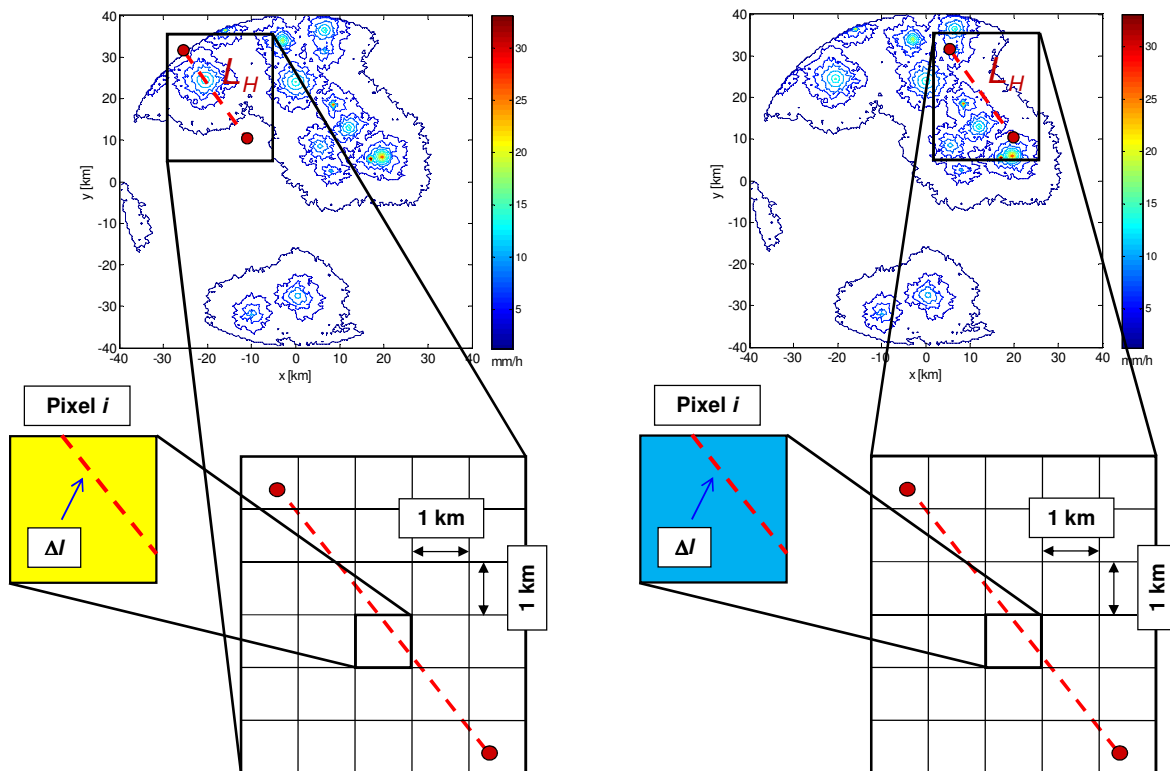
Figure 4-4. Simulation of the interaction between the link and the synthetic rain map generated by MultiEXCELL

4) Rigidly move the geometry reported in Figure 4-4 across the whole rain map to consider all the possible positions of the link with respect to the rain field and thus obtain an attenuation map (make reference to Figure 4-5). This procedure increases the statistical stability of the results and implicitly assumes the validity of the quasi-ergodicity property, which, as discussed in the previous chapter, lies at the basis of MultiEXCELL.

5) Repeat the steps above for all the synthetic rain maps and cumulate all the predicted attenuation values (all maps, all pixels) to obtain the rain attenuation statistics, $P(A)$.
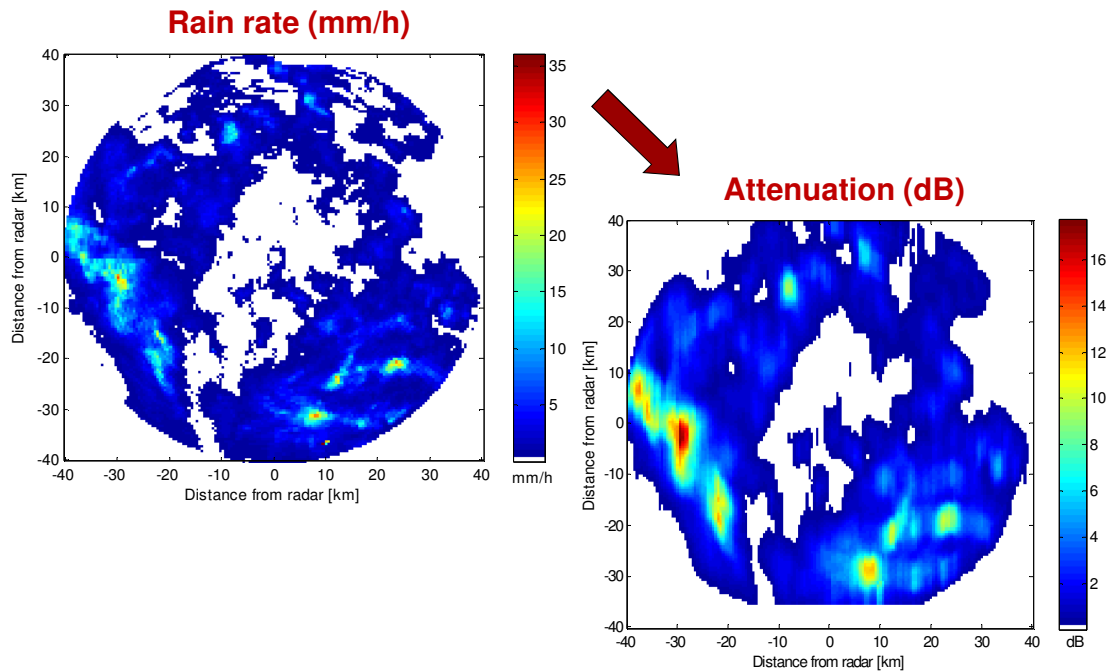
Figure 4-5. Conversion of the rain rate map into attenuation map (example using a radar derived rain rate map); southward pointing link

4.1.7. SAM (Simple Attenuation Model)

The Simple Attenuation Model developed by [Stutzman and Dishman, 1984] is based on an effective rain rate profile with an exponential shape. Specifically, the spatial rainfall distribution along the slant path is given by:

$$R(l) = \begin{cases} R_0 & R_0 \leq 10 \text{ mm/h} \\ R_0 \exp\left[-\Gamma \ln\left(\dfrac{R_0}{10}\right) l \cos(\theta)\right] & R_0 > 10 \text{ mm/h} \end{cases} \quad \text{(mm/h)} \quad (4\text{-}53)$$

where:

l (km) is the coordinate along the slant path: $0 \leq l \leq L_s$

R_0 (mm/h) is the point rainfall rate

L_s is the slant path length, defined as:

$$L_s = \frac{(h_R - h_s)}{\sin(\theta)} \quad \text{(km)} \quad (4\text{-}54)$$

The SAM model relies on an effective rain height inherited from [Crane, 1978]:

$$h_R = \begin{cases} h_0 & R_0 \leq 10 \text{ mm/h} \\ h_0 + \ln\left(\dfrac{R}{10}\right) & R_0 > 10 \text{ mm/h} \end{cases} \quad \text{(km)} \qquad (4\text{-}55)$$

where h_0 is the 0 °C isotherm height, calculated as:

$$h_0 = \begin{cases} 4.8 & |\phi| \leq 30° \\ 7.8 - 0.1|\phi| & |\phi| > 30° \end{cases} \quad \text{(km)} \qquad (4\text{-}56)$$

The total attenuation associated to a point rainfall rate R_0 is found by integrating the specific attenuation along the path:

$$A(R_0) = \int_{L_s} k[R(l)]^\alpha \, dl = \begin{cases} k(R_0)^\alpha L_s & R_0 \leq 10 \text{ mm/h} \\ k(R_0)^\alpha \dfrac{1 - \exp\left[-\alpha\Gamma\ln\left(\dfrac{R_0}{10}\right)L_s\cos(\theta)\right]}{\alpha\Gamma\ln\left(\dfrac{R_0}{10}\right)\cos(\theta)} & R_0 > 10 \text{ mm/h} \end{cases} \quad \text{(dB)}(4\text{-}57)$$

The value $\Gamma = 1/14$ was found by minimizing the model prediction error using as reference an extensive database of measurements (both attenuation and rain rate statistics data available).

4.1.8.   SC EXCELL (Stratiform/Convective EXponential CELL)

The SC EXCELL (Stratiform/Convective EXponential CELL) model, duly described in [Capsoni et al., 2009], relies on the same cellular approach of MultiEXCELL. As key features, it separately takes into account the different effects induced by stratiform and convective cells on the link and it includes the extra attenuation caused by the presence of the melting layer during stratiform events.

In SC EXCELL, synthetic rain cells are still assumed to be exponentially shaped:

$$R(\rho) = \begin{cases} (R_M + R_{low}) \, e^{-\frac{\rho}{\rho_0}} - R_{low} & \rho \leq \rho_l \\ 0 & \rho > \rho_l \end{cases} \quad \text{(mm/h)} \qquad (4\text{-}58)$$

where R is the rain rate (mm/h), ρ (km) is the distance from the cell peak, R_M (mm/h), $\rho_l = \rho_0 \ln(1 + R_M/R_{low})$ (km) is the finite distance from the cell center at which the rain profile $R(\rho)$ is zero, R_{low} is the cell lowering factor and, finally, ρ_0 (km) is the parameter driving the dimension of the cell (refer to Figure 4-6).

Unlike in MultiEXCELL, rain cells are not combined to generate synthetic rain fields but, rather, they are considered as isolated entities, each of them causing a separate impairment on the communication link. SC EXCELL takes separately into account the effects of stratiform and convective precipitation, as well as the extra-attenuation caused by the melting layer, whose presence is associated only to the former type of events.
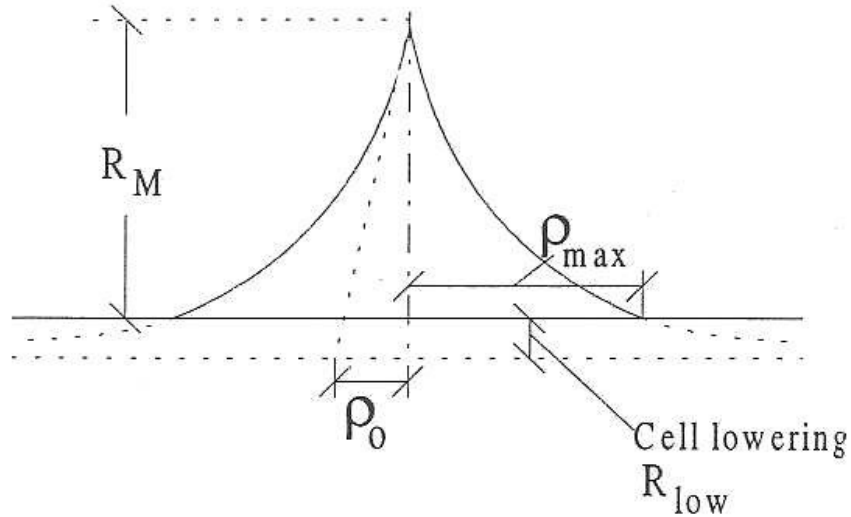
Figure 4-6. Rain cell model including the lowering factor R_{low}

The whole procedure to estimate the rain attenuation statistics using SC EXCELL consists in the following steps (further details can be found in [Capsoni et al., 2009] and in [Capsoni and Luini, 2013], the latter including some improvements to the model):

1) Determine the probability of occurrence of rain cells, $N(\rho_0, R_M)$, based on the knowledge of the local rainfall statistics, $P(R)$ (CCDF of the rain rate):

$$N(R_M, \rho_0) = -\frac{1}{4\pi \overline{\rho_0}^2} \frac{\partial^3 \overline{P}(R)}{\partial \ln(R + R_{low})^3} e^{-\frac{\rho_0}{\overline{\rho_0}}} \tag{4-59}$$

where:

$$\overline{\rho_0}(R_M) = 1.7 \left[\left(\frac{R_M}{6}\right)^{-10} + \left(\frac{R_M}{6}\right)^{-0.26} \right] \quad R_M \geq 5 \text{ mm/h} \quad (\text{km}) \tag{4-60}$$

and:

$$\overline{P}(R) = P_0 \ln^n\left(\frac{R_a + R_{low}}{R + R_{low}}\right) \tag{4-61}$$

being P_0, n, R_a and R_{low} fitting coefficients to be determined so as to guarantee the best agreement between the expression in (4-61) and the input $P(R)$. As a result, the knowledge of the local rainfall statistics is sufficient to determine the probability to have a given kind of synthetic rain cell, univocally identified by ρ_0 and R_M.

2) Classify rain cells as stratiform or convective based on their peak rain cell value R_M and on the rain cells' probability of occurrence $N(\rho_0, R_M)$; the classification procedure is outlined in detail in [Capsoni et al., 2006].

3) Calculate $H_{BB}(f)$, the thickness of the equivalent rain layer modeling the extra attenuation caused by the melting layer. $H_{BB}(f)$ is a function of frequency as indicated in (4-62):

$$H_{BB}(f) = 4.454 \, e^{-0.0656 f} + 0.826 \quad (\text{km}) \tag{4-62}$$

4) Calculate the stratiform (h_{str}) and convective (h_{cvn}) rain heights as follows:

$$h_{str} = \frac{\sum_{i=1}^{12} \alpha_i p_i h_i}{\sum_{i=1}^{12} \alpha_i p_i} \qquad h_{cnv} = \frac{\sum_{i=1}^{12} \beta_i p_i h_i}{\sum_{i=1}^{12} \beta_i p_i} \quad \text{(km)} \tag{4-63}$$

h_i (km) is the monthly mean values of the 0 °C isotherm height (conditioned to the presence of rain), p_i is the monthly mean values of the 6-hour rainy periods probability, β_i is the monthly mean values of the ratio between the convective and the total rain amounts calculated over each successive 6 hour period, $\alpha_i = 1 - \beta_i$ and $i = 1,..,12$ is the index of the month. All the above mentioned meteorological quantities are extracted from the ERA15 database made available by the European Center for Medium-Range Weather Forecast (ECMWF).

5) Derive the effective stratiform rain height $H_{strRain}$, which includes the presence of the melting layer:

$$H_{strRain} = h_{str} + H_{BB}(f) \quad \text{(km)} \tag{4-64}$$

6) Derive the effective convective rain height $H_{cnvRain}$:

$$H_{cnvRain} = 1.1 h_{cnv} \quad \text{(km)} \tag{4-65}$$

The enhancement of the convective rain height h_{cnv} takes into account that during convective events hydrometeors are pushed well beyond the 0 °C isotherm heights due to strong updrafts.

7) Estimate the attenuation due to stratiform cells by simulating the interaction of each rain cell (rain height equal to $H_{strRain}$) with the radio link (integration of the specific attenuation along the path; additional details can be found in [Capsoni et al., 1987]); the superimposed contribution of all cells to attenuation, weighted with the associated probability of occurrence $N(\rho_0, R_M)$, provides the rain attenuation statistics due to stratiform rain, $P(A)_{str.}$

8) Repeat the previous step but using convective rain cells (rain height equal to $H_{cnvRain}$), which provides the rain attenuation statistics due to convective rain, $P(A)_{cnv.}$

9) Combine rain attenuation statistics due to stratiform and convective rain cells:

$$P(A)_{tot} = P(A)_{str} + P(A)_{cnv} \tag{4-66}$$

4.2.   Assessment of the accuracy of rain attenuation prediction models

4.2.1.   The reference database

The Study Group 3 of the International Telecommunication Union – Radio communication Sector (ITU-R) maintains extensive databases of measurements (named DBSG3) collected during propagation experiments, typically used for model development and test. The database relative to Earth-satellite links includes rain attenuation data collected worldwide by means of beacon receivers and radiometers. Specifically, the database contains measured rain attenuation statistics ($P(A)$), local rainfall statistics typically measured by a raingauge or a disdrometer colocated with the receiving equipment ($P(R)$), as well as all the

geometrical (e.g. receiver site, satellite orbital position, …) and electrical (frequency, polarization, …) characteristics of the links required for the applications of prediction models.

The experiments included in the database differ not only in terms of geometrical and electrical features of the link, but also in terms of completeness and reliability of the data, type of equipment (beacon receiver or radiometer), duration of measurements (mostly 1 year) and type of reference data included (attenuation due only to rain or to all atmospheric constituents).

In the tests presented here, only experiments performed with beacon receivers (rain attenuation estimates derived from radiometric data, especially above approximately 15 GHz, have to be handled with great care) with operational frequency higher than 17 GHz (and containing rain-only attenuation data) have been selected. The reason of this selection in frequency is twofold: on one side, 17 GHz represents a good compromise between the preference in considering experiments at higher frequency (being the present research activity focused on satellite communication links operating in the Q/V and W bands) and the need to gather a sufficient number of experiments (this number decreases as frequency increases) for a significant assessment of the models' prediction accuracy; on the other hand, experiments at higher frequency are likely to include more reliable data because they have been collected, in principle, with more advanced and accurate equipment.

As a result, 49 rain attenuation statistics (1-year duration) have been selected, whose location is depicted in Figure 4-7, which shows that the sites are prevalently characterized by a temperate climate, the same one which Rome NY is subject to.

Figure 4-7. Location of the experimental sites selected for the models' testing activity

4.2.2. Prediction error

In order to quantitatively assess the prediction accuracy of the selected rain attenuation models, the following error figure, adopted by ITU-R in recommendation P.311-13 [ITU-R P.311-13, 2009], has been employed:

$$\varepsilon(P) = \begin{cases} 100\left(\dfrac{A_r(P)}{10}\right)^{0.2} \ln\left(\dfrac{A_p(P)}{A_r(P)}\right) & A_r(P) < 10 \text{ dB} \\[4mm] 100\ln\left(\dfrac{A_p(P)}{A_r(P)}\right) & A_r(P) \geq 10 \text{ dB} \end{cases} \tag{4-67}$$

where, as shown in Figure 4-8, $A_r(P)$ and $A_p(P)$ represent the rain attenuations, both correspondent to probability level P, extracted respectively from the reference and model predicted $P(A)$. Finally probability levels equal to or higher than $5 \times 10^{-3}\%$ have been considered in the tests so as to maintain a good degree of statistical stability in the $P(A)$s.
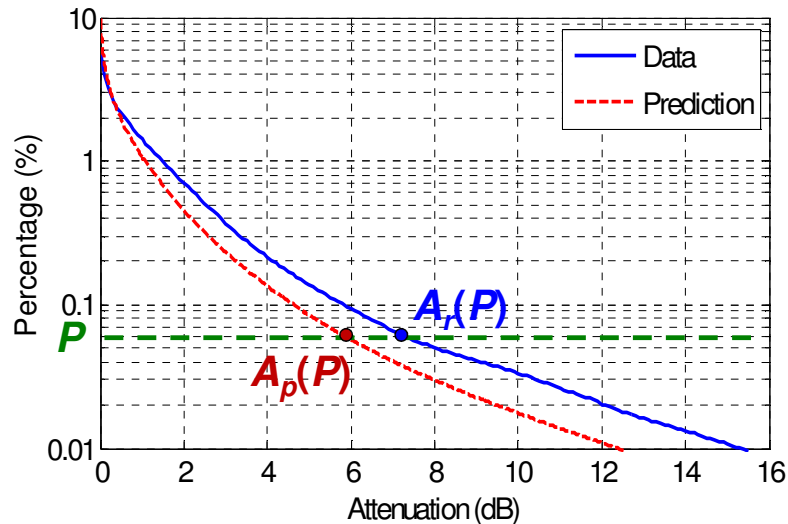
Figure 4-8. Comparison of reference and predicted rain attenuation statistics for the models' testing activity

Figure 4-9 and Figure 4-10 gives an example of the predictions obtained from the models for an experiment whose details are reported in the figure title (models' results for the same experiment have been shown in two separate figures to improve clarity and readability), whilst an overall evaluation of the models' performance is provided by Table 4-1, which lists the average (E), standard deviation (STD) and root mean square (RMS) value of the error figure $\varepsilon(P)$ considering all the probability values of each rain attenuation distribution and all the 49 selected experiments. These results have been obtained using as input to the models the measured $P(R)$s included in the DBSG3 database. This applies also to the Crane Two-Component model which, indeed, recommends the use of rain rate distributions extracted from the ad-hoc defined rain climate regions, unfortunately not available in electronic format for this activity. The P range of all the input $P(R)$s was limited according to the flags (included in the DBSG3 database as well) with the goal of discarding less reliable values in the listed rainfall statistics.

Looking at the results in Table 4-1, where models are sorted in ascending order on the basis of their RMS value, it is clear that the method included in recommendation ITU-R P.618-10 is the best performing model, both in terms of standard deviation (lowest value overall) of the error and of bias (only model showing null bias). The second best score is associated to the Assis-Einloft model, which, notwithstanding its limited RMS (0.24), shows quite a high positive bias (0.13). A similar performance is achieved by the Assis-Einloft, MultiEXCELL, Bryant, SC EXCELL and SAM models (their RMS ranges between 0.24 and 0.27), although the lowest bias is delivered by MultiEXCELL (0.05). Finally, the Brazil and Crane Two-component show a much lower prediction accuracy.
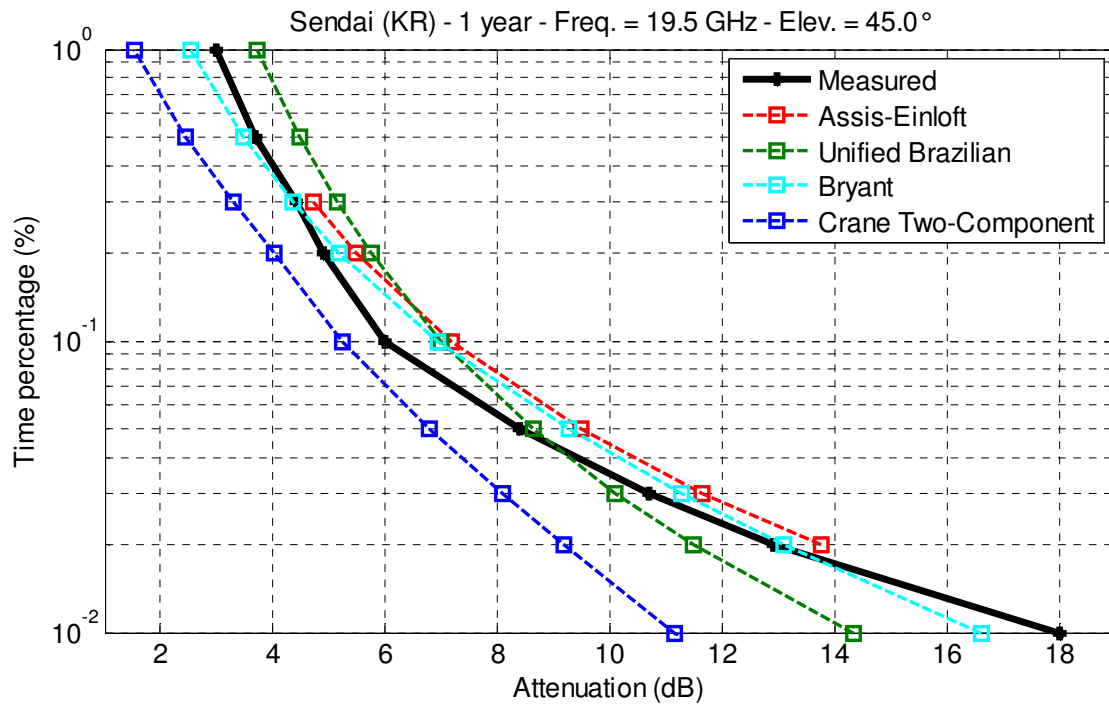
Figure 4-9. Comparison of reference and predicted rain attenuation statistics for the models' testing activity
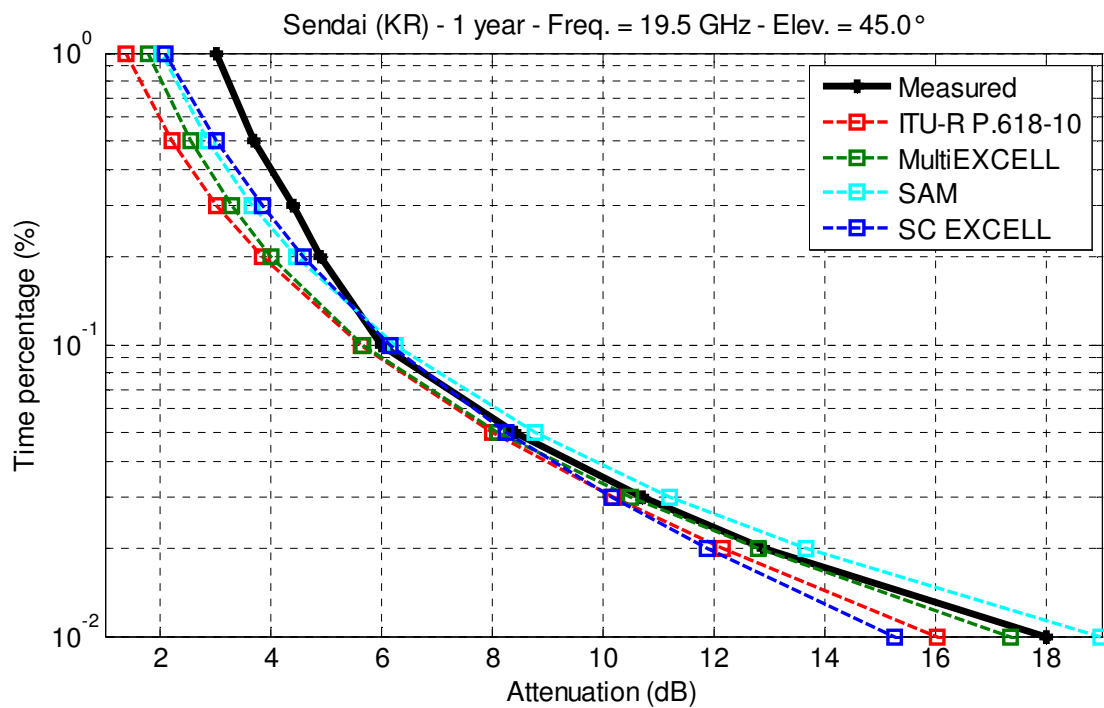
Figure 4-10. Comparison of reference and predicted rain attenuation statistics for the models' testing activity

Table 4-1. Models' accuracy evaluated against the selected 49 experiments (all P values); measured P(R) in the DBSG3 database used as input to the models

Model	E	STD	RMS
ITU-R P.618-10	0	0.16	0.16
Assis-Einloft	0.13	0.21	0.24
MultiEXCELL	0.05	0.24	0.25
Bryant	0.15	0.21	0.26
SC EXCELL	0.07	0.25	0.26
SAM	0.09	0.25	0.27
Brazil	0.11	0.29	0.31
Crane Two-Component	-0.02	0.32	0.32

The following figures provide additional details on the models' performance by showing the E and RMS as a function of the probability level ($5 \times 10^{-3}\% \leq P \leq 5\%$). Specifically, in order to improve readability and clarity, Figure 4-11 and Figure 4-12 are relative to the following models (GROUP 1): Assis-Einloft, Brazil, Bryant, Crane Two-component; whilst Figure 4-13 and Figure 4-14 include the following models (GROUP 2): ITU-R P.618-10, MultiEXCELL, SAM and SC EXCELL.

GROUP 1: All the models tend to underestimate and overestimate the rain attenuation at low and high *P* level, respectively. The Brazil and Bryant model show the most stable trend with *P*, both in terms of E and RMS, although their prediction is limited to *P* = 1%; on the opposite, the Brazil and Crane Two-Component are associated to larger excursions in E and RMS and to an overall lower performance. All the models in this group tend to provide more accurate predictions for $10^{-2}\% \leq P \leq 10^{-1}\%$.

GROUP 2: The models in this group generally offer a better performance with respect to those in group 1. The ITU-R model shows the most stable trend of the prediction accuracy with *P*, especially in the slightly restricted range $10^{-2}\% \leq P \leq 1\%$. As expected, since they rely on the same cellular approach, MultiEXCELL and SC EXCELL provide a similar performance, comparable to the one delivered by the ITU-R model in the $10^{-2}\% \leq P \leq 10^{-1}\%$ decade, and progressively decreasing with the increase in *P*. SAM tends to underestimate and overestimate the rain attenuation at low and high probability levels, respectively, and, in general, it is less accurate than the other models in this group.

Both when considering Table 4-1 and the figures above, the ITU-R model clearly emerges because of its very high accuracy, especially considering the significant gap between its performance and the one associated to the other models. This finding is likely to be in tight relationship with the fact that the ITU-R model is mainly of empirical nature and, in its development, the measured data included in the DBSG3 database have been employed in order to optimize the model's coefficients. On the contrary, this is not true for other models such as MultiEXCELL and SC EXCELL which strongly rely on physical concepts and do not include empirically derived expressions.
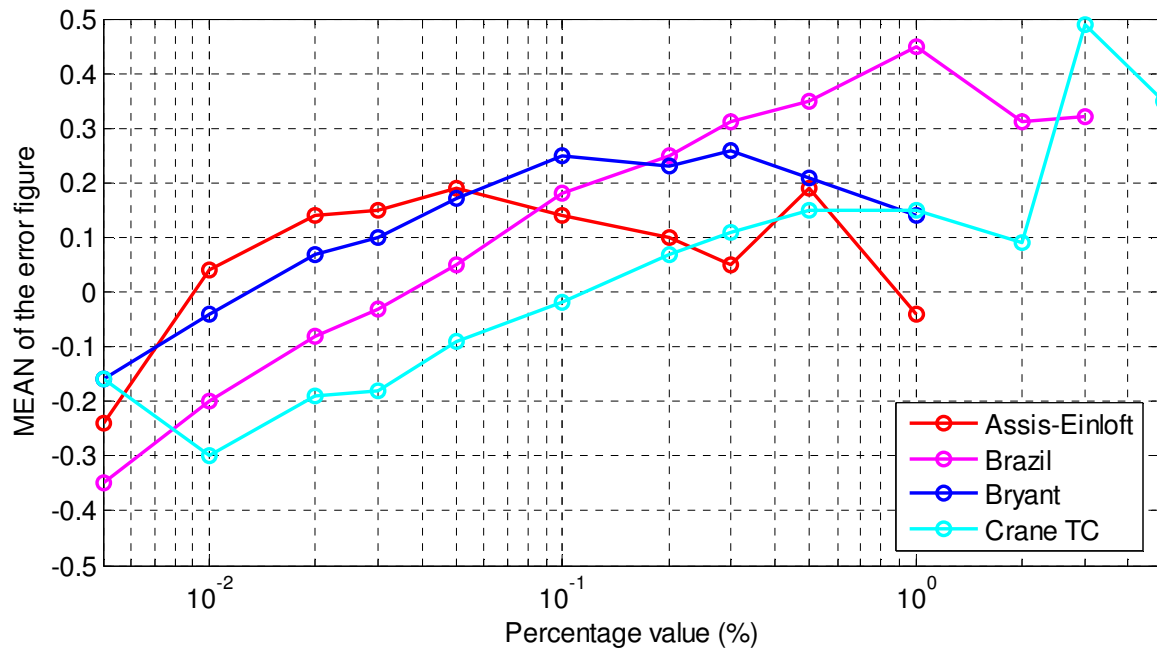
Figure 4-11. Trend of E with the probability level P (group 1)
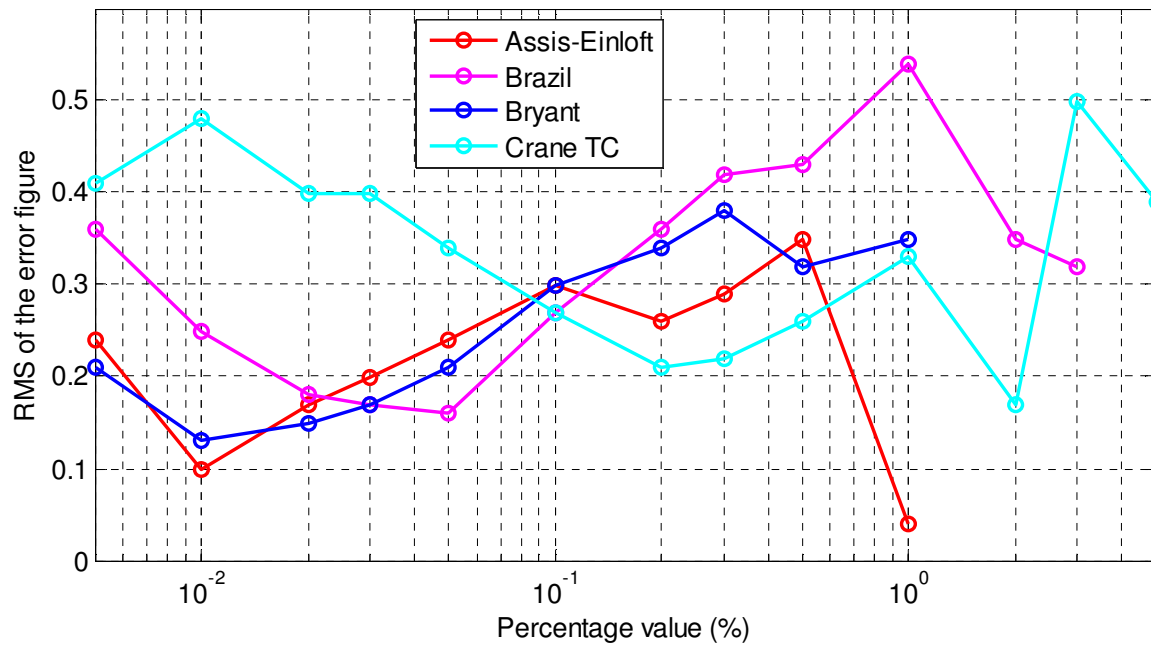
Figure 4-12. Trend of RMS with the probability level P (group 1)
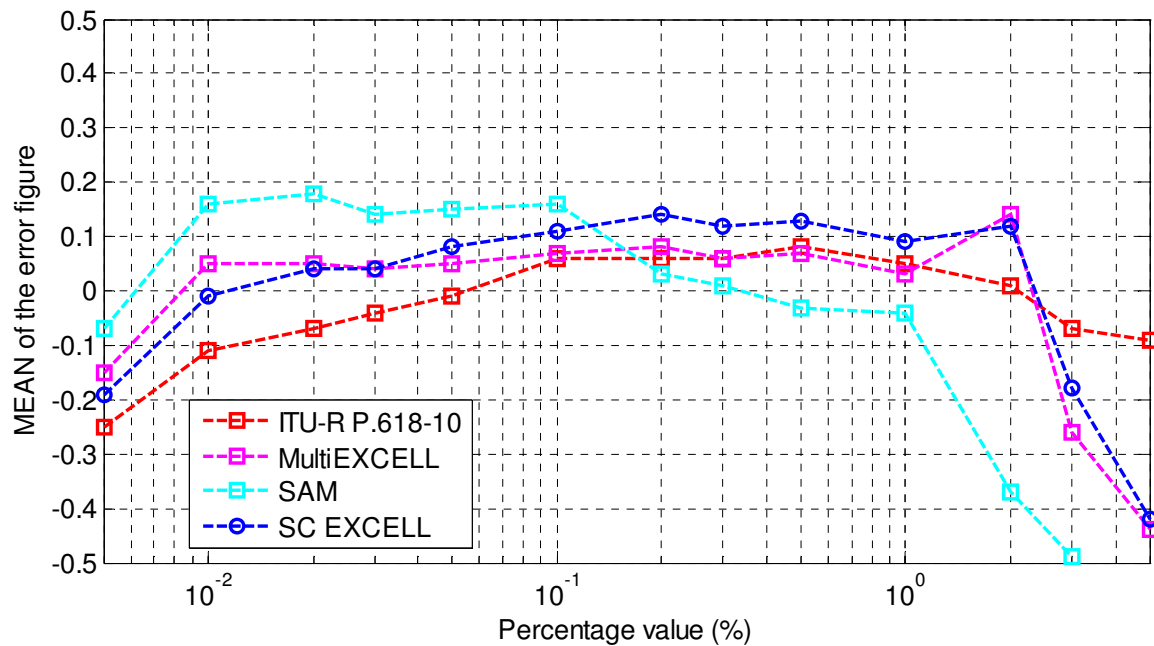
Figure 4-13. Trend of E with the probability level P (group 2)
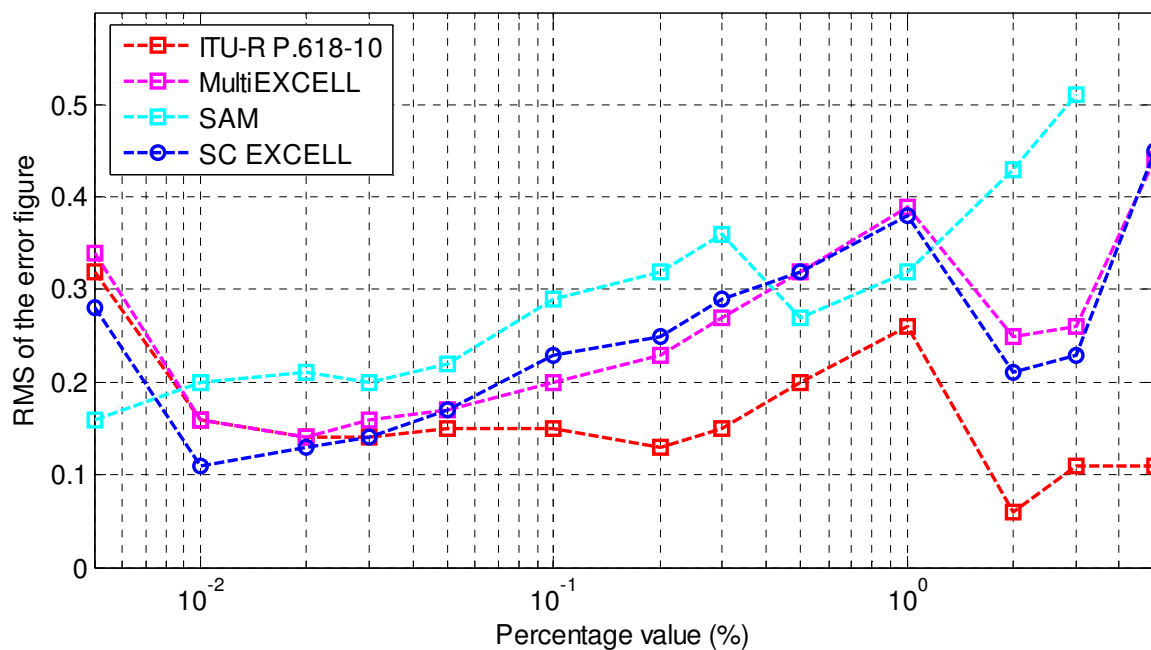
Figure 4-14. Trend of RMS with the probability level P (group 2)

A confirmation of the discussion above appears to come from Table 4-2, which reports the prediction accuracy when models receive as input the $P(R)$ predicted using recommendation ITU-R P.837-6 [ITU-R P.837-6, 2012] instead of the one included in the DBSG3 database: whilst most of the models show only a slight decrease in the performance due to a less accurate input, the prediction accuracy of the ITU-R model (and of the Brazil model as well) reduces drastically (RMS shifting from 0.16 to 0.26), which highlights the extreme sensitivity of this model to the input $P(R)$ (more precisely, to $R_{0.01\%}$), as well as its adjustment to the DBSG3 data. In turn, as also discussed in [Brost and Cook, 2012], this behavior may reveal particularly critical when the ITU-R model is used to predict rain attenuation statistics at frequencies higher than 50 GHz because no measurements of this kind are included in the DBSG3 database and, therefore, could contribute to the optimization of the model itself. On the opposite, physically-based models such as MultiEXCELL and SC EXCELL are expected to provide more reliable results also outside the range of frequency of the measurements currently available, i.e above 50 GHz.

Table 4-2. Models' accuracy evaluated against the selected 49 experiments (all P values); P(R) used as input to the models have been derived from recommendation ITU-R P.837-6

Model	E	STD	RMS
ITU-R P.618-10	0.01	0.26	0.26
MultiEXCELL	-0.03	0.26	0.26
SC EXCELL	0	0.28	0.28
Bryant	0.13	0.26	0.29
SAM	0.03	0.31	0.31
Assis-Einloft	0.07	0.31	0.32
Crane Two-component	-0.02	0.32	0.32
Brazil	0.17	0.34	0.38

4.3.　　Models of clouds attenuation statistics

In this study, only SMOC and the model currently adopted by ITU-R (P.840-5) for cloud attenuation prediction [ITU-R P.840-5, 2012] have been selected for the testing activity because of the limited accuracy of some models proposed in the past (e.g [Altshuler and Marr, 1989], [Dintelmann and Ortgies, 1989]) and due to the difficulty in obtaining the cloud databases necessary for the application of other models such as [Dissanayake et al., 1997].

4.3.1.　　ITU-R P.840-5

In the ITU-R model, cloud attenuation statistics are calculated according to a physically-based procedure which involves the Rayleigh approximation for the calculation of the extinction properties of the suspended droplets forming clouds and fogs (the same one included in the Liebe's model and introduced in section 2.1.3.1). In fact, due to the small size of such droplets (assumed to be of spherical shape) with respect to the wavelength for frequencies below 300 GHz, the specific attenuation due to clouds and fog γ_C can be calculated as:

$$\gamma_C = K_l w \quad \text{(dB/km)} \tag{4-68}$$

where w is the liquid water content in the cloud or fog (g/m^3), whilst, considering the Rayleigh approximation and the double-Debye model for the dielectric permittivity of water ε, K_l can be written as:

$$K_l = \frac{0.819\, f}{\varepsilon''\left(1+\eta^2\right)} \quad \text{(dB/km)/(g/m}^3) \tag{4-69}$$

In (4-69), $\eta = (2+\varepsilon')/\varepsilon''$, whist ε' and ε'' are the real and imaginary part of the dielectric permittivity of water, respectively:

$$\varepsilon'(f) = \varepsilon_2 + \frac{(\varepsilon_0 - \varepsilon_1)}{1+(f/f_D)^2} + \frac{(\varepsilon_1 - \varepsilon_2)}{1+(f/f_S)^2} \tag{4-70}$$

$$\varepsilon''(f) = \frac{f\,(\varepsilon_0 - \varepsilon_1)}{f_D\,[1+(f/f_D)^2]} + \frac{f\,(\varepsilon_1 - \varepsilon_2)}{f_S\,[1+(f/f_S)^2]} \tag{4-71}$$

where:

$\varepsilon_0 = 77.67 + 103.3\,(\Theta - 1)$

$\varepsilon_1 = 5.48$ and $\varepsilon_2 = 3.51$

$f_D = 20.09 - 142\,(\Theta - 1) + 294\,(\Theta - 1)^2$ and $f_S = 590 - 1500\,(\Theta - 1)$ (GHz)

$\Theta = 300/T$ (with T in Kelvin).

As is clear from (4-69), besides being function of the frequency, K_l also depends on the temperature T through the dielectric permittivity of water. As a consequence, the exact calculation of the total attenuation A due to a cloud would require the knowledge of the complete profile of temperature and liquid water content within the cloud. A possible way to simplify the calculation of A is to use an effective value of the vertical integral of w (much easier to handle than the whole profile), L_{red}, which embeds the information on the variation of temperature (and, thus, of the specific cloud attenuation) with height. According to this, the total path attenuation due to clouds can be calculated as:

$$A = \frac{K_l\!\left(T = 0\,°C\right) L_{red}}{\sin(\theta)} \quad \text{(dB)} \tag{4-72}$$

where θ is the elevation angle, $K_l\!\left(T = 0\,°C\right)$ is the coefficient in (4-69) calculated for $T = 0\,°C$ and L_{red} is the integrated liquid water content reduced to the 0 °C temperature. In other words, equation (4-72) gives the total path attenuation as if the temperature within the cloud was always 0 °C, regardless of the layers' height, and this deviation from the actual values of T along the profile is taken into account by modifying w into w_{red} along the profile.

Without going too much into the details on how w_{red} (hence L_{red}) can be calculated (fully available in [Salonen et al., 1990]), it is worth noting that, besides its obvious dependence on temperature and integrated liquid water content, L_{red} also depends on the frequency. Yearly exceedance probabilities of L_{red}, made available worldwide by ITU-R in recommendation P.840-5, have been calculated from vertical profiles of pressure, temperature and relative humidity extracted from the ERA40 database with latitude/longitude grid resolution equal to 1.125°×1.125°, considering the frequency range 20-50 GHz. As a consequence, results from the application of the ITU-R model in the Q/V and W bands should be handled with care

because L_{red} statistics should be recalculated for such higher frequency range. Finally, an additional inaccuracy of the ITU-R model may occur for low elevation links (θ lower than approximately 15-20 degrees) owing to the stratified atmosphere assumption, which, as shown in (4-72), allows to scale the zenith attenuation using the cosecant of the elevation angle. In fact, the lower the elevation angle, the longer is the portion of the link potentially affected by clouds, the more important is the knowledge of the spatial structure of the clouds (especially heavy clouds), both in terms of vertical profile and of horizontal variation.

4.3.2.   SMOC (Stochastic MOdel of Clouds)

The prediction of cloud attenuation statistics using SMOC is achieved by integrating the contribution to attenuation of each cloud affecting the propagation path. To this aim, since different types of cloud are associated with different thickness and develop at different altitudes, as a first step, the following relationship, depicted in Figure 4-15, can be used to estimate the cloud thickness ΔH from the vertically integrated liquid water content values (L) of the synthetic clouds maps generated by SMOC (L is expressed in mm):

$$\Delta H = 12.22 L^{0.39} - 7.53 L^{0.36} \quad \text{(km)} \tag{4-73}$$

Equation (4-73) has been derived from radiosonde data collected in some stations in Europe, whose sites, subject to very different climates, range from North (e.g. Sodankyla, Finland) to South (e.g. Trapani, Italy). Specifically, temperature, pressure and relative humidity profiles have been used to derive the liquid water content as a function of height by means of the HUT cloud detection algorithm [Salonen and Uppala, 1991] and, afterwards, the integrated liquid water content and the thickness of each cloud have been extracted and their relationship investigated. The main assumption behind (4-73) is that only one (liquid water) cloud is present in each profile; this happens for most of the analyzed profiles and, when this is not the case, there is always one cloud markedly prevailing over the others, both in terms of thickness and of total liquid water content.
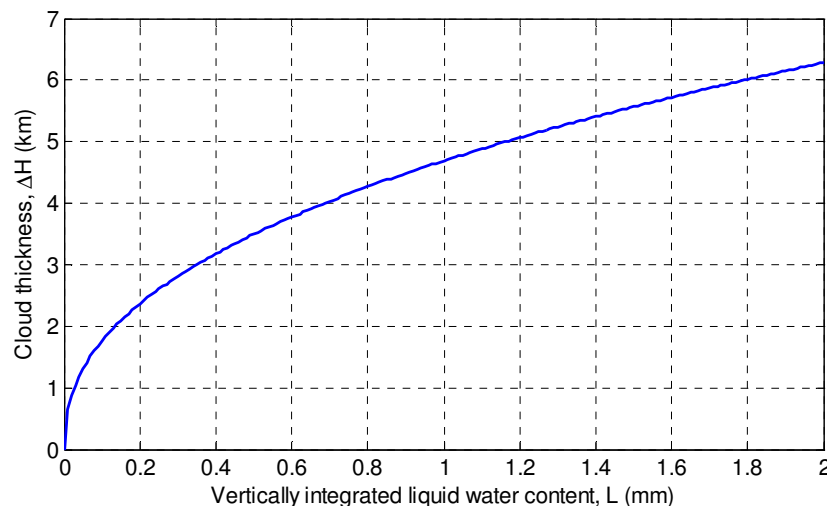
Figure 4-15. Relationship between the vertically integrated liquid water content, L, and the cloud thickness, ΔH

From L and ΔH, the effective liquid water content of the cloud can be calculated as:

$$w_{eff} = \frac{L}{\Delta H} \quad (g/m^3) \tag{4-74}$$

As a result, by employing (4-73) and (4-74), it is possible to convert L values included in the synthetic cloud maps generated by SMOC into clouds with a given thickness and associated effective liquid water content which, as indicated in Figure 4-16, is assumed to be constant along the whole cloud profile (this is why w_{eff} is an effective parameter).

The final a-priori information required to properly calculate the cloud attenuation along the propagation path is the cloud base height h_0. Actually, this information is necessary when clouds relative to different pixels in the map tend to have a very different h_0. Indeed, making reference to Figure 4-16, it is possible to assume that at least all the clouds simultaneously affecting the link have approximately the same h_0. This is absolutely reasonable for stratiform clouds which typically extend uniformly over large areas, while it could be more questionable for convective clouds, which, on the other side, tend to be quite concentrated in space. In addition, as can be deduced from the bottom side of Figure 4-16 sketching the interaction between clouds and the Earth-satellite link, an error in estimating the cloud base height is not expected to dramatically affect the resulting total path attenuation.

According to this scheme, by combining the geometrical characteristics of the link with the maps of ΔH and w_{eff}, it is possible to calculate L_p, the integrated liquid water content affecting the propagation path.

As shown in Figure 4-16, the final step to calculate the total path attenuation due to clouds would be to integrate the specific attenuation along the path, which, in turn, would also require to know the temperature of each cloud layer affecting the path (refer to (4-69)). As discussed in section 4.3.1, while in the ITU-R model the need of such information is circumvented by introducing the reduced liquid water content, in SMOC the simplifying solution comes from the concept of mass absorption coefficients ($a_V(f)$ and $a_L(f)$ in (4-75) and (4-76), respectively), widely employed in the remote sensing community to easily and accurately relate the water vapor and liquid water path integrals (V and L, respectively) to the associated attenuation at a given frequency f (A_V and A_L, respectively) [Luini et al., 2007]:

$$A_V(f) = a_V(f)V \quad (dB/mm) \tag{4-75}$$

$$A_L(f) = a_L(f)L \quad (dB/mm) \tag{4-76}$$

An example of a_L at 31.6 GHz derived from an extensive radio sonde database (plus the HUT algorithm for cloud detection [Salonen and Uppala, 1991] and the Liebe's MPM93 [Liebe et al., 1993] for cloud extinction calculations) collected at Milano/Linate airport is shown in Figure 4-17 (data data published in [Luini et al., 2007]): results in the figure, especially the correlation coefficient in the bottom right end corner, indicate that (4-76) is sufficiently accurate to model the relationship between the integrated liquid water content and the associated attenuation.

With this approach the variation of the temperature within the cloud profile (and of the associated specific attenuation) is no more embedded in L but is taken into due account by the mass absorption coefficient a_L. This solution introduces the advantages of working with a physical quantity (L), instead of an effective one (L_{red}), which can be more easily obtained directly from different sources such as Numerical Weather Prediction (NWP) data (e.g.

ERA40 database), radio soundings and Earth Observation (EO) satellites (e.g. MODIS, Meteosat Second Generation, …). Moreover, by adopting mass absorption coefficients, there is no need to recalculate L_{red} for different frequency ranges.
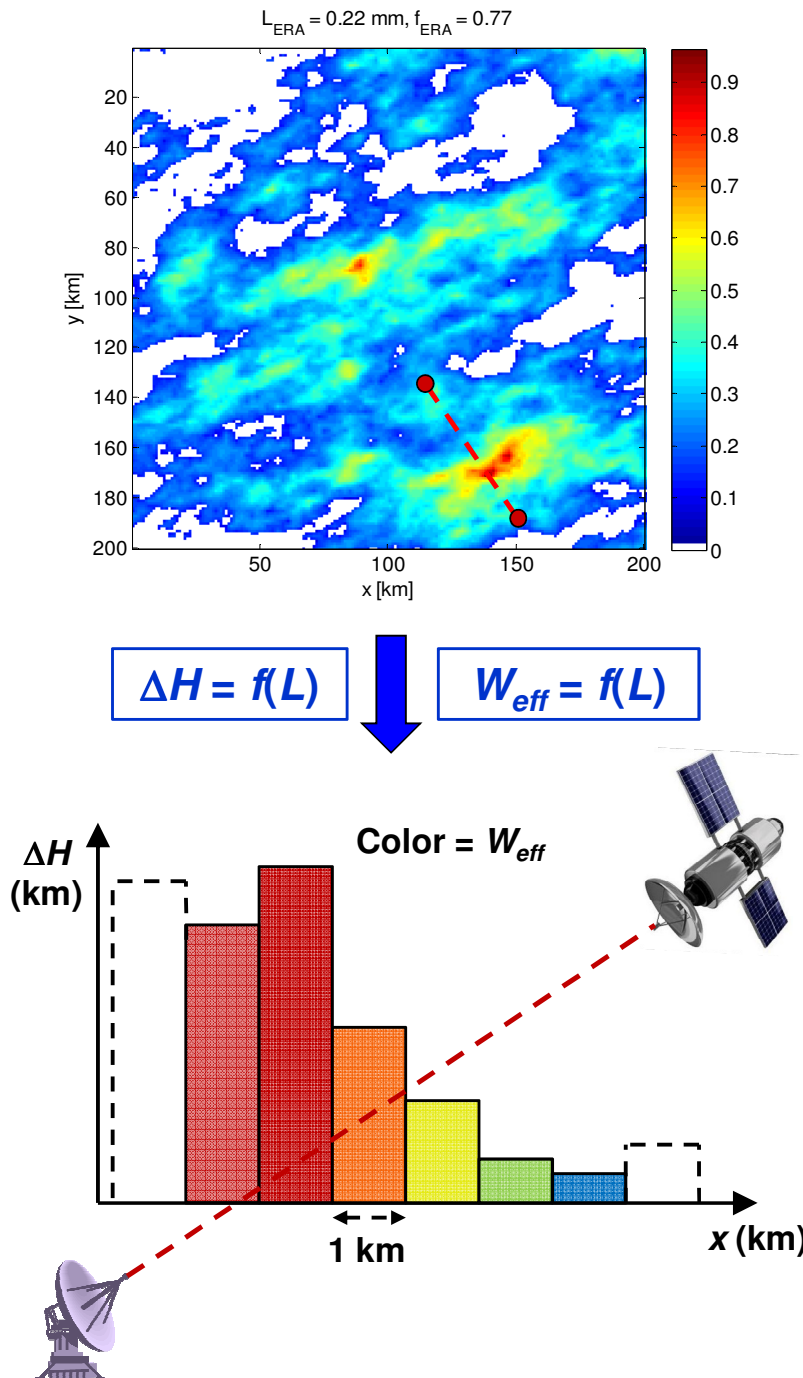
Figure 4-16. Reference geometry for the calculation of the attenuation due to clouds. The vertically integrated liquid water content (L) is used to estimate the cloud thickness (ΔH) and the associated effective liquid water content (w_{eff}) using (4-73) and (4-74), respectively
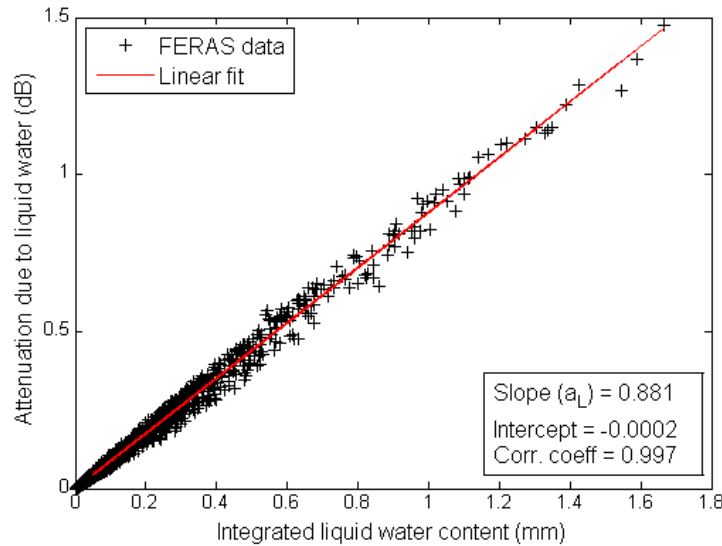
Figure 4-17. Calculation of the mass absorption coefficient a_L at 31.6 GHz using an extensive radio sonde database collected at Milano/Linate airport. Example based on the data published in [Luini et al., 2007]

Although mass absorption coefficients are expected to depend on the site, negligible differences in a_L have been found (at equal frequency) when repeating the exercise in Figure 4-17 for different stations in Europe (the same set of data used in the derivation of (4-73)). As a result of such an investigation, the following expression, valid for temperate climate, can be used to accurately calculate a_L as a function of frequency:

$$a_L(f) = \frac{0.819\, a f^{b}}{\varepsilon''\left(1+\eta^2\right)} \quad \text{(dB/mm)} \tag{4-77}$$

where $a = 1.4704$ and $b = 0.9057$, 5 GHz $\leq f \leq$ 100 GHz, whilst the real and imaginary parts of the electric permittivity of water (see equations following (4-69)) are calculated for $T = 0$ °C. As a result, equation (4-77), which turns out to be a slight deviation from (4-69), can be used to calculate the total path attenuation A, for frequencies between 5 GHz and 100 GHz, as a function of the L_p values derived from SMOC synthetic cloud maps.

Similarly to the procedure used in MultiEXCELL, the position of the link in Figure 4-16 can be moved across the whole map in order to increase the statistical significance of the results and, thus, each cloud map can be converted into a cloud attenuation map. Finally, the accumulation of the attenuation values obtained from all the maps generated by SMOC allows to calculate the predicted yearly cloud attenuation distribution, i.e. the probability to exceed a given cloud attenuation threshold.

4.4.   Assessment of the accuracy of cloud attenuation prediction models

4.4.1.   The reference database

Unlike for rain attenuation, no global standardized catalogues of cloud attenuation statistics are available nowadays. Therefore, measurements for model's testing have been extracted from papers available in the open literature. Table 4-3 provides details on the

gathered statistics; specifically, the fifth column of Table 4-3 indicates that basically three types of measurements are available:

- RAOBS (RAdio sonde OBServations): as described in Chapter 2, cloud attenuation statistics can be estimated stating from radio sonde-derived profiles of temperature, pressure and relative humidity that are first used as input to cloud detection algorithms, such as the HUT [Salonen and Uppala, 1991], in order to derive the variation of the liquid (and ice) water content w with height. Afterwards the specific attenuation profile (hence, the total path attenuation) is calculated from w using physically-based models (see equation (4-68) and following ones). As a result, this approach allows the estimate of cloud attenuation statistics at different frequencies as shown in the first and sixth lines of Table 4-3.

- Beacon receivers: in this case, cloud attenuation statistics are estimated using high-sensitivity beacon receivers usually deployed in the framework of propagation experiments such as the ACTS and the ITALSAT programs. The isolation of the sole contribution of clouds (i.e. the removal of the signatures due to precipitation and gases) is quite critical as it can be achieved only by exploiting the additional information provided by radiometers.

- Radiometers: as outlined in Chapter 2, cloud (and gaseous) attenuation statistics can be derived from brightness temperature data collected by radiometers. After typically filtering out rain events (again by means of ancillary data and equipments), the inversion of brightness temperatures measured by (at least) two channels allows the accurate estimate of L and V, hence of attenuation statistics due to liquid water and water vapor, respectively.

Table 4-3. Cloud attenuation statistics gathered from the literature for models' testing

Site	Lat [°N]	Lon [°E]	Frequency [GHz]	Source	Reference
Berlin (DE)	52.29	13.25	20, 40, 50, 70, 80, 90	RAOBS	[Capsoni et al., 2012]
Clarksburg (USA)	39.24	-77.28	20.2, 27.5	Beacon RX (ACTS)	[Dissanayake et al., 2001]
Darmstadt (DE)	49.87	8.65	20, 30	Radiometer	[Dissanayake et al., 2001]
Madrid (ES)	40.42	-3.7	50	Beacon RX (ITALSAT)	[Al-Ansafi et al., 2003]
New York (USA)	40.71	-74	35	RAOBS	[Dissanayake et al., 1997]
Spino d'Adda (IT)	45.4	9.5	58, 72, 81, 93	RAOBS	[Capsoni et al., 2009b]
York (UK)	53.96	-1.08	93	Radiometer	[Davies et al., 1998]

4.4.2. Prediction error

In order to quantify the models' accuracy in predicting cloud attenuation statistics, the same error figure in (4-67) has been used. In this case, all yearly probability values higher than 0.1% have been considered for each of the 17 reference curves available and the models' performance has been quantified through the average (E) and root mean square (RMS) values of ε in (4-67). They are reported in Figure 4-18 and Figure 4-19, respectively, where different colors in the x-axis labels are associated with different sites.
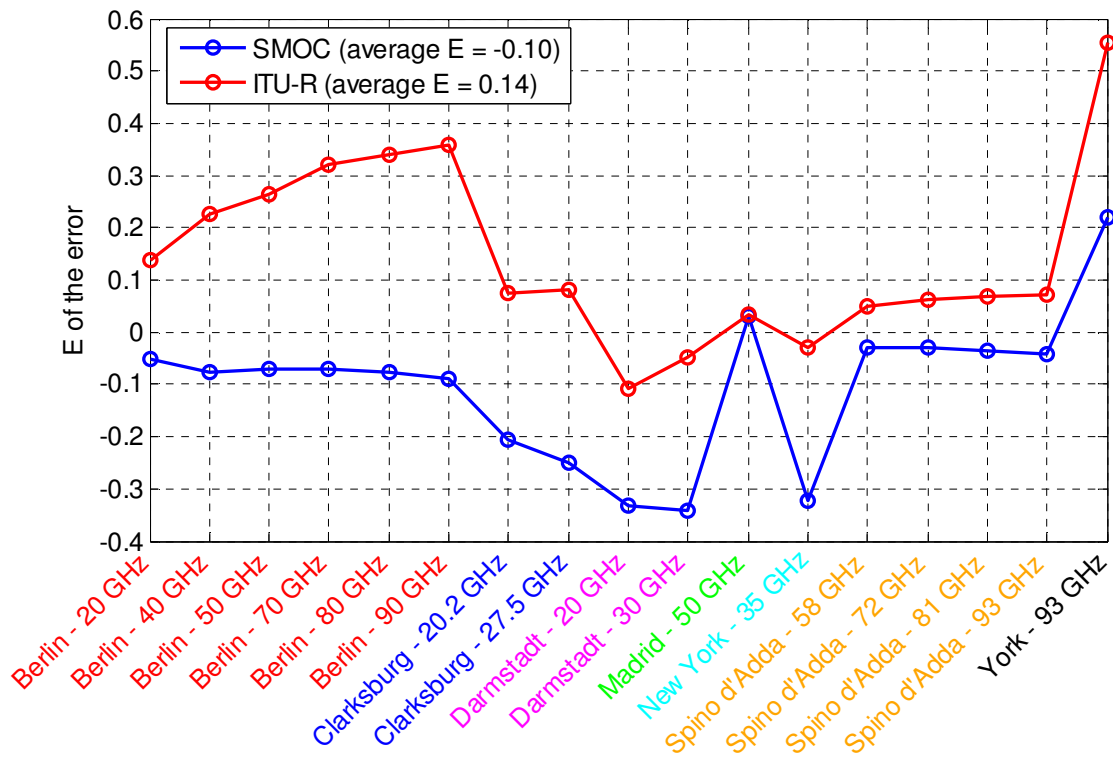
Figure 4-18. Models' accuracy in predicting cloud attenuation statistics: average value of the prediction error
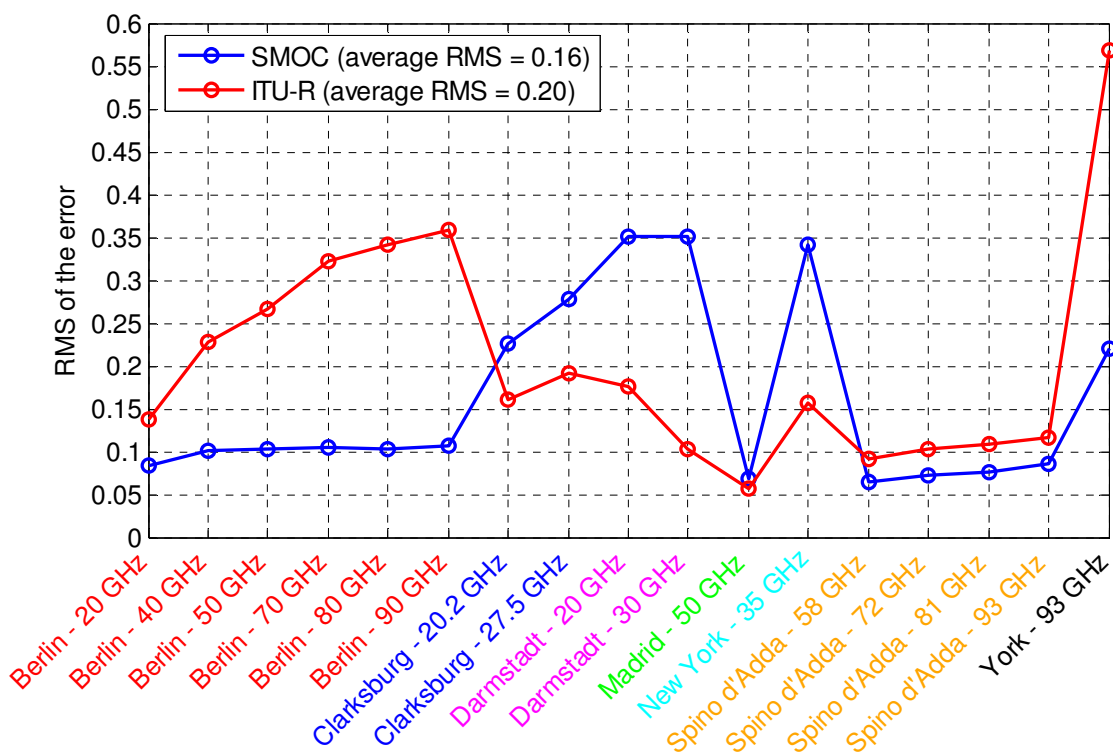
Figure 4-19. Models' accuracy in predicting cloud attenuation statistics: root mean square value of the prediction error

Results indicate that SMOC is less biased that the ITU-R model (average E equal to -0.1 and 0.14, respectively) and that the former is generally more accurate than the latter (average RMS equal to 0.16 and 0.20, respectively), though, as is clear from Figure 4-18 and Figure 4-19, the prevalence of one model on the other in terms of prediction accuracy is definitely dependent on the site. In turn, this is linked to the fact that the prediction error can be split into two parts: a fraction of the error is associated with the prediction of the local statistics of integrated cloud liquid water content ($P(L)$), whilst an additional contribution to the error comes from the estimation of the path attenuation from $P(L)$.

The first part of the error is dependent both on the uncertainty of the cloud data included in the ERA40 database and on how they are processed to obtain the integral information of the cloud liquid water content for the site of interest. Whilst this error can be quantified for SMOC by comparing L statistics obtained from the synthetic cloud fields with those obtained from RAOBS data, such comparison is not possible for the ITU-R model because it relies on an effective value of L. On the other side, instead, the second part of the error can be highlighted by inspecting results relative to sites where cloud attenuation statistics were obtained from RAOBS. In fact, looking specifically at the results relative to Berlin (and also at the curves in Figure 4-20), both models show an increase in the RMS as the frequency shifts from 20 GHz to 90 GHz. This effect is actually very limited for SMOC, whilst it is much more marked for the ITU-R model, being probably linked to the increasingly limited suitability of the reduced liquid water content L_{red} for cloud attenuation prediction when L_{red} is used outside the frequency range for which it has been calculated (20-50 GHz).
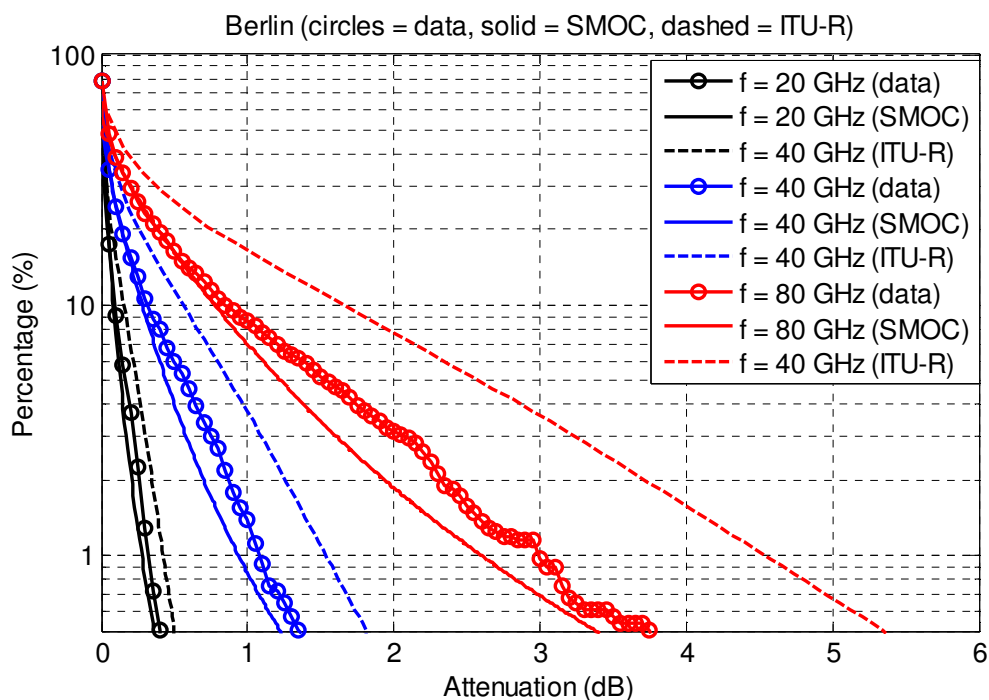
Figure 4-20. *Models' accuracy in predicting cloud attenuation statistics: results for Berlin*

As additional results of the curves predicted by SMOC and the ITU-R model, Figure 4-21 and Figure 4-22 show the results respectively relative to Madrid (f = 50 GHz), for which both

models provide accurate predictions, and to Clarksburg (f = 20.2 GHz), for which, on the contrary, the ITU-R model performs better than SMOC.
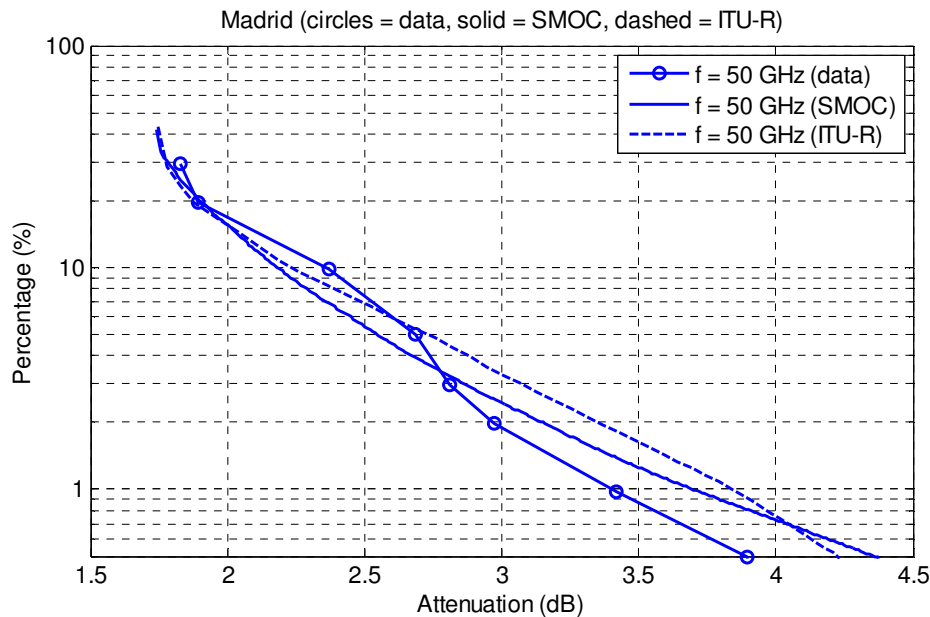
Figure 4-21. Models' accuracy in predicting cloud attenuation statistics: results for Madrid. The attenuation statistics in the figure include also the gaseous component; as suggested in [Al-Ansafi et al., 2003], 1.74 dB have been added to all probability levels (as per recommendation ITU-R P.676-9 [ITU-R P.676-9, 2012]) to allow a fair comparison of the models' output with the measured data
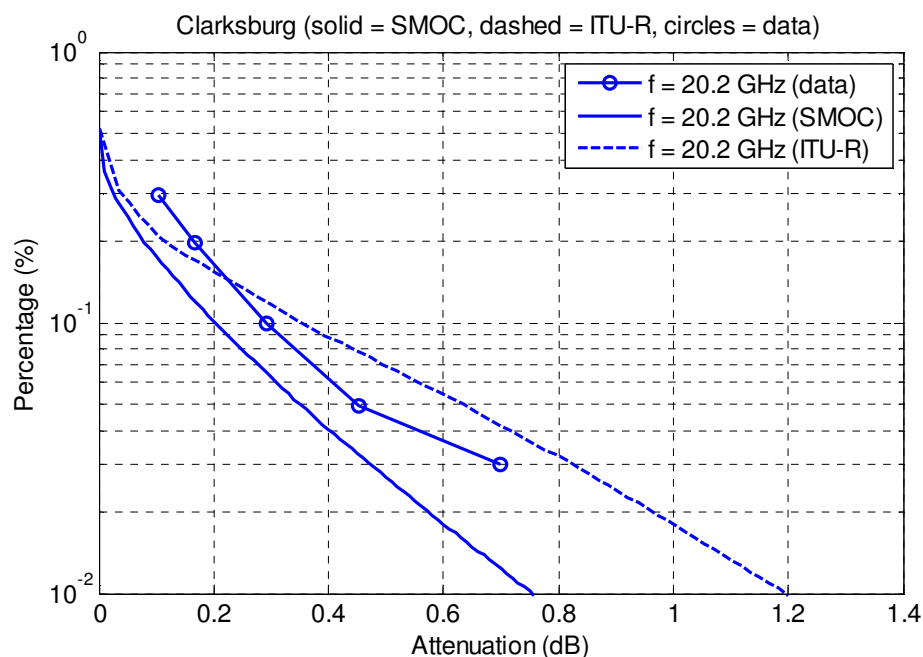
Figure 4-22. Models' accuracy in predicting cloud attenuation statistics: results for Clarksburg

4.5.　　Models of site diversity

In this study, only the following models for the performance assessment of site diversity systems have been selected: the ITU-R model, included in section 2.2.4.1 of recommendation P.618-10 [ITU-R P.618-10, 2009], not only because it is the current reference against which other models are typically compared, but also because it is the most acknowledged example of that class of models relying on the a-priori assumption that rain attenuation follows a given statistical distribution (e.g. lognormal in [ITU-R P.618-10, 2009] and [Gremont and Filip, 2004], inverse Gaussian in [Kourogiorgas et al., 2012]); EXCELL and MultiEXCELL as examples of those models based on the cellular approach for the simulation and performance assessment of site diversity systems.

4.5.1.　　ITU-R P.618-10

Based on the work presented in [Barbaliscia and Paraboni, 2002], the model for site diversity prediction included in recommendation ITU-R P.618-10 [ITU-R P.618-10, 2009] (section 2.2.4.1) relies on the postulation that the attenuation due to rain A (as well as the rain intensity) follows the lognormal distribution. This assumption is considered to be valid both in time (i.e. rain attenuation statistics measured by a beacon receiver in a specific point) and in space (i.e. rain attenuation simultaneously exceeded in a given area), which allows to express the joint attenuation statistics (relative to two or more stations) as the combination of multiple Gaussian distributions whose mutual correlation depends on the distance between the considered sites.

The method aims at calculating P_j, the probability that attenuations a_1 and a_2 are simultaneously exceeded in site 1 and 2, respectively, i.e.:

$$P_j(A_1, A_2) = P(a_1 > A_1, a_2 > A_2) \quad (\%) \tag{4-78}$$

This joint probability can be calculated as the combination of two terms:

$$P_j(A_1, A_2) = 100 \cdot P_R \cdot P_A(A_1, A_2) \quad (\%) \tag{4-79}$$

where P_R, the probability that rain is simultaneously affecting both sites, is defined by the following bivariate normal distribution:

$$P_R = \frac{1}{2\pi\sqrt{1-\rho_R^2}} \int_{R_1}^{\infty}\int_{R_2}^{\infty} \exp\left[-\left(\frac{r_1^2 - 2\rho_R r_1 r_2 + r_2^2}{2(1-\rho_R^2)}\right)\right] \mathrm{d}r_1 \mathrm{d}r_2 \quad (\%) \tag{4-80}$$

The term ρ_R in (4-80) takes into account the spatial correlation between the sites 1 and 2 as a function of their separation distance d:

$$\rho_R = 0.7 \exp\left(-\frac{d}{60}\right) + 0.3 \exp\left[-\left(\frac{d}{700}\right)^2\right] \tag{4-81}$$

The rain intensity thresholds R_1 and R_2 in (4-80) can be derived for the two sites as:

$$R_i = Q^{-1}\left(\frac{P_R^i}{100}\right) \tag{4-82}$$

where $i = 1$ or 2, Q^{-1} is the inverse complementary cumulative normal distribution and P_R^i is the probability to have rain in site i, which, in turn, is derivable from local rainfall statistics or, when the latter are not available, from the following expression [ITU-R P.837-6, 2012]:

$$P_R^i = P_{r6h}\left[1 - \exp\left(-0.0079 M_s / P_{r6h}\right)\right] \tag{4-83}$$

M_s and P_{r6h}, respectively defined as the mean yearly amount of stratiform rain and mean yearly probability to have rain in a 6-hour time slot, can be extracted worldwide from the ERA40 database included in recommendation ITU-R P.837-6 [ITU-R P.837-6, 2012].

The term P_A in (4-78), which takes into account the spatial correlation of the rain attenuation, is expressed by the following bivariate normal distribution:

$$P_A(A_1, A_2) = \frac{1}{2\pi\sqrt{1-\rho_A^2}} \int_{\frac{\ln A_1 - \mu_1}{\sigma_1}}^{\infty} \int_{\frac{\ln A_2 - \mu_2}{\sigma_2}}^{\infty} \exp\left[-\left(\frac{a_1^2 - 2\rho_A a_1 a_2 + a_2^2}{2(1-\rho_A^2)}\right)\right] da_1 da_2 \quad (\%) \tag{4-84}$$

where the proper degree of spatial correlation for the rain attenuation is obtained from:

$$\rho_A = 0.94 \exp\left(-\frac{d}{30}\right) + 0.06 \exp\left[-\left(\frac{d}{500}\right)^2\right] \tag{4-85}$$

The values (μ_1, σ_1) and (μ_2, σ_2), the mean and standard deviation of the logarithm of the rain attenuation A for the two sites, can be obtained by fitting the single-site complementary cumulative distribution function of the rain attenuation A (P_s) with the following distribution:

$$P_i = P_R^i Q\left(\frac{\ln A - \mu_i}{\sigma_i}\right) \tag{4-86}$$

Once the joint rain attenuation probability P_j is obtained, the site diversity gain can be calculated, as explained in section 4.6.1, from the additional knowledge of the single-site distribution P_s.

4.5.2.   EXCELL (EXponential CELL)

The first application of the EXCELL model was proposed in [Capsoni et al., 1987b], which presents how the simulation of the interaction of the synthetic rain cells generated by EXCELL with a radio link allows to evaluate the statistics of the induced signal attenuation A. This procedure (the first step towards the evaluation of a site diversity system) is very similar to the one presented in section 4.1.6 for MultiEXCELL for $P(A)$ prediction; however, thanks to the simple exponential shape of the rain cells synthesized by EXCELL and to the introduction of the "kernel" concept, the $P(A)$ prediction is less computationally intensive than using MultiEXCELL, where rain maps have to be integrated numerically.

The $P(A)$ can be predicted using EXCELL by superposing the effects of all the cells according to their probability of occurrence $N(\rho_0, R_M)$:

$$P(A) = \int_{\ln(R_E)}^{\infty} \int_{\rho_{0\min}}^{\infty} S(R_E, L, \alpha, R_M, \rho_0) N(R_M, \rho_0) d\rho_0 \, d\ln(R_M) \tag{4-87}$$

where α is extracted from recommendation ITU-R P.838-3 [ITU-R P.838-3, 2005] for rain rate to specific attenuation conversion; l is the projection to the ground of the link length

affected by rain (refer to Figure 4-23); R_E is the equivalent rain intensity, obtained as the integral of the rain rate along the path (refer to Figure 4-24 in which x and y are the coordinates of the central point of the link):

$$R_E^\alpha(\overline{x}, \overline{y}) = \frac{1}{L} \int_{\overline{x}-L/2}^{\overline{x}+L/2} R^\alpha(x, \overline{y}) \, dx \qquad (4\text{-}88)$$

The term S in (4-87) is the "kernel" area of the equivalent rain intensity R_E, in other words, the total area for which a fixed value of R_E is exceeded. Equation (4-88) should be solved numerically, but accurate analytical approximations can be derived (more details are given in [Capsoni et al., 1987b]), yielding:

$$S = \pi M^2 + L M \qquad (4\text{-}89)$$

where $M = \ln[(R_M+R_{low})/(R_E+R_{low})] \; (\rho_0-\rho_{0min})$, $\rho_{0min} = 0{:}125 \; \alpha \; l \; t \; (3\text{-}t)/(1\text{-}t)$ and, finally, $t = (R_E/ R_M)^a$. The expression of the total path attenuation due to rain is therefore:

$$A = k R_E^\alpha \qquad (4\text{-}90)$$

where, according to Figure 4-23, $L = l/\cos(\theta) = h_R \sin(\theta)$. Since (4-90) is a monotonic relationship between A and R_E, the kernel S given by (4-89) is also the kernel of A. Obviously, for a given value of attenuation A, the equivalent value of R_E must be first derived from (4-90) and afterwards used in (4-89).

In [Bosisio and Riva, 1998], the EXCELL model has been employed for the evaluation of the performance of site diversity systems. Considering a two-site system, in principle, the joint-attenuation $P(A)$ could be calculated by translating the synthetic cells, one at a time as typical of the EXCELL model, over the region where the two stations are located and, each time, by selecting the minimum attenuation value among those experienced by the two radio links. However, this procedure requires a high computational load, as it should be repeated for all the synthetic rain cells.
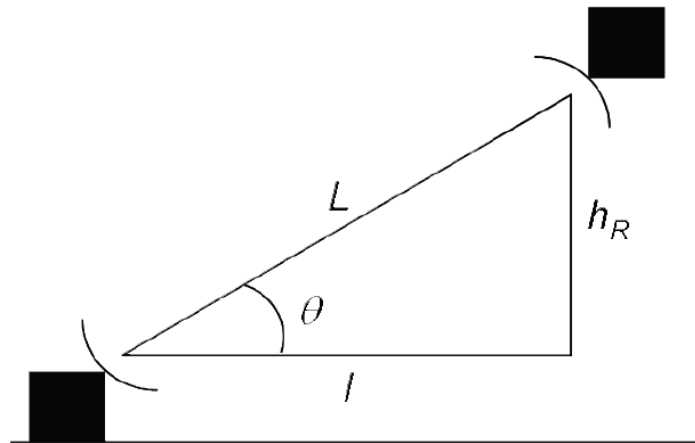
Figure 4-23. Reference geometry for the calculation of rain attenuation

An alternative analytical solution, as proposed in [Bosisio and Riva, 1998], makes use again of the concept of kernel already mentioned above. When the equivalent rain intensity R_E is considered, the area of the kernel can be accurately approximated by ellipses (see (4-89)). As it is derived by considering all the possible positions of the cell over the transmission link, the kernel is proportional to the probability that the given R_E value is exceeded. In the case of dual site diversity systems, for each cell and attenuation value, two distinct kernels are calculated, depending on the characteristics of the two stations (e.g. altitude above the mean sea level). The probability of exceeding the same attenuation value on both links is proportional to the area common to the two (or more than two, depending on the number of diversity sites considered) kernels, as shown in Figure 4-25. The joint-attenuation $P(A)$ (hence the site diversity gain G) can be obtained by superimposing the contribution of all the synthetic rain cells weighted with the rain cells' probability of occurrence.
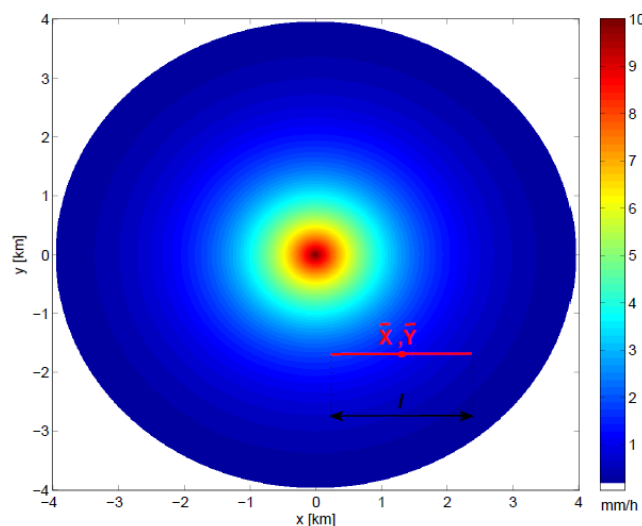
Figure 4-24. Integration of the rain intensity for the calculation of R_E
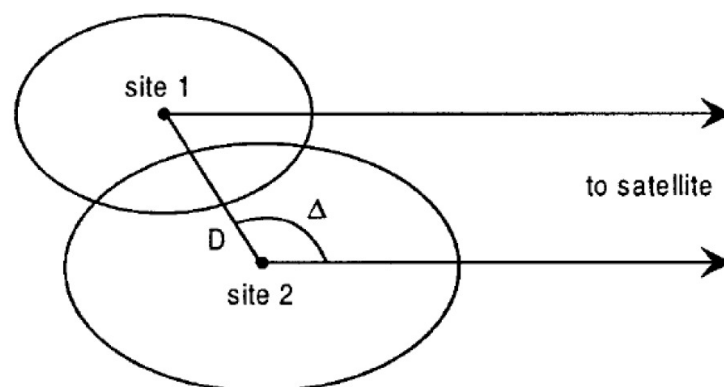
Figure 4-25. Schematic representation of a dual site diversity system (D and Δ are respectively the baseline distance and orientation); the kernels of the two links are represented by the ellipses

4.5.3.   MultiEXCELL (Multi EXponential CELL)

The simulation and performance assessment of site diversity using MultiEXCELL relies on the same physically-based methodology aimed at calculating rain attenuation statistics from synthetic rain fields (refer to section 4.1.6). The additional step required to simulate site diversity schemes (whose geometry is depicted in Figure 4-26) is to consider the simultaneous interaction between the rain field and the two (or more) links, as sketched in Figure 4-27: the rain attenuation affecting both links (A_1 and A_2) for a given position of the system within the rain field is first calculated and, afterwards, the attenuation value that would impair an ideal system ("instantaneous" choice of the less impaired link) is obtained as the minimum between A_1 and A_2.
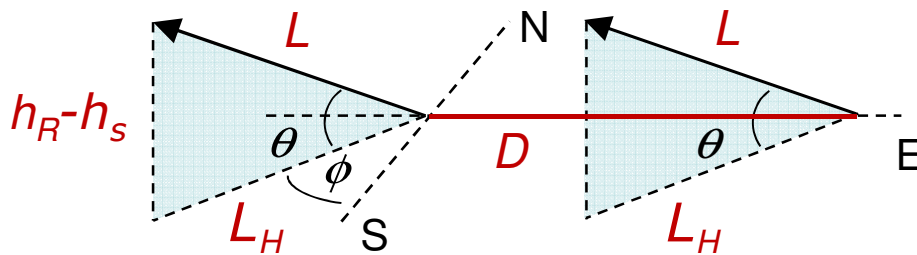
Figure 4-26. Reference geometry for the simulation and performance evaluation of site diversity
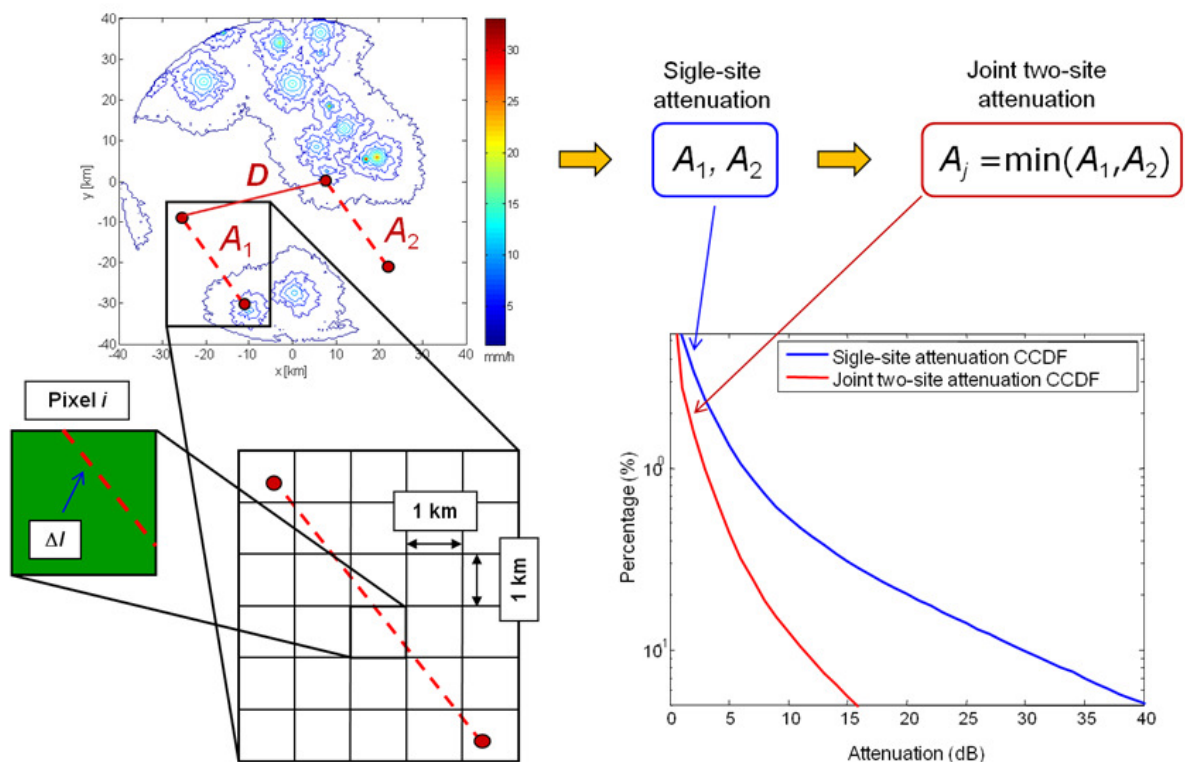
Figure 4-27. Reference geometry for the calculation of simultaneous rain attenuation statistics using the synthetic rain maps generated by MultiEXCELL

As a result, by considering different positions of the diversity scheme within the rain field and by cumulating all the results obtained from all the MultiEXCELL maps, it is possible to build up single- and joint-site rain attenuation statistics (refer again to Figure 4-27).

Although more computationally intensive, the methodology relying on MultiEXCELL offers the chance to deal with site diversity schemes with increased complexity, e.g. considering more than two sites and different baselines between them (both in terms of length and orientation).

4.6. Assessment of the accuracy of site diversity prediction models

4.6.1. The reference database

As for rain attenuation, the ITU-R Study Group 3 maintains a global database of two-site diversity experiments. Specifically, the database contains measured single- ($P_s(A)$) and joint-site ($P_j(A)$) rain attenuation statistics, whilst concurrent rainfall statistics measurements are seldom included. In addition, the database contains the electrical (frequency, polarization, …) and geometrical (e.g. receiver site, satellite orbital position, …) characteristics of the links, from which the details on the site diversity scheme can be deduced (basically, the baseline orientation and length).

The database contains 59 entries associated mostly to experiments with 1-year duration, although some of them have been filtered out in the testing activity because their $P_s(A)$s and/or $P_j(A)$s included less than 3 samples. As a result, 46 site diversity experiments have been selected, whose locations are depicted in Figure 4-28. Sites are prevalently characterized by a temperate climate, the same one which Rome, NY is subject to.

Figure 4-28. Location of the sites where site diversity experiments have been performed

As a preliminary step of the testing activity, single- and joint-site attenuation statistics have been processed to derive the site diversity gain, defined as (make reference to Figure 4-29):

$$G(D, A_s) = A_s(P) - A_j(D, P) \quad \text{(dB)} \tag{4-91}$$

where A_s and A_j are the attenuation values extracted from $P_s(A)$ and $P_j(A)$ (both for the same probability level P), respectively, and D is the site separation distance.
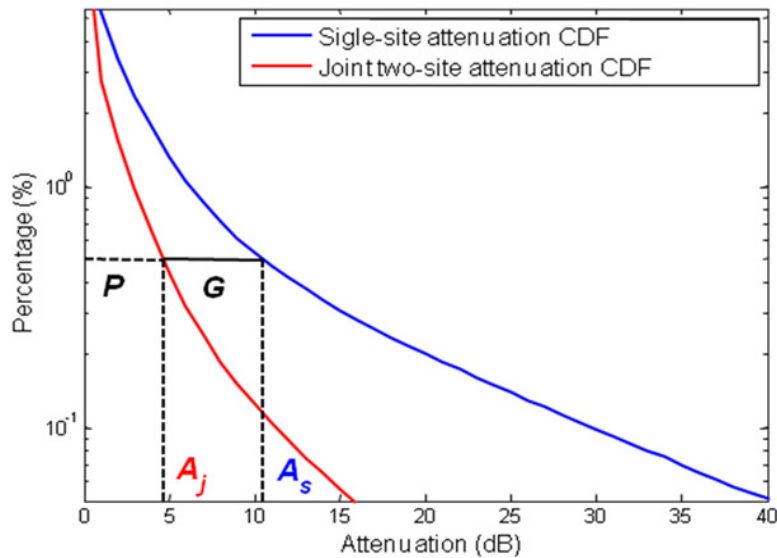
Figure 4-29. Calculation of the site diversity gain from $P_s(A)$ and $P_j(A)$

As an example of the data contained in the ITU-R database, Figure 4-30 shows, on the left side, the single-site rain attenuation distributions measured at the two sites and the joint curve elaborated from the measured time series; the right side of the figure shows the site diversity gain *G* calculated using as a reference in (4-91) the $P_s(A)$ measured at site *A* (G_A) and at site *B* (G_B), as well as the average value obtained as $G_M(A_s) = (G_A(A_s) + G_B(A_s))/2$.
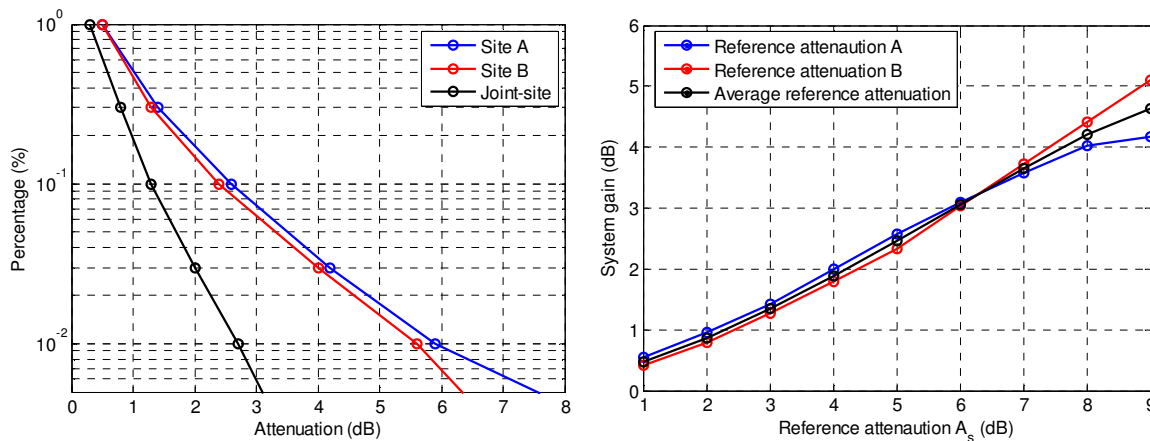
Figure 4-30. Example of the data included in the DBSG3 database for site diversity: reference experiment site = La Conception (Canada); latitude = 46.2° N; longitude = 285.3° E; frequency = 13 GHz; elevation angle = 18 °; baseline length = 31.8 km; baseline orientation = 6.6°

Figure 4-30 allows to point out a general feature of the database, i.e. that for each experiment the rain attenuation statistics measured in the two sites always present some differences (though very small in some cases) mainly due to the limited duration of the experiments (mostly 1-year), but also to the different height of the two sites (information available only for some experiments) and to possible influence coming from the orography/topography. As a result, for a fair comparison between the DBSG3 data and the

models' output, in the tests, the average value of the diversity gain G_M has been considered as reference.

4.6.2. Prediction error

In order to quantitatively assess the prediction accuracy of the selected site diversity models, the following customary error figure has been adopted:

$$\varepsilon(D, A_s) = 100 \frac{G_e(D, A_s) - G_m(D, A_s)}{A_s} \qquad (4\text{-}92)$$

where, as shown in Figure 4-31, $G_m(D, A_s)$ and $G_e(D, A_s)$ represent the site diversity gain, both correspondent to the reference attenuation value A_s, calculated respectively from the reference and model predicted attenuation curves. Finally probability levels of the single- and joint-site attenuation statistics equal to or higher than $5 \times 10^{-3}\%$ have been considered in the tests so as to maintain a good degree of statistical stability in the results. As the last remark, since very few measured rainfall rate statistics are available for the site diversity experiments included in the DBSG3, in all the tests, the $P(R)$ predicted using recommendation ITU-R P.837-6 (Annex 1) have been provided as input to the selected prediction models.
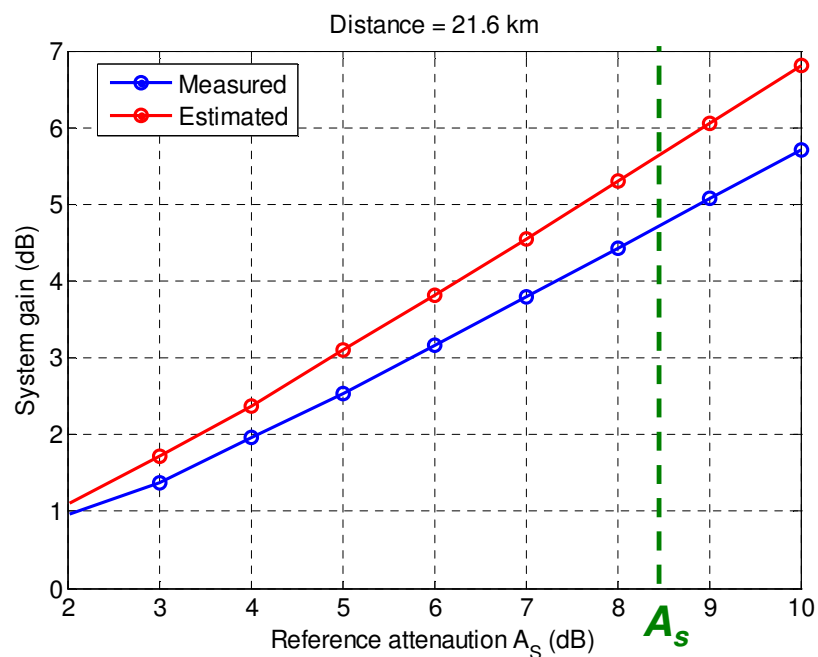
Figure 4-31. Graphical definition of the error figure used for the assessment of the site diversity models' accuracy

Whilst Figure 4-32 shows an example of the models' prediction accuracy (reference experiment site = Palmetto (USA), latitude = 33.5° N, longitude = 275.3° E, f = 17.8 GHz, D = 46.9 km, elevation angle = 38.2°), the overall evaluation of the models' performance is given in Table 4-4 which lists the average (E), standard deviation (STD) and root mean square (RMS) value of the error figure ε in (4-92) considering all the A_s values and all the 46 selected experiments. Looking at the results in this table, where models are sorted in ascending order

on the basis of their RMS value, it is clear that all the three methods provide similar prediction accuracy, at least in term of RMS. More specifically, MultiEXCELL is showing the lowest RMS, whilst EXCELL and the ITU-R model provide the lowest and the highest bias, respectively. Notwithstanding the difference in E, all the models tend to overestimate the site diversity gain derived from the DBSG3 curves.
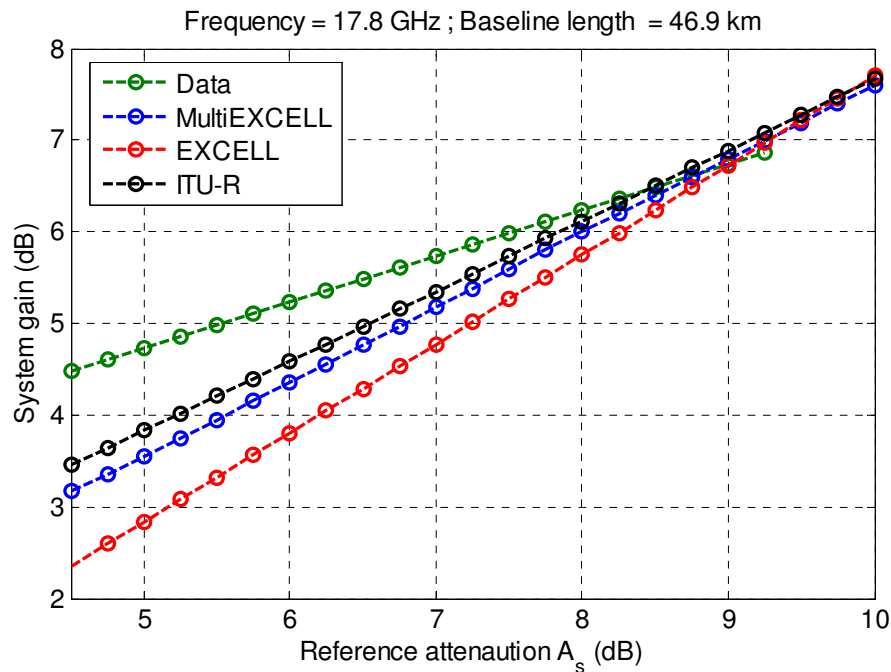
Figure 4-32. Example of the models' prediction accuracy

Table 4-4. Site diversity models' accuracy evaluated against the selected 46 experiments

Model	E (%)	STD (%)	RMS (%)
MultiEXCELL	8.2	11.5	14.1
EXCELL	4.2	13.9	14.5
ITU-R P.618-10	10.4	10.7	14.9

Figure 4-33 and Figure 4-34 provide additional details on the models' performance by showing E and RMS relative to all the 46 selected experiments. Although all the models show comparable average values of E and RMS (Table 4-4), it is worth noticing that the both the trends of E and of RMS associated to MultiEXCELL are more stable if compared to the results provided by the other two models. As an example, the lowest and highest values of RMS for EXCELL are 2.6% and 39.1%, whilst for MultiEXCELL the correspondent numbers are 2.7% and 31.7%. The variability of the models' prediction accuracy can be quantified by calculating the standard deviation of E (σ_E) and RMS (σ_{RMS}), which are reported in Table 4-5: while similar values are obtained for σ_E, a clear difference in σ_{RMS} emerges, which indicates that, overall, the prediction accuracy delivered by MultiEXCELL is more stable from experiment to experiment, which, in turn, provides an increased reliability to the model's users.
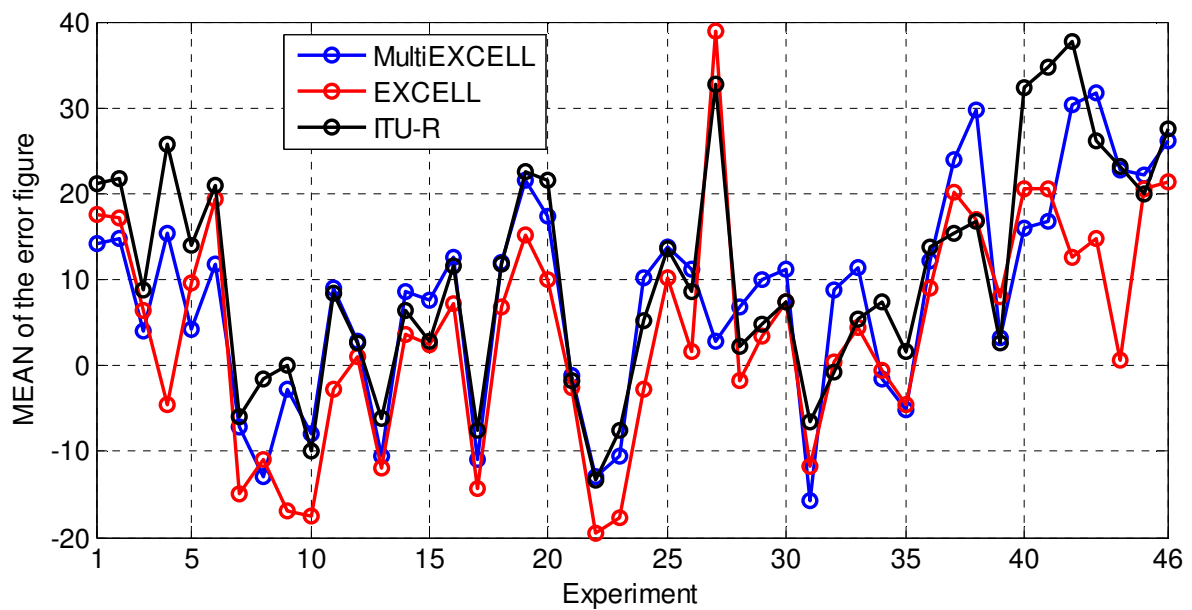
Figure 4-33. Results of the testing activity on site diversity models: mean of the error figure (E) for all the 46 selected experiments
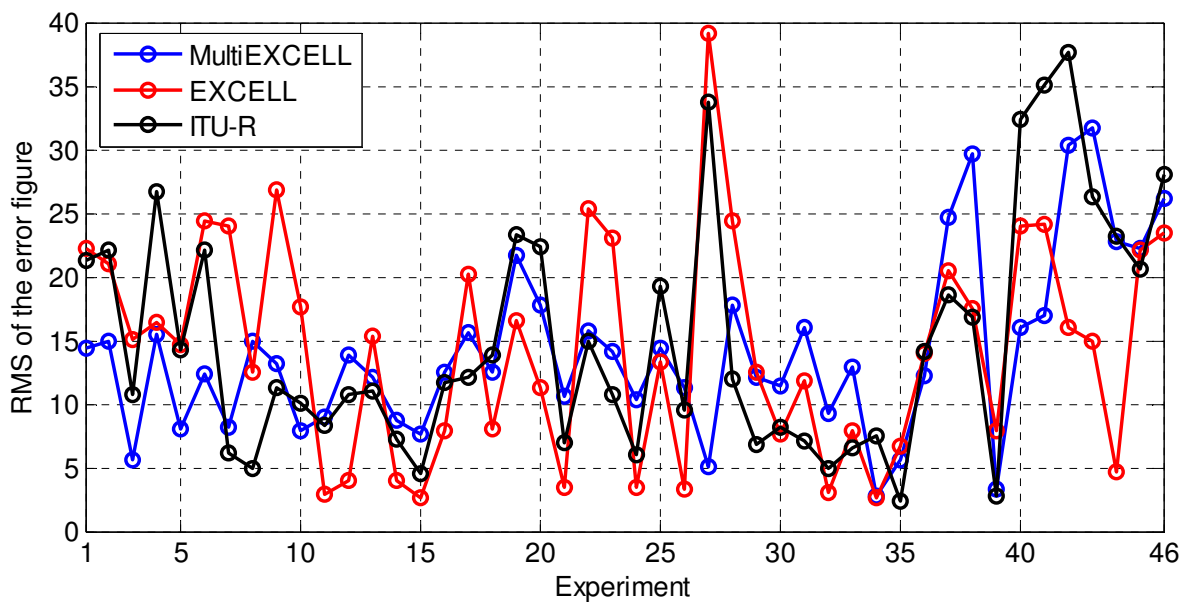
Figure 4-34. Results of the testing activity on site diversity models: root mean square of the error figure (RMS) for all the 46 selected experiments

Table 4-5. Stability of the performance of the selected site diversity models:
standard deviation of E (σ_E) and of RMS (σ_{RMS}) over all the 46 experiments

Model	σ_E	σ_{RMS}
MultiEXCELL	12.2	6.8
EXCELL	13	8.5
ITU-R P.618-10	12.9	9.2

5. SIMULATION AND PERFORMANCE EVALUATION OF SATELLITE COMMUNICATION (SATCOM) SYSTEMS

This chapter illustrates the prediction of the attenuation due to gases, clouds and rain impairing satellite communication (SatCom) systems operating at high frequency (Q/V and W bands). First the application scenario is duly defined and afterwards MultiEXCELL and SMOC (together with the ITU-R models for gases) are employed to accurately estimate the attenuation statistics due to clouds and rain, as well as the advantage originating from the implementation of site diversity schemes for the mitigation of strong fades.

5.1. Definition of the application scenario

The reference ground station is located in Rome, NY (USA) and, specifically: latitude = 43.22° N, longitude = 75.41° W, altitude h_s = 150 m a.m.s.l. . The orbital position of the geostationary satellite is 100° W, which allows a fair coverage of the whole USA territory. As a result, with reference to Figure 5-1 depicting the Earth-space link geometry, its elevation θ is 34.4° and its orientation ϕ is 146.2°.
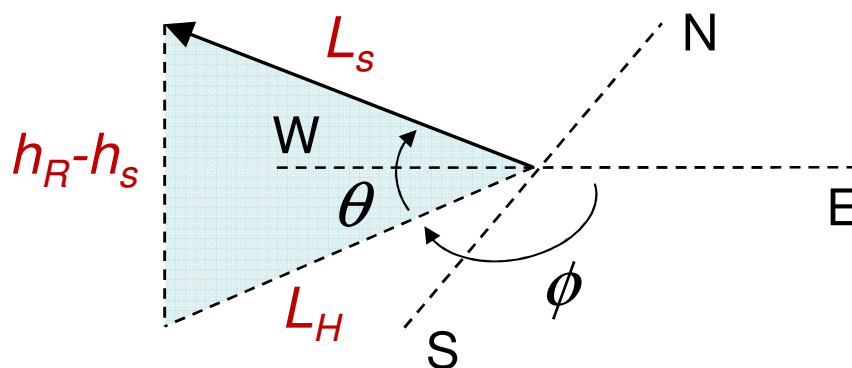
Figure 5-1. Reference geometry of the Earth-space link

In Figure 5-1, h_R is the rain height, the knowledge of which is necessary to predict rain attenuation statistics.

The reference operational frequencies have been uniformly sampled in the 50-90 GHz band, though avoiding the oxygen absorption peak which makes any Earth-space link unfeasible: therefore, the selected frequencies are 50, 70, 80 and 90 GHz. Finally, the vertical polarization angle has been chosen because it minimizes the attenuation induced by rain drops which are typically modeled as oblate spheroids elongated along the plane perpendicular to their fall direction; if no canting angle for the rain drops is considered, such plane is parallel to the ground [Paraboni et al., 2011].

Table 5-1 summarizes the main geometrical and electrical characteristics of the reference Earth-space link considered in this study.

Table 5-1. Main geometrical and electrical characteristics of the reference Earth-space link considered in this study

Reference site name	Rome, NY (USA)
Site latitude	43.22° N
Site longitude	75.41° W
Site altitude h_s	150 m a.m.s.l.
Satellite orbital position	100° W
Link elevation θ	34.4°
Link orientation ϕ	146.2°
Frequency	50, 70, 80, 90 GHz
Wave polarization	Vertical

5.2. Single-site tropospheric attenuation

5.2.1. Prediction of gaseous attenuation statistics

Thanks to their strong physical soundness and good prediction accuracy (simplified version of the Liebe's MPM93 model [Liebe et al., 1993]), the methods included in recommendations ITU-R P.676-9 [ITU-R P.676-9, 2012] have been employed to estimate the attenuation due to water vapor and oxygen impairing the reference Earth-space link.

Figure 5-2 shows the water vapor attenuation statistics for the 4 selected frequencies: since no water vapor absorption peaks are present in the Q/V and W bands, the attenuation grows monotonically with frequency: the value exceeded for 0.1% of the yearly time shifts from approximately 1.2 to 3.7 dB when moving from 50 to 90 GHz, whilst for $P = 1\%$, the attenuation ranges from 0.8 dB to 2.5 dB for the same frequencies.
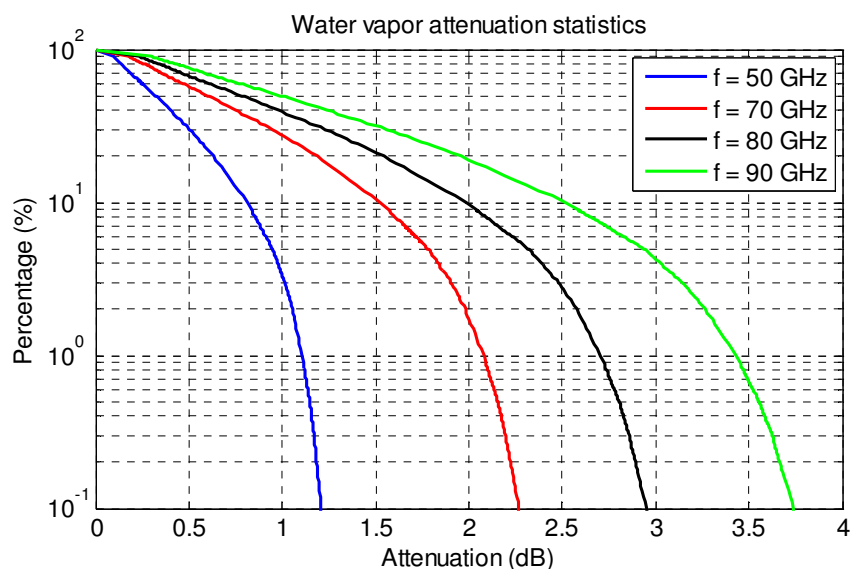
Figure 5-2. Water vapor attenuation statistics estimated according to recommendation ITU-R P.676-9

As for the oxygen attenuation, due to its very limited variability throughout the year in temperate areas, results are listed Table 5-2 in terms of oxygen attenuation values associated to the following probability levels. 1%, 50% (median) and 100% of the yearly time.

Table 5-2. Oxygen attenuation values associated to the following cumulative probability levels: 1%, 50% (median) and 100% of the yearly time

Frequency (GHz)	$P = 100\%$ (dB)	$P = 50\%$ (dB)	$P = 1\%$ (dB)
50	2.21	2.75	2.87
70	2.16	2.67	2.80
80	0.45	0.57	0.69
90	0.24	0.31	0.33

The attenuation due to oxygen prevails over the water vapor attenuation at 50 and 70 GHz (median value around 2.7 dB at both frequencies) owing to the oxygen absorption band centered at 60 GHz. Indeed, at 80 and 90 GHz, far from such a peak, the impact of oxygen is very limited (median attenuation roughly between 0.3 and 0.6 dB) and definitely less significant than the effect induced by water vapor.

As a complement of the results shown above, Figure 5-3 depicts the attenuation statistics due to both water vapor and oxygen, where the effects of the two gases have been combined using the rule included in recommendation ITU-R P.676-9 [ITU-R P.676-9, 2012] (summation of attenuation values on equiprobable basis). 70 GHz turns out to be the frequency mostly impaired by gaseous absorption (proximity to the oxygen absorption band), whilst the 80 GHz carrier appears as the most advantageous (almost at all probability levels) as far as only gases are of considered. Overall, the gaseous attenuation exceeded for 50% and 1% of the yearly time ranges from 1.25 to 2.91 dB and from 3.31 to 4.87 dB, respectively.
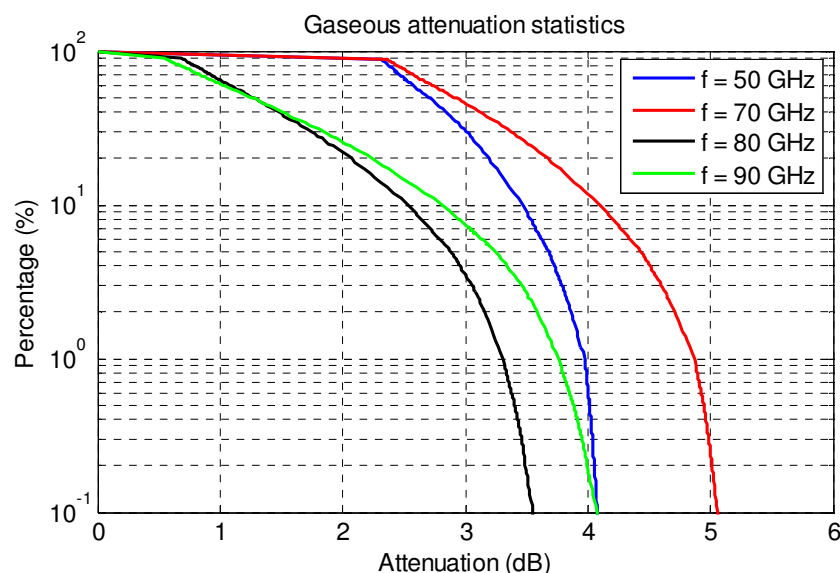
Figure 5-3. Gaseous (water vapor and oxygen) attenuation statistics estimated using recommendation ITU-R P.676-9

5.2.2.   Prediction of cloud attenuation statistics

Figure 5-4 shows the cloud attenuation CCDFs predicted by SMOC and by the model included in recommendation ITU-R P.840-5 [ITU-R P.840-5, 2012], which estimate the presence of clouds for 56% and 69% of the yearly time, respectively. Based on the test activity on cloud attenuation models, SMOC provides an overall better prediction performance with respect to the ITU-R model; indeed, as mentioned in the previous chapter, the latter is subject to an intrinsic inaccuracy when used to predict cloud attenuation in the Q/V and W bands because the reduced liquid water content used as part of the ITU-R model has been derived with reference to the 20-50 GHz range. This is clearly evident not only in the decrease in the prediction performance as the frequency increases (see previous chapter) but also in the increasing difference between the two predictions.

Besides its better accuracy, the use of SMOC removes the constraint set in the ITU-R model by the truncation, for $P \geq 1\%$, of the reduced liquid water content statistics used as input for the prediction of cloud attenuation. This truncation is introduced as part of the procedure included in recommendation ITU-R P.618-10 [ITU-R P.618-10, 2009] to combine the attenuation due to gases, clouds and rain.
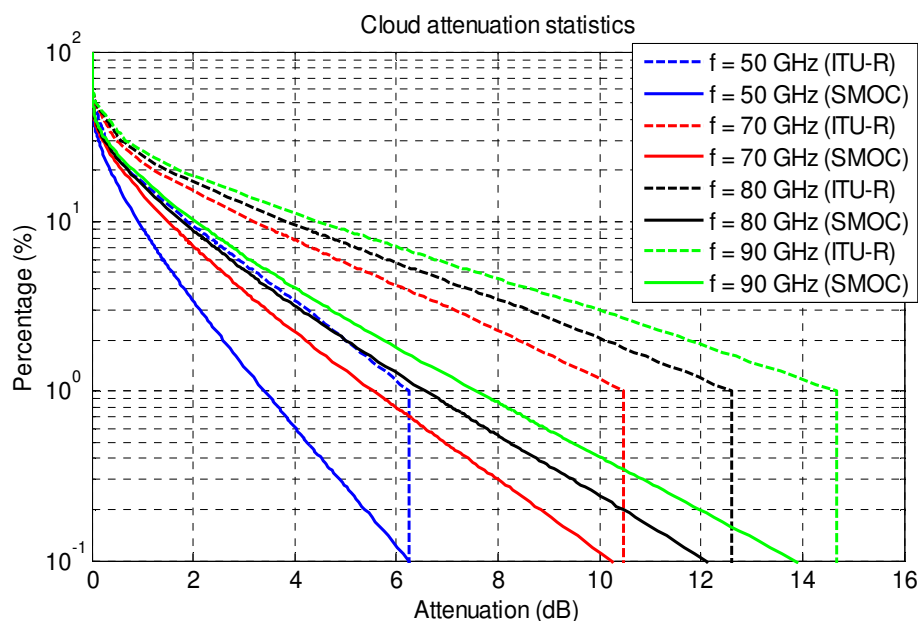
Figure 5-4. Cloud attenuation statistics estimated using SMOC and according to recommendation ITU-R P.840-5

Overall, taking as reference SMOC, clouds tend to have a higher impact than the one due to gases for all the four frequencies considered in this analysis: the cloud attenuation exceeded for 1% and 10% of the yearly time ranges between 3.41 and 7.58 dB and between 0.92 and 2.05 dB, respectively.

5.2.3.   Prediction of rain attenuation statistics

For the prediction of rain attenuation statistics, knowledge of the local 1-minute integrated rain rate CCDF, $P(R)$, is needed. Since no measured $P(R)$ is available for Rome in

this study, the local rainfall statistics have been estimated using the method included in Annex 1 of recommendation ITU-R P.837-6 [ITU-R P.837-6, 2012], which has proven to show an overall root mean square (RMS) of the relative percentage error of roughly 30% [ESA b]. As mentioned in Chapter 2, an alternative way to predict the 1-minute integrated $P(R)$ relies on models aimed at converting rainfall statistics from long (e.g. 1 hour) to short integration time T, which generally provide a considerably better accuracy than the ITU-R P.837-6 Annex 1 model [Emiliani et al., 2010]. Here, the EXCELL RSC model [Capsoni and Luini, 2009], showing a good prediction performance (RMS around 15%) and now adopted by ITU-R in Annex 3 of recommendation P.837-6, has been used to estimate the 1-minute integrated $P(R)$ starting from the 1-hour integrated rain rate time series collected in Fulton, NY, approximately 80 km far from Rome (see Figure 5-5). These rainfall data have been measured for 12 years (2000-2011) using a raingauge deployed by the National Centers for Environmental Prediction (NCEP). Being the distance between the two sites quite limited, the long-term $P(R)$ (as a rule of thumb, at least 10 years) measured in Fulton and in Rome are likely to be quite similar on the basis of the quasi-ergodicity of the rain field, whose validity, however, is also dependent on the orography and topography of the area.
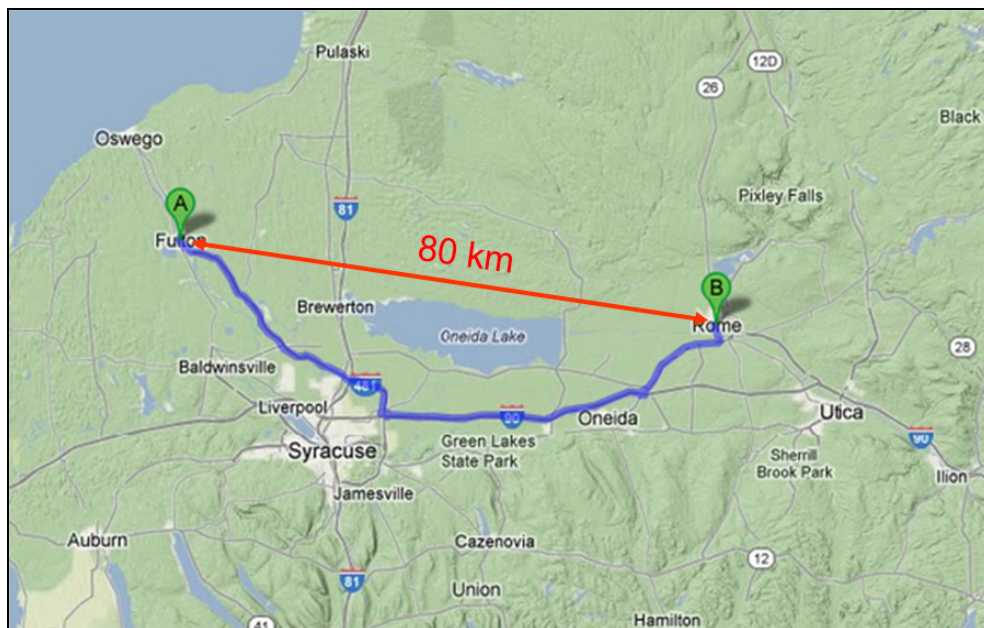
Figure 5-5. Rome and Fulton, site of the NCEP meteorological station whose 1-hour integrated rainfall data have been used as input to EXCELL RSC

Figure 5-6 depicts the $P(R)$ predicted using the two methods mentioned above: the good agreement between the two curves (the maximum difference between them is around 5 mm/h) definitely adds confidence to their use for rain attenuation prediction.
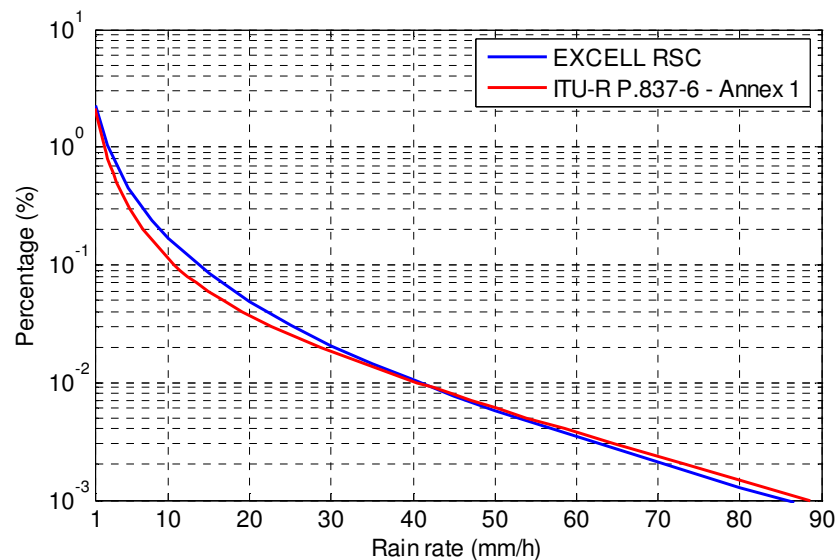
Figure 5-6. Rain statistics for Rome, NY: comparison between predictions obtained from recommendation ITU-R P.837-6 (Annex 1) and EXCELL RSC (input data derived from the NCEP raingauge located in Fulton, NY)

In this study, MultiEXCELL and the ITU-R model included in recommendation P.618-10 [ITU-R P.618-10, 2009] have been employed to estimate the rain attenuation affecting the station in Rome. The former was chosen because of its physical soundness, its good accuracy (as shown in the previous chapter) and for consistency in its use also to evaluate the performance of site diversity schemes (section 5.3); the latter has been selected as reference.

For the practical application of the two models, the $P(R)$ derived from recommendation ITU-R P.837-6 has been used, whilst the rain height has been estimated using recommendation ITU-R P.839-3 [ITU-R P.839-3, 2001], which yields h_R = 3.491 + 0.36 = 3.851 km. As for the calculation of the specific attenuation due to rain $\gamma = kR^{\alpha}$, k and α have been derived from recommendation ITU-R P. 838-3 [ITU-R P.838-3, 2005] for both models; their values are listed in Table 5-3 for the four frequencies and according to the other parameters of the link reported in Table 5-1, namely linear vertical polarization and elevation angle equal to 34.4°. Indeed, marked differences in the specific rain attenuation come from the variation of the Drop Size Distribution (DSD) which may occur from event to event and, sometimes, also during the same event. This issue has to be considered when applying instantaneous frequency scaling algorithms in ULPC (Up Link Power Control) mitigation techniques. On the other hand, for the prediction of local rain attenuation statistics, it is convenient to make reference to the k and α coefficients proposed in ITU-R recommendation P.838-3 in order to avoid confusion. Nevertheless, it is worth stressing that the above figures originate from a best fit procedure and their full appropriateness for the W band is still to be verified.

Figure 5-7 and Figure 5-8 depict the rain attenuation statistics estimated using MultiEXCELL and the ITU-R model, respectively. As expected, both models predict an increase in the attenuation due to rain with frequency, which is more marked in the lower

portion of the considered band (for $P = 10\times^{-2}\%$, the attenuation difference is 17 and 8.5 dB moving from 50 to 70 GHz and from 70 to 90 GHz, respectively).

Table 5-3. Values of the k and a coefficients extracted from recommendation ITU-R P.838-3 for the prediction of rain attenuation statistics

Frequency (GHz)	k	α
50	0.6492	0.7906
70	1.0263	0.7236
80	1.1674	0.7036
90	1.2797	0.6887
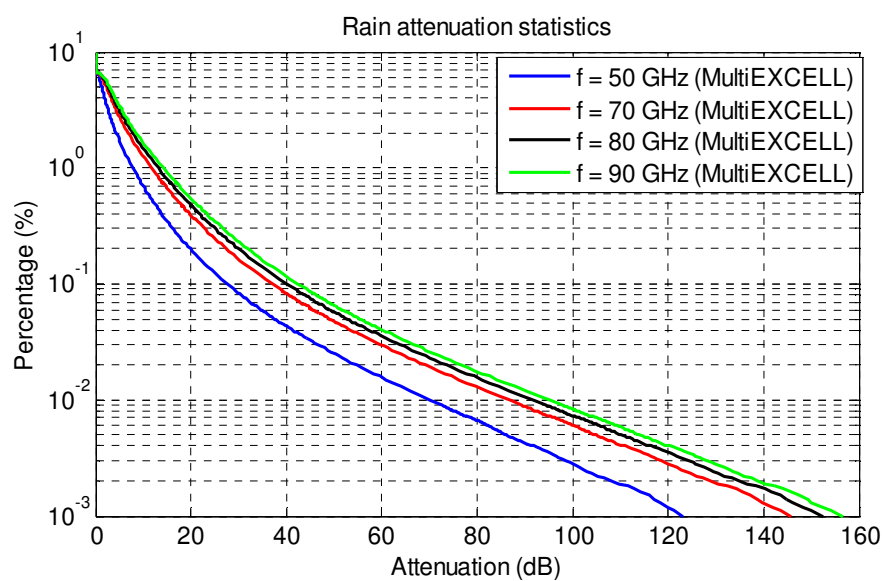
Figure 5-7. Prediction of rain attenuation statistics using MultiEXCELL
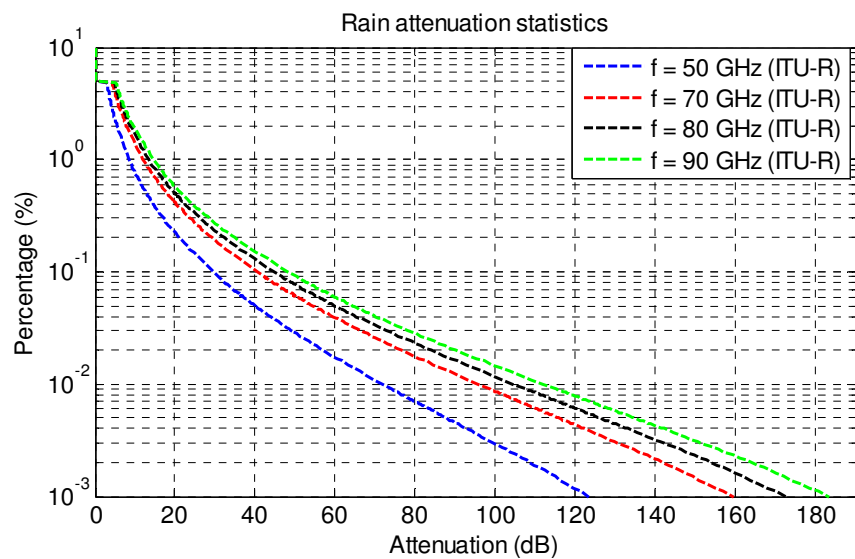
Figure 5-8. Prediction of rain attenuation statistics using recommendation ITU-R P.618-10

Distribution A: Approved for public release; distribution is unlimited.

The results predicted by the two models can be more conveniently compared looking at the curves in Figure 5-9, where the four frequencies are reported separately.
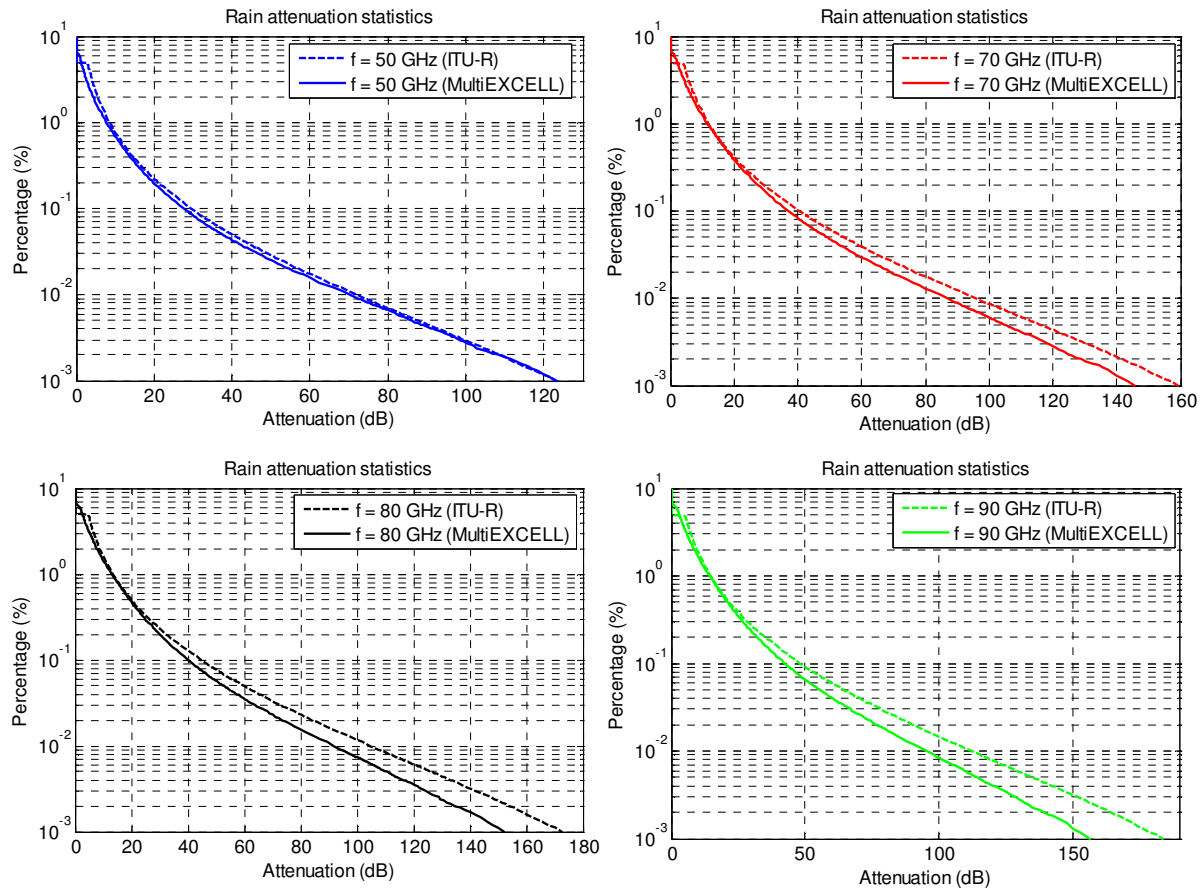
Figure 5-9. Prediction of rain attenuation statistics: comparison between MultiEXCELL and recommendation ITU-R P.618-10

The first difference between the two models emerges in the low attenuation range: the probability to have rain attenuation in an average year as predicted by MultiEXCELL is approximately 7%, whilst the same information cannot be obtained from the ITU-R model, whose validity is limited to probability values ranging between 10^{-3}% and 5%. Whilst the curves predicted by the two models are in good agreement for $f = 50$ GHz, the ITU-R model tends to predict more and more attenuation than MultiEXCELL as the frequency increases: as a reference, for $P = 10\times^{-2}$%, the percentage difference between the two models ranges from 10% to 17% shifting from 70 to 90 GHz, whilst it is only 3% at 50 GHz. This behavior is likely linked to the marked frequency dependence of the empirical components of the ITU-R model, whose effects can be all included in the *adjustment factor* (*AF*) contained in (5-1) (refer to section 4.1.5):

$$A(P) = k \, R_{0.01}^{\alpha} \, L_s \, AF(P, f) \quad (\%) \tag{5-1}$$

where $R_{0.01}$ and $A(P)$ are the rain rate and path attenuation values exceeded for 0.01% and P% of the time in a year, respectively, whilst L_s is the slant path of the link; $AF(P,f)$ is the

frequency dependent adjustment factor introduced to empirically take into account the horizontal and vertical variability of the rain rate, as well as to relate the shape of the $P(A)$ to $R_{0.01}$. Figure 5-10, extracted from [Brost and Cook, 2012], clearly indicates a significant increase of $AF(0.01\%,f)$ with frequency for the ITU-R model, especially if compared to the adjustment factors of other empirical models proposed in the literature. Indeed it is worth underlining that, because of the limited set of measurements available, which was used both to derive $AF(P,f)$ and to test the models' accuracy, the applicability of the method included in ITU-R P.618-10 is recommended for frequencies lower than 55 GHz.
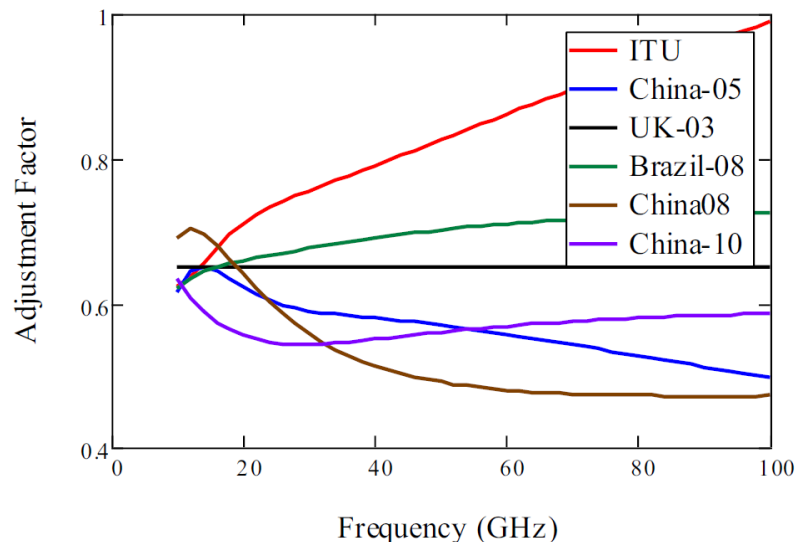
Figure 5-10. Trend of the adjustment factor with frequency for various empirical prediction models available in the literature

5.2.4. Prediction of total attenuation statistics

Figure 5-11 and Figure 5-12 show the total attenuation statistics estimated according to two different procedures. In the former case (procedure A), ITU-R recommendations have been used for all the constituents (P.676-9 for gases, 840-5 for clouds and 618-10 for rain), whilst in the latter case (procedure B) recommendation ITU-R P.676-9 has been combined with SMOC and MultiEXCELL for the prediction of the attenuation due to gases, clouds and rain, respectively. In both cases, total attenuation statistics A_T have been obtained by applying the following formulation adopted in recommendation ITU-R P.618-10:

$$A_T(P) = A_R(P) + A_C(P) + A_G(P) \quad (\%) \tag{5-2}$$

In (5-2), subscripts R, C, G refer respectively to rain, clouds and gases, and all the contributions are added on equiprobable basis.

Figure 5-13 allows a convenient comparison between the two models by showing separately the predictions for the four different frequencies. In both cases, it is possible to identify an irregularity in the curves associated to the statistics of rain attenuation: in the case of MultiEXCELL this point corresponds to the probability of having rain attenuation in the site (around 7%), whilst, for the ITU-R model, a more marked discontinuity occurs for $P = 5\%$ due to the truncation of the predicted curve. Whatever the exceedance probability

level considered, as expected from Figure 5-4 and Figure 5-9, the total attenuation statistics estimated using procedure A are always higher than those predicted according to procedure B.
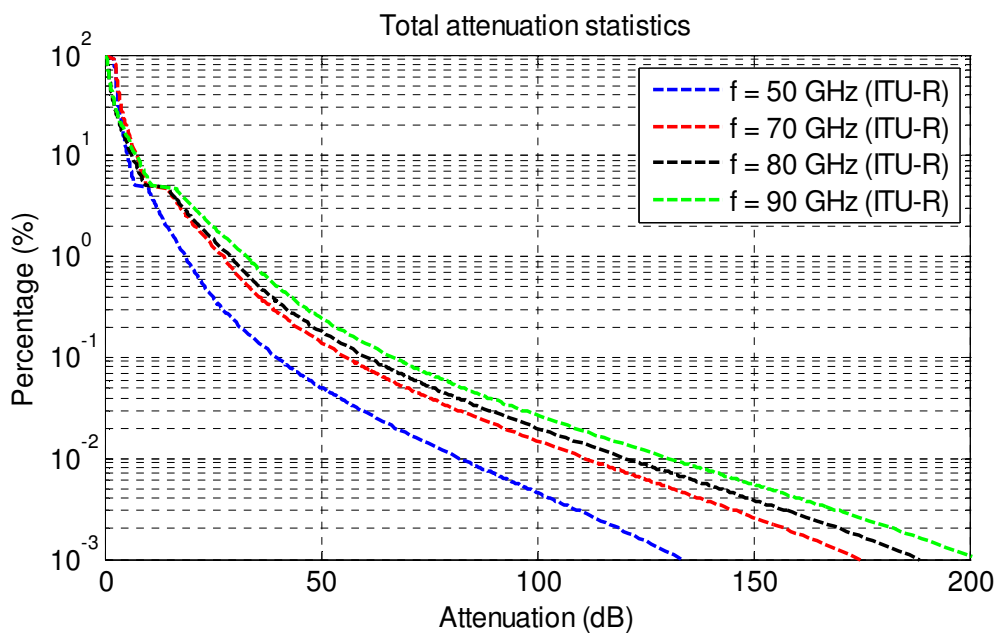
Figure 5-11. Prediction of total attenuation statistics using ITU-R recommendations for all constituents
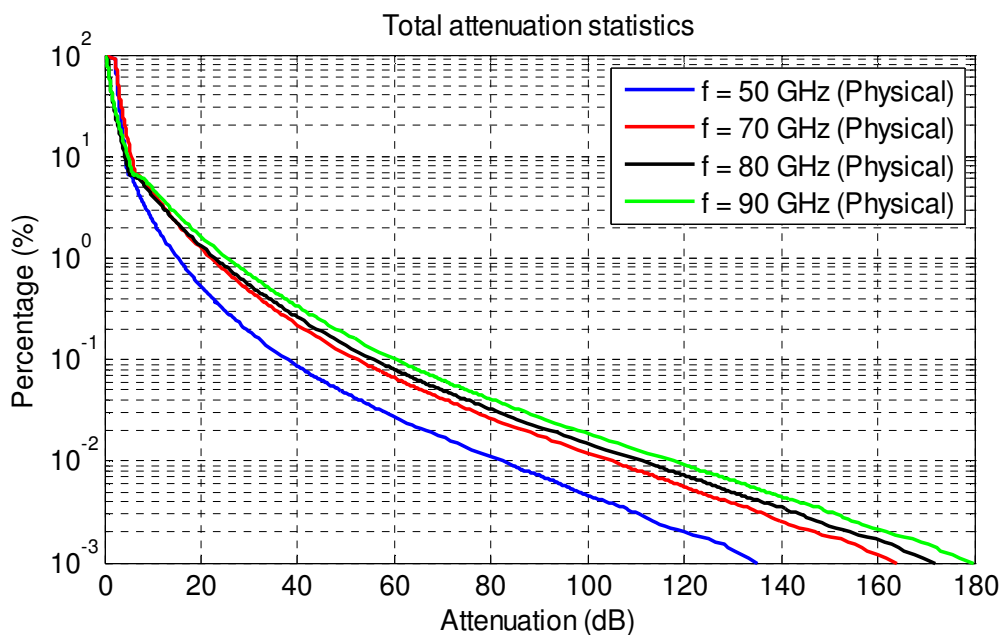
Figure 5-12. Prediction of total attenuation statistics using ITU-R recommendations for gases, SMOC for clouds and MultiEXCELL for rain

Making reference to the results obtained from procedure B, a system margin equal to 82, 105, 111 and 118 dB would be required to guarantee the system availability for 99.99% of the time in a year using f = 50, 70, 80 and 90 GHz, respectively. Obviously such margins cannot

be achieved: as shown in the next sections, a viable way to overcome this limitation is to adopt site diversity schemes, which, notwithstanding their increased complexity, require much more limited power margins to achieve the desired quality of service also in high-availability systems.
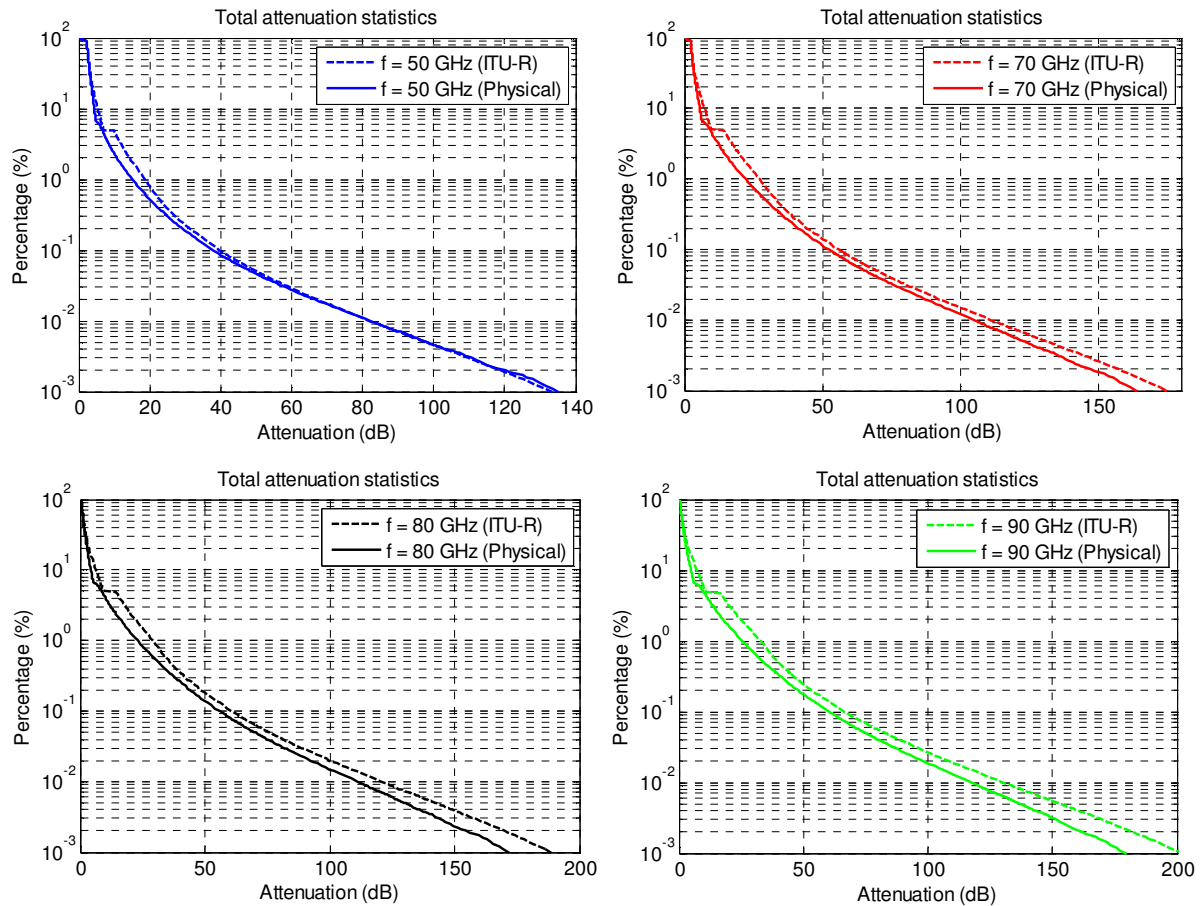
Figure 5-13. Prediction of total attenuation statistics: comparison between procedure A and procedure B

5.3. Site diversity (rain)

Site diversity schemes represent an extremely effective solution in the mitigation of the fades due to rain, especially at high operational frequencies as those considered in this study. In this section, MultiEXCELL has been applied to investigate and quantify the advantages of implementing site diversity for a system deployed in the area of Rome. This model has been chosen not only in the light of the good accuracy shown in the testing activity performed in the previous chapter, but also because it allows to easily implement schemes involving more than two stations. Indeed, the two reference schemes shown in Figure 5-14 have been investigated (*D* is the site separation distance; master and slave links are depicted in green and red, respectively):

- *Scheme A*: it combines the results obtained separately by using the horizontal and the vertical baselines to increase the statistical significance; in fact, due to the isotropy of the

rain maps generated by MultiEXCELL, no differences are expected in the results relative to the two baselines, except for the very short distances between the stations, for which the orientation of the link (with respect to the chosen baseline) plays an important role (the lower is the angle between the baseline and the link direction, the lower is the gain).

- *Scheme B*: it takes advantage of three stations to increase even more the benefit coming from the implementation of the diversity concept; the lowest attenuation value simultaneously experienced in the three sites is always selected to produce the joint attenuation distribution. Although more complex and expensive than scheme A, it is anyway worthwhile evaluating the increase in the gain achievable by using scheme B.

It is clear that any scheme with arbitrary number and topology of the stations can be easily implemented using MultiEXCELL. In both schemes A and B, the distance between the stations spans from 2 to 82 km with 4-km increments and, before calculating the site diversity gain according to (4-91), the single- and joint-site CCDFs of rain attenuation have been combined (according to (5-2)) with the CCDFs of gaseous and cloud attenuation respectively predicted using recommendation ITU-R P.676-9 and SMOC. This choice obviously introduces an approximation in the predicted diversity system gain (though less and less marked as the reference probability level decreases, i.e. for high-availability systems) but, on the other side, makes the results more interesting for system planning.

Figure 5-15, Figure 5-16, Figure 5-17 and Figure 5-18 show the results obtained for 50, 70, 80 and 90 GHz, respectively: the top graph reports the single-site CCDF of total attenuation (blue), as well as the joint curves relative to scheme A (red) and scheme B (green) for the largest separation distance considered (D = 82 km). The bottom side of the figure shows the trend with distance of the site diversity gain for scheme A (left) and scheme B (right). Curves are depicted for different reference attenuation levels A_s starting from 10 dB with a progressive increment of 20 dB; such values are indicated by the vertical black dashed lines in the top graph, whilst the horizontal ones (same probability level) identify on the single- and joint-site CCDFs the attenuation values used for the calculation of the site diversity gain. Values of A_s have been chosen to so as to span the whole range of outage probability (the correspondent legend lies on the right of the top graph), i.e. considering both high- and low-availability systems; also extremely high values of A_s have been selected (e.g. 130 dB at 50 GHz) because they correspond to much lower power margins when taking advantage of the site diversity concept (e.g. 25 dB at 50 GHz for scheme A).
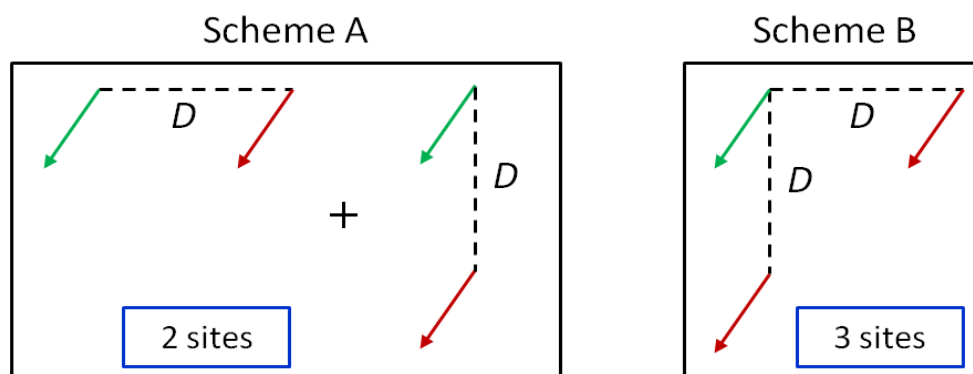
Figure 5-14. Reference site diversity schemes considered
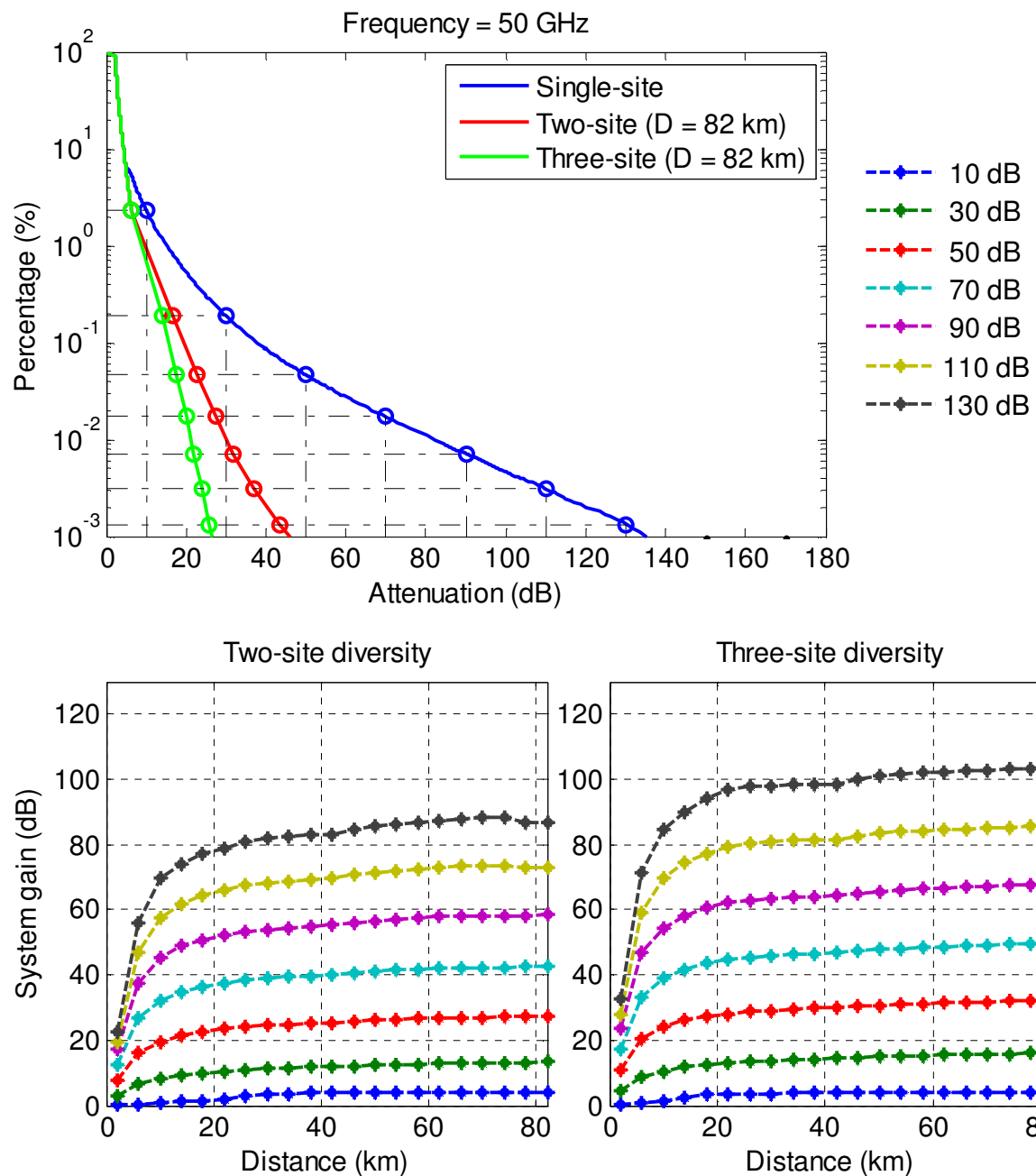
Figure 5-15. Prediction of the advantage in implementing site diversity in Rome for a system operating at 50 GHz. Top side: single- and joint-site (schemes A and B) CCDFs of total attenuation for the largest separation distance (D = 82 km); bottom side: site diversity gain for schemes A (left) and B (right)
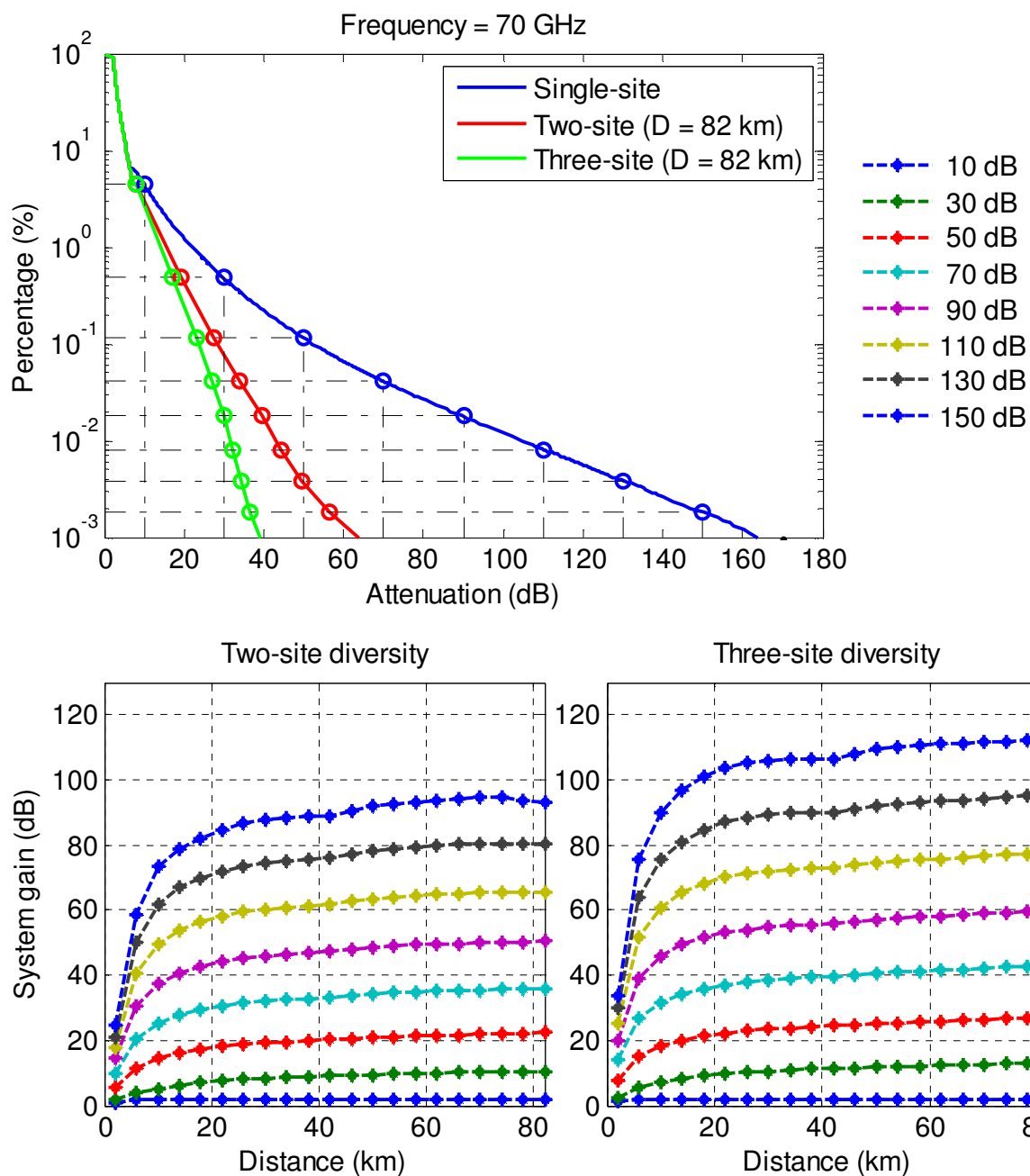
Figure 5-16. Prediction of the advantage in implementing site diversity in Rome for a system operating at 70 GHz. Top side: single- and joint-site (schemes A and B) CCDFs of total attenuation for the largest separation distance (D = 82 km); bottom side: site diversity gain for schemes A (left) and B (right)
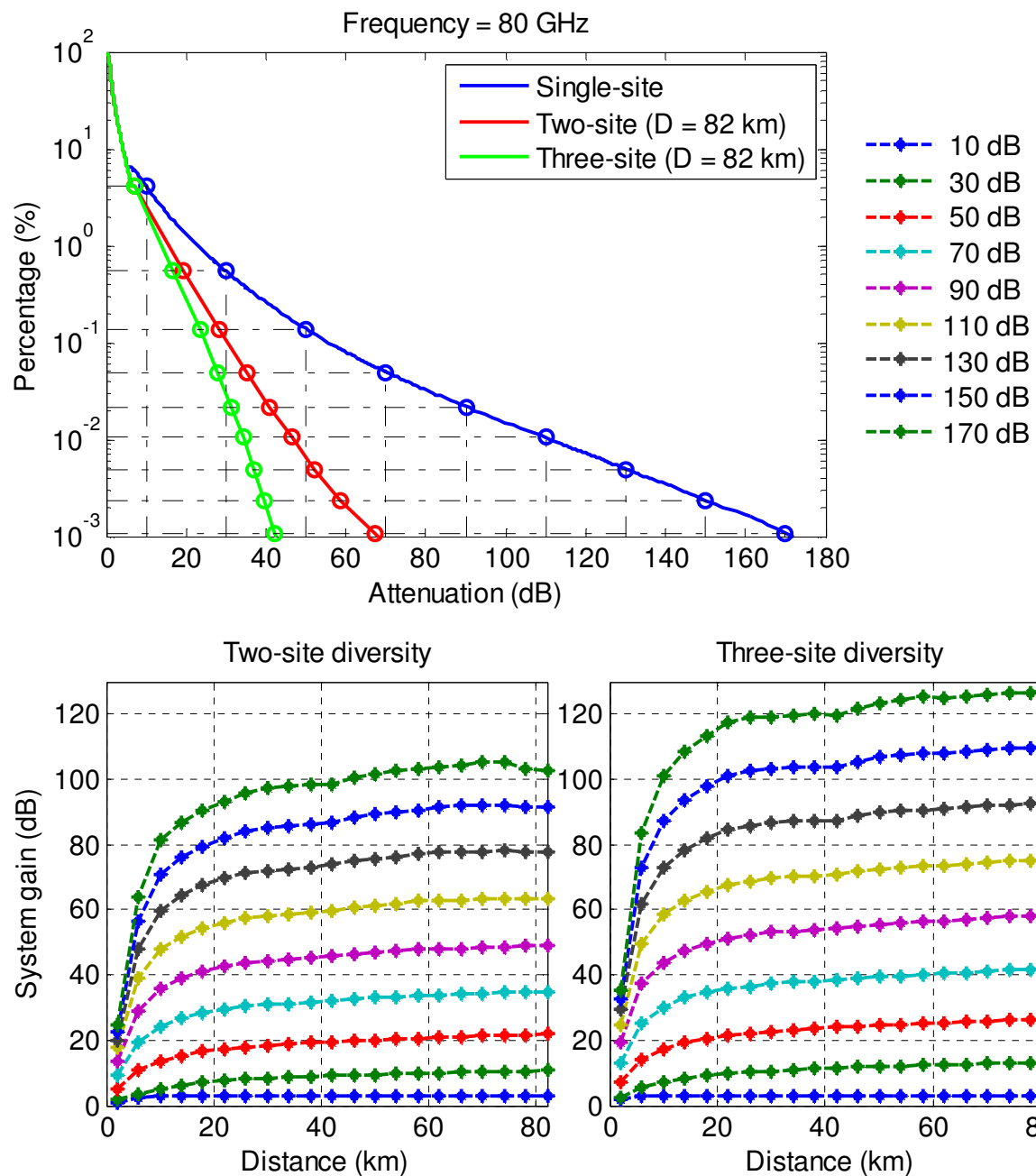
Figure 5-17. Prediction of the advantage in implementing site diversity in Rome for a system operating at 80 GHz. Top side: single- and joint-site (schemes A and B) CCDFs of total attenuation for the largest separation distance (D = 82 km); bottom side: site diversity gain for schemes A (left) and B (right)
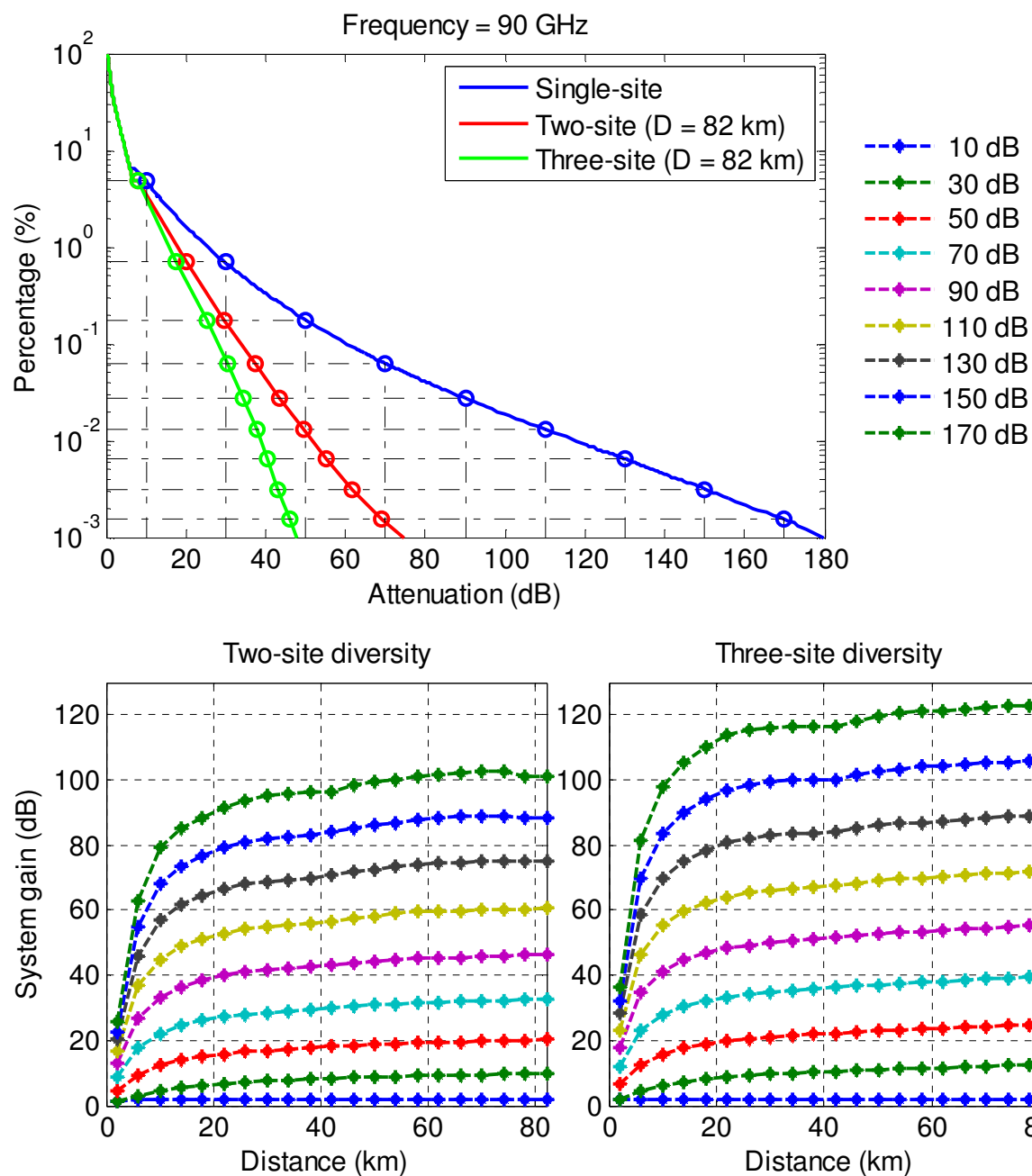
Figure 5-18. Prediction of the advantage in implementing site diversity in Rome for a system operating at 90 GHz. Top side: single- and joint-site (schemes A and B) CCDFs of total attenuation for the largest separation distance (D = 82 km); bottom side: site diversity gain for schemes A (left) and B (right)

Results clearly indicate the effectiveness of site diversity in mitigating rain attenuation. On the average, considering low outage probabilities (roughly 0.01%) for which the reduction in the attenuation is more needed, approximately 60%-65% of the attenuation can be compensated using two stations, whilst this percentage increases to 70%-75% in the case of three stations. The increase in the gain with distance is quite steep for separation distances approximately lower than 20 km, after which the gain tends to stabilize. This effect is expected and it is tightly linked to the decorrelation characterizing rain fields, which is particularly fast in the first 15-20 km [Luini and Capsoni, 2012c]. As expected, for the same probability level, the gain increases with frequency but so does the rain attenuation as well, such that the required margin increases in the site diversity configurations as well. Overall, taking as reference a maximum power margin of 40 dB, a two-site diversity system would experience outage for 2.1×10^{-3}% and 4.4×10^{-2}% of the time in a year at 50 and 90 GHz respectively, whilst the yearly outage time would be lower than 10^{-3}% at 50 GHz and would reduce to 7.1×10^{-3}% at 90 GHz. Table 5-4 and Table 5-5 provide, for schemes A and B respectively, more comprehensive information on the outage time expected for different power margins.

Table 5-4. Outage probability for given power margins using a two-site diversity scheme (A)

	Power margin (scheme A)		
	30 dB	**35 dB**	**40 dB**
f = 50 GHz	10^{-2}%	4.2×10^{-3}%	2.1×10^{-3}%
f = 70 GHz	7.9×10^{-2}%	3.5×10^{-2}%	1.6×10^{-2}%
f = 80 GHz	10^{-1}%	5×10^{-2}%	2.5×10^{-2}%
f = 90 GHz	1.7×10^{-1}%	8.5×10^{-2}%	4.4×10^{-2}

Table 5-5. Outage probability for given power margins using a three-site diversity scheme (B)

	Power margin (scheme B)		
	30 dB	**35 dB**	**40 dB**
f = 50 GHz	$< 10^{-3}$%	$< 10^{-3}$%	$< 10^{-3}$%
f = 70 GHz	1.9×10^{-2}%	3.2×10^{-3}%	$< 10^{-3}$%
f = 80 GHz	3.1×10^{-2}%	8.7×10^{-3}%	1.9×10^{-3}%
f = 90 GHz	6.8×10^{-2}%	2.4×10^{-2}%	7.1×10^{-3}%

5.4.　　Site diversity (cloud)

In the Q/V and W bands clouds play an important role in the determination of the power margin required for proper system planning and operation. As a consequence, besides accurately predicting the CCDF of cloud fade, it is also worth quantifying the benefit of site diversity originating from the spatial inhomogeneity of clouds. Indeed, whilst for high availability systems the implementation of site diversity is crucial for the feasibility of the system itself, at high outage probabilities (e.g. *P* approximately higher than > 1%), for which

light rain (or no rain at all) is typically expected in temperate climate, site diversity allows to increase the quality of service (QoS).

In this section the site diversity gain associated to clouds has been estimated by exploiting the spatially-correlated fields of total liquid water content synthesized by SMOC. The prediction of single- and joint-site cloud attenuation curves is achieved following the same procedure defined for MultiEXCELL (movement of the site diversity scheme across each of the synthetic maps) but obviously using the method described in section 4.3.2 to estimate the attenuation due to clouds impairing each of the links. In addition, similarly to the solution adopted in the previous section, the single- and joint-site CCDF of cloud attenuation have been combined (according to (5-2)) with the CCDF of gaseous attenuation predicted using recommendation ITU-R P.676-9. The distance between the stations spans from 2 to 102 km with 4-km increments. Also in this case the two schemes depicted in Figure 5-14 (two or three stations) have been taken into account in evaluating the diversity performance.

Figure 5-19, Figure 5-20, Figure 5-21 and Figure 5-22 show the results obtained for 50, 70, 80 and 90 GHz, respectively: the top graph reports the single-site CCDF of the attenuation due to clouds plus gases in blue, as well as the joint curves relative to the two-site (red) and three-site (green) diversity schemes (scheme A and scheme B in Figure 5-14, respectively) for the largest separation distance considered ($D = 102$ km). The bottom side of the figures shows the trend with distance of the site diversity gain (scheme A on the left, scheme B on the right). Curves are depicted for different reference attenuation levels A_s with a progressive increment of 1 dB (the correspondent legend lies on the right of the top graph); such values are indicated by the vertical black dashed lines in the top graph, whilst the horizontal ones (same probability level) identify on the single- and joint-site CCDFs the attenuation values used for the calculation of the site diversity gain. Only A_s values associated to outage probabilities higher than 1% have been considered because for $P < 1\%$ the effects of rain definitely prevails on those caused by clouds and gases.
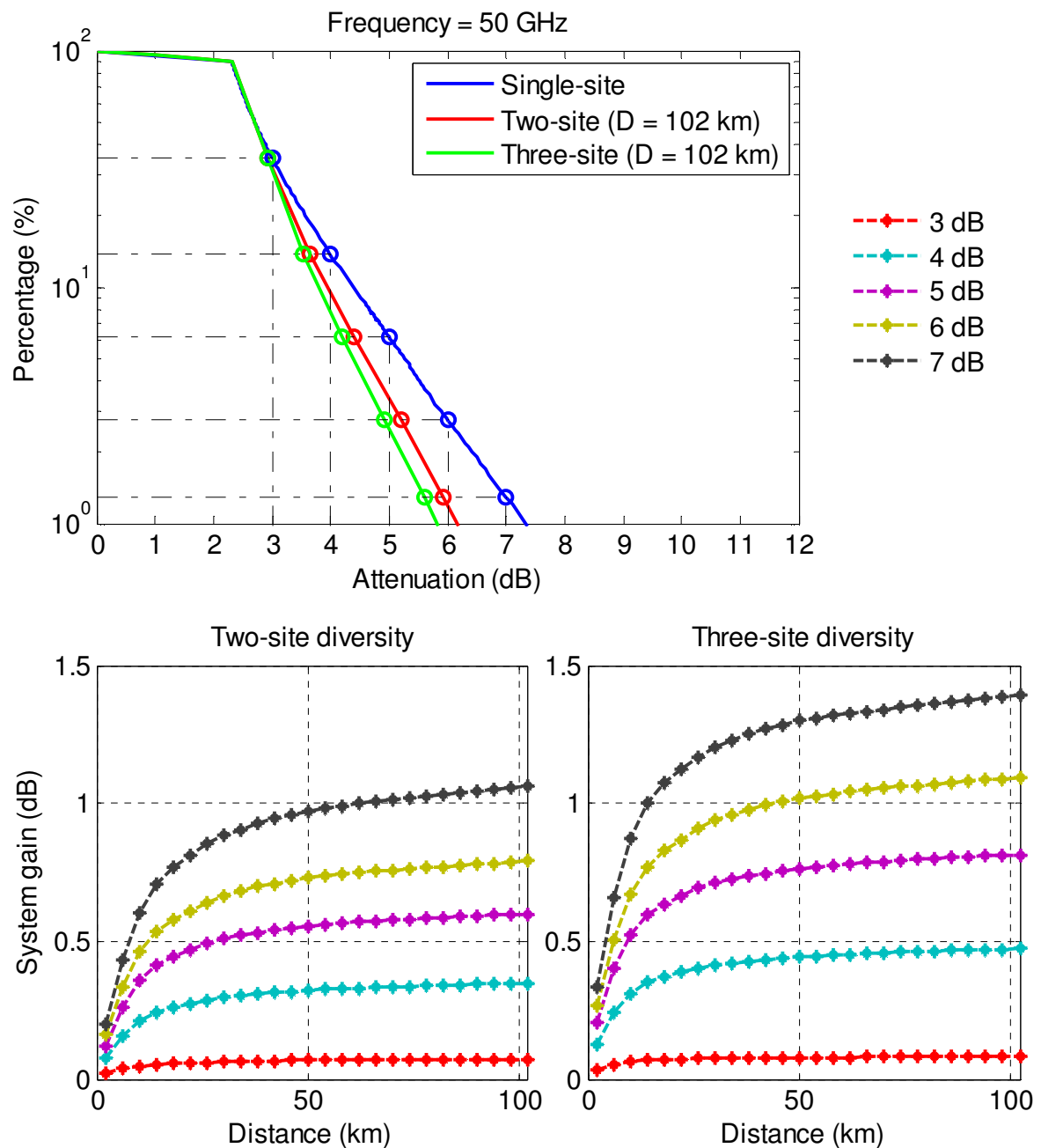
Figure 5-19. Prediction of the site diversity advantage associated to the inhomogeneity of clouds for a system operating at 50 GHz. Top side: single- and joint-site CCDFs of the attenuation due to clouds plus gases for the largest separation distance (D = 102 km); bottom side: site diversity gain (scheme A on the left, scheme B on the right)
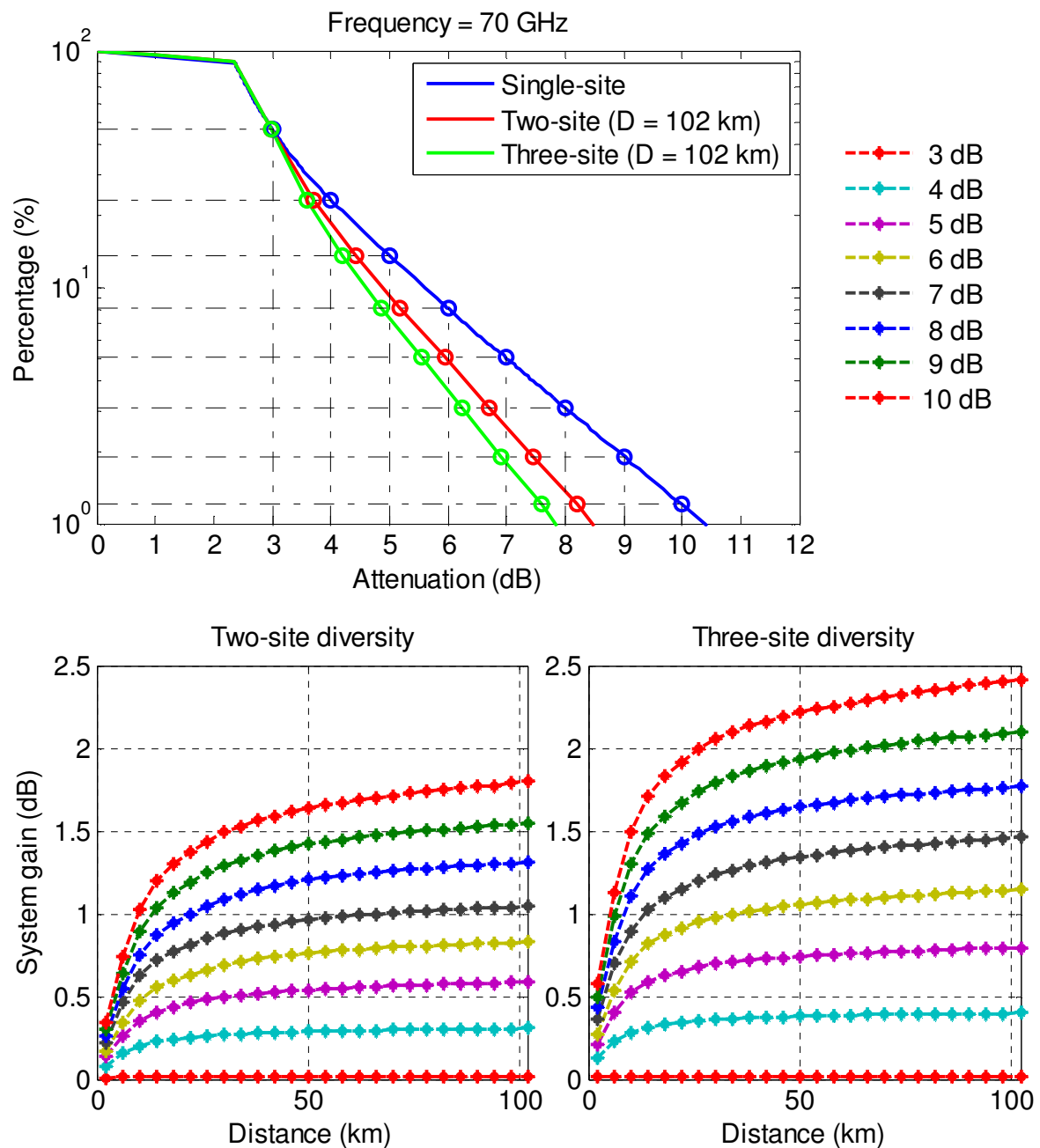
Figure 5-20. Prediction of the site diversity advantage associated to the inhomogeneity of clouds for a system operating at 70 GHz. Top side: single- and joint-site CCDFs of the attenuation due to clouds plus gases for the largest separation distance (D = 102 km); bottom side: site diversity gain (scheme A on the left, scheme B on the right)
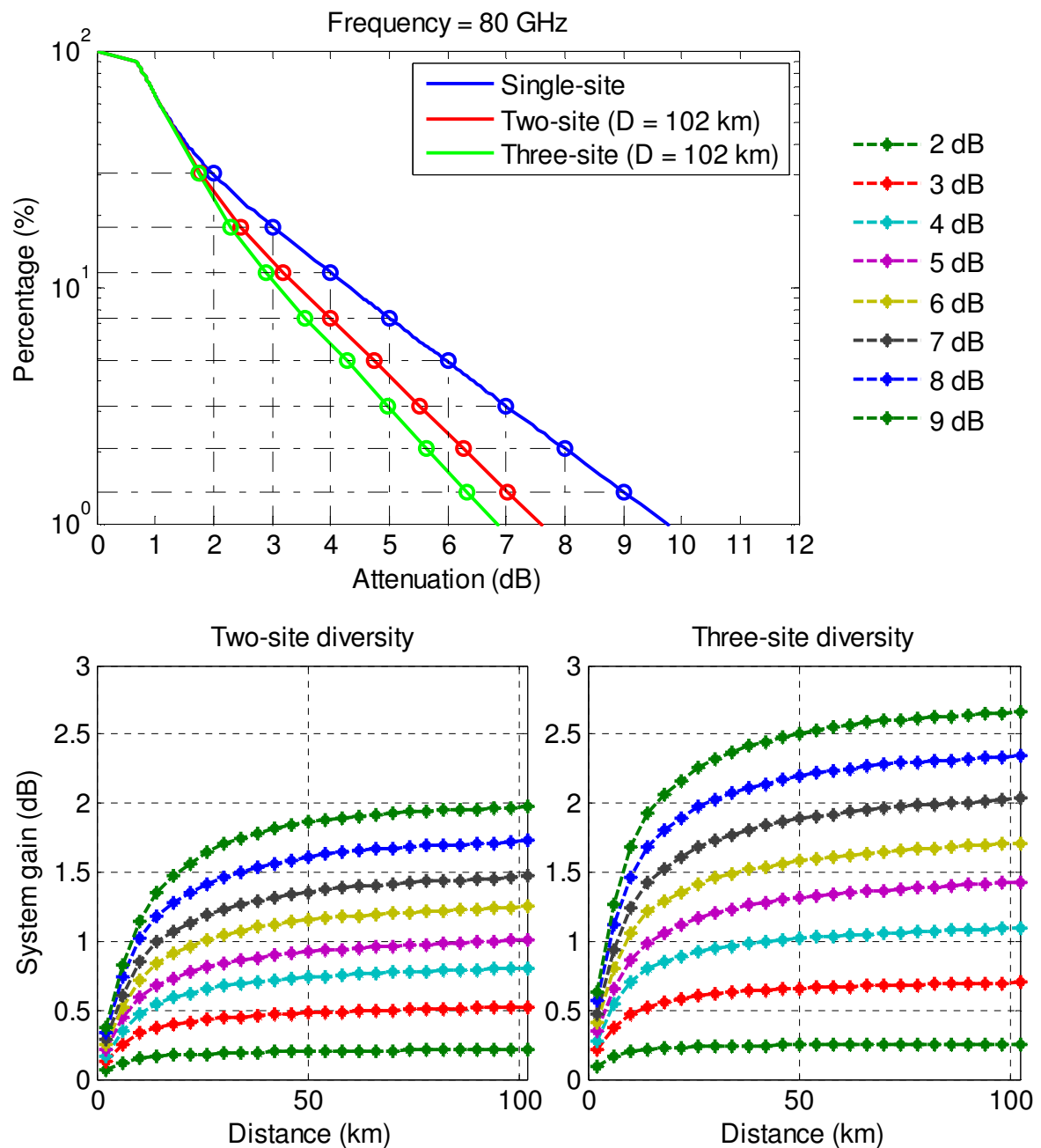
Figure 5-21. Prediction of the site diversity advantage associated to the inhomogeneity of clouds for a system operating at 80 GHz. Top side: single- and joint-site CCDFs of the attenuation due to clouds plus gases for the largest separation distance (D = 102 km); bottom side: site diversity gain (scheme A on the left, scheme B on the right)
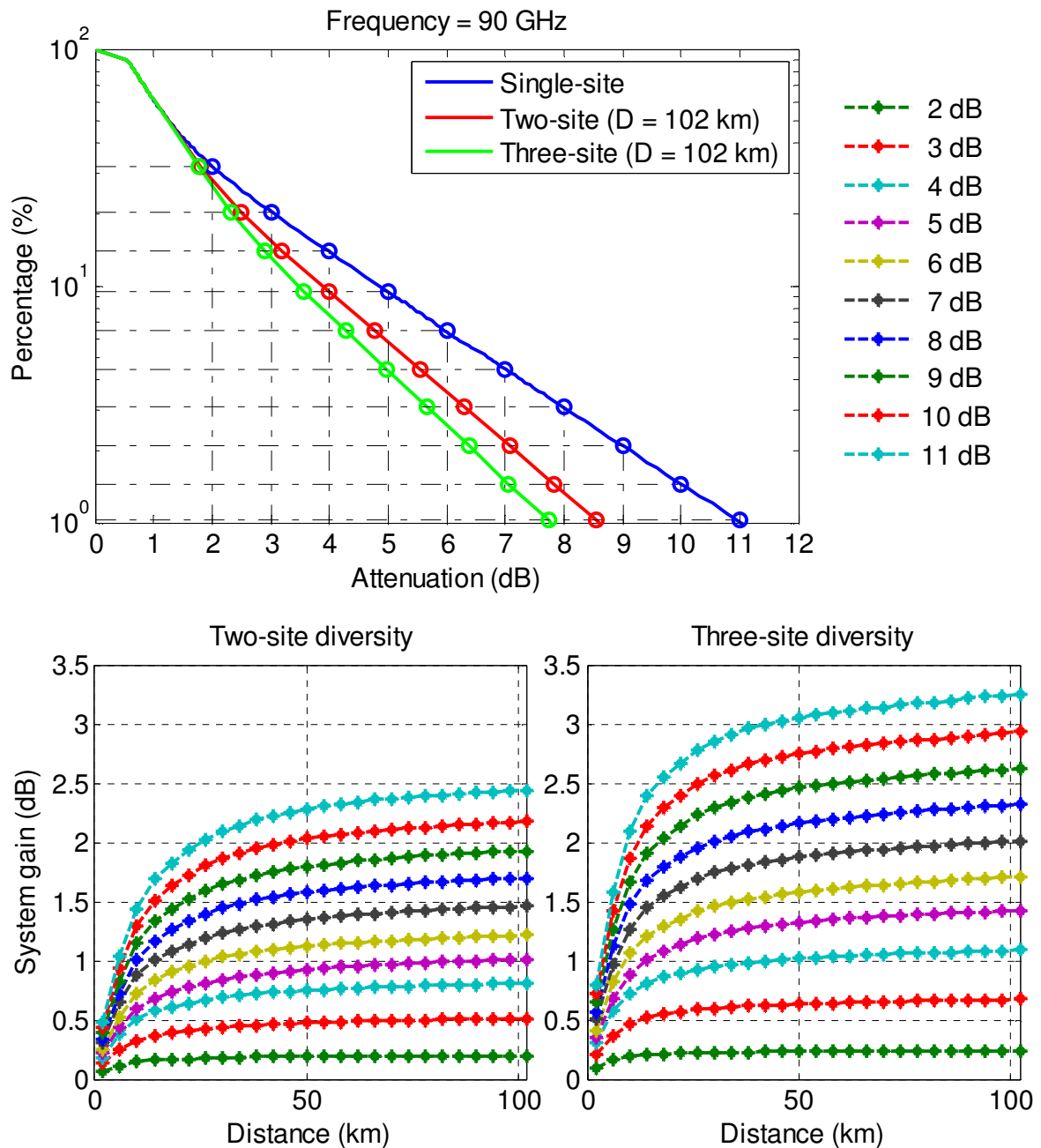
Figure 5-22. Prediction of the site diversity advantage associated to the inhomogeneity of clouds for a system operating at 90 GHz. Top side: single- and joint-site CCDFs of the attenuation due to clouds plus gases for the largest separation distance (D = 102 km); bottom side: site diversity gain (scheme A on the left, scheme B on the right)

Results clearly indicate that the effectiveness of site diversity in mitigating cloud attenuation is rather limited, especially if compared to the results included in the previous section. On the average, considering probability levels close to 5% (light rain/no rain), only approximately 12% and 17% of the attenuation can be compensated using respectively two and three stations at 50 GHz, whilst this percentage increases to roughly 20% and 28% in the two cases at 90 GHz. On the other hand, a considerable advantage is achieved shifting from two to three stations: the percentage increase in the gain ranges between 40% and 50% (D approximately higher than 40 km) when focusing mainly on the effects of clouds, whilst results in the previous section shows that such an increase is limited to 20%-30% for outage probabilities mainly affected by rain.

The increase in the gain with distance is less steep than the one associated to the inhomogeneity of rain: the fastest increase in G is found approximately for distances up to 40 km, after which the increase is slower and tends to stability around 80 km. This trend is in clear relationship with the spatial distribution of clouds which, as shown in Figure 3-21, preserve a non negligible correlation even for high separation distances (e.g. $\rho \approx 0.4$ for $D \approx 100$ km), especially if compared to rain fields (e.g. $\rho \approx 0.15$ for $D \approx 100$ km). Figure 3-21 also clearly shows that the decorrelation of the cloud liquid water content with distance is not as steep as the one of rain rate, which explains the slower increase in G with D.

As for rain, for the same probability level, the gain increases with frequency and with A_s. Overall, the maximum gain range (i.e. for $P \approx 1\%$) in the 50-90 GHz is 1.06-2.45 dB and 1.4-3.25 dB for scheme A and B, respectively: although the gain originating from the spatial inhomogeneity of clouds is not as high as the one associated with rain, nevertheless it would allow to further increase the already high QoS (data rate) typically achievable in nonrainy conditions.

6. CONCLUSIONS

This study assessed the feasibility and the performance of a SatCom system operating at Q/V and W bands with transceiver(s) located in the area of Rome, NY (USA), and transponders in the 100° W orbital position. Given the lack of direct beacon measurements and the limited availability of radiometric measurements at frequencies higher than 50 GHz, in order to achieve this goal, the first part of the work was devoted to the identification of reliable and accurate propagation prediction models to be used for the assessment of the impairments induced by atmospheric constituents.

The main propagation prediction models available in the literature were reviewed, focusing on models for the estimation of attenuation statistics associated to gases (water vapor and oxygen), clouds and hydrometeors (both effects of rain and of the melting layer), separately, as well as on methodologies for the prediction of rain rate statistics (the main input to any rain attenuation model) and of the advantage, in terms of system availability, achieved using site diversity schemes under rainy conditions. In the review, a clear distinction was underlined between prevalently empirical models and methodologies relying on physical concepts: whilst the former privilege simplicity, indeed the latter turn out to be of key importance for this activity not only because they typically offer increased reliability, especially at high frequencies for which no direct measurements are available for models' testing (e.g. Q to W bands), but also because of their flexibility and consistency (e.g. application of the same mathematical framework to various propagation related issues). In the light of this, specific attention was paid to the description of MultiEXCELL (Multi EXponential CELL) and SMOC (Stochastic MOdel Of Clouds), two models recently conceived at Politecnico di Milano for the simulation of the interaction of SatCom systems with rain fields and cloud fields, respectively. Both models possess a solid physical basis (they have been developed starting from the observation of the main features of rain and cloud fields) and, thus, can be used with confidence to achieve the goals of this study.

Besides MultiEXCELL and SMOC, other propagation models available in the literature and/or recommended by the ITU-R were selected on the basis of their soundness and reliability. Comprehensive tests have been carried out to evaluate the accuracy of such models. In detail, eight models for the prediction of the attenuation statistics were identified and reviewed: Improved Assis-Einloft, Brazilian Unified, Bryant, Crane Two-Component, ITU-R P.618-10, MultiEXCELL, SAM, SC EXCELL. The reference database for rain attenuation used in the testing activity consisted in measurements gathered by Study Group 3 of the International Telecommunication Union – Radio communication sector (ITU-R). Specifically, only experiments performed with beacon receivers with operational frequency higher than 17 GHz have been selected. This choice represents a good compromise between the preference in considering experiments of more interest for this study (focus on higher frequency links) and the need to gather a sufficient number of experiments (49 statistics collected worldwide) for a significant assessment of the models' prediction accuracy. Overall results indicate that the method included in recommendation ITU-R P.618-10 is the best performing one for rain attenuation prediction and that the Assis-Einloft, SAM, Bryant, MultiEXCELL and SC EXCELL models offer a (similar) satisfactory accuracy, though the latter two exhibits the most stable trend of the prediction accuracy as a function of the system outage probability level. For the proper interpretation of these results, it should be kept in

mind that the ITU-R model, notwithstanding its very good performance, is mainly of empirical nature and, in its development, the measured data included in the DBSG3 database (the same one used for the testing activity) have been exploited to optimize the model's coefficients. On the contrary, this is not true for other models such as MultiEXCELL and SC EXCELL which rely on physical concepts and do not include empirically derived expressions. For these reasons, the latter are expected to provide reliable results also outside the frequency range of the measurements currently available (above 50 GHz).

Concerning cloud attenuation statistics, in this study, SMOC and the model included in recommendation ITU-R P.840-5 have been selected for the testing activity. Since no global standardized catalogues of cloud attenuation statistics are available nowadays, measurements for models' testing have been extracted from papers available in the open literature. A total of 17 cloud attenuation statistics collected in 7 sites worldwide were gathered with frequency spanning from 20 to 93 GHz. Results indicate that SMOC is less biased than the ITU-R model and that it is generally more accurate. Tests also highlighted that the prediction error can be split into two parts: a fraction of it is associated with the prediction of the local statistics of integrated cloud liquid water content, $P(L)$, whilst an additional contribution comes from the estimation of the path attenuation starting from $P(L)$. In tight relationship with the latter contribution to the error is the decrease in accuracy shown in the tests when frequency shifts from 20 GHz to 90 GHz. Whilst this effect was found to be very limited for SMOC, it revealed much more marked for the ITU-R model, being likely linked to the increasingly limited suitability of the reduced liquid water content L_{red} for cloud attenuation prediction when L_{red} is used outside the frequency range for which it has been calculated (20-50 GHz). Further advantages of SMOC over the ITU-R model underlined during the tests are the chance to use synthetic clouds fields also for site diversity predictions and a more reasonable prediction of path attenuations also at low elevation angles, where the validity of the simple cosecant scaling adopted in the ITU-R model (which assumes horizontal homogeneity of atmospheric layers) becomes questionable and provides unrealistically high fade values.

Tests were also performed on models aiming to predict the effectiveness of site diversity schemes under rainy conditions. Specifically, the ITU-R model included in recommendation P.618-10, EXCELL and MultiEXCELL were applied to estimate the SatCom system gain and their performance was evaluated against 46 sets of measurements collected worldwide and gathered in the DBSG3 database of ITU-R. Results show that all the three methods provide a similar prediction accuracy, in terms of root mean square of the error, with the ITU-R model providing the highest bias. Notwithstanding the comparable average performance, when considering separately all experiments, tests also highlighted that the prediction accuracy associated to MultiEXCELL is more stable if compared to the results provided by the other two models, which, in turn, provides an increased reliability to the model's users. As a further advantage, MultiEXCELL is more flexible as it clearly allows to easily implement any site diversity scheme with arbitrary number and topology of the stations.

Based on the discussion above, MultiEXCELL and SMOC have been selected for the performance assessment of the SatCom system of interest in this study. First the application scenario has been duly defined by specifying the following electrical and geometrical features: reference site located in Rome, NY; 100° W satellite orbital position; 34.4° link elevation; vertical wave polarization; four operational frequencies selected in the Q/V and W

bands, namely 50, 70, 80 and 90 GHz (60 GHz excluded because of the high absorption peak of oxygen).

The attenuation statistics due to gases have been predicted using recommended ITU-R P.676-9: 70 GHz turns out to be the frequency suffering the most from gaseous absorption, mainly due to the proximity to the 60 GHz oxygen absorption line, whilst the 80 GHz carrier appears as the most advantageous as far as only gases are considered. Overall the gaseous attenuation exceeded for 50% and 1% of the yearly time ranges from 1.25 to 2.91 dB and from 3.31 to 4.87 dB, respectively.

Cloud attenuation statistics have been predicted using both recommendation ITU-R P.840-5 and SMOC, which estimated presence of clouds for 56% and 69% of the yearly time, respectively. As expected from the testing activity performed, the difference between the predictions by the two models was found to increase with frequency. Overall, taking as reference SMOC, clouds tend to have a higher impact on the considered SatCom than the one due to gases for all the four frequencies: the cloud attenuation exceeded for 1% of the yearly time ranges between 3.41 and 7.58 dB.

As a first step towards the prediction of rain attenuation statistics, the rain rate distribution ($P(R)$) for Rome has been derived from recommendation ITU-R P.837-6 and the confidence in its use has been confirmed by the good agreement of such $P(R)$ with the one obtained by converting to 1-minute integration time the long-term rain rate statistics collected with 1-hour integration time in a site close to Rome (Fulton, NY, roughly 80 km far from Rome). MultiEXCELL and the ITU-R model in recommendation P.618-10 have been afterwards employed to estimate rain attenuation statistics. Whilst the curves predicted by the two models are in good agreement for 50 GHz, the ITU-R model was found to predict more and more attenuation than MultiEXCELL as the frequency increases. As shown in [Brost and Cook, 2012], this behavior may be linked to the frequency dependent empirical expressions introduced in the ITU-R model to take into account the horizontal and vertical variability of the rain rate: having been obtained through a regression on existing measurements, such expressions could not be the most appropriate at frequencies higher than 55 GHz. Overall, taking as reference MultiEXCELL, the predicted rain attenuation exceeded for 0.01% of the yearly time (high-availability system) ranges from 70 to 95 dB.

With the aim of assessing the feasibility and overall performance of the SatCom system, total attenuation statistics have been estimated according to two different procedures: using ITU-R recommendations for all the constituents (procedure A); using recommendation ITU-R P.676-9 for gases, SMOC for clouds and MultiEXCELL for rain (procedure B). In both cases, total attenuation statistics have been obtained by applying the combination method recommended in ITU-R P.618-10 (summation of attenuation values on equiprobable basis). Whatever the exceedance probability level considered, the total attenuation statistics estimated using procedure A was found to be always higher than those predicted according to procedure B. Making reference to the latter, as an example of the results obtained, a system margin equal to 82, 105, 111 and 118 dB would be required to guarantee the system availability for 99.99% of the time in a year using 50, 70, 80 and 90 GHz, respectively.

Being impossible to directly counteract such high fades, MultiEXCELL and SMOC have been applied to estimate the effectiveness of site diversity, respectively considering rainy and cloudy (with no rain) conditions. Two reference schemes, with 2 and with 3 stations, have

been investigated to exploit at best the potentialities of the two models. Site separation distances up to 100 km have been considered. Results confirm the effectiveness of site diversity in mitigating rain attenuation: considering low outage probabilities (roughly 0.01%), approximately 60%-65% and 70%-75% of the attenuation can be compensated using two and three stations, respectively. The increase in the gain with distance is quite steep for separation distances approximately shorter than 20 km, after which the gain tends to stabilize. Overall, taking as reference a power margin of 40 dB, a two-site diversity system would experience outage for 2.1×10^{-3}% and 4.4×10^{-2}% of the time in a year at 50 and 90 GHz respectively, whilst the yearly outage time would be lower than 10^{-3}% at 50 GHz and would reduce to 7.1×10^{-3}% at 90 GHz.

As expected the effectiveness of site diversity in mitigating cloud attenuation is rather limited, in tight relationship with the spatial distribution of clouds which tend to preserve a non negligible correlation even for high separation distances: on the average, considering outage probability levels close to 5% (light rain/no rain), approximately 12% and 17% of the attenuation can be compensated using respectively two and three stations at 50 GHz, whilst this percentage increases to roughly 20% and 28% in the two cases at 90 GHz. On the other hand, a considerable advantage was found in shifting from two to three stations, with a percentage increase in the gain in the order of 40%-50% for large separation distances (*D* approximately higher than 40 km). Overall, the maximum gain range (i.e. for outage probabilities close to 1%) in the 50-90 GHz band is 1.06-2.45 dB and 1.4-3.25 dB for two and three stations, respectively: although the gain originating from the spatial inhomogeneity of clouds is not as high as the one associated with rain, nevertheless it would allow to further increase the already high QoS (data rate) typically achievable in nonrainy conditions.

Overall the results obtained in this study indicate the feasibility of the considered SatCom system, provided that site diversity schemes are implemented. High-availability (approximately 99.99% of the yearly time) can be achieved up to 70 GHz using three stations at large distance (approximately higher than 50 km) and a very high margin ($\approx$ 30 dB), whilst more stations are necessary at higher frequencies to obtain the same service level. The use of two stations and the same power margin would guarantee high availability at 50 GHz and below.

Considering the very high frequency range and, therefore, the high sensitivity of radio waves to both clouds and rain, it would be definitely useful to integrate MultiEXCELL and SMOC into a model able to synthesize concurrent rain rate and cloud fields preserving their own features as well as their spatial mutual correlation. This concept, which could also include water vapor fields, would possibly yield more realistic predictions of the total atmospheric attenuation, as well as a means to evaluate more accurately the effectiveness of site diversity in mitigating the attenuation induced by all constituents.

REFERENCES

[Al-Ansafi et al., 2003] K. Al-Ansafi, P. Garcia, J. M. Riera, A. Benarroch, 2003, "A one-year cloud attenuation results at 50 GHz", Electronics Letters,Vol: 39 (1), pp: 136 – 137.

[Altshuler and Marr, 1989] E. Altshuler, R. Marr, 1989, "Cloud attenuation at millimetre wavelengths", IEEE Transactions On Antennas and Propagation, 37, 1473-1479.

[Assis and Einloft, 1977] M. S. Assis, C. M. Einloft, 1977, "A Simple Method for Estimating Rain Attenuation Distributions", Proc. URSI, La Baule, p. 301.

[Barbaliscia et al., 1995] F. Barbaliscia, M. Boumis, A. Martellucci, 1995, "Study of scaling of propagation effects from microwave to optical frequencies", ESA/ESTEC Contract 10195/92/NL/GS.

[Barbaliscia and Paraboni, 2002] F. Barbaliscia, A. Paraboni, "Multiple-Site Attenuation Prediction Models Based on the Rainfall Structures (Stratified and Convective) for advanced TLC or Broadcasting Systems", XXVIIth General Assembly of the International Union of Radio Science, Maastricht, The Netherlands, August 17-24, 2002.

[Bell, 1987] T. L. Bell, 1987, "A Space-Time Stochastic Model of Rainfall for Satellite Remote-Sensing Studies", Journal Of Geophysical Research, Vol. 92, No. D8, pp. 9631-9643.

[Bolea-Alamañac, 2004] A. Bolea-Alamañac, 2004, "Fade Mitigation techniques to optimise the radio resource in a fixed satellite communications link", Ph.D. of SUPAERO, Toulouse, France.

[Bosisio and Riva, 1998] A. V. Bosisio, C. Riva, "A novel method for the statistical prediction of rain attenuation in site diversity systems: theory and comparative analysis against experimental data", Int. J. Satell. Commun., 16, 47-52 (1998).

[Blackmore and Taubvurtzel, 1999] W. H. Blackmore, B. Taubvurtzel, 1999, "Environmental chamber tests on NWS radiosonde humidity sensors", 11th Symposium on Meteorological Observations and Instrumentation, Dallas, TX, Amer. Meteor. Soc., 259–262.

[Brost and Cook, 2012] G. A. Brost, W. G. Cook, 2012, "Analysis of Empirical Rain Attenuation Models for Satellite Communications at Q to W Band Frequencies", EuCAP 2012, pp. 1-5, 26-30 March, Prague, Czech Republic.

[Bryant and Allnut, 1990] D. L. Bryant, J. E. Allnutt, 1990, "Use of closely-spaced height diversity antennas to alleviate the effects of low angle non-absorptive fading on satellite slant paths", Electron. Lett., 26(7) , pp. 479-480.

[Bryant et al., 2001] G. F. Bryant, I. Adimula, C. Riva, G. Brussaard, 1999, "Rain Attenuation Statistics from Rain Cell Diameters and Heights", Int. J. Satell. Commun., 2001; 19: 263-283.

[Brussaard and Watson, 1994] G. Brussaard, P. A. Watson, 1994, "Atmospheric Modelling and Millimetre-Wave Propagation", Chapman-Hall, ISBN: 0-412-56230-8, London.

[Burgueño et al., 1988] A. Burgueño, M. Puicerver, E. Vilar, 1988, "Influence of rain gauge integration on the rain rate statistics used in microwave communications", Ann. Telecommun., 43, 522-527.

[Callaghan and Vilar, 2007] S. Callaghan, E. Vilar, 2007, "Fractal generation of rain fields: synthetic realisation for radio communications systems", Microwaves, Antennas and Propagation, IET, Vol. 1, Issue 6, Dec., Page(s): 1204-1211.

[Capsoni et al., 1987] C. Capsoni, F. Fedi, C. Magistroni, A. Paraboni, A. Pawlina, 1987, "Data and theory for a new model of the horizontal structure of rain cells for propagation applications", Radio Science, Volume 22, Number 3, Pages: 395-404, May-June.

[Capsoni et al., 1987b] C. Capsoni, F. Fedi, A. Paraboni, 1987, "A comprehensive meteorologically oriented methodology for the prediction of wave propagation parameters in telecommunication applications beyond 10 GHz", Radio Science, 22, 387-393.

[Capsoni et al., 2006] C. Capsoni, L. Luini, A. Paraboni, C. Riva, 2006, "Stratiform and convective discrimination deduced from local $P(R)$", IEEE Transactions on Antennas and Propagation, vol. 54, issue 11, pp. 3566-3569, Nov.

[Capsoni et al., 2009] C. Capsoni, L. Luini, A. Paraboni, C. Riva, A. Martellucci, 2009, "A new global prediction model of rain attenuation that separately accounts for stratiform and convective rain", IEEE Transactions on Antennas and Propagation, Vol 57, No. 1, Page(s): 196 - 204.

[Capsoni et al., 2009b] C. Capsoni, L. Luini, R. Nebuloni, A. Paraboni, C. Riva, 2009, "Electromagnetic Propagation at frequencies above 50 GHz: the challenge of the atmosphere", EuCAP 2009, pp.: 2668-2672, 23-27 March, Berlin, Germany.

[Capsoni et al., 2012] C. Capsoni, C. Riva, A. Martellucci, R. Nebuloni, L. Luini, 2012, "W-band Atmospheric Radiowave Propagation - A Challenge for Satellite TLC Systems", ASMS-SPSC 2012, pp. 1-8, 5-7 September, Baiona, Spain.

[Capsoni and Luini, 2009] C. Capsoni, L. Luini, 2009, "A physically based method for the conversion of rainfall statistics from long to short integration time", IEEE Transactions on Antennas and Propagation, vol. 57, no. 11, Page(s): 3692 – 3696.

[Capsoni and Luini, 2013] C. Capsoni, L. Luini, 2013, "The SC EXCELL Model for the Prediction of Monthly Rain Attenuation Statistics", EuCAP 2013, 8-12 April, Goteborg, Sweden.

[Chebil and Rahman, 1999] J. Chebil, T. A. Rahman, 1999, "Rain rate statistical conversion for the prediction of rain attenuation in Malaysia", IEEE Electronics Letters, Volume: 35 Issue: 12, Page(s): 1019-1021;

[COST 255, 2002] COST Action 255 Final Report, 2002, "Precipitation, Clouds and Other Related Non-Refractive Effects", J.P.V. Poiares Baptista, Ed. Noordwijk, The Netherlands: ESA Publication Division, ch. 3.2, March.

[Costa, 1983] E. Costa, 1983, "An analytical and numerical comparison between two rain attenuation prediction method for Earth-satellite paths", Proc. URSI Comm. F, Louvain-la-Neuve, pp. 213.

[Crane, 1978] R. K. Crane, 1978, "A global model for rain attenuation prediction", EASCON Rec., pp. 391-395.

[Crane, 1980] R. K. Crane, 1980, "Prediction of attenuation by rain", IEEE Transaction on Communications, COM-28, pp. 1717-1733.

[Crane, 1982] R. K. Crane, 1982, "A two-component rain model for the prediction of attenuation statistics", Radio Science, Vol. 17, No. 6, pp. 1371-1387.

[D'Amico et al., 1998] M. G. D'Amico, A. R. Holt, C. Capsoni, 1998 , "An anisotropic model of the melting layer", Vol. 33, Issue 3, pp: 535–552, May-June.

[Davies et al., 1998] O. T. Davies, R. G. Howell, P. A. Watson, 1998, "Measurement and modelling of cloud attenuation at millimetre wavelengths", Electronics Letters, 34, 2433-2434.

[Deirmendjian, 1969] D. Deirmendjian, 1969, "Electromagnetic Scattering on Spherical Polydispersions", Elsevier, 290 pp.

[Dintelmann and Ortgies, 1989] F. Dintelmann, G. Ortgies, 1989, "Semi-empirical model for cloud attenuation prediction", Electronics Letters, 25, 1487-1479.

[Dissanayake et al., 1997] A. Dissanayake, J. Allnutt, F. Haidara, 1997, "A prediction model that combines rain attenuation and other propagation impairments along Earth-satellite paths", IEEE Transactions on Antennas and Propagation, Vol. 45, No. 10, pp. 1546-1558.

[Dissanayake et al., 2001] A. Dissanayake, J. Allnutt, F. Haidara, 2001, "Cloud attenuation modelling for SHF and EHF applications", Int. J. Satell. Commun.; 19: 335-345.

[Drufuca, 1974] G. Drufuca, 1974, "Rain attenuation statistics for frequencies above 10-GHz from rain gauge observations", J. Rech. Atmos., 1-2, 399-411.

[Drufuca, 1977] G. Drufuca, 1977, "Radar-derived statistics on the structure of precipitation patterns", J. Appl. Meteorol, 16, 1029-1035.

[Dutton and Dougherty, 1974] E. J. Dutton, H. T. Dougherty, R. F. Jr. Martin, 1974, "Prediction of European rainfall and link performance coefficients at 8 to 30 GHz", Inst. Telecommun. Sci., U.S. Dep. Commerce.

[Eltahir and Bras, 1993] E. A. B. Eltahir, R. L. Bras, 1993, "Estimation of the fractional coverage of rainfall in climate models", J. Climate, Vol. 6, pp. 639-644.

[Emiliani et al., 2009] L. D. Emiliani, L. Luini, C. Capsoni, 2009, "Analysis and parameterization of methodologies for the conversion of rain rate cumulative distributions from various integration times to one minute", IEEE Antennas and Propagation Magazine, Volume 51, Issue 3, Page(s): 70 - 84.

[Emiliani et al., 2010] L. D. Emiliani, L. Luini, C. Capsoni, 2010, "On the optimum estimation of 1-minute integrated rainfall statistics from data with longer integration time", EuCAP 2010, pp. 1-5, 12-16 April 2010, Barcelona, Spain.

[ESA] ESTEC/Contract num. 17877/04/NL/JA, "Recongurable Ka band antenna front end for active rain fade compensation".

[ESA b] ESTEC/Contract num. 18278/04/NL/US, "Assessment of radiowave propagation for satellite communication and navigation systems in tropical and sub-tropical areas".

[Flavin, 1996] R. K. Flavin, 1996, "Satellite link rain attenuation in Brisbane and a proposed new model for Australia", Telstra Research Laboratories, Report N. 8375.

[Féral et al., 2003] L. Féral, H. Sauvageot, L. Castanet, J. Lemorton, 2003, "HYCELL - A new hybrid model of the rain horizontal distribution for propagation studies: Part 1, Modeling of the rain cell", Radio Science, 38(3).

[Féral et al., 2006] L. Féral, H. Sauvageot, L. Castanet, J. Lemorton, F. Cornet, K. Leconte, 2006, "Large-scale modeling of rain fields from a rain cell deterministic model", Radio Science, Vol. 41.

[Fiser, 1986] O. Fiser, 1986, "Interaction of Electromagnetic Field with Rain Medium with Respect to Satellite Links Rain Attenuation Prediction in Frequency Range above 10 GHz", Dissertation, CTU Prague.

[Gibbins and Walden, 2003] C. J. Gibbins, C. J. Walden, 2003, "A study into the derivation of improved rain attenuation regression coefficients", Radiocomunications Agency Contract AY 4359.

[Goldhirsh, 1990] J. Goldhirsh, 1990, "Spatial variability of rain rate and slant path attenuation distributions at 28 GHz in the mid-Atlantic coast region of the United States", IEEE Trans. Ant. and Prop., Vol. 38, Issue 10, Page(s):1711-1716, Oct.

[Goldhirsh et al., 1997] J. Goldhirsh, B. H. Musiani, A. W. Dissanayake, L. Kuan-Ting, 1997, "Three-site space-diversity experiment at 20 GHz using ACTS in the Eastern United States", Proc. IEEE, Vol. 85, pp. 970-980, June.

[Gremont and Filip, 2004] B. C. Gremont, F. Filip, 2004, "Spatio-temporal rain attenuation model for application to fade mitigation techniques", IEEE Trans. Ant. and Prop., Vol. 52, No. 5, May.

[Gunn and Kinzer, 1949] R. Gunn, G. D. Kinzer, 1949, "The Terminal Velocity of Fall for Water Drops in Stagnant Air", Journal of Meteorology, Vol. 6, pp. 243-248.

[Hahn et al., 1996] C. J. Hahn, S. G. Warren, J. London, 1996, "Edited synoptic cloud reports from ships and land stations over the globe", 1982-1991, NDP026B, Carbon Dioxide Information AnalysisCenter, Oak Ridge National Laboratory, Oak Ridge, TN.

[Haïdara et al., 1992] F. Haïdara, T. Pratt, C. W. Bostian, 1992, "Measurement of cross correlation between spaced receivers from the Virginia Tech Olympus experiment", Digest, IEEE Antennas and Propagat. Int. Symp., Chicago, USA, vol. 2, pp. 740-743.

[Hodge, 1982] D. B. Hodge, 1982, "An improved model for diversity gain on Earth-space propagation paths", Radio Sci., 17(6) , 1982, pp. 1393-1399.

[ITU-R P.311-13, 2009] Recommendation ITU-R P.311-13, 2009, "Acquisition, presentation and analysis of data in studies of tropospheric propagation", Propagation in non-ionized media, Geneva.

[ITU-R P.530-10, 2001] Recommendation ITU-R P.530-10, 2001, "Propagation data and prediction methods required for the design of terrestrial line-of-sight systems", Propagation in non-ionized media, Geneva.

[ITU-R P.618-10, 2009] Recommendation ITU-R P.618-10, 2009, "Propagation data and prediction methods required for the design of Earth-space telecommunication systems", Propagation in non-ionized media, Geneva.

[ITU-R P.676-9, 2012] Recommendation ITU-R P.676-9, 2012, "Attenuation by atmospheric gases", Propagation in non-ionized media, Geneva.

[ITU-R P.836-4, 2009] ITU-R Recommendation P.836-4, 2009, "Water vapour: surface density and total columnar content", Propagation in non-ionized media, Geneva.

[ITU-R P.837-6, 2012] ITU-R Recommendation P.837-6, 2012, "Characteristics Of Precipitation For Propagation Modelling", Propagation in non-ionized media, Geneva.

[ITU-R P.838-3, 2005] ITU-R Recommendation P.838-3, 2005, "Specific attenuation model for rain for use in prediction methods", Propagation in non-ionized media, Geneva.

[ITU-R P.839-3, 2001] ITU-R Recommendation P.839-3, 2001, "Rain height model for prediction methods", Propagation in non-ionized media, Geneva.

[ITU-R P.840-5, 2012] ITU-R Recommendation P.840-5, 2012, "Attenuation due to clouds and fog", Propagation in non-ionized media, Geneva.

[ITU-R P.1510, 2001] Recommendation ITU-R P.1510, 2001, "Annual mean surface temperature", Propagation in non-ionized media, Geneva.

[Jeannin et al., 2012] N. Jeannin, L. Féral, H. Sauvageot, L. Castanet, F. Lacoste, 2012, "A Large-Scale Space-Time Stochastic Simulation Tool of Rain Attenuation for the Design and Optimization of Adaptive Satellite Communication Systems Operating between 10 and 50 GHz", International Journal of Antennas and Propagation, vol. 2012, Article ID 749829, 16 pages.

[Karasawa and Matsudo, 1991] Y. Karasawa, T. Matsudo, 1991, "One-minute rain rate distributions in Japan derived from AMeDAS one-hour rain rate data", IEEE

Transaction on Geoscience and Remote Sensing, Volume: 29, Issue: 6, Page(s): 890-898.

[Konefal et al., 2000] T. Konefal, P. A. Watson, A. K. Shukla, A. Akram, 2000, "Prediction of monthly and annual availabilities on 10-50 GHz satellite to Earth and aircraft to aircraft links", IEE Proceedings – Microwaves, Antennas and Propagation, 147(2), 122-127.

[Kourogiorgas et al., 2012] C. I. Kourogiorgas, A. D. Panagopoulos, J. D. Kanellopoulos, 2012, "On the Earth-Space Site Diversity Modeling: A Novel Physical-Mathematical Outage Prediction Model", IEEE Transactions on Antennas and Propagation, vol. 60, no. 9, Page(s): 4391 – 4397, Sep.

[Lane and Stutzman, 1980] S. O. Lane, W. L. Stutzman, 1980, "A Gaussian rain cell model for prediction of rain effects on millimeter wave propagation", Rep. SATCOM-80-3 under NASA contract NAS5–22577, VA. Polytech. Inst. and State Univ., Electr. Eng. Dep., Blacksburg, VA.

[Leitao and Watson, 1986] M. J. Leitao, P. A. Watson, 1986, "Method for prediction of attenuation on Earth-space links based on radar measurements of the physical structure of rainfall," IEE Proceedings , Vol. 133, Pt. F, No.4, Jul.

[Liebe et al., 1993] H. J. Liebe, G. A. Hufford, M. G. Cotton, 1993, "Propagation modeling of moist air and suspended water/ice particles at frequencies below 1000 GHz", in Proc. AGARD 52nd Spec. Meeting EM Wave Propag. Panel, Palma De Maiorca, Spain, pp. 3.1–3.10.

[Liljegren et al., 2005] J. C. Liljegren, S. A. Boukabara, K. Cady-Pereiria, S. A. Clough, 2005, "The Effect of the Half-Width of the 22-GHz Water Vapour Line on Retrievals of Temperature and Water Vapour Profiles with a Twelve-Channel Microwave Radiometer", IEEE Trans. Geosci. Rem. Sensing, 43, 1102-1108.

[Luini et al., 2007] L. Luini, C. Riva, C. Capsoni, A. Martellucci, 2007, "Attenuation in non rainy conditions at millimeter wavelengths: assessment of a procedure", IEEE Transactions on Geoscience and Remote Sensing, pp. 2150-2157, Vol. 45, Issue 7, July.

[Luini and Capsoni, 2011] L. Luini, C. Capsoni, 2011, "MultiEXCELL: a new rain field model for propagation applications", IEEE Transactions on Antennas and Propagation, vol. 59, no. 11, Page(s): 4286 – 4300, Nov.

[Luini and Capsoni, 2012] L. Luini, C. Capsoni, 2012, "Estimating the Spatial Cumulative Distribution of Rain from Precipitation Amounts", Radio Sci., 47, RS1005.

[Luini and Capsoni, 2012b] L. Luini, C. Capsoni, 2012, "A Methodology to Generate Cloud Attenuation Fields From NWP Products", EuCAP 2012, pp. 1-5, 26-30 March, Prague, Czech Republic.

[Luini and Capsoni, 2012c] Luini, C. Capsoni, 2012, "The Impact of Space and Time Averaging on The Spatial Correlation of Rainfall", Radio Sci., 47, RS3013, doi:10.1029/2011RS004915.

[Marshall and Bostian, 1982] R. E. Marshall, C. W. Bostian, 1982, "Using site diversity reception to overcome rain depolarization in millimeter wave satellite communications systems", IEEE Trans. Antennas Propag., AP-30(5) , 1982, pp. 990-991.

[Martellucci et al., 2002] A. Martellucci, J. P. V. Poiares-Baptista, G. Blarzino, 2002, "New climatological databases for ice depolarisation on satellite radio links", paper presented at COST Action 280, First Int. workshop, PM3037, Jul.

[Matricciani, 1991] E. Matricciani, 1991, "Rain attenuation predicted with two-layer rain model", European Transactions on Telecommunication, 2(6), 715-727.

[Matricciani, 1994]   E. Matricciani, 1994, "Prediction of site diversity performance in extension of the two layer rain model", Eur. Trans. Telecommun., 5(3) , pp. 27-36.

[Matricciani, 2008]   E. Matricciani, 2008, "Global formulation of the Synthetic Storm Technique to calculate rain attenuation only from rain rate probability distributions", IEEE International Symposium on Antennas and Propagation, San Diego, Jul.

[Mattioli et al., 2005] V. Mattioli, E. R. Westwater, S. Gutman, V. Morris, 2005, "Forward Model Studies of Water Vapour using Scanning Microwave Radiometers, Global Positioning System and Radiosondes during the Cloudiness Inter-Comparison Experiment", IEEE Trans. Geosci. and Rem. Sens., 43 (5), pp. 1012-1021.

[Mattioli et al., 2007] V. Mattioli, E. R. Westwater, D. Cimini, J. S. Liljegren, B. M. Lesht, S. I. Gutman, F. J. Schmidlin, 2007, "Analysis of Radiosonde and ground-based remotely sensed PWV data from the 2004 North Slope of Alaska Arctic Winter Radiometric Experiment", AMS Journal of Atmospheric and Oceanic Technology, vol. 24, Issue 3, pp. 415-431.

[Miloshevich et al., 2006] L. M. Miloshevich, H. Vömel, D. N. Whiteman, B. M. Lesht, F. J. Schmidlin, F. Russo, 2006, "Absolute accuracy of water vapour measurements from six operational radiosonde types launched during AWEX-G and implications for AIRS validation", J. Geophys. Res., 111, D09S10, doi:10.1029/2005JD006083.

[Misme and Waldteufel, 1980] P. Misme, P. Waldteufel, 1980, "A model for attenuation by precipitation on a microwave earth-space link", Radio Science, 15, p. 655.

[Moupfouma and Martin, 1995] F. Moupfouma, L. Martin, 1995, "Modelling of the rainfall rate cumulative distribution for the design of satellite and terrestrial communication systems", International Journal of satellite communications, Page(s): 105-115, vol.13.

[Northrop, 1975] P. Northrop, 1975, "A Clustered Spatial-Temporal Model of Rainfall", Proceedings: Mathematical, Physical and Engineering Sciences, Vol. 454, No. 1975 (Jul. 8, 1998), pp. 1875-1888.

[Oguchi, 1983] T. Oguchi, 1983, "Electromagnetic wave propagation and scattering in rain and other hydrometeors", Proc. IEEE, vol. 71, pp. 1029-1077.

[Onof and Wheater, 1996] C. Onof, H. Wheater, 1996, "Analysis of the spatial coverage of British rainfall fields", Journal of Hydrology, 176 (1996), 97-113.

[Paraboni et al., 2011] A. Paraboni, A. Martellucci, C. Capsoni, C. Riva, 2001, "The Physical Basis of Atmospheric Depolarization in Slant Paths in the V Band: Theory, Italsat Experiment and Models", IEEE Transactions on Antennas and Propagation, 59(11), 4301–4314.

[Pavageau et al., 2001] A. Pavageau, L. Castanet, C. Riva, J. P. V. Poiares Baptista, 2001, "Test of rain attenuation and total attenuation prediction models for Earth-space paths", ITU-R 3J-3M meeting, Budapest, Hungary.

[Pawlina and Binaghi, 1995] A. Pawlina, M. Binaghi, 1995, "Radar rain intensity fields at ground level: new parameters for propagation impairments prediction in temperate regions", 7th Commission F, Triennal Symposium, URSI, Ahmedabad, India.

[Poiares Baptista, 1994] J. P. V. Poiares Baptista (General Editor), 1994, "OPEX Reference Book on Radar", Second Workshop of the OLYMPUS Propagation Experimenters, ESA WPP-083, 1, ESA ESTEC, Noordwijk, The Netherlands.

[Pruppacher and Klett, 1980] H. R. Pruppacher, J. D. Klett, 1980, "Microphysics of Clouds and Precipitation", Kluwer Academic Publishers.

[Ray, 1972] P. S. Ray, 1972, "Broadband complex refractive indices of ice and water", Appl. Opt., Vol. 11, pp. 1836-1844.

[Raynaud et al., 2000] L. Raynaud, I. Chenerie, J. Lemorton, 2000, "Modeling of Radiowave Scattering in the Melting Layer of Precipitation", IEEE Transactions on Geoscience and Remote Sensing, 38(4), 1574–1584.

[Riva, 2002] C. Riva (Editor), 2002, "Testing of Prediction Models", Chapter 2.6 of COST 255 Final Report "Radiowave propagation modelling for SatCom services at Ku-band and above", ESA Publications Division, SP-1252.

[Riva et al., 2006] C. Riva, C. Capsoni, M. D'Amico, L. Luini, E. Matricciani, A. Paraboni, L. Castanet, T. Deloues, V. Fabbro, L. Feral, F. Lacoste, J. Lemorton, E. Kubista, T. Prechtl, M. Schönhuber, 2006, "Characterisation and Modelling of Propagation Effects in 20-50 GHz Band", Final report for the European Space Agency under ESTEC Contract No. 17760/03/NL/JA.

[Rice and Holmberg, 1973] P. L. Rice, N. R. Holmberg, 1973, "Cumulative time statistics of surface point rainfall rates", IEEE Trans. Commun., vol. COM-21, pp. 1131-1136.

[Rosenkranz, 1998]   P. W. Rosenkranz, 1998, "Water Vapour Microwave Continuum Absorption: A Comparison of Measurements and Models", Radio Science, 33, 4, 919-928.

[Salonen et al., 1990] E. Salonen, S. Karhu, P. Jokela, W. Zhang, S. Uppala, H. Aulamo, S. Sarkkula, 1990, "Study of propagation phenomena for low availabilities", Final Report for the European Space Agency under ESTEC contract 8025/88/NL/PR, Nov., 316 p.

[Salonen et al., 1991] E. Salonen, S. Uppala, J. P. V. Poiares-Baptista, 1991, "Prediction of cloud attenuation", First OPEX Workshop Proceedings, Noordwijk, 3.6.1-11.

[Salonen and Uppala, 1991] E. Salonen, S. Uppala, 1991, "New prediction method of cloud attenuation", Electronics Letters, 27(12), 1106 1108.

[Salonen et al., 1994] E. Salonen, S. Karhu, S. Uppala, R. Hyvönen, 1994, "Study of improved propagation predictions", Final Report for ESA/ESTEC Contract 9455/91/NL/LC(SC), Helsinki University of Technology and Finnish Meteorological Institute.

[Segal, 1986] B. Segal, 1986, "The influence of rain gauge integration time on measured rainfall-intensity distribution functions", J. Atmos. Oceanic Technol., 3(4), 662-671.

[Shettle, 1989]   E. P. Shettle, 1989, "Models of aerosols, clouds and precipitation for atmospheric propagation studies", in AGARD conference 454(15), pp:. 1-13.

[Silva Mello and Pontes, 2012] L. da Silva Mello, M. S. Pontes, 2012, "Unified method for the prediction of rain attenuation in satellite and terrestrial links", J. Microw. Optoelectron. Electromagn. Appl., vol.11, no.1, São Caetano do Sul, June.

[Stutzman and Dishman, 1984] W. L. Stutzman, W. K. Dishman, 1984, "A simple model for the estimation of rain-induced attenuation along earth-space paths at millimeter wavelengths", Radio Science, Vol. 19, p. 946.

[STD ATM]   U.S. Standard Atmosphere, 1976, Report Number: NASA-TM-X-74335; NOAA-S/T-76-1562, 241 pages, U.S. Government Printing Office, Washington, D.C.

[Turner et al. 2003] D. Turner, B. M. Lesht, S. A. Clough, J. C. Liljegren, H. E. Revercomb, D. C. Tobin, 2003, "Dry bias and variability in Vaisala RS80-H radiosondes: The ARM experience", J. Atmos. Oceanic Technol., 20, 117–132.

[Uppala et al., 2005] S. M. Uppala, P. W. Kallberg, et al., 2005, "The ERA-40 Re-analysis", Quart. J. Roy. Meteor. Soc., 131, pp. 2961-3012.

[Van de Hulst, 1957] H. C. Van de Hulst, 1957, "Light Scattering by Small Particles", Wiley (NY, 1957; Dover, NY, 1981).

[Vömel et al., 2003] H. Vömel, M. Fujiwara, M. Shiotani, F. Hasebe, S. J. Oltmans, J. E. Barnes, 2003, "The behavior of the Snow White chilled-mirror hygrometer in extremely dry conditions", J. Atmos. Oceanic Technol., 20, 1560–1567.

[von Hardenberg et al., 2003] J. von Hardenberg, L. Ferraris, A. Provenzale, 2003, "The shape of convective rain cells", Geophysical Res. Lett., Vol. 30, No. 24.

[Westwater et al., 2003] E. R. Westwater, B. Stankov, D. Cimini, Y. Han, J. A. Shaw, B. M. Lesht, C. N. Long, 2003, "Radiosonde Humidity Soundings and Microwave Radiometers during Nauru99", J. Atmos. Oceanic. Technol., 20 (7), 953-971.

[Wrench et al., 1999] C. L. Wrench, P. G. Davies, J. Ramsden, 1999, "Global prediction of slant path attenuation on Earth space links at EHF", International Journal of Satellite Communications, 17, 177-186.

[Zhang et al., 1996] W. Zhang, J. Tervonen, E. Salonen, 1996, "Backward and forward scattering by the melting layer composed of spherical hydrometeors at 5-100 GHz", IEEE Transactions On Antennas and Propagation, 44(9), 1208-1219.

LIST OF SYMBOLS, ABBREVIATIONS, AND ACRONYMS

ACM	Adaptive Coding and Modulation
ACTS	Advanced Communications Technology Satellite
CAPPI	Constant Altitude Plane Position Indicator
CCDF	Complementary Cumulative Distribution Function
CDF	Cumulative Distribution Function
CETUC	Centro de Estudos em Telecomunicações
COST	European Cooperation in Science and Technology
DAH	Dissanayake-Allnut-Haidara
DBSG3	Data Base Study Group 3
DSD	Drop Size Distribution
EBCM	Extended Boundary Condition Method
ECMWF	European Centre for Medium-range Weather Forecast
EO	Earth Observation
ERA15	ECMWF Re-Analysis 15
ERA40	ECMWF Re-Analysis 40
ESA	European Space Agency
EXCELL	EXponential CELL
EXCELL RSC	EXponential CELL Rainfall Statistics Conversion
FERAS	FUB/ESA RAdio Sonde
FIM	Fredholm-Integral-Method
FMT	Fade Mitigation Techniques
FUB	Fondazione Ugo Bordoni
GARP	Global Atmospheric Research Programme
GATE	GARP Atlantic Tropical Experiment
HUT	Helsinki University of Technology
HYCELL	HYbrid CELL
IAD	InterAggregate Distance
ICD	InterCellular Distance
ITU-R	International Telecommunication Union – Radio communication sector
LR	Long Range
M&P	Marshall and Palmer
MLE	Maximum Likelihood Estimation
MODIS	MODerate resolution Imaging Spectroradiometer
MPM93	Microwave Propagation Model 1993
MultiEXCELL	Multi EXponential CELL
NASA	National Aeronautics and Space Administration
NCEP	National Centers for Environmental Predictio
NND	Nearest Neighbor Distance
NNIAD	Nearest Neighbor InterAggregate Distance
NNICD	Nearest Neighbor InterCellular Distance
NOAA	National Oceanic and Atmospheric Administration

NPC	Nastri Pioggia Cartesianizzati
NWP	Numerical Weather Prediction
PDF	Probability Density Function
POLIMI	Politecnico di Milano
PPI	Plane Position Indicator
PSD	Particle Size Distribution
QoS	Quality of Service
RAOBS	RAdio sonde OBServation
RMS	Root Mean Square
RTE	Radiative Transfer Equation
SAM	Simple Attenuation Model
SatCom	Satellite Communications
SC EXCELL	Stratiform/Convective EXponential CELL
SMOC	Stochastic MOdel of Clouds
SST	Synthetic Storm Technique
STD	Standard Deviation
TOGA-COARE	The Tropical Ocean Global Atmosphere Coupled Ocean-Atmosphere Response Experiment
ULPC	Up Link Power Control
UTC	Coordinated Universal Time
VSAT	Very Small Aperture Terminals